

HIGH-THROUGHPUT SYNTHESIS OF METAL–ORGANIC FRAMEWORKS IN A CONTINUOUS FLOW REACTOR

by

Sujay Dilip Bagi

M.S., Materials Science & Engineering, The University of Texas at Arlington (2012)
B.E., Mechanical Engineering, B.M.S. College of Engineering (2009)

Submitted to the Department of Mechanical Engineering
in partial fulfillment of the requirements for the degree of

Doctor of Philosophy in Mechanical Engineering

at the

MASSACHUSETTS INSTITUTE OF TECHNOLOGY

September 2021

© Massachusetts Institute of Technology 2021. All rights reserved.

Author
Department of Mechanical Engineering
July 16, 2021

Certified by
Yuriy Román-Leshkov
Professor of Chemical Engineering
Thesis Supervisor

Accepted by
Nicolas Hadjiconstantinou
Professor of Mechanical Engineering
Chairman, Committee on Graduate Students

High-Throughput Synthesis of Metal–Organic Frameworks In A Continuous Flow Reactor

By

Sujay Dilip Bagi

Submitted to the Department of Mechanical Engineering on July 16, 2021
in partial fulfillment of the requirements for the degree of
Doctor of Philosophy in Mechanical Engineering

Abstract

Metal–organic frameworks (MOFs) are promising materials for a wide range of applications given their chemical stability and structural tunability. MOFs are crystalline coordination complexes consisting of organic linkers and inorganic polynuclear metal clusters forming highly ordered 2D and 3D structures. The past decade has seen an exponential growth in the number of new MOF structures reported in the literature and their potential applications in water harvesting, carbon capture, gas storage, catalysis, separation, among others. A major bottleneck in widespread deployment of MOF-based platforms stem from the high cost of synthesis in traditional batch reactors that use excess solvents, require long crystallization times, suffer from low yields and intrinsic inefficiencies in heat/mass transfer processes. This thesis focuses on developing low-cost, high-throughput and energy-efficient synthesis routes using a continuous flow reactor for MOFs used in Atmospheric Water Capture (AWC) and Zr MOFs with coordinatively unsaturated open metal sites.

The first part of the thesis describes the modules used in the flow reactor platform, design of heated reaction zone (crystallizer), injection strategies for viscous reaction mixtures and scale-up scenarios. The flow platform is then used to develop a continuous manufacturing process for MOF-808—a Zr-MOF widely studied as a catalyst and an adsorbent in industrially important processes—that can achieve high process yields with minimal solvent use. Under flow optimized conditions (150 °C, 5 min), the *N,N*-dimethylformamide solvent and formic acid modulator amounts were decreased by 84% and 67% in volume, respectively, and resulted in an increase in productivity (defined in units of $kg_{MOF} m^{-3} day^{-1}$) by two orders of magnitude with similar yields, compared to the established batch synthesis (130 °C, 48 hours). A techno-economic model based on laboratory-demonstrated synthesis routes was developed to compare energy and cost savings for the flow system compared to batch, indicating that solvent use was the largest contributor to the overall cost. The flow platform was then used to evaluate the kinetics of crystallization for MOF-808 using time resolved powder X-ray diffraction measurements. The role of temperature and linker concentration on MOF-808 crystallization were investigated by determining the rate constants for nucleation (k_N) and growth (k_G), which are obtained from non-linear fitting of the crystallization curves with the Gualtieri model. The activation energies

obtained using Arrhenius plots for nucleation ($E_a(N)$) and growth ($E_a(G)$) are $64.7 \pm 4 \text{ kJ mol}^{-1}$ and $59.2 \pm 5 \text{ kJ mol}^{-1}$ respectively. The use of higher flow rates at the same residence time and temperature resulted in higher crystal sizes with a narrow CSD—a simpler route for controlling crystal sizes. Finally, the flow platform is employed for process intensification of $\text{Ni}_2\text{Cl}_2(\text{BTDD})$ MOF synthesis—an optimal candidate for AWC which has tremendous potential to address global shortage of clean drinking water. Flow synthesis achieved higher yields, reduced solvent volume by ~50% with a simultaneous increase in process productivity by 3-fold. A computational fluid dynamics (CFD) model was developed to quantitate productivity enhancements in the flow reactor based on improved heat-transfer rates, larger surface-area to volume ratios, and effective residence times. This work adds critical facets to the growing body of research suggesting that the synthesis of MOFs in flow reactors offers unique opportunities to increase production rates and reduce synthesis costs.

Thesis Committee:

- Prof. Yuriy Román-Leshkov (Supervisor), Professor of Chemical Engineering
- Prof. Ahmed Ghoniem (Chair), Professor of Mechanical Engineering
- Prof. A. John Hart, Professor of Mechanical Engineering

Acknowledgements

This thesis was a culmination of my work over the past 4.5 years at MIT and I am sincerely indebted to a lot of my colleagues, friends, and family who constantly supported and cheered me through all the vicissitudes of grad school. First, I would like to thank my advisor Prof. Yuriy Román who gave me an opportunity to work in his group and to help me become the scientist I am today. I've always admired and at times awestruck with your enthusiasm for research, constantly pushing the boundaries of the field and the crazy suggestions which I'd have never pursued if it wasn't for you. I am forever grateful for giving me full responsibility and independence to pursue ideas be it MOF synthesis or building high-throughput reactors both batch & flow, and encouraging me to discuss all my ideas and concerns freely in our meetings. There are many valuable lessons I learnt working for you, which I'll proudly take with me in my future endeavors. I'm also incredibly grateful to have a wonderful thesis committee comprising of Prof. Ahmed Ghoniem and Prof. A. John Hart whose feedback and suggestions for research directions have been invaluable. I'd also like to thank Prof. Mircea Dincă and Prof. Allan Myerson for our collaboration on MOF synthesis and elucidating kinetics of crystallization. I'd like to thank Dr. Tian Tian, Prof. Wai Cheng, Prof. Timothy Gutowski, Dr. Carl Justin Kamp, Leslie Regan, and Janet Maslow for your guidance and support through my time at MIT.

Reaching this point was not possible without the support of my colleagues in the Román group. All the invaluable suggestions from porous materials subgroup (Soonhyoung, Shuai, John, Hussain, Ydna, Blake, Kim) helped me in advancing my research and create innovative solutions for hard problems. Beyond the science, I also want to thank my other labmates and friends Thejas, Amber, Maddie, Julie, Bhavish, Mickey, Kaylee, Alexi for your support and encouragement. I would like to thank the Román group alumni Manish, Stan, Daniel, Mark, Will, Eric and Jen for fruitful discussion on diverse set of topics. I'd like to acknowledge the support from Tata Center, especially Rob, Jason, Diane and Chintan. I will always cherish my time working with the center on various projects. There is a long list of friends at MIT and elsewhere who made me feel at home; I cannot thank you enough for it. All the time I spent with you exploring the city, hiking, sailing, biking, going on fun trips among others, have had a major role in making my time at MIT more enjoyable and meaningful. Looking forward to more adventures with you all in the near future. Lastly and most importantly, a very big thank you to my family. Mom and Dad, you went

through enormous sacrifices to ensure my life was comfortable and always stood by me. Thank you for being wonderful role models and your values, love and affection made me the person I have become today and I couldn't have hoped for anything better. I'm glad to have an amazing brother Sourabh who always cheered me. And finally, a big thank you to my fiancée Parnika. You are one of the most amazing people I have known and I am so grateful to be with you. Your unconditional love & steadfast support mean the world to me.

Table of Contents

Abstract.....	3
Acknowledgements.....	5
Table of Contents.....	7
List of Figures.....	10
List of Tables.....	18
1. Brief Introduction to Metal–Organic Frameworks (MOFs).....	22
1.1. Organic and Inorganic Building Units.....	22
1.2. Stability of MOFs.....	24
1.3. Synthesis Routes for MOFs and Challenges to Scaling-up the Production.....	28
1.4. Potential Applications of MOFs.....	32
1.4.1. Sorbents for Atmospheric Water Capture (AWC).....	33
1.5. Aims and Scope of Thesis.....	35
2. Developing a Modular Flow Reactor Platform for Accelerated Crystallization of MOFs and Zeolites.....	37
2.1. Introduction.....	37
2.2. Experimental Apparatus.....	37
2.3. Scale-up Strategies for Flow Synthesis.....	45
2.4. Product Ecosystem Approach for the Flow Synthesis Platform.....	47
3. Continuous Flow Chemistry Approach for Ultrafast and Low-Cost Synthesis of MOF-808 ..	50
3.1. Introduction.....	50
3.2. Results and Discussion.....	52
3.3. Conclusions.....	62
3.4. Supporting Information.....	63

3.4.1. Materials and Methods.....	64
3.4.2. Techno-economic Analysis (TEA)	66
4. Elucidating Solvothermal Crystallization of MOF-808 in a Continuous Flow Reactor and Effects of Mixing on Crystal Size Distribution.....	95
4.1. Introduction.....	95
4.2. Results and Discussion	97
4.3. Conclusions.....	108
4.4. Supporting Information.....	109
4.4.1. Materials and Methods.....	110
4.4.2. Evaluation of Kinetic Data with Avrami–Erofeev Model	111
4.4.3. Influence of Mixing Effects on CSD	112
5. Accelerated synthesis of Ni ₂ Cl ₂ (BTDD) metal–organic framework in a continuous flow reactor for atmospheric water capture.....	130
5.1. Introduction.....	130
5.2. Results and Discussion	132
5.3. Conclusions.....	142
5.4. Supporting Information.....	142
5.4.1. Materials and Methods.....	142
5.4.2. Synthesis Scale-up	146
6. A Compact Device for Practical Atmospheric Water Harvesting	164
6.1. Introduction and Motivation	164
6.2. Results and Discussion	166
6.2.1. Device Operation	167
6.2.2. Computational Models.....	173
6.2.3. Device Fabrication and Assembly	176
7. Conclusions and Outlook.....	178

7.1. Conclusions.....	178
7.2. Outlook and Future Work	181
7.2.1. Future Work	182
References.....	185

List of Figures

Figure 1-1 The reticular table showing select binary combinations of linker and SBU geometries encountered in MOFs. Figure adapted from Kalmutzki et al. ²	23
Figure 1-2 (a) Basic geometries used in the synthesis of MOFs and (b) commonly used organic units in the construction of linkers. Figure adapted from Yaghi et al. ¹	25
Figure 1-3 Degradation of UiO-66 (Zr-oxo clusters and Terephthalic acid linker) in presence of water, HCl and NaOH. Figure adapted from Kalmutzki et al. ⁷	27
Figure 2-1 Three stage modular design for continuous flow synthesis apparatus.	39
Figure 2-2 Cross-section for Stage 1 and 3 of the Continuous Flow Reactor Platform.	40
Figure 2-3 Phenomenological model of crystallization using a biphasic slug flow generated from two immiscible fluids in a T-junction.	41
Figure 2-4 Biphasic liquid-liquid slug flow showing a droplet of zeolite gel (dispersed phase) flowing in a tube with 1/16" ID.	43
Figure 2-5 (a) Schematic of T-junction using SS (Stainless Steel) capillary inserts. (b) Schematic of T-junction using PTFE capillary insert. (c) Modular T-junction apparatus that is used for creating miniaturized droplets of reagents (rather than slugs created by standard T-junction)....	43
Figure 2-6 (a) Schematic of capillary T-junction with heating tape wrapped around the stem. (b) Variac can be used to modulate temperature subjected to the precursor at the T-joint before injection. (c) Schematic showing the use of surfactant in the continuous phase (oil) that can help in keeping reagent slugs apart and prevent them from agglomeration, which otherwise may lead to reactor clogging with crystallized solids.....	44
Figure 2-7 Experimental setup and schematic showing reinforced BD plastic syringe, which can be used to inject highly acidic precursors (pH < 2).	45
Figure 2-8 Proposed scale-up scheme for the platform by increasing the tube diameter.	46
Figure 2-9 Comparing variations in Reynolds number (Re) and SA/Vol. with increasing flow rate. Calculations.....	47
Figure 2-10 Product Ecosystem for a High-Throughput Flow Synthesis Platform.	48
Figure 2-11 An overview of different modules and functional blocks for an automated Flow Synthesis Platform.	49

Figure 3-1 (a) Synthesis scheme for MOF-808 showing flow and batch routes. (b) PXRD patterns showing evolution of crystallinity with residence time for samples synthesized in flow at 150 °C, compared to batch (130 °C, 48 h). (c) TEM images showing morphology of microcrystalline MOF-808 nanoparticles at short residence times (1 to 15 min) and the corresponding batch sample. 54

Figure 3-2 Chemical design space of MOF-808 explored using flow synthesis at 150 °C by varying (a) residence time and solvent composition (FA:DMF) and (b) H₃BTC linker concentration and solvent composition (FA:DMF) on product crystallinity at 15 min residence time. The linker concentration in the precursor mixture in (a) is three times higher than batch composition, while M:L = 3 is maintained for all conditions explored. Red and blue circles represent amorphous and semi-crystalline regions, while green squares denote crystalline region in the chemical space. The labels for every data point represents the relative crystallinity in percentage (% RC). 57

Figure 3-3 (a) N₂ adsorption (closed symbol) and desorption (open symbol) isotherm at 77 K for samples synthesized in batch and flow. (b) Pore size distribution (PSD) for all samples computed using NLDFT method. 59

Figure 3-4 Comparison of process productivity (*kgMOF m⁻³ day⁻¹*) and BET surface area (*m² g⁻¹*) for flow synthesized MOF-808 as a function of residence time (min) compared to batch with a reaction time of 48 h. (b) Thermal energy input required to crystallize a gram of MOF for batch and flow syntheses. Additional details on the TEA model and assumptions are listed in SI. 62

Figure 3-5 (a) Continuous flow-reactor setup used for the synthesis and optimization of MOF-808. (b) Bubble-point pressures of multiple reaction components calculated by Aspen. 72

Figure 3-6 (a) PXRD patterns for MOF-808 synthesized in flow, showing different levels of crystallinity (shades of green), compared against batch sample and simulated pattern. (b) Background correction scheme used for semi-crystalline sample to quantify intensity contributions in PXRD patterns originating from crystalline phase in the sample. A hump in the low 2 theta region indicates 73

Figure 3-7 SEM images for MOF-808 synthesized in in flow (a-e), at 150 °C and short residence times (1, 2, 3, 5 and 15 min) compared to batch sample (130 °C and 48 h). Green labels on individual nanoparticles indicate average size of the solids obtained. 74

Figure 3-8 TEM images for MOF-808 synthesized in in flow (a-e), at 150 °C and short residence times (1, 2, 3, 5 and 15 min) compared to batch sample (130 °C and 48 h). Red labels on individual nanoparticles indicate average 75

Figure 3-9 Morphology of isolated MOF-808 nanoparticles synthesized at 3, 15 and 60 min residence time in flow at 150 °C. (d) SAED (Selected Area Electron Diffraction) pattern for MOF-808 synthesized at 60 min. The diffuse concentric rings from a single nanoparticle sample in SAED could result from damage to the sample due to the electron beam in the TEM column. (e) Unit cell of MOF-808 (FCC lattice, $a = 35.076 \text{ \AA}$) viewed in (111) direction highlighted using a red plane. 76

Figure 3-10 Average crystal sizes for MOF-808 nanoparticles measured from TEM and SEM images correlate well. Nearly 60 measurements were made on nanoparticles for each synthetic condition in flow and batch; their averages and corresponding error bars are reported. For the residence time of 77

Figure 3-11 Ternary phase diagram exploring the chemical design space for MOF-808 at 150 °C and 15 min residence time. Axes for H_3BTC (Benzene-1,3,5-tricarboxylic acid) linker, Zr metal and Formic acid are in mole fractions. Synthesis compositions with a molar ratio of Metal:Linker ($M:L = 1$) are preferred to synthesize single crystals, while $M:L = 3$ is used for microcrystalline powder samples. 78

Figure 3-12 Plot of linear region of the BET equation satisfying the first criterion for application of BET theory from N_2 isotherm. Isotherm data-points lying within 0.05-0.15 P/P_0 were selected. Panel (a-g) shows curve fitting and R^2 values obtained from linear regression for flow-synthesized samples with residence time of 1, 3, 5, 15, 30, 60, and 120 min, while panel (h) is from batch.. 79

Figure 3-13 (a) TGA trace for batch and flow samples showing weight loss (%) with temperature at heating rate of $5 \text{ }^\circ\text{C}\cdot\text{min}^{-1}$ in air. (b) Derivative weight loss for all samples indicating greatest rate of change on the weight loss curves. 80

Figure 3-14 (a) Simplified block diagram for batch and flow synthesis of MOFs showing flow of materials, energy consumed and waste generation for each unit operation. (b) System boundary for the TEA model used to compare the baseline (batch synthesis) with flow synthesis. Startup/shutdown costs and associated energy consumption are considered in the model. 81

Figure 3-15 Illustration of Scenarios 1 and 2 for batch and flow syntheses that are modeled in the study. Volume of the reaction vessel required to synthesize equivalent amount of MOF in both scenarios is highlighted. 82

Figure 3-16 (a) Total cost of MOF synthesis for batch and flow under two scenarios modeled. The costs represent minimum cost for MOF-808 production under a typical lab-scale environment. (b) Breakdown of materials cost for batch and flow synthesis comprising of metal salt, linker, modulator and solvents. 82

Figure 3-17 Cost incurred from the use of (a) DMF and (b) FA (Formic Acid), with scaling-up the batch and flow syntheses to manufacture MOF-808 at industrial-scale (tens of kilograms) from lab-scale (several grams), assuming constant process yields. The difference in cost between batch and flow syntheses at 10, 30 and 50 kg are highlighted. Slope of the lines represent \$ spent on DMF or FA per *gMOF* (gram of MOF synthesized). 83

Figure 3-18 Process energy intensity (*kWh g⁻¹*) and corresponding process emissions (*kgCO₂ – eq g⁻¹*) for batch and flow syntheses providing an overview of energy consumption and GHG emissions normalized to a gram of MOF synthesized. Additional details on the TEA model and assumptions are listed in SI. 84

Figure 3-19 Sensitivity analysis performed to evaluate influence of electricity cost (\$/kWh) on total cost of MOF synthesis. Base electricity cost used in the analysis is \$0.12 per kWh. 85

Figure 4-1 Extent of crystallization αt plotted against time t (closed symbols) and the corresponding Gualtieri fitting (solid curves) to investigate (a) influence of reaction temperature (110 °C to 150 °C) at 3X linker concentration, and (b) influence of linker concentration (1X to 3X) at 150 °C on the rates of crystallization. 102

Figure 4-2 Extent of crystallization αt plotted against time t (closed symbol) and the corresponding Gualtieri fitting (red curve) as well as probability of nucleation PN (blue curve). The crystallization curve was obtained at 130 °C with a linker concentration of 3X. 103

Figure 4-3 Arrhenius plots for the temperature-dependent rate constants of nucleation (red circles) and growth (grey squares) obtained from evaluation of the Gualtieri model. 105

Figure 4-4 (a) Schematic representation of biphasic liquid-liquid slug flow at different volumetric ratios of silicone oil (continuous phase) and the precursor or reaction mixture (dispersed phase), generated using a T-joint. (b) Illustration of three different reactor configurations used in the study

with same tube ID (1/16 inch or 1.58 mm). (c) Average crystal sizes obtained from 5 mL, 9 mL, and 16 mL reactors along with error bars representing one standard deviation for all volumetric ratios of ‘Oil:Precursor’. (d) CSD as a function of reactor volume for the single-phase flow condition (Precursor Only). 108

Figure 4-5 (a) The schematic for the flow reactor setup used for crystallization of MOF-808. (b) Bubble-point pressures of multiple reaction components calculated by Aspen. 113

Figure 4-6 Simplified schematic of the rapid sampler module (sample collection) illustrating different modes of operation. The cross symbol (X) implies a closed valve for the flow of reagents. (a) Reaction mixture containing MOF-808 crystals exiting the reactor after crystallization, bypassing the module and flowing into an overflow reservoir. (b) Reaction mixture being collected in the sample coil (~5 mL volume). (c) Pressurized N₂ gas used for evacuation of reaction mixture out of the sample coil, which is collected in an external vessel (50 mL centrifuge tube) for separation of solids and characterization. (d) Solvent (hexane) is injected in the sample coil for rinsing before collecting the next sample. 114

Figure 4-7 Powder XRD pattern for MOF-808 showing miller indices for prominent peaks below 12° 2 theta. Area under the curve for peaks corresponding to the plane (400) is monitored as a function of time to generate extent of crystallization αt curves for specific reaction conditions. 115

Figure 4-8 Superimposition of extent of crystallization αt plotted against time t , obtained from integration of area under the curve for peaks corresponding to reflections from 400 and 331 planes respectively, at (a) 110 °C and (b) 150 °C. 116

Figure 4-9 Extent of crystallization αt plotted against time t (closed symbols) and the corresponding AE fitting (red curves) at (a) 110 °C, (b) 120 °C, (c) 130 °C, and (d) 150 °C. The reaction mixture for all conditions has a 3X linker concentration. 117

Figure 4-10 Extent of crystallization αt plotted against time t (closed symbols) and the corresponding AE fitting (red curves) at a linker concentration of (a) 1X, (b) 2X, (c) 2.5X, and (d) 3X. The reaction temperature for all conditions was held constant at 150 °C. 118

Figure 4-11 Extent of crystallization αt plotted against time t (closed symbols) and the corresponding Gualtieri fitting (red curves) as well as the probability of nucleation PN (blue curves) at (a) 110 °C, (b) 120 °C, (c) 130 °C, and (d) 150 °C. The reaction mixture for all conditions has a 3X linker concentration. 119

Figure 4-12 Extent of crystallization at plotted against time t (closed symbols) and the corresponding Gualtieri fitting (red curves) as well as the probability of nucleation PN (blue curves) at a linker concentration of (a) 1X, (b) 2X, (c) 2.5X, and (d) 3X. The reaction temperature for all conditions was held constant at 150 °C.....	120
Figure 4-13 Arrhenius plots for the temperature-dependent rate constants (black squares) obtained from evaluation of the AE model.....	121
Figure 4-14 TEM images for MOF-808 synthesized in a 5 mL flow reactor (at 150 °C, 15 min residence time and 3X linker concentration), using volumetric flow ratios of ‘Oil:Precursor’ (a) 1:1, (b) 1:3, (c) 1:5, (d) 1:10, and (e) Precursor Only. (f) A line histogram of CSD obtained from TEM measurements for all biphasic slug-flow configurations.....	122
Figure 4-15 TEM images for MOF-808 synthesized in a 9 mL flow reactor (at 150 °C, 15 min residence time and 3X linker concentration), using volumetric flow ratios of ‘Oil:Precursor’ (a) 1:1, (b) 1:3, (c) 1:5, (d) 1:10, and (e) Precursor Only. (f) A line histogram of CSD obtained from TEM measurements for all biphasic slug-flow configurations.....	123
Figure 4-16 TEM images for MOF-808 synthesized in a 16 mL flow reactor (at 150 °C, 15 min residence time and 3X linker concentration), using volumetric flow ratios of ‘Oil:Precursor’ (a) 1:1, (b) 1:3, (c) 1:5, (d) 1:10, and (e) Precursor Only. (f) A line histogram of CSD obtained from TEM measurements for all biphasic slug-flow configurations.....	124
Figure 5-1 Schematic for the modular flow synthesis platform. Inset picture with red boundaries illustrates the phenomenological model of crystallization using a biphasic slug flow generated from two immiscible fluids in a T-junction.	134
Figure 5-2 Map of synthesis space investigated for $Ni_2Cl_2(BTDD)$ using flow synthesis varying (a) reaction temperature and residence time; and (b) volumetric ratios of Methanol:DMF and HCl:DMF solvents at a fixed temperature of 140 °C and 60 min residence time. Labels represent relative crystallinity in percentages (% RC), which were quantified by the intensity contribution in powder X-ray diffraction (PXRD) patterns originating from crystalline phase in the samples. The metal:ligand (M:L) molar ratio was maintained at 2.2 in all cases.	137
Figure 5-3 Characterization of $Ni_2Cl_2(BTDD)$ synthesized at optimal flow reaction conditions using (a) PXRD patterns, (b) N_2 adsorption isotherm at 77 K, (c) water vapor adsorption isotherm at 298 K, and (d) SEM image.	138

Figure 5-4 (a) Axial temperature profile along the length of reactor tube plotted against position of the precursor slug from reactor inlet. (b) Three dimensional (3D) slice plots at the entrance region of flow reactor showing both the temperature gradient and the growth of thermal boundary layers in the heated reaction zone as a function of tube ID. Outer diameter and tube wall is held at 140 °C and fluid flow has linear velocity of 13.4 cm/min to achieve residence time of 60 min (8 m reactor tube length). 141

Figure 5-5 Continuous flow-reactor setup used for synthesis and optimization..... 149

Figure 5-6 Bubble-point pressures of multiple components calculated by Aspen. 149

Figure 5-7 (a) PXRD patterns of Ni₂Cl₂(BTDD) obtained at different flow syntheses conditions showing varied levels of crystallinity, compared against simulated pattern. (b) Background correction scheme used to quantify intensity contributions from crystalline domains in the sample. 150

Figure 5-8 Characterization of Ni₂Cl₂(BTDD) synthesized at three different batch conditions (100°C, 120°C, 140°C at 48 hour) and their comparison with the ‘flow optimized’ condition (140°C and 1 hour). The volumetric ratio of “DMF:CH₃OH:HCl = 1:0.5:0.38” was used for all synthetic conditions which corresponds to the reaction mixture composition optimized in the flow reactor. (a) PXRD patterns, (b) N₂ adsorption isotherm at 77 K, (c) water vapor adsorption isotherm at 298 K, and (d) Batch samples (pre- and post-synthesis) in a 120 mL Pyrex glass bottle..... 151

Figure 5-9 SEM images of Ni₂Cl₂(BTDD) synthesized in batch (a-c) and flow (d-f)..... 152

Figure 5-10 TEM images of Ni₂Cl₂(BTDD) synthesized in batch (a-c) and flow (d-f). 152

Figure 5-11 TEM images of Ni₂Cl₂(BTDD) synthesized in flow showing a “bouquet of crystals”. Higher resolution images (c-d) show needle-like crystal morphology. 153

Figure 5-12 Physics-controlled meshing sequences with different tube diameters to model fluid flow and non-isothermal heat transfer using the COMSOL Multiphysics platform. 154

Figure 5-13 2D plots showing the growth of the thermal boundary layers (radially inward toward tube axis @r=0) for different tube IDs. Tube wall is held at 140 °C and fluid flow had linear velocity of 13.4 cm/min to achieve residence time of 60 min (~ 8 m reactor tube length). 155

Figure 5-14 Variation in precursor flow rate as a function of reactor tube ID. Effective residence time (τ_{eff}) decreases with reactor tube ID and is > 90% for tube IDs below 38 inch. 156

Figure 5-15 (a) Production output as a function of reactor tube ID and parallelization scenarios to achieve 1 kg of Ni₂Cl₂(BTDD) per month. We consider 30 days per month for calculations. (b)

Solid and liquid reagents consumed per month based on the chosen reactor configuration. All cases assumed 80% yield and a productivity of 0.765 kgMOF m⁻³day⁻¹. 157

Figure 6-1 Moisture Battery with sorbent coating 168

Figure 6-2 External case or enclosure (condenser)..... 169

Figure 6-3 Water harvesting cycle (WHC) composed of water-vapor capture and release cycles. Solid arrows indicate saturation of MOF battery and release of vapor when heated, which condenses to water collected in the external case. Dotted arrows indicate exposure of unsaturated MOF battery to fresh ambient air for adsorbing atmospheric water-vapor. 170

Figure 6-4 (a) Day-time operation of MOTTLE and (b) Night-time operation of MOTTLE ... 171

Figure 6-5 (a) Pressure gradients over moisture battery when exposed to ambient air (6 mph wind speed) at 50% RH and 298 K. (b) Cross-section of MOTTLE showing velocity field in cavities, when water-vapor is released at 40 mg/s. 173

Figure 6-6 A simplified heat transfer model for estimating temperature distribution in the MOF coated Al rod..... 175

Figure 6-7 3D slice-plot showing temperature distribution in an Al rod with 1.5 mm MOF coating 176

Figure 7-1 The current landscape for MOF-based industrial applications and the immense potential for widespread deployment of MOFs with reduced synthesis costs..... 182

List of Tables

Table 3-1 Residence time for multiple flow rates in a reactor volume of 16 mL. The reactor tubing had an inner diameter of 1/16 in (0.159 cm) with a heated reaction zone length of 8 m.	86
Table 3-2 Physiochemical properties of silicone oil (continuous phase) and dimensions of tubing used in the reactor for crystallization of MOF-808.	86
Table 3-3 Summary of MOF-808 reaction conditions investigated for rapid optimization of synthesis space using the flow reactor platform at 150 °C. ‘FA:DMF’ denotes the volumetric ratio of Formic Acid to DMF used in the precursor mixture. Every reaction mixture was prepared in a fixed volume of 30 mL where volumetric ratio of FA:DMF was varied. ‘M:L’ represents molar ratio of Zr metal (in the form of $ZrOCl_2 \cdot 8H_2O$) and H_3BTC linker (benzene-1,3,5-tricarboxylic acid, also known as Trimesic Acid). Linker concentration is varied only in precursor mixtures with M:L = 3, to probe the influence of concentrated precursor on MOF-808 crystallinity. Linker concentration of 1 corresponds to 70 mg of H_3BTC in a 30 mL reaction mixture. Higher the concentration of precursor, lower is the ‘Acid:Metal’ molar ratio, which represents moles of Formic Acid to Zr metal in the precursor mixture. Run # 39 was the composition reported by Jiang et al. ³ to synthesize MOF-808 in batch, and was used as a starting composition for optimizing flow synthesis.	86
Table 3-4 Yields are calculated based on the conversion of Zr metal to MOF-808. Chemical formula for MOF-808 ($Zr_6O_4(OH)_4(BTC)_2(HCOO)_6$) has a molecular weight of 1363.8 g/mol. H_3BTC linker has a molecular weight of 210.14 g/mol. About 64.67 mg (0.2 mmol) of Zr salt was used in the precursor mixture. Below is an example calculation for yield in case of a flow synthesized sample, Run #21 in Table S3. The procedure has been adapted from Garzon-Tovar et al. ¹⁶ and Furukawa et al. ⁸⁰	89
Table 3-5 Calculation of process productivity ($kgMOF m^{-3} day^{-1}$) for batch and flow synthesis of MOF-808 is shown in the table below. Productivity is defined as kg of solids synthesized, per m^3 of precursor mixture per day. Solids obtained for 1 and 3 min are amorphous and semi-crystalline.	90
Table 3-6 Details of equipment used in batch and flow syntheses and calculation of operational cost of equipment (in \$/day).	90
Table 3-7 Raw material costs for reagents used in the precursor mixture and solvents. Prices reflect the cheapest rates available for purchase from EMD Millipore Chemicals, Acros Organics, and	

Sigma-Aldrich. Bulk purchase price in case of commodity chemicals would be cheaper than the prices mentioned below.	91
Table 3-8 Energy accounting for each unit operation to synthesize MOF-808 in batch and flow process. Crystallization step is different for both processes, while rest of the operations remain the same.	92
Table 3-9 Definitions of parameters used in the techno-economic analysis.	92
Table 3-10 Thermal properties of reaction mixture used in Batch and Flow synthesis.	94
Table 4-1 Kinetic parameters obtained by fitting the crystallization curves obtained at four different temperatures using the Gualtieri model. The linker concentration for all conditions was 3X.	101
Table 4-2 Kinetic parameters obtained by fitting the crystallization curves obtained at four different linker concentrations using the Gualtieri model. The reaction temperature for all conditions was held at 150 °C.	101
Table 4-3 Activation energies for nucleation and growth obtained from Arrhenius plots for kN and kG . The linker concentration for all conditions was 3X.	105
Table 4-4 Residence time and corresponding flow rates in a reactor with 16 mL volume. The reactor tubing had an inner diameter of 1/16 in (0.159 cm) and a length of ~8 m for the heated reaction zone.	125
Table 4-5 Summary of MOF-808 reaction mixture compositions investigated for evaluating kinetic parameters. ‘FA:DMF’ denotes the volumetric ratio of Formic Acid to DMF used in the reaction mixture. Every reaction mixture was prepared in a fixed volume of 30 mL. ‘M:L’ represents molar ratio of Zr metal ($ZrOCl_2 \cdot 8H_2O$) and H_3BTC linker (benzene-1,3,5-tricarboxylic acid, also known as Trimesic Acid) and was held constant across all compositions ($M:L = 3$). Four different temperatures and linker concentrations are evaluated to probe their effect on extent of crystallization <i>at</i> of MOF-808. Linker concentration of 1X corresponds to 70 mg (0.33 mmol) of H_3BTC dissolved in a 30 mL reaction mixture of Formic Acid and DMF in a 2:1 volumetric ratio. Linker concentration of 2X would correspond to a 2-fold increase in the linker concentration of the 30 mL reaction mixture volume with a M:L ratio of 3 maintained constant. Higher the concentration of precursors (metal salt and linker), lower is the ‘Acid:Metal’ molar ratio, which represents moles of Formic Acid modulator to Zr metal in the reaction mixture.	126

Table 4-6 Values for the induction time t_0 and residence time for complete crystallization t_f for all the reaction conditions explored in the study.	127
Table 4-7 Kinetic parameters obtained by fitting the crystallization curves at four different temperatures using the AE model. The linker concentration for all conditions explored was 3X.	127
Table 4-8 Kinetic parameters obtained by fitting the crystallization curves at four different linker concentrations using the AE model. The reaction temperature for all conditions explored was held at 150 °C.	128
Table 4-9 Activation energies of nucleation E_{AN} and crystal growth E_{AG} reported for other MOFs in the literature compared to MOF-808 (this study).	128
Table 4-10 Residence times and corresponding flow rates for the Oil and Precursor phase in three different flow reactor volumes investigated in the study.	129
Table 4-11 Values for dimensionless Péclet number Pe calculated as a function of total flow rates for three different reactor configurations. The characteristic mixing times t_{mix} are estimated based on a scaling argument (Eqn. S3) for the 1:1 Oil:Precursor biphasic slug flow configuration. ...	129
Table 5-1 Residence time for multiple flow rates in a reactor volume of 16 mL. The reactor tubing had an inner diameter of 1/16 in (0.159 cm) with a heated reaction zone length of 8 m.	158
Table 5-2 Physiochemical properties of silicone oil (continuous phase) and dimensions of tubing used in the reactor for crystallization of $Ni_2Cl_2(BTDD)$	158
Table 5-3 Data for Figure 5-15 that evaluates scale-up scenarios by enlarging the reactor inner diameter. All the values assume 80% process yield and a productivity of 0.765 kgMOF m ⁻³ day ⁻¹ . Flow rates reported are for precursor only (volumetric flow ratio of 1:2 for Oil:Precursor was maintained). Changes in the reagents consumption due to variation in the reaction conditions were considered in the calculations. Silicone oil is immiscible with the reaction mixture and can be reused in the synthesis.	159
Table 5-4 Summary of $Ni_2Cl_2(BTDD)$ reaction conditions investigated for rapid optimization of synthesis space using the flow reactor platform. Amount of DMF, and molar ratio of metal to ligand (M:L) was constant in all cases. ‘HCl:DMF’ and ‘CH ₃ OH:DMF’ ratios denote the volumetric ratio of hydrochloric acid to DMF and methanol to DMF used in the precursor mixture.	

Run # 38, 39 are duplicates of Run # 22 and 23 to show reproducibility. Molar ratio of ‘Acid:Metal’ represents moles of HCl to Ni metal in the precursor mixture. 159

Table 5-5 BET surface areas and corresponding % RC (Relative Crystallinity) for batch and flow samples presented in Figure 5-8. 162

Table 5-6 Yields were calculated based on the conversion of the limiting reagent (H₂BTDD ligand) into Ni₂Cl₂(BTDD). A factor of 80% is used for mass retained after activation as we expect to lose 10-30% of mass (from solids obtained after synthesis) when activated, due to removal of water and other solvents from pores of Ni₂Cl₂(BTDD). 162

Table 5-7 Process productivity for the batch and flow synthesis of Ni₂Cl₂(BTDD) using volume of reaction mixture. 163

Table 5-8 Process productivity for the batch and flow synthesis of Ni₂Cl₂(BTDD) using volume of reactor. 163

Table 6-1 Comparing key attributes of existing AWH device and the MOTTLE 166

Table 6-2 Thermal properties for Al and MOF/Binder coating used in the model. 175

1. Brief Introduction to Metal–Organic Frameworks (MOFs)

Progress in solving societal challenges relies on discovery of new materials that are cheaper to synthesize, durable, and can incorporate multiple functionalities among other features. The field of synthetic metal-organic chemistry has emerged from principles and practices in coordination chemistry. The coordination polymers have been synthesized since 1960s, however porous coordination polymers (PCPs) and metal-organic frameworks (MOFs) were developed by the late 1990s which widened the scope and functionality of inorganic-organic hybrid materials.¹ MOFs are an emerging class of porous materials constructed from metal-containing nodes coordinated by organic linkers. A strategy for developing these materials is being realized in reticular chemistry (i.e. net-like structures) by studying the linking of discrete building units (molecules or clusters) by coordination bonds to make extended crystalline structures.² The term secondary building unit (SBU) was originally used in the description of zeolites where the primary units TO_4 tetrahedra (T=Si, Al, Ge etc.) form larger periodic frameworks with unique pore sizes and connectivity. In the context of MOFs, a SBU typically comprises of polynuclear metal clusters that forms the nodes in the framework and coordinates with an organic linker to form 2D and 3D structures. The architectural, mechanical, and chemical stability of MOFs imparted by their SBUs also gives rise to unique framework chemistry. The unique chemical nature of SBUs makes MOFs useful in many applications including adsorption, separation processes, and SBU-mediated catalysis.³ The permanent porosity exhibited by MOFs is another unique feature. The porosity of a material can be defined as a ratio of volume of the pores to the total volume occupied by the solid. Since porous materials are partially composed of empty space that can be accessed by guest molecules, they are described in terms of gas or vapor adsorption characteristics. MOFs typically have pores within the microporous (below 2 nm) or mesoporous (2 nm to 50 nm) regime.

1.1. Organic and Inorganic Building Units

The design of MOFs with predetermined topologies begins by determining the chemical building units required to construct the selected frameworks. This design process includes determination of not only the connectivity of individual building units, but also of the exact geometry dictated by the local symmetry of the positions they occupy in the targeted framework or the net. The building units with two points of extension are referred to as “links” and to the units with three or more points of extension as “nodes.” These links and nodes are assembled into the simple net, which

does not distinguish between vertices of identical connectivity but different geometry. The geometrical and chemical variety of SBUs and organic linkers facilitates the formation of a wide range of structures as illustrated in **Figure 1-1**. The structural diversity of MOFs originates largely from the accessibility of SBU geometries and their stability. Reticulation of the building units of the same geometry and connectivity but different chemistry leads to isorecticular frameworks, which have the same topology but different functionalities. For instance, the pore size of MOF-5 was expanded to $\sim 29\text{\AA}$ by using longer ditopic linkers with similar binding moiety (carboxylate groups) to create isorecticular structures (IRMOF-6, IRMOF-8, IRMOF-16 etc.).⁴ The linkers could also be functionalized with groups such as $-\text{NH}_2$, $-\text{Br}$, $-\text{OR}$ ($\text{R}=\text{C}_3\text{H}_7$, C_4H_9), to prepare isorecticular analogs of MOF-5.


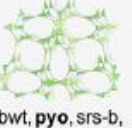




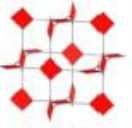
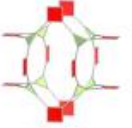

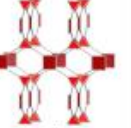
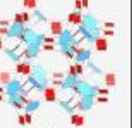
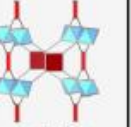
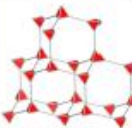
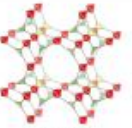


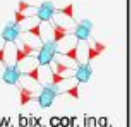

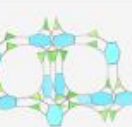
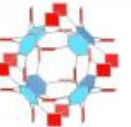

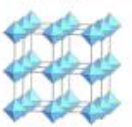
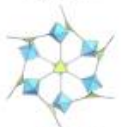
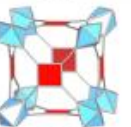
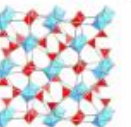
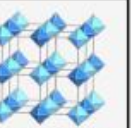
Building unit 1 \ Building unit 2	2-c Linear	3-c Triangle	4-c Square	4-c tet	6-c Hexagon	6-c oct
3-c Triangle	 srs	 bwt, pyo, srs-b, ths-b	 fjh, fmj, gee, iab, yac, yao	 asn, ept, ofp	 cys, dnf*	 anh, ant, apo, brk, cep*, cml, czz, eea, qom, rtl, tsx, zzz
4-c Square	 nbo, lvt, rhr	 pto, tbo	 cev, cdl, cdm, cdm, cds, cdz, mot, muo, qdl, qzd, ssd, sse, ssf, sst	 pts	 nts	 myd, ybh
4-c tet	 dia, lcs, qtz, sod	 bor, ctn	 fgl, mog, pds, pth, pti, ptr, ptt	 bnl, byl, cag, cbt, coe, crb, fel, icm, kea, lon, pcl, qtz-b, sca, tpd, ucn	-	 alw, bix, cor, ing, spl, toc
6-c Hexagon	 hxg	 cys, dnf	 she	-	 hxg-b	-
6-c oct	 pcu, bcs, crs, reo	 pyr, spn	 soc	 gar, iac, ibd, toc	-	 pcu-b, bcs-b

Figure 1-1 The reticular table showing select binary combinations of linker and SBU geometries encountered in MOFs. Figure adapted from Kalmutzki et al.²

Organic linkers employed in MOF synthesis are commonly built from rigid unsaturated hydrocarbon fragments, which help to provide chemical and mechanical stability to the frameworks. The organic linkers connecting the SBUs typically have two, three, four, six, eight, or twelve points of extension and the terminologies ditopic, tritopic, tetratopic, and so on are used to describe them (**Figure 1-2a**). The number of accessible linker shapes is large; however, since organic chemistry is based on carbon, angular constraints are introduced leading to certain shapes being easier to access. In general, organic linkers are built from three fragments comprising of the core unit of the linker that defines the geometry of the backbone, the binding groups that coordinate to the SBUs, and the extending units that define the size and functionality of the linker (**Figure 1-2b**). The binding groups such as carboxylic acids are commonly used in linkers; they neutralize the positive charges of the metal nodes, thus allowing for the formation of neutral frameworks and obviating the need for a counter ion. Carboxylate-based linkers favor the formation of polynuclear SBU clusters with a fixed coordination geometry and connectivity, along with a strong bond between the linkers and metal centers of the SBUs – results in an enhanced chemical, mechanical and thermal stability. For a given number of points of extension, a variety of different linker geometries are possible. The number of points of extensions defines the number of connections a linker can make to adjacent SBUs within a framework structure.

1.2. Stability of MOFs

The stability of MOFs is affected by multiple factors, namely: operating temperature, nature of building units, coordination geometry, hydrophobicity, solvents etc. The instability of many frameworks under ambient environment containing moisture has considerably limited their real-world application and commercialization. The relatively labile coordination bonds supporting the framework are believed to be responsible for the limited stability of MOFs.⁵ A stable MOF structure would feature strong coordination bonds between the organic and inorganic building units, which would survive the interaction with guest molecules in the pores or possess steric hindrance to prevent the intrusion of guest molecules to the metal nodes. The metal–ligand bond strength determines the thermodynamic stability of MOFs under the operating environment. Therefore, the stability of MOFs can be roughly predicted by examining the strength of the bonds that form the framework. It is well known that the metal–ligand bond strengths with a given ligand are positively correlated to charges of the metal cations and negatively correlated to the ionic radius. The effects of charge and radius can be combined into the concept of charge density. When

the ligands and the coordination environment remain the same, high-valent metal ions with high charge densities can form stronger coordination bonds and thus a more stable framework. This trend is in line with Pearson's hard/soft acid/base (HSAB) principle and corroborated by many observations in MOF research.⁶

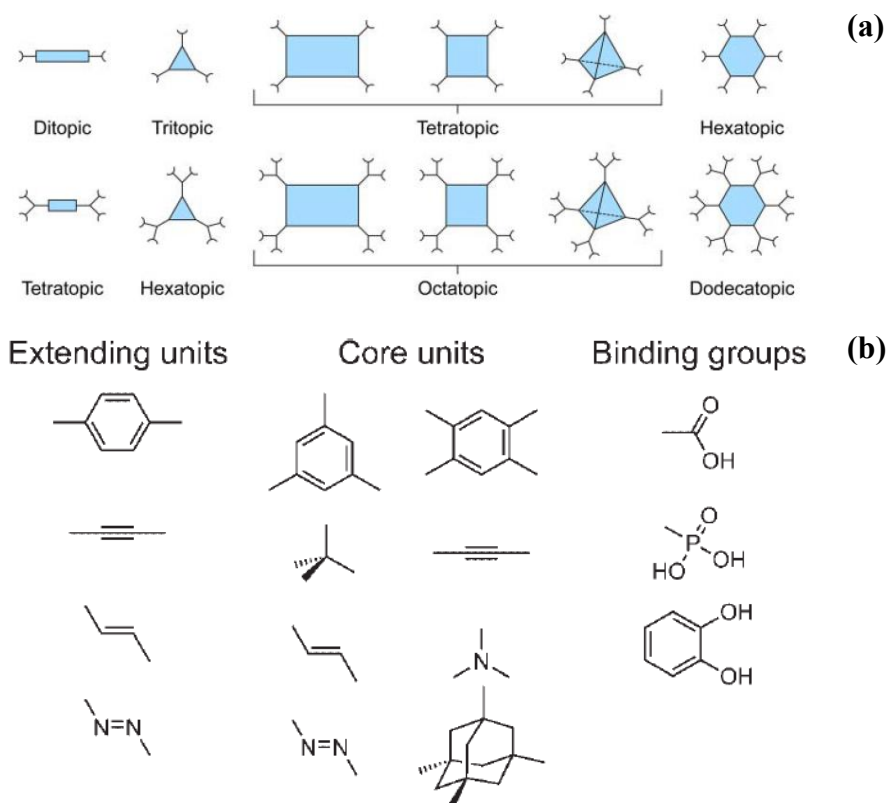
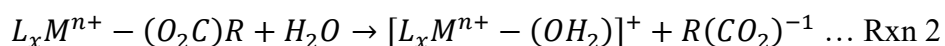
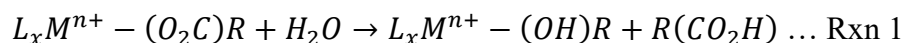


Figure 1-2 (a) Basic geometries used in the synthesis of MOFs and (b) commonly used organic units in the construction of linkers. Figure adapted from Yaghi et al.¹.

According to the HSAB concept (Pearson acid-base concept), hard acids prefer binding to the hard bases to produce ionic complexes, whereas the soft acids prefer binding to soft bases to give covalent complexes. For instance, coordination between soft azolate ligands such as imidazoles, triazoles etc., and soft divalent metal ions (Zn^{2+} , Cu^{2+} , Ni^{2+}) results in stable MOFs. While carboxylate-based ligands regarded as hard bases for stable MOFs together with high-valent metal ions such as Zr^{4+} , Ti^{2+} , Al^{3+} etc. As a rule of thumb, dense structures formed by highly connected metal-oxo clusters and rigid organic linkers are more stable, while longer linker lengths results in reduced stability. Over the past few years, degradation of MOFs in water-vapor has been thoroughly studied as MOFs used in applications such as carbon capture, water harvesting,

photocatalysis, separation etc., are exposed to varying amounts of moisture in their operating environment.

The two pathways for degradation of MOFs in presence of water are hydrolysis and linker displacement (Rxn 1 and Rxn 2). Hydrolysis occurs when the metal-linker bond is broken by addition of hydroxyl groups resulting in the liberation of a free, protonated linker, while the linker displacement mechanism involves insertion of water into the metal-linker bond, followed by the release of a free, deprotonated linker.⁷ Compared to neutral water molecules, proton and hydroxide ions are much more destructive to MOFs. Therefore, it is exceedingly challenging to construct stable MOFs with good resistance to proton and hydroxide ions. Moreover, the chemical conditions of acidic and basic solutions are distinct, which leads to the different stability of MOFs in acids and bases. Many MOFs constructed from high-valent metal ions and carboxylate-based ligands exhibit excellent robustness in acids, while their resistance to base is much weaker. A typical example of UiO-66 constructed from a 12-connected Zr^{4+} and carboxylate linkers maintains its crystallinity in concentrated crystallinity in acidic solutions (such as concentrated HCl), however it readily decomposes in dilute alkali solutions. On the other hand, MOFs constructed from low-valency metal ions and azolate-based ligands show remarkable stability in basic solutions, but decompose readily in acids. In acidic environment, the degradation results from competition between proton and metal ion for coordinating with linkers, while in basic solutions, MOF decomposes owing to replacement of linkers by hydroxide ions that competitively coordinate to metal cations.



Kinetic inertness of the metal centers constituting the SBUs can increase the water stability of thermodynamically unstable compounds, a concept well established in coordination chemistry. The structural degradation by hydrolysis or linker displacement is initiated by the formation of water clusters close to the SBU prior to diffusion of water molecules to the metal centers. The formation of water clusters in close proximity to the SBUs can be avoided by decorating the linker with hydrophobic fluorinated functional groups or alkyl groups.⁸ Depending on the chemical nature of the MOF, two types of hydrophobicity can be distinguished, internal and external. Internal hydrophobicity allows water to enter the pore system but prevents it from getting too close

to the SBU, whereas external hydrophobicity prevents water from entering the pore system and can be directly quantified by measuring the contact angle on the surface of the materials.⁹ Different strategies can be employed in the synthesis of hydrophobic MOFs.

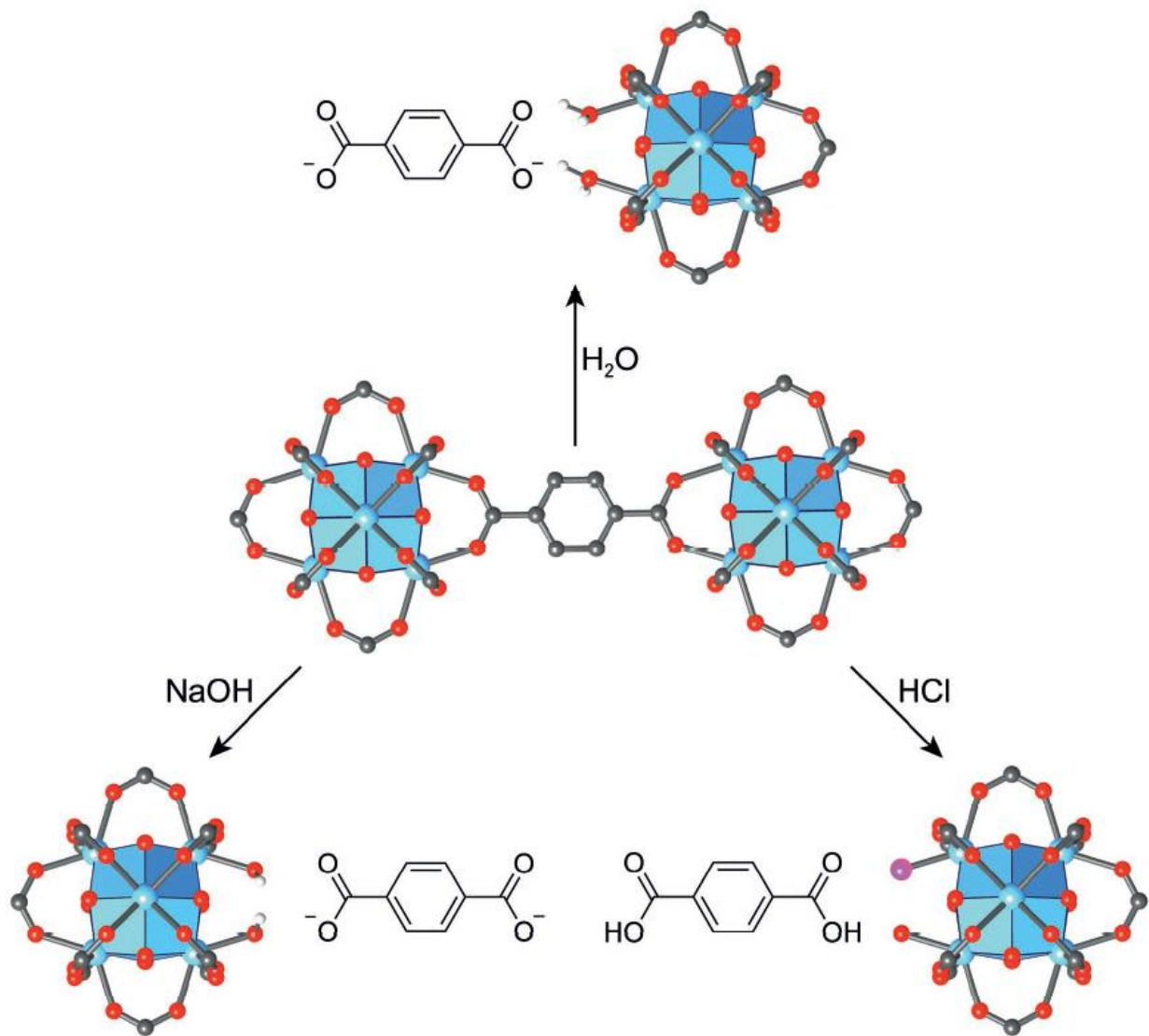


Figure 1-3 Degradation of UiO-66 (Zr-oxo clusters and Terephthalic acid linker) in presence of water, HCl and NaOH. Figure adapted from Kalmutzki et al.⁷

1.3. Synthesis Routes for MOFs and Challenges to Scaling-up the Production

Traditional lab-scale synthesis (ca. 10s of milligrams) for MOFs is carried out in batch reactors (Parr autoclaves or glass jars) wherein the metal salt and organic linkers are solubilized in solvents such as *N,N*-DMF (*N,N*-dimethylformamide) followed by heating for several hours or days. Scaling-up the production of MOFs to an industrially relevant scale (ca. 10s or 100s of kilograms per day), in an energy- & cost-efficient manner would be key for their widespread utilization in real-world applications. For instance, the use of MOFs for CH₄ storage¹⁰ in vehicle fuel tanks would generate a demand of hundreds of metric tons per year, while CO₂ capture¹¹ from coal or gas fired power stations releasing 8x10⁹ kg of CO₂ annually would necessitate millions of tons of MOF to capture them. Scaling-up the batch synthesis from laboratory scale to industrial scale would be challenging as the reaction conditions do not scale linearly for batch. MOF synthesis is often a delicate balance of a number of competing factors and could produce metastable products – implying a narrow set of reaction conditions for successful synthesis. There is a large gap between the process workflow for a laboratory synthesis and the processes required for scaling up the production efficiently. A key parameter to access scalability of a synthesis process is the process productivity (defined in terms of $kg\ m^{-3}\ day^{-1}$), kg of MOF produced per m³ of reaction mixture per day. An absolute value for production rate in $kg\ h^{-1}$ is also important to compare the output for various synthesis routes. Some of the key challenges that are commonly encountered for scaling-up the MOF production are:

- The use of expensive organic solvents such as *N,N*-DMF (*N,N*-dimethylformamide), growth modulators, along with solvents such as Acetone, Methanol for downstream processing. At scale, their cost makes the process economically unattractive and presents other issues related to toxicity, flammability and recyclability. Most MOFs have a low “solids-to-solvent” ratio resulting in use of excess solvents during the synthesis process.
- Typically, metal salts comprising of nitrates or chlorides are used as metal source and result in corrosive byproducts after the synthesis. This requires an additional step during the recycling and disposal stage.
- Bulk purchase of most ligands is a far-fetched reality. This severely limits our options for scaling-up the production of a specific MOF with tailored physicochemical properties targeted for an industrially relevant application.

- Precise control of experimental parameters during synthesis is crucial. The synthesis conditions used in reactors (Batch, PFR, CSTR etc.) at a lab-scale often need re-optimization when scaling-up the reactor volume.
- Downstream processing of MOFs, which includes solid-separation, washing, solvent-exchange and activation needs to be re-designed for a large-scale production. These steps can be customized depending on the real-world application and the type of MOF used.
- For many applications, MOF powder needs to be pelletized or combined with a binder for a coating. This requires additional studies to optimize the process and ensure the durability of the MOF. All these challenges are specific for each family of MOF owing to their composition, coordination environment, operating conditions among others.

Over the past decade, a number of new syntheses approaches such as electrochemical, microwave, mechanochemical, spray drying and continuous flow (PFR, CSTR) methods have been developed for MOFs to address some of these above mentioned challenges.¹² Electrochemical synthesis of MOFs was developed by BASF and their initial purpose was to exclude anions by using metal electrodes as metal sources.¹³ The synthesis consisted of immersing a copper plate in a solution containing the organic linker, 1,3,5-benzenetricarboxylic acid (BTC), and an electrolyte. The copper plate, which acts as the electrode, was used as the source of Cu(II) ions. When a certain current or voltage was applied, the Cu(II) ions were released from the copper electrode into the solution and reacted with the dissolved linker.¹⁴ Electrosynthesis of MOFs can be broadly classified in two categories: (i) the anodic dissolution, which is employed by BASF, and (ii) the cathodic deposition. In the anodic deposition, an applied electric potential induces the release of metal ions from the electrode, which then react with an organic linker present in the solution leading to the formation of a MOF film. In the cathodic deposition, a solution containing the organic linker, the metal ions, and a probase is contacted with a cathodic surface. In this route, the MOF film deposition results from increasing the pH near the cathodic surface, where the electrochemical reduction of the probase occurs. For instance, a probase are the nitrite ions originating from the reduction of nitrates, which can deprotonate the organic linker to form the MOF.¹⁵ Microwave-assisted synthesis, flow chemistry and spray-drying synthesis allow for a faster crystallization rate and production of smaller MOF crystals.¹⁶⁻¹⁷ In mechanochemical synthesis, no external heating or solvent is needed, reducing the washing and activation steps after the synthesis.¹⁸ The processes under ‘mechanochemistry’ use mechanical energy to induce a

chemical reaction. The central concept behind this synthesis method is to promote chemical reactions by milling or grinding solids with minimal or no amount of solvents.¹⁹ Using this approach the conventional solvothermal MOF reactors are substituted by a mortar and pestle or in a mechanical process by automated ball mills.²⁰ In general, the mechanical milling process is higher in energy and ensures the reproducibility between batches. In addition to the solvent free conditions, this approach leads to a faster and more efficient synthesis of MOFs obtaining quantitative yields and allows using MOF precursors with a lower solubility such as oxides, hydroxides and carbonates. However, the big limitation lies in up-scaling mechanosynthesis; it essentially is a batch processing technique with a relatively low rate of production. Moreover, the steps involved for downstream processing still use expensive solvents and alternative routes for separation, solvent-exchange and activation need to be developed for a truly ‘solvent-free’ process. The three different mechanochemical approaches used for MOF production described in the literature²¹⁻²³ are: a) Solvent-Free Grinding (SFG) which is the simplest method and avoids the use of solvent, b) Liquid-Assisted Grinding (LAG) which is more versatile, quicker, as it uses small amounts of liquid to increase the mobility of the reagents, and c) Ion-and-Liquid Assisted Grinding (ILAG) which uses a catalytic liquid with traces of salt additives to accelerate the MOF formation. Using these techniques, the synthesis for many MOF families has been demonstrated. A more detailed review of these alternative synthesis routes is covered elsewhere.^{12, 24} It is important to remember that these alternative synthesis routes do not universally work across all MOF families owing to wide variability in the type of building units, solvents, and reaction conditions that are required to synthesize crystalline MOFs.

Advances in reactor engineering over the past two decades have seen the emergence of continuous flow reactors as an alternative high-throughput synthetic route to batch reactors and have revolutionized materials synthesis in the field of porous materials,²⁴⁻²⁵ polymer chemistry,²⁶ organic synthesis,²⁷ pharmaceuticals,²⁸⁻²⁹ photochemistry,³⁰ and multi-phase systems (gas-liquid, liquid-liquid, solid-liquid etc.).³¹⁻³² The unique advantages reported for flow reactors in terms of fast heat and mass transfer, efficient mixing, precise control over experimental conditions, and ease of scalability stem from reduced system dimensions that accelerate critical heat and mass transport processes.³³⁻³⁴ An added benefit of flow chemistry platforms is the ability screen reaction synthesis space in less time than in conventional batch systems, which accelerates optimization times for decreasing the use of expensive solvents and lowering crystallization time, thereby

improving overall process productivity.³⁵ Continuous synthesis of MOFs is accomplished using two types of flow reactors (plug flow reactors, and milli- or micro-fluidic reactors) along with continuously stirred tank reactors (CSTR), where the MOF precursors are introduced into a tank reactor while MOF is continuously crystallized and removed at the outlet.³⁶ This thesis focuses on process intensification of MOF synthesis using millifluidic flow reactors.

Downstream processing (DSP) is a crucial part of the synthesis workflow. The reaction mixture usually is a slurry after MOF crystallization, wherein the solids are separated using a centrifuge or Buchner filter at a lab-scale. The MOF solids are then immersed in *N,N*-DMF overnight, followed by immersion into a low surface tension solvent such as acetone or methanol, to exchange the guest species trapped within the pores of the structure. The solvent exchanged solids are then subjected to a dynamic vacuum (with or without heat) to evacuate all guest species from the pores and activate the framework which generates coordinatively unsaturated open metal sites. Despite promising advances in MOF synthesis, there are challenges remaining related to the downstream processing. On a laboratory scale, these processes are well established and sufficient to obtain 10s of milligram amounts of material. However, these conventional downstream methods are not well suited for high production rates. The first stage, the washing and separation of the small crystals from the mother liquid still is a major obstacle for the large-scale production MOFs. Equipment for solid–liquid separation such as centrifuges, cyclones, settling chambers, or filters, in addition to the direct evaporation of the mother liquor can be customized for this step. However, the small size of the MOF particles and their low concentration in the solvent, coupled to a similar density of the solvent (due to the high porosity), makes separation via conventional methods inefficient or expensive at an industrial scale.³⁶ For the activation step, several strategies exist to remove the unreacted and solvent molecules trapped in the pores of the MOFs without collapsing the framework. Each MOF has its optimal protocol in order to obtain the highest surface area but generally, the activation temperature should be between the boiling point of the solvent and the decomposition temperature of the structure. An alternative activation route involves the use of supercritical CO₂. This relatively new strategy consists of exchanging the synthetic solvent for a one that is miscible with liquid CO₂ such as ethanol or methanol and then subsequently exchanging this second one for liquid CO₂ at high pressure and temperature for several hours. The difference here is that the CO₂ supercritical phase eliminates surface tension and capillary forces making this activation method much milder than the conventional and solvent exchange methods. A few other

variations for supercritical CO₂ treatment have been presented in the literature, but none of them have been used for activation at industrial scale.

In order for any MOF production process to be industrially viable a number of key aspects need to be considered:

- A versatile method to synthesize maximum number of MOF structures with the same piece of equipment.
- Avoiding harsh processing conditions such as high temperature and pressure, which would reduce capital and operating costs and alleviate safety concerns.
- Switching from batch to continuous processing would be beneficial offering higher process productivity, reducing downtimes, labor cost among others.
- Customized downstream processes that can efficiently handle 100s of kg scale in a low-cost and energy-efficient manner.

1.4. Potential Applications of MOFs

Although there have been numerous studies that demonstrate the use of MOFs in industrially relevant processes, there are a handful of MOFs which are sold commercially (on a gram or kilogram scale) and only a few examples of successful deployment in real-world applications.³⁷⁻³⁸

One of the recent example for commercial use of MOFs was pioneered by NuMat Technologies for gas storage, targeting the electronics manufacturing and semiconductor industry.³⁹ There is a long way to go before MOFs become commodity chemicals that can be deployed on a larger scale.

The growing market size of MOFs will create the conditions for more suppliers to emerge and create low-cost and sustainable synthesis processes. A detailed review of potential MOF applications is provided in previous studies.⁴⁰⁻⁴⁶ Shaping of MOF powders is another prerequisite for its use in devices or processes.

Powdered MOFs are usually difficult to handle and result in contamination of equipment and loss of activity. Pelletization of MOF powders under pressure combined with a binder is one of the most common methods used for densifying MOFs. For instances, extruded or compact beads, pellets or monoliths would be crucial for use in gas separation and storage. Two factors affecting the adsorption properties of MOFs during pelletization are: 1) the applied pressure could crush the structure of MOF owing to its low mechanical stability and 2) the binder molecules/compound can block the pores and reduce the available surface area (m²/g) for guest species. The pressure applied during pelletization depends

on the type of MOF and is usually in the range of 1–1000 MPa.⁴⁷⁻⁵¹ Binders used during pelletization serve to improve the cohesion between MOF crystals and mechanical stability. Commonly used binders include graphite, siloxanes, acrylates, polyvinyl alcohols, polyurethanes among others.⁵²⁻⁵⁵ The presence of binders is necessary for shaping processes such as extrusion, granulation and cake crushing. MOF powders are first dispersed in a slurry of binder mixture; for a thin coating, the device parts are dip-coated into the slurry and dried before use.⁵⁶ For extrusion, the slurry is introduced into a mold and cured before final use.

1.4.1. Sorbents for Atmospheric Water Capture (AWC)

The use of water-stable sorbents such as zeolites or MOFs can be used for water harvesting from air in passive and adsorption-based devices, especially in dry climates with little or no infrastructure for potable water supply. This technology requires adsorbents that can be tailored for a maximum working capacity, temperature response, and the relative pressure range in which reversible adsorption occurs. In this regard, metal–organic frameworks (MOFs) are promising candidates owing to their structural diversity and the precision of their functionalization for adjusting both the pore size and hydrophilicity, thereby facilitating the rational design of their water-sorption characteristics. Earth’s atmosphere holds nearly 10% of all the fresh water resource (~13,000 trillion liters of water at any given time), which can be accessed in a decentralized fashion in a sustainable way, using renewable energy sources such as sunlight.⁵⁷⁻⁵⁸ Existing sorbents such as silica gel, zeolites, CaCl₂ etc. have low gravimetric uptake capacity (g of water per g of MOF) and exhibit strong affinity to water requiring higher energies for regeneration, thereby making them unattractive for use in water capture devices. The ideal sorbents should exhibit high water-uptake capacities, hydrolytic stability, cycling stability, tailored hydrophilicity, low energy for regeneration and adjustable pore sizes to modulate the adsorption kinetics. Several MOF families hold the potential to meet all the requirements owing to their modular construction from a large variety of organic and inorganic building units and functionalization. To access hydrolytic stability of MOFs, they should be subjected to 100s of adsorption/desorption cycles and characterized with powder X-ray diffraction (PXRD), gas uptake measurements (BET) and SEM/TEM for evaluating changes in crystal morphology. Water adsorption in MOFs occurs in three distinct mechanisms: 1) Chemisorption on open metal sites at P/P_0 below 0.3, which translates to relative humidity (RH) below 30%, 2) Physisorption in the form of layers or clusters around the SBU and in the pores of the MOF and 3) Capillary condensation ($D > D_c$). The coordination sphere of the metal clusters

(SBU) is completed by terminal ligands, which can be removed during the activation stage resulting in open metal sites. The water molecules at low RH (below 10%) strongly bind to these sites and require high thermal energy to regenerate the MOF for its release. High regeneration temperatures are undesirable for most applications based on adsorption-desorption cycles. Physisorption of water in pores of the MOF is initiated by nucleation on primary adsorption sites and the growth of water clusters rather than single or multilayer adsorption.⁵⁹ The primary adsorption sites are typically close to the polar, hydrophilic centers within the structure (i.e. SBUs). Water molecules adsorbed on these sites can act as additional adsorption sites, initiating the formation of water clusters as evidenced by the step shape of the isotherm.⁶⁰ The size of the pores and the type of adsorbate dictates if the adsorbate would condense into the pores (capillary condensation) or would fill the pore reversibly and readily desorb without any hysteretic losses in the adsorption isotherms (pore filling). For MOFs (or any porous materials) with pore diameter larger than the critical diameter (D_c) for capillary condensation, the adsorbate would condense in the pores and require additional energy for phase change and release of the condensed species. The critical diameter (D_c) can be calculated using the equation, $[D_c = (4\sigma T_c / (T - T_c))]$, wherein σ is the Van der Waals diameter of the adsorbate, while T and T_c are the adsorption temperature and critical temperature of the adsorbate respectively.⁶¹ The critical diameter for water at 25 °C is ~20.76 Å. The MOFs with pore diameter below 20.76 Å would uptake the water via the pore filling regime while larger diameters would see capillary condensation. A hysteresis loop between the adsorption and desorption branch of the ‘S’ shaped isotherm would be seen for MOFs with pore sizes larger than D_c . Water adsorption isotherms of microporous hydrophilic MOFs can be of different types (e.g., Type I, II, IV) depending on the chemical nature of the MOF. Typically, no hysteresis is observed unless the adsorption of water results in a distortion, structural change, or degradation of the framework, or open metal sites are present. For MOFs closer to the upper limit of microporous materials, large working capacities (g of H₂O per g of MOF) in a range of 10-30% RH can be expected by maximizing the pore diameter upto D_c , as reported by Dincă and co-workers⁶²⁻⁶³ for M₂Cl₂(BTDD) where M=Ni, Co, along with other functional analogues.

An ideal system or a device for water harvesting from air, should be powered by low grade, renewable and abundant energy sources such as sunlight, while using porous materials with a large working capacity. The water capture cycle in these devices, comprise of three steps: adsorption of water from air at low temperatures and high RH, desorption of water vapor at elevated

temperatures and condensation of water vapor to generate clean drinking water. Most devices consist of an enclosure equipped with a condenser and an adsorbent sub-assembly. The enclosure can be opened and closed during the adsorption step to allow for a controlled exchange of water vapor in the atmosphere. The selection of adsorbent materials is governed by several factors including the water stability of the MOF, cycling stability over 100s of cycles, gravimetric uptake capacity, pressure and temperature swing conditions, sorption kinetics, thermal conductivity and spectral properties. There is no standardized procedure for testing of adsorbents as the operating environment and device specifications dictate the requirements for the MOF. A comparison of the water uptake capacities of different porous materials in a range of relative humidity (30%, 60% and 90%) is described elsewhere.⁷ More details on AWC sorbents and designs for the device will be covered later in the thesis.

1.5. Aims and Scope of Thesis

This thesis seeks to advance the development of low-cost and sustainable synthesis pathways for MOFs using continuous flow reactors. Major goals of the thesis are summarized below:

- To design and develop a semi-automated flow synthesis platform with a wide operational window for ultrafast synthesis of MOFs and other porous materials namely Zeolites.
- Develop protocols for rapid optimization of synthesis space parameters such as reaction temperature, residence time, amount of solvents/precursor, with systematic use of DoE (Design of Experiments) to aid early stage materials discovery.
- To develop a techno-economic framework and CFD models to evaluate potential scalability & trade-off scenarios for manufacturing industrially relevant MOFs at kg scale, with an overall goal to reduce synthesis costs for widespread deployment.
- Elucidate nucleation and crystal growth mechanisms for self-assembled porous materials and compute crystallization kinetic parameters to determine activation energies and rate constants for nucleation & growth of MOFs.
- Employ the flow reactor platform for process intensification of $\text{Ni}_2\text{Cl}_2(\text{BTDD})$ MOF, an ideal candidate for atmospheric water capture.

Chapter 2 describes the various modules developed for the flow reactor platform, which help accelerate crystallization of MOFs. Chapter 3 compares batch and flow synthesis routes used for manufacturing Zr-based MOF-808 along with a lab-scale techno-economic model to access cost

and energy-efficiency of these synthesis. Chapter 4 elucidates the solvothermal crystallization of MOF-808 and control of crystal sizes using a flow reactor. Chapter 5 highlights the use of flow reactor for synthesis optimization of $\text{Ni}_2\text{Cl}_2(\text{BTDD})$ MOF, used in atmospheric water capture. Chapter 6 introduces a design concept for a compact device used for practical water harvesting. Chapter 7 summarizes the results from the thesis and provides future directions for research. Each chapter of the thesis was written based on a separate manuscript, which is either submitted to a journal for review, or published at the time of writing this thesis. As such, the chapters can be read independently. The chapter 1 introduces some fundamental concepts for MOFs, which would be necessary to understand technical description in further chapters.

2. Developing a Modular Flow Reactor Platform for Accelerated Crystallization of MOFs and Zeolites

2.1. Introduction

Conventional synthesis routes for synthesizing MOFs and Zeolites involve the use of autoclaves or batch reactors heated at 100-200°C and involve long crystallization times typically over several days. Although batch reactors may offer a straightforward way for materials synthesis, they suffer from drawbacks like large gradients in heat & mass transfer, difficult to be scaled-up, lack the flexibility for real-time monitoring, poor control over experimental conditions, and low energy efficiency.^{24, 64} Developing a continuous flow process helps cut down crystallization time significantly, offers precise control on synthesis conditions, easy to scale-up, and highly efficient heat & mass transfer inside the reaction mixture droplets in a biphasic liquid-liquid slug flow, along with minimal use of reagents for screening the chemical synthesis space. Moreover, the use of biphasic slug-flow configuration results in narrow residence time distribution compared to a plug flow reactor. Figure 2-1 provides a schematic for the three-stage modular flow reactor platform. The three stages in the apparatus offers flexibility concerning tuning crystallization conditions, addition of reagents, aging conditions etc. Some of the studies that could be accomplished with such an apparatus include but not limited to: **a)** Understanding Inter-zeolite transformation, **b)** Understanding nucleation and crystal growth events in different stages, to optimize product (crystallite) parameters, **c)** Addition of secondary reagents, **d)** Rapid screening technique to run a wide variety of tests in a short-time and optimize synthesis parameters and **e)** Growing two different crystalline material on over each other (core-shell type) that may have endless applications in developing next generation of catalysts, microporous materials etc.

2.2. Experimental Apparatus

The flow reactor comprises of commercially available components and a few custom-built critical modules to achieve optimal mixing, ultrafast heat transfer, isothermal temperature distribution, and rapid sampling. Key modules are summarized below:

- Liquid handling and fluidic connections: A positive displacement pump (Vici M6 from Valco Instruments) and a syringe pump (PHD Ultra from Harvard apparatus) were used to inject the

continuous phase (silicone oil - Alfa Aesar #A1272822) and the dispersed phase (the precursor mixture), respectively, into a polytetrafluoroethylene (PTFE) T-joint to generate a biphasic slug flow. Both pumps were programmed for desired flow profiles and operated in the flow rates ranging from 100 nl/min to 10 ml/min. The reactor tubing (1/8" OD, 1/16" ID) made from PTFE was acquired from Cole-Parmer with an operational temperature up to 260 °C. Length of the tubing used in the heated reaction zone (i.e. the crystallizer unit) was ~8 m. Other fluidic connections such as compression unions and ferrules were made from PTFE and procured from Parker Hannifin. Pressurized reactor components were rated for a maximum allowable working pressure (MAWP) of 25 atm (370 psi).

- Crystallizer and heating apparatus: The platform was designed as a modular apparatus with three stages composed of two crystallizer units and one mixing unit. Although, for the current study only one crystallizer unit was used. The unit was custom built using the following commercially available parts: a sleeve heater furnace from Tempco, three 9 in long and 1.01 mm wide K-type thermocouples from Omega and a digi-sense programmable temperature controller from Cole-Parmer. The high temperature insulation made from ceramic wool, along with fixtures, clamps and lab jacks to support the crystallizer unit were purchased from McMaster-Carr. The core of the reactor was machined from aluminum blocks and tubes. The inner core tube had a diameter of 1 in, on top of which 8 m long PTFE tubing was wound in a clockwise direction. Two concentric aluminum blocks were used to hold the tubing firmly maintaining a continual contact along the length of the winding. This ensured fast heat transfer from the heater element to the precursor slugs in the tubing and a uniform temperature distribution in the heated reaction zone. A concentric air gap of 6 mm was held between the heater element and the reactor core to ensure no direct contact between heating element and Al block. This prevented local hot-spots and thermal runaway during the temperature ramp-up. Electric timer switches were used to program the heater operation for synthesis running longer than 12 h. The total floor space occupied by the crystallizer unit was ~18 cm².
- Sampling and valves: High-pressure cylinders of 150 mL with female NPT connections (for sample inflow and pressurizing the chamber) were acquired from Swagelok. Every sample cylinder was connected to two 3-way valves, which helped regulate flow of sample and release of pressure—designed to collect sample synthesized for a specific condition without disrupting the ongoing synthesis in the reactor. A rapid sampler was also custom-designed for the flow

platform to collect multiple samples synthesized under identical reaction conditions for crystallization kinetics data.

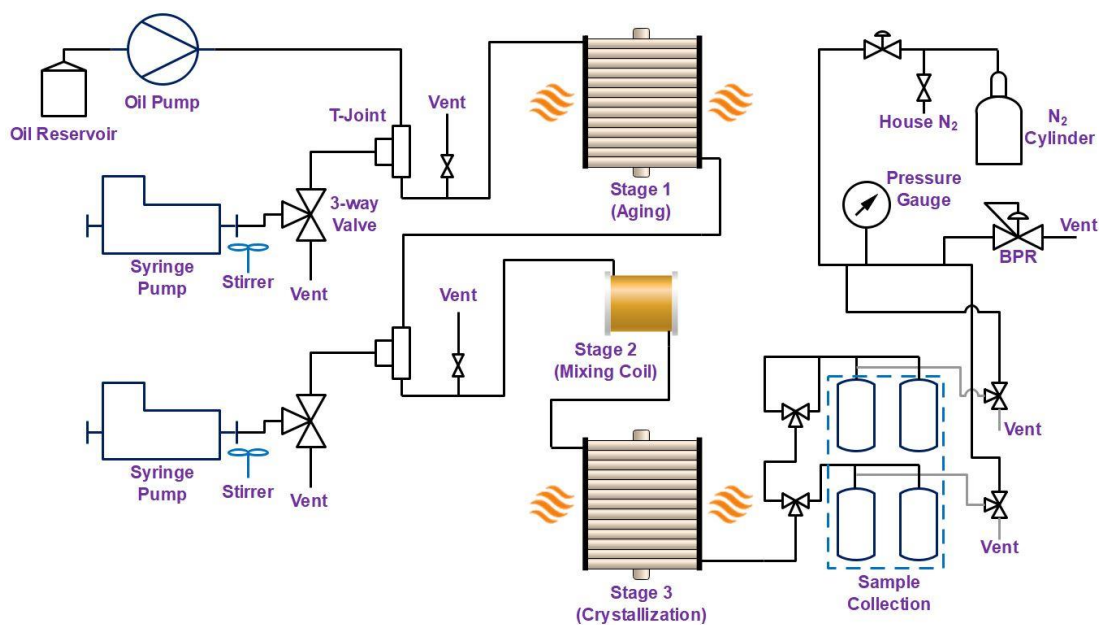


Figure 2-1 Three stage modular design for continuous flow synthesis apparatus.

Stage 1 and 3 of the apparatus (‘crystallizer’) is at the heart of the platform used in the high-throughput flow system (Figure 2-2). It is designed for fast heat transfer while being compact, scalable, robust and offering precise control over experimental parameters. The resistive heating furnace is connected to a temperature controller and can be programmed to achieve specific temperature setpoint. The core of the reactor consists of 1/8” PTFE tubing (reactor vessel), wrapped around the aluminum tubing (1” OD) and held together in-place with an aluminum block that is 1/8” thick. A concentric air-gap of 1/4” exists between the reactor core and the furnace ensuring uniform heating of the reactor core without temperature hotspots across the length of the reactor. Fixtures, heating blocks and other support structures were custom designed and machined at MIT.

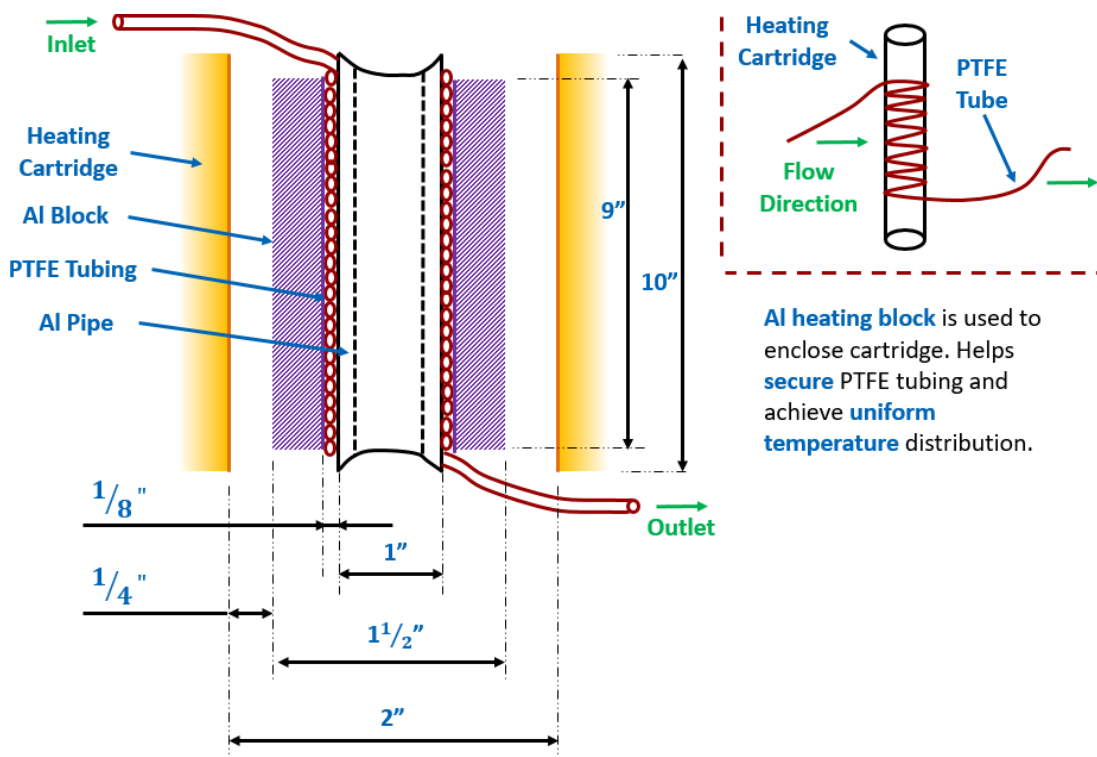


Figure 2-2 Cross-section for Stage 1 and 3 of the Continuous Flow Reactor Platform.

Continuous flow systems enable the miniaturization of reactions by compartmentalizing reactions in droplets of femoliter to microliter volumes. Compartmentalization in droplets provides rapid mixing of reagents, control of the timing of reactions on timescales from milliseconds to months, control of interfacial properties, and the ability to synthesize and transport solid reagents and products.⁶⁵ Figure 2-3 illustrates a phenomenological model of solvothermal or hydrothermal synthesis to crystallize Zeolites and MOFs in-flow. Paraffin or silicon oil plugs that separate the precursor segments help in preventing clogs in the reactor tubing which may happen due to rapid crystal growth. Each precursor segment in flow synthesis is analogous to a series of micro-batch reactors with highly efficient mixing characteristics, heat transfer and high surface area to volume ratio. As the precursor solution enters the heating zone (or the reactor core), crystallization reactions proceed giving rise to viable nucleation sites (that emerge from short-range crystalline order) and grain growth, culminating into Zeolite and MOF crystals. Residence times can be varied from 2 minutes to several days to probe evolution of product crystallinity with time. Reactor can be programmed to temperatures upto 250oC and MAWP of 370 psi (25.1 atm).

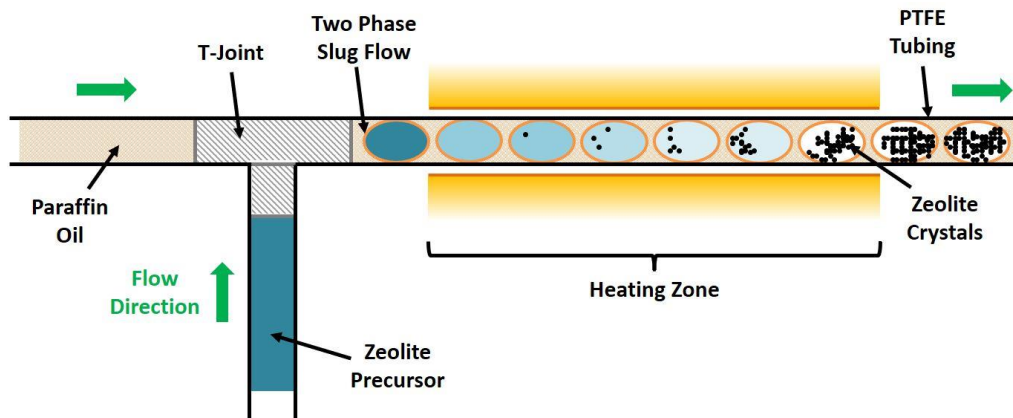


Figure 2-3 Phenomenological model of crystallization using a biphasic slug flow generated from two immiscible fluids in a T-junction.

Silicone oil is injected into the stream using a high-pressure piston pump in order to help crystals move thru the reactor tube avoiding any clogs, especially in case of zeolites. The smaller reagent segments also limits the size of crystals formed in-flow (due to limited availability of precursor for crystal growth) thereby maintaining accurate control on size distribution based on the amount of precursor solution present in each segment. The microliter-sized droplets serve as compartments for reactions. Multiple reactions can be performed by varying the reaction conditions within these droplets. Issues related to evaporation, complicated fluid handling, dispersion, and diffusion could be overcome by using multiphase flows of *immiscible liquids* to form droplets in microfluidic channels. Segmented flows in our case comprise of the reaction mixture (precursor) plugs that are encapsulated by an immiscible continuous phase. Reactions occur within the plugs. Droplets of the disperse phase are produced because of the shear force and interfacial tension at the fluid–fluid interface when being injected at the T-junction. A reagent flowing through a side channel can be injected directly into droplets through a T-junction. A smaller capillary (1/32” ID) can also be used at the T-junction to reduce the diameter at point of injection of the precursor, which results in much smaller droplets (and larger oil film), that would help in reducing the risk of clogging reactor tubes. Chaotic advection is used to achieve complete mixing of reagents that are encapsulated in plugs. It relies on the principle of repeated folding and stretching of fluid layers wherein the layers become exponentially thinner until mixing by diffusion becomes rapid.⁶⁶

A continuous wall-film of the continuous phase (silicone oil) does exist and helps carry the plugs thru PTFE tubing. The film thickness increases with volumetric flow rate. Figure 2-4 provides a

snapshot of the biphasic plug flow. A well-defined internal circulation is present in both phases. The curvature of the interface does not exert any of the effect on the circulation vortices.⁶⁷ The slug generation process is related to the dynamic pressure profile within the T-junction. When the first phase is flowing through the junction, the flow of the second phase is hindered due to the immiscibility of the two liquids and pressure builds up. When the pressure reaches a certain point, the first liquid is driven back and a slug is generated. This *alternating cyclic build-up* and release of pressure is responsible for the segmentation of the liquids and leads to a reproducible slug length. The maximum pressure drop is found to be proportional to the interfacial tension of the biphasic systems.⁶⁸ The higher the interfacial tension between the two liquids, the higher the pressure drop in the system.

In order to accommodate dense or high viscosity gels, especially for zeolites, we developed alternative injection strategies that prevent clogging of the reactor tubes, while maintaining product crystallinity under similar reaction conditions. We built a modular device using capillary inserts capable of dispensing reagent on a nanoliter or microliter scale. This results in a droplet flow rather than the standard slug flow as created by the T-joint (Figure 2-5). The oil film surrounding the droplets is a few hundred microns, while the oil film thickness around the slug tends to be tens of microns. The capillary inserts do not alter the operational range (flow-rate, temp. or pressure) of the flow synthesis platform. Both capillary inserts have the dimensions of: 1/32" ID and 1/16" OD, while the PTFE tubing used in the reactor has the dimensions of 1/16" ID and 1/8" OD.

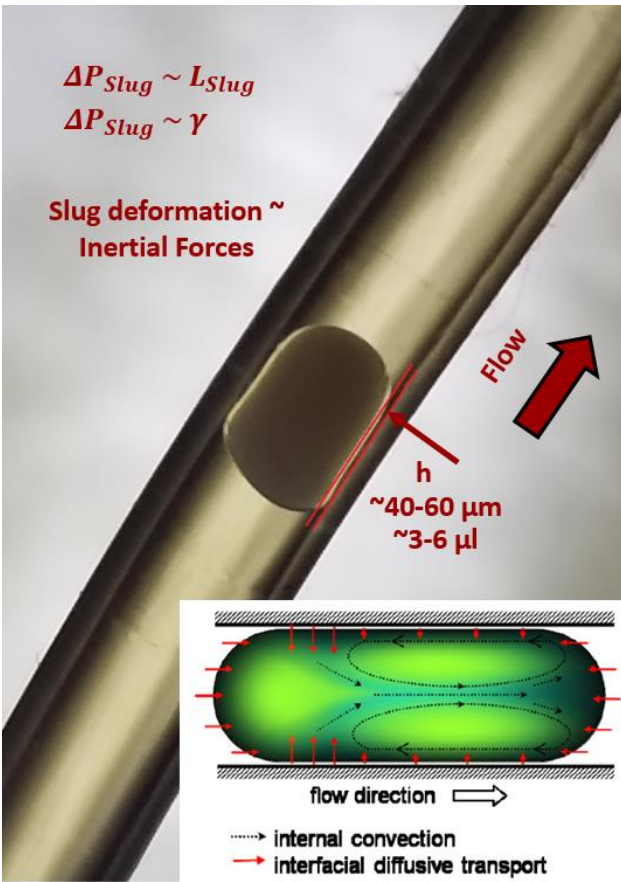


Figure 2-4 Biphase liquid-liquid slug flow showing a droplet of zeolite gel (dispersed phase) flowing in a tube with 1/16" ID.

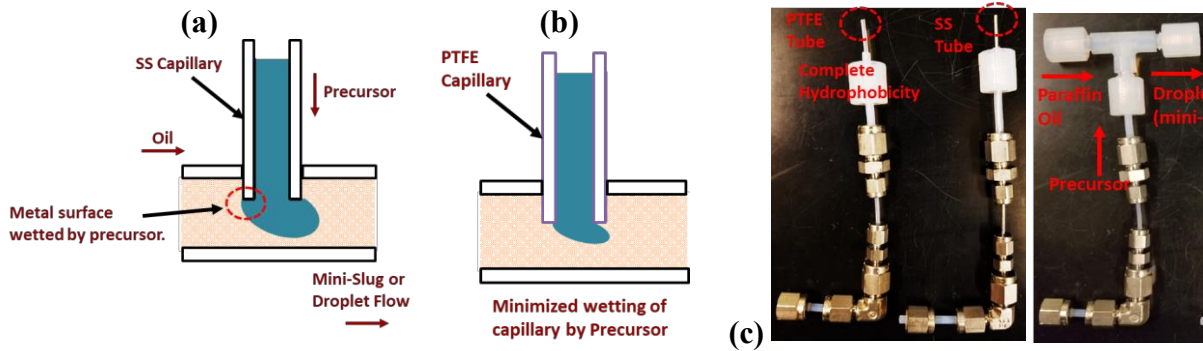


Figure 2-5 (a) Schematic of T-junction using SS (Stainless Steel) capillary inserts. (b) Schematic of T-junction using PTFE capillary insert. (c) Modular T-junction apparatus that is used for creating miniaturized droplets of reagents (rather than slugs created by standard T-junction).

We also developed additional approaches to help facilitate the ease of high viscosity gels in the reactor. The first one being the use of heated capillary injection devices that can lower the viscosity of the gels at the T-junction before injection (Figure 2-6). This also helps in greatly reducing the ΔP experienced by the pump and improves longevity. The energy input to the heating tape can be precisely controlled using a Variac transformer that facilitates accurate measurement of temperature at the T-junction. Care must be taken to make sure that the heating tape is used to reduce the viscosity of the dense gel while injection, but must not be heated to a level wherein the gel starts to crystallize in the device. The use of benign surfactants in the continuous phase can also help in preventing precursor slugs from coalescing when heated in the reactor. Commercially available surfactants such as sorbitan monooleate or monostearate can be used at a treat rate of 0.3-5 wt. % in the continuous phase (oil).

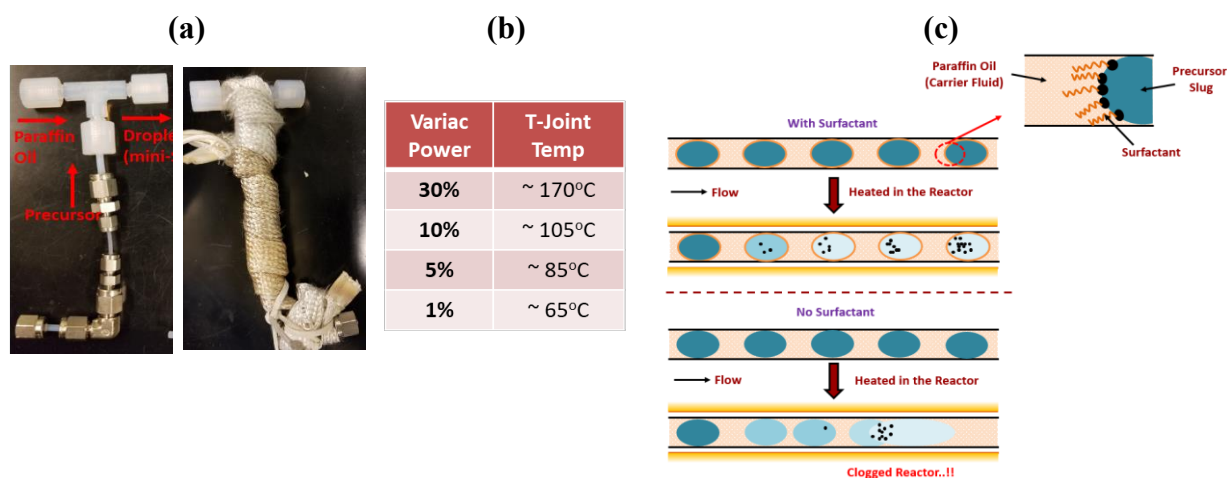


Figure 2-6 (a) Schematic of capillary T-junction with heating tape wrapped around the stem. (b) Variac can be used to modulate temperature subjected to the precursor at the T-joint before injection. (c) Schematic showing the use of surfactant in the continuous phase (oil) that can help in keeping reagent slugs apart and prevent them from agglomeration, which otherwise may lead to reactor clogging with crystallized solids.

For the synthesis platform to be truly versatile, it must allow injection of reaction mixtures that span the entire range of pH (0 to 14). Herein, we develop methods that help accommodate acidic precursors (primarily for MOFs) and basic (primarily Zeolites). Stainless steel (SS) syringes (Grade 316) can handle basic environments (pH > 11) and do not contaminate the precursor. For

highly acidic environments ($\text{pH} < 2$), the SS syringes can be coated with an anti-corrosive coating using PVD or CVD techniques available thru commercial vendors; however in the long run, coatings are subject to wear thereby exposing the metal surface beneath and results in contamination of the precursor. Acidic precursors can also be injected using reinforced BD plastic syringes. They are connected to the T-junction using luer fittings, so that the assembly can be used under pressures upto 140 psi (9.52 atm). A stir bar can be introduced in both syringes that helps in homogeneous mixing of the precursor when precipitates are formed, especially while aging the gel before being injected. Figure 2-7 shows the experimental setup for reinforced BD plastic syringe.

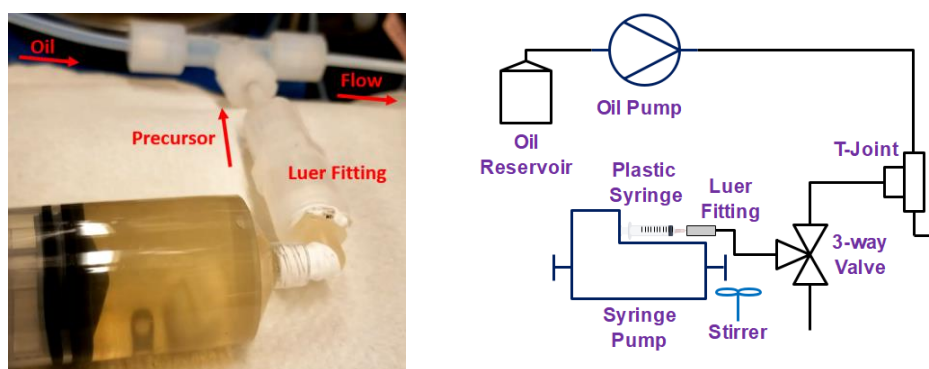


Figure 2-7 Experimental setup and schematic showing reinforced BD plastic syringe, which can be used to inject highly acidic precursors ($\text{pH} < 2$).

2.3. Scale-up Strategies for Flow Synthesis

For widespread deployment of MOF based platforms, scaling-up the synthesis in a cost effective manner along with manufacturing capacities of the order of several kilograms to tons is required. Scaling-up flow reactor is accomplished relatively easily compared to batch reactors where the entire equipment/infrastructure needs to be upgraded. There are two scale-up strategies for flow synthesis: a) Increasing the critical dimensions (tube diameter) of the reactor for higher throughput, and b) Increasing the number of tubes of similar diameter vis-à-vis ‘Parallelization’.⁶⁹ In the latter case of parallelization, the output of the platform is the summation of the outputs of all parallelized reactors. In the former case of increased tube diameter, the volumetric flow rate increases with the square of tube diameter ($Q \sim d^2$), however the surface area to volume of the tubing is inversely proportional to tube diameter ($\text{SA}/V \sim 1/d$); maintaining a higher SA/V is beneficial as it provides

excellent heat and mass transfer characteristics.³³ With larger volume per slug resulting from increased tube diameter, the system starts to have ‘batch’ like characteristics wherein mixing and slow heat transfer may adversely affect crystallization rates. The equipment such as pumps, heater and sample collection system has to be appropriately sized for higher throughput capability. Current platform uses 1/16” ID tubing and has a volume of 16ml; the platform in the current form is capable of being upgraded to ¼” ID with minimal modifications. A computational fluid dynamics (CFD) model was developed to quantitate productivity enhancements in the flow reactor based on improved heat-transfer rates, larger surface-area to volume ratios, and effective residence times. These findings will be presented in Chapter 5.

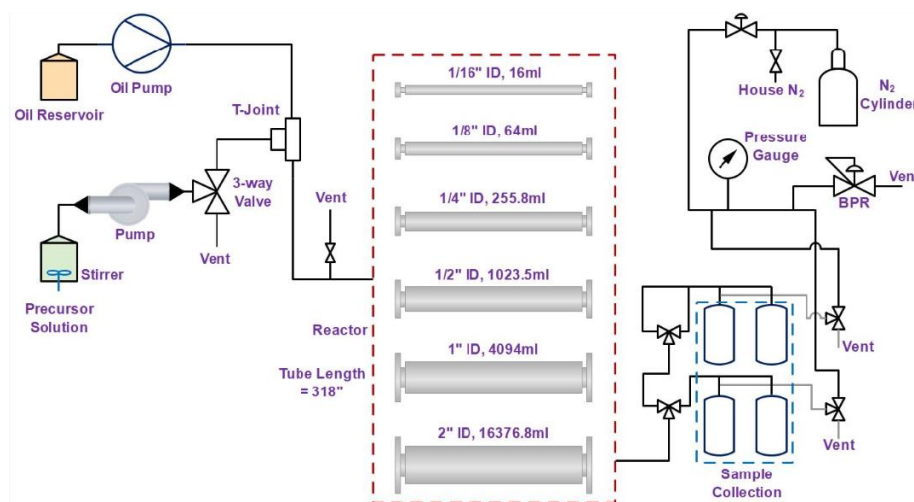


Figure 2-8 Proposed scale-up scheme for the platform by increasing the tube diameter.

Scaling-up the platform comes with its unique challenges. Since the flow system has more moving parts compared to batch, maintaining operational control of the system relies on availability and durability of components (such as valves, pumps, servo controls etc.). With a decrease in Surface Area to Volume (SA/V) ratio, flow reactors run the risk of inefficient mixing of reagents (‘dead circulation zones’), longer time delays for reagent in the slugs to reach temperature affecting crystallization rates thru the volume, analogous to batch crystallization that leads to a wide distribution of crystal sizes and poor operational control. The degree of reagent mixing is directly related to the flow dynamics in the tube, as described by the dimensionless Reynolds Number (Re).²⁴ For large volume slugs that do not have fully developed counter-rotating vortices, in the laminar-flow regime ($Re < 2100$) and in the absence of any additional static mixers, reagent mixing

is achieved solely by molecular diffusion.⁷⁰ However, under turbulent flow regimes ($Re > 4000$) there is an increase in the lateral diffusion of reagents in the slug over molecular diffusion. Therefore the anticipated drop in available surface area for nucleation as well as for efficient heat transport (due to increased tube diameter), is attenuated by an associated increase Re (moving from laminar to turbulent flow). In case of smaller reagent slug volume, there is a higher degree of mixing even at low Re (during longer residence time synthesis), due to the presence of fully-developed counter rotating vortices or eddys that homogenize the reagent composition in the slug. The downside to using lower volume slugs with increased tube diameter (for better mixing in the slug), would be lower throughput of reagent in the tubes leading to lower productivity (amount of material synthesized from amount of reagent injected per unit time). Figure 2-9 shows the relationship of Re and SA/V with tube diameter and flow rate. Maintaining a higher Re and high SA/V is optimal for flow synthesis.

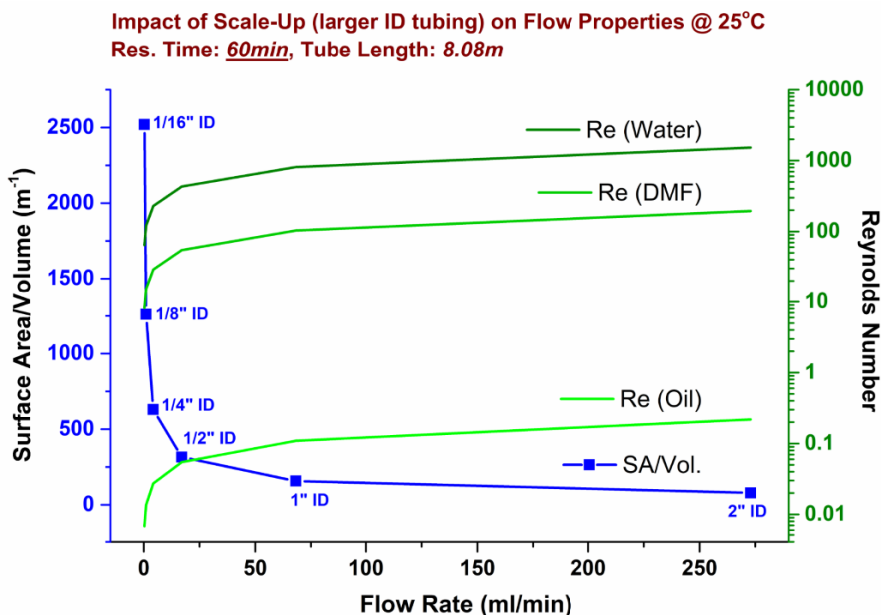


Figure 2-9 Comparing variations in Reynolds number (Re) and $SA/Vol.$ with increasing flow rate. Calculations

2.4. Product Ecosystem Approach for the Flow Synthesis Platform

The continuous flow reactor in a broader sense can be thought as a materials discovery and synthesis platform, packaged into a product ecosystem. Major components of the ecosystem comprise of the reactor apparatus, optimization of synthesis parameters for high-throughput

production, materials characterization techniques and development of a TEA (techno-economic analysis) model in order to provide a quantitative value proposition of the process and efficient synthesis routes. The platform can be used to accelerate early stage materials development process and discovery loops. The ecosystem can be augmented by Machine learning (ML) algorithms that help with time-consuming complex steps, which are required in the development cycle. The target Zeolite or MOF once synthesized can be used in novel applications as well as scaling-up the production of frameworks that are hard to synthesize in a conventional batch process.

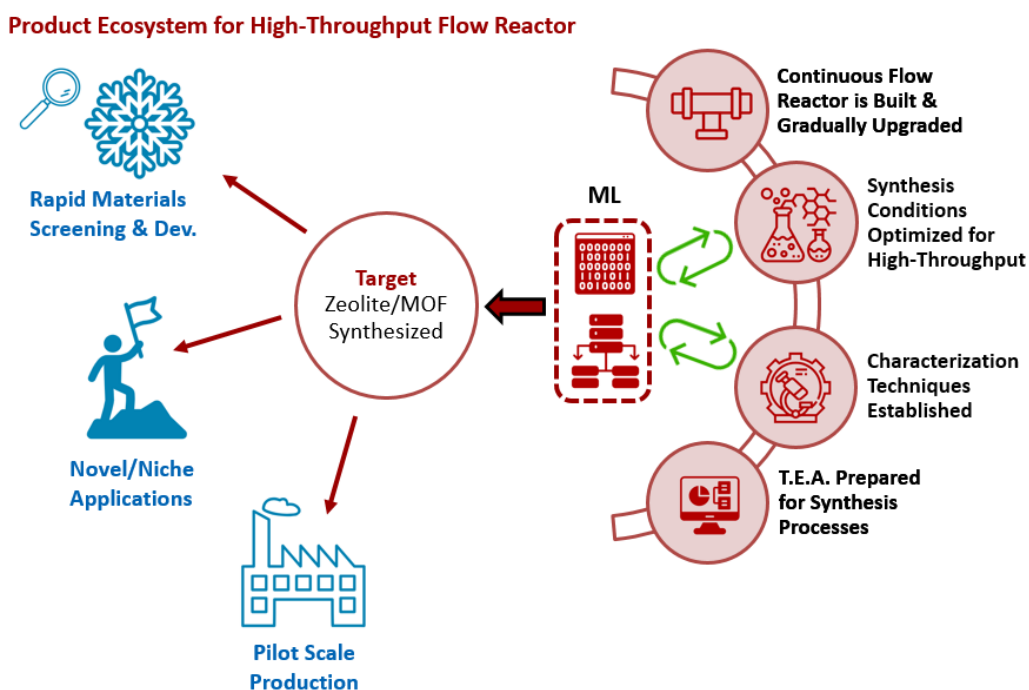


Figure 2-10 Product Ecosystem for a High-Throughput Flow Synthesis Platform.

Cost-competitiveness would be crucial in the commercializing novel applications where versatility and high process productivity of the flow system can be leveraged over batch. Realizing the value-proposition for continuous flow synthesis would be key moving forward. High-throughput material synthesis and rapid characterization modules are necessary for an accelerated materials discovery platform. Automation of the platform would also be key for developing an integrated continuous manufacturing system. Use of microcontrollers, feedback loops, sensors, and process control software with some pre-programmed synthesis conditions (for certain zeolites and MOFs) would help in limited or no human interface during the course of synthesis.

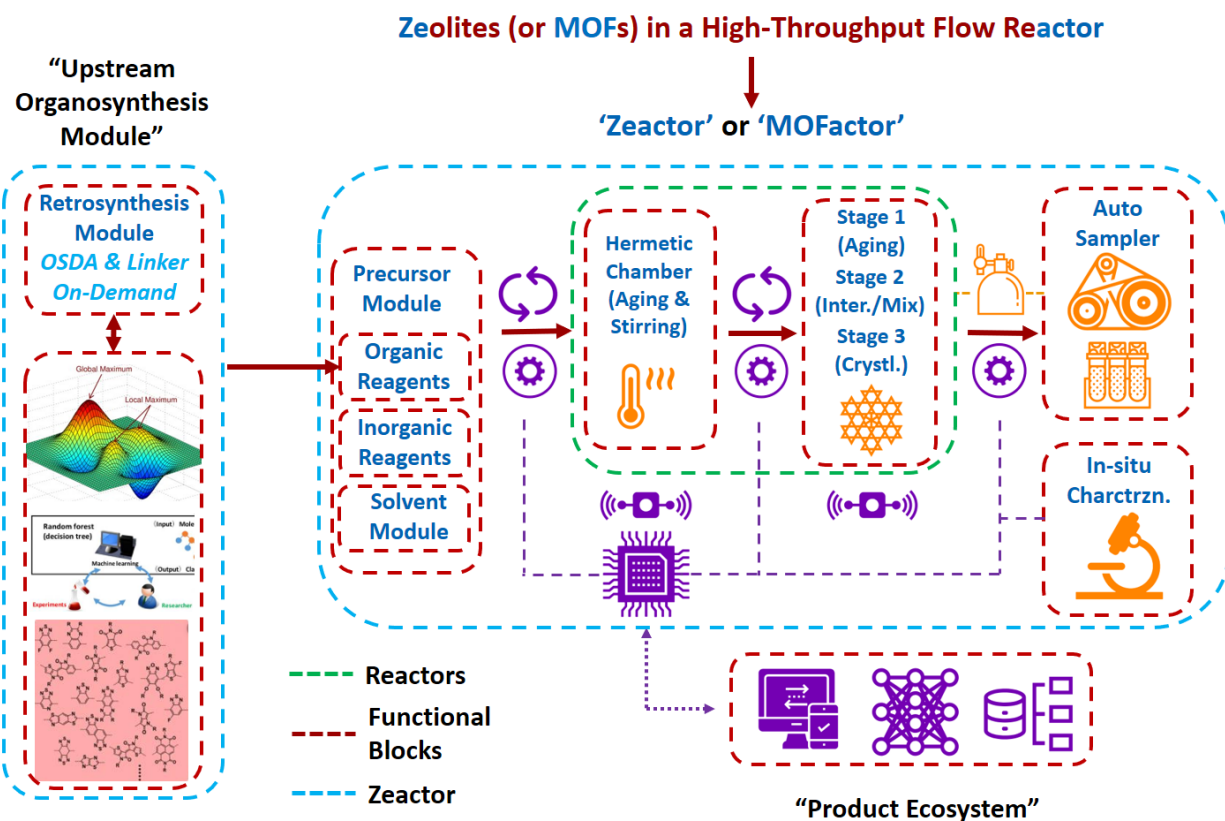


Figure 2-11 An overview of different modules and functional blocks for an automated Flow Synthesis Platform.

3. Continuous Flow Chemistry Approach for Ultrafast and Low-Cost Synthesis of MOF-808

Metal–organic frameworks (MOFs) are promising materials for a wide range of applications given their chemical stability and structural tunability. Most traditional MOF syntheses involve batch reactors that have intrinsic inefficiencies due to poor heat and mass transfer which impacts process productivity during scale-up. In this chapter, we report a low-cost and energy-efficient continuous manufacturing process for MOF-808—a Zr-MOF widely studied as a catalyst and adsorbent in industrially important processes—using flow-through reactors that can achieve high process yields with minimal solvent use. The flow platform allowed us to investigate the influence of several synthesis parameters, including residence time, linker concentration and volumetric ratio of modulator and solvent on the crystallization process. Under optimal conditions, the *N,N*-dimethylformamide solvent and formic acid modulator amounts were decreased by 84% and 67% in volume, respectively, and resulted in an increase in productivity (defined in units of $kg_{MOF} m^{-3} day^{-1}$) by two orders of magnitude with similar yields, compared to established batch synthesis methods. A techno-economic model based on laboratory-demonstrated synthesis routes was developed to compare energy and cost savings for the flow system compared to batch, indicating that solvent use was the largest contributor to the overall cost. The methodology presented in this work opens new pathways for critical assessment and optimization of continuous manufacturing routes on a lab-scale environment, serving as a prerequisite for sustainable and low-cost industrial-scale MOF synthesis.

3.1. Introduction

Metal–organic frameworks (MOFs) are an emerging class of crystalline porous materials exhibiting high surface areas and tunable pore environments.⁷¹⁻⁷² MOFs are coordination complexes consisting of organic linkers and inorganic polynuclear clusters forming two-, and three-dimensional structures. In terms of possible combinations of metal clusters with organic linkers, the number of accessible frameworks is theoretically limitless, which opens new pathways for applications ranging from gas storage,⁷³⁻⁷⁴ separation,⁷² drug delivery,⁷⁵⁻⁷⁶ and catalysis.⁷⁷⁻⁷⁸ Among the large number of MOF structures reported in the Cambridge Structure Database,⁷⁹ Zr-based MOFs are particularly interesting due to their high chemical stability as well as amenability

to post-synthetic modification (PSM).⁸⁰ For instance, MOF-808 a Zr-MOF first reported by Furukawa et al.,⁸¹ features large cavities (diameter of 18.4 Å) and high Brunauer-Emmett-Teller (BET) surface areas exceeding 2000 m².g⁻¹. The high oxidation state of Zr(IV) in the SBU results in high charge density and bond polarization leading to strong coordination bond between Zr and O atoms in the structure, which imparts MOF-808 with remarkable stability in hydrothermal and acidic environments.⁸² The inorganic secondary building unit (SBU) in MOF-808 comprises Zr₆(μ₃-O)₄-(μ₃-OH)₄(CO₂)₁₂ clusters (referred to as Zr₆-clusters) and their terminal formate anions can be further replaced by other functionalized ligands during MOF synthesis or by PSM, allowing for facile incorporation of targeted functionalities.³ The presence of large cavities with open coordination sites and stability with a prospect of PSM, has made MOF-808 an attractive candidate for use in industrial processes such as methane oxidation to methanol,⁸³ heavy metal ion capture,⁸⁴⁻⁸⁵ superacid catalysis,^{3, 86} water capture,⁸¹ shape selective catalysis⁸⁷⁻⁸⁸ and others.

Synthesis of microcrystalline MOF-808 is typically carried out solvothermally in batch reactors on the gram-scale under laboratory conditions.^{79, 81, 83-87} In particular, the synthesis of 1 g of MOF-808 requires the dissolution of 1.134 g of ZrOCl₂.8H₂O and 0.245 g of benzene-1,3,5-tricarboxylic acid (H₃BTC) in a solvent mixture comprising of 45 mL *N,N*-DMF and 45 mL of formic acid, followed by heating at 130 °C for 48 h in a batch reactor to generate crystalline solids with ca. 75% yield.³ Monocarboxylic ligands such as formate, acetate, and propionate have been employed as growth modulators in MOF-808 synthesis to regulate crystal growth, tune pore sizes, and improve framework crystallinity.^{82, 89} Slow crystallization times coupled with high solvent-to-solid ratios severely limit process productivity, and this problem is exacerbated due to heat and mass transfer limitations during scale-up of batch reactors.⁹⁰ These inefficiencies translate to higher synthesis costs and more difficult quality control of the final crystal structure.⁶⁴ Advances in reactor engineering over the past two decades have seen the emergence of continuous flow reactors as an alternative high-throughput synthetic route to batch reactors and have revolutionized materials synthesis in the field of porous materials,²⁴⁻²⁵ polymer chemistry,²⁶ organic synthesis,²⁷ pharmaceuticals,²⁸⁻²⁹ photochemistry,³⁰ and multi-phase systems (gas-liquid, liquid-liquid, solid-liquid etc.).³¹⁻³² The unique advantages reported for flow reactors in terms of fast heat and mass transfer, efficient mixing, precise control over experimental conditions, and ease of scalability stem from reduced system dimensions that accelerate critical heat and mass transport processes.³³⁻³⁴ An added benefit of flow chemistry platforms is the ability screen reaction synthesis space in

less time than in conventional batch systems, which accelerates optimization times for decreasing the use of expensive solvents and lowering crystallization time, thereby improving overall process productivity.³⁵ To this end, we surmised that switching the synthesis of MOF-808 from batch to flow would improve our understanding of early stage crystallization processes as well as provide an alternative low-cost and high-throughput route to match industrial-scale production at competitive market prices.⁹¹⁻⁹²

Only a handful of studies⁹³⁻⁹⁵ have demonstrated the feasibility of synthesizing MOF-808 in flow, however a comprehensive understanding on the influence of synthetic parameters on product crystallinity, pathways to achieve high process yields and minimizing solvent use have not been explored. Herein, we report a continuous flow method for the synthesis of MOF-808 under mild solvothermal conditions achieving crystalline product in minutes. We performed a rigorous design of experiments (DoE) to map the chemical design space with an overall goal of minimizing the use of reagents such as formic acid and DMF, while increasing the concentration of linker in the precursor mixture to deliver high production rates. We use a streamlined techno-economic analysis (TEA) to quantify metrics influencing MOF-808 manufacturing costs both in flow batch reactors. Two different production scenarios in a lab-scale environment are analyzed to quantify the cost drivers, and potential savings as a function of synthesis routes. Our efforts presented in this work open new pathways for a sustainable and low-cost MOF synthesis, which would make them commercially viable for use in industrially relevant applications.

3.2. Results and Discussion

The scheme for MOF-808 production illustrated in Figure 3-1 considers well-established batch synthesis method and the continuous flow process developed in this study. While reagents in the precursor mixture and the final product obtained remain the same, the major difference in the two processes originates from reaction conditions (i.e., temperature, residence time and reagent concentration), the process yield and production rates. A continuous flow reactor offers the ability to fine-tune product characteristics such as crystal size distribution, tailored physiochemical properties, and explore the synthesis space more easily than batch syntheses.^{92, 96} In our flow reactor, we rely on a biphasic liquid-liquid slug flow profile generated using a T-junction to perform continuous microbatch MOF crystallization reactions in a compact heated zone (Figure 3-5). Silicone oil is used as an immiscible continuous phase as it preferentially wets the PTFE

reactor tubing and encapsulates the slugs (or μL droplets) of the dispersed phase containing the MOF precursors. This results in miniaturization of the reaction system that reduces diffusion lengths, aids in rapid mixing of reagents, enables fast heat and mass transport, allows for seamless control of residence time (order of milliseconds) and reduces crystallization time.^{65, 97-98} As the precursor enters the heated reaction zone, crystallization reactions give rise to viable nucleation sites that emerge from short-range crystalline order, proceeding to grain growth, and culminating into MOF crystals.⁹⁹⁻¹⁰¹ Additional details pertaining to volumetric flow rates and residence times are summarized in Figure 3-5 and Table 3-1 and Table 3-2 of the Supporting Information (SI), while flow reactor operation and various components used are covered in our previous work.¹⁰² Powder X-ray diffraction (PXRD) patterns in Figure 3-1b were obtained for MOF-808 synthesized in flow at 150 °C and varying residence times from 1 min to 120 min to probe evolution of crystallinity, compared to the batch sample (130 °C and 48 h). Long range crystalline order started to develop at residence times as low as 2 min in flow and attained full crystallinity at 5 min, beyond which there were no changes detected in the PXRD patterns. Moreover, PXRD patterns show no mismatch in 2 theta positions and confirm the single-phase nature of microcrystalline powder samples synthesized in flow. SEM images (Figure 3-7) of samples with residence times below 15 min confirm the octahedral shape of MOF-808 nanoparticles synthesized in flow. TEM images in Figure 3-1c show the changes in morphology of MOF-808 nanoparticles at short residence times (1 to 15 min). MOF-808 particles synthesized in flow measured on average ca. 140 nm compared to 360 nm in batch (Figure 3-10). Average crystal sizes are obtained from measurements of ~ 80 nanoparticles for each residence time, while the error bars correspond to one standard deviation. Smaller monodisperse crystalline particles are advantageous for practical applications such as adsorption, separation, and catalysis as they improve active surface area and minimize diffusion limitations.^{94, 103-104} Average crystal sizes for Zr-MOFs can be tuned by coordination modulation mechanism, where the formate ligand (growth modulator) with a similar chemical functionality as the H₃BTC linker competes for coordination with the SBU.^{89, 101} A higher linker concentration in the reaction mixture enhances the linker coordination with the SBU by reducing the competitive coordination of the formate ligand, leading to an increase in the number of nucleation sites that grow at a faster rate—results in smaller crystal sizes.¹⁰⁵ In line to this, tuning the amount of modulator and linker concentration in the reaction mixture to achieve desired size, porosity,

crystallinity and yield with the least residence time is imperative from an efficient process development standpoint.

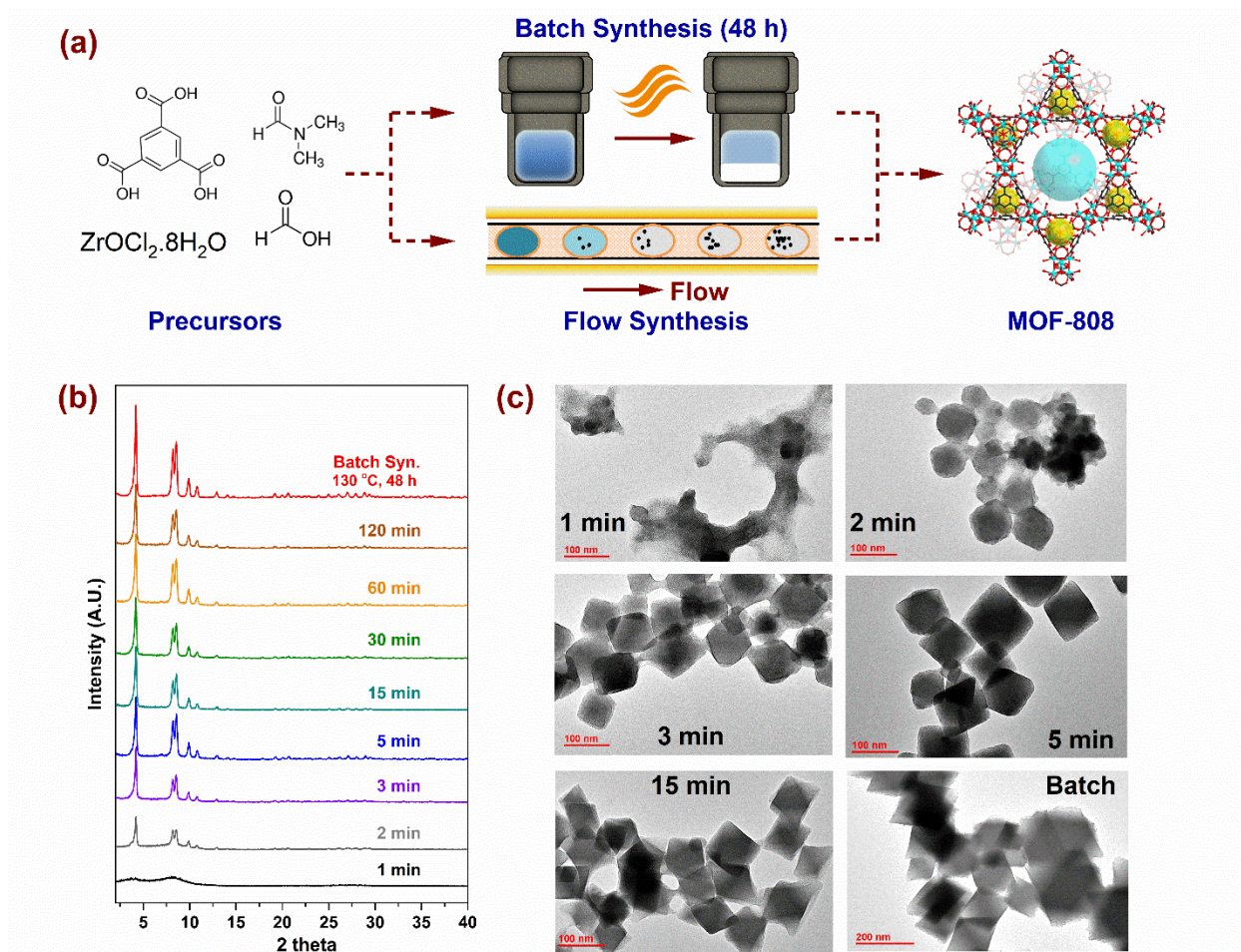


Figure 3-1 (a) Synthesis scheme for MOF-808 showing flow and batch routes. (b) PXRD patterns showing evolution of crystallinity with residence time for samples synthesized in flow at $150\text{ }^\circ\text{C}$, compared to batch ($130\text{ }^\circ\text{C}$, 48 h). (c) TEM images showing morphology of microcrystalline MOF-808 nanoparticles at short residence times (1 to 15 min) and the corresponding batch sample.

Several studies¹⁰⁶⁻¹⁰⁹ report on the merits of combining green chemistry principles, such as lower solvent usage, and higher productivity with statistical DoE for improved process efficiency. The process window for MOF-808 comprises of a critical range of parameters such as molar ratios of reagents in the precursor mixture, residence time and reaction temperature which dictate the outcome such as product crystallinity and production rates. Owing to a wide range of synthetic conditions reported in the previous studies for MOF-808 which result in diverse outcomes,^{3, 81, 83-}

^{84, 86, 93-94} we fixed parameters such as reaction temperature (150 °C) and the metal:linker molar ratio (M:L) to a value of 3 to synthesize microcrystalline powder samples. We performed experiments by changing one process variable at a time (OVAT) to screen the effects of residence time, volumetric ratio of formic acid (FA) and *N,N*-dimethylformamide (FA:DMF), and linker concentration in the precursor. In Figure 3-2, the variation in product crystallinity is mapped as a function of these process parameters, where labels for every data point represents the relative crystallinity in percentage (% RC). The RC quantifies the amount of crystalline phase present in the synthesized product using PXRD patterns (Figure 3-6 and Table 3-3 provide complete set of analysis and synthesis conditions). The RC of a simulated pattern obtained from single crystal data (Figure 3-6a) was defined to be at 100% and rest of the samples synthesized in flow are normalized to this value. The outcome was divided into three categories based on RC: samples with >80% RC were classified as crystalline, samples with 30% < RC < 80% classified as semi-crystalline and samples with RC < 30% were classified amorphous.

The effect of residence time and FA:DMF on product crystallinity is highlighted in Figure 3-2a. The linker concentration used for all synthetic conditions explored was 1 mmol in a 30 mL reaction mixture (this corresponds to ~3 times the value used in batch synthesis) and a constant molar ratio of M:L = 3 was maintained. Residence times were varied from 15–120 min for all conditions explored, while short residence times in the range of 1–5 min were run only for the composition with FA:DMF = 2, which yielded solids with the highest level of crystallinity (~87% RC). At volumetric ratios of FA:DMF = 1 and 2, we observed the formation of crystalline MOF-808 at all residence times beyond 5 min, while residence time in the range of 1–3 min led to amorphous and semi-crystalline products (Figure 3-2a). Increasing the amount of formic acid in the precursor mixture (FA:DMF = 3) resulted in a semi-crystalline product at all residence times, possibly due to competitive coordination of the formate ligand with the SBU which reduces the chances of linker coordination, resulting in defects and a low crystalline product. A further increase in the amount of formic acid (FA:DMF = 4) yields amorphous solids at residence times below 30 min and a semi-crystalline product showing short range order with increasing residence time. These results suggest that longer induction periods may be necessary to overcome the reduced rate of nucleation and crystal growth due to the influence of excess formate ions in the precursor solution.^{89, 104} The highest level of formic acid (FA:DMF = 5) in the precursor mixture resulted in amorphous solids at all residence times, due to the H₃BTC linker precipitating out of the solution

that changes the precursor composition and coordination equilibria required to obtain MOF-808. Lower levels of formic acid (FA:DMF = 0.67, and 0.25) generated amorphous solids in the form of a dense residue resulting from fast coordination reactions between the linker and SBU – lacking long-range order.¹⁰¹

Flow reactors can usually operate at higher concentrations, provided reagents stay in solution, offering great benefit in the current scenario for using higher concentration of metal salt and linker to increase the process productivity while maintaining similar yields.^{102, 110-111} Figure 3-2b shows the influence of linker concentration and FA:DMF on MOF-808 crystallinity (at residence time of 15 min and a constant M:L = 3). Optimization of the linker concentration and solvent composition in flow synthesis was done relative to the conventional batch crystallization mixture³ (FA:DMF = 1 and Linker Concentration = 1), highlighted as ‘Batch Optimized’ in Figure 3-2b. Interestingly, the standard batch composition did not yield any solids in flow synthesis. We increased the linker concentration in discrete steps of the initial composition by 2-, 2.5- and 3-times the amount used in batch (per unit mass) to investigate the effects of higher linker concentration in the reaction mixture. Crystalline solids were obtained at reaction conditions with FA:DMF = 1, and 2, and linker concentration at 2- to 3-times higher than batch composition. In particular, the composition with linker concentration of 3, yielded a three-fold increase in crystalline solids on a volumetric basis of precursor mixture and is labelled ‘Flow Optimized’ (Figure 3-2b). This resulted in lower solvent amounts required per unit mass of solids synthesized and a lower residence time for crystallization, thereby improving the overall process productivity. Other compositions explored in the synthesis space resulted in semi-crystalline or amorphous solids. Increasing the linker concentration beyond 3 led to an incomplete dissolution of the metal salt and linker in the precursor mixture and thus were not explored. While tuning various synthetic parameters, an important metric to monitor would be the molar ratio of modulator and the metal salt (Acid:Metal) used in the precursor mixture, stated in Table 3-3 for all compositions explored in the study. The composition used in batch had a molar ratio of Acid:Metal = 396, while the composition optimized in flow had a molar ratio of 176. Crystalline products obtained in flow synthesis had a narrow range of molar ratios (176 to 264) in the precursor mixture, provided all reagents stay in solution before synthesis. Furthermore we also explored the synthetic conditions with M:L = 1 that are typically used to make single crystal MOF-808 and require an induction time from 3-7 days under batch solvothermal conditions.^{81, 88} In order to illustrate a wider chemical design space to map the

influence of metal salt, linker and the modulator on crystallinity of MOF-808, we constructed a ternary phase diagram (Figure 3-11) to identify the regions that yield crystalline product. The axes in the ternary diagram represent mole fractions of the modulator, linker, and the metal salt; all the explored compositions were subjected to 150 °C and 15 min residence time in the flow reactor. The molar ratios of Acid:Metal in compositions with M:L = 1 were either significantly high (~1050) or below 170, which resulted in a predominantly semi-crystalline or amorphous product under the residence time explored. While compositions with M:L = 3 represent the data shown in Figure 3-2b. Table 3-4 and Table 3-5 provide calculations for yield and productivity for batch and flow syntheses. The yield is calculated based on the conversion of $ZrOCl_2 \cdot 8H_2O$ into MOF-808 (Table 3-4); the yield obtained in flow synthesis was ~80% while batch synthesis resulted in ~75% which is consistent with previous studies.^{3, 81, 94} The maximum productivity achieved in batch synthesis was $335.5 \text{ kg}_{MOF} \text{ m}^{-3} \text{ day}^{-1}$ while flow synthesis at a residence time of 5 min resulted in $95,155 \text{ kg}_{MOF} \text{ m}^{-3} \text{ day}^{-1}$, representing a two order of magnitude increase in productivity.

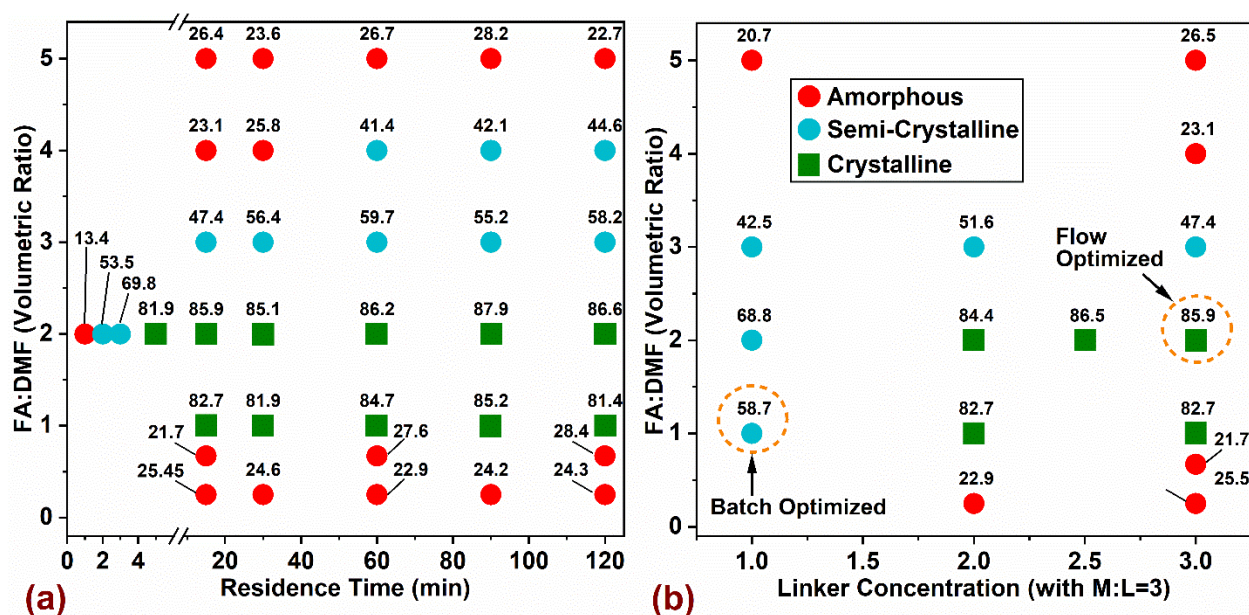


Figure 3-2 Chemical design space of MOF-808 explored using flow synthesis at 150 °C by varying (a) residence time and solvent composition (FA:DMF) and (b) H_3BTC linker concentration and solvent composition (FA:DMF) on product crystallinity at 15 min residence time. The linker concentration in the precursor mixture in (a) is three times higher than batch composition, while M:L = 3 is maintained for all conditions explored. Red and blue circles represent amorphous and

semi-crystalline regions, while green squares denote crystalline region in the chemical space. The labels for every data point represents the relative crystallinity in percentage (% RC).

Samples synthesized in flow at optimal reaction conditions were characterized further to compare attributes such as surface area, porosity, and thermal stability, with batch-synthesized samples. We collected N₂ adsorption isotherms at 77 K (Figure 3-3a) to investigate the porosity of the solids. Isotherms for all samples measured (except 1 min) are of Type I with a step at P/P₀ ~0.03, consistent with previous studies.^{3, 81-82, 112} The samples synthesized in flow at residence times beyond 15 min exhibit slightly higher adsorption characteristics compared to the samples with short residence times below 5 min, possibly due to longer time available for structure reorganization to generate better crystallinity with minimal defects.^{89, 113} To satisfy the first criteria of the BET equation,¹¹⁴ isotherm data lying within 0.05-0.15 P/P₀ were selected for curve-fitting with R² > 0.997 (Figure 3-12). The BET surface area (Figure 3-4a) showed a correlation with residence time values from ~1600 m²g⁻¹ to ~2000 m²g⁻¹ with increasing residence time from 5 min to 15 min, beyond which it remained constant. Surface area for the batch-synthesized sample was ~1900 m²g⁻¹ similar to previous reports.^{81, 84, 115} Pore size distribution was calculated using non-local density functional theory (NLDFT) based on the carbon slit-pore model as shown in Figure 3-3b. The average diameter of pores for all samples was ~16.8 Å. Samples with 3 and 5 min residence time showed a lower density of pore sizes beyond 16 Å. Thermogravimetric analysis (TGA) showing weight loss with temperature is plotted in Figure 3-13. The overall thermal stability attributes exhibited for all samples were similar, however samples with 15–120 min residence time follow a similar trace compared to the batch sample, while samples with short residence times below 5 min follow a slightly different trace, which may result from the differences in the nature of coordinated molecules and defects in the structure.^{80, 88, 116} All samples were activated before thermal analysis; an initial weight loss of ~3% below 140 °C is attributed to the loss of physisorbed water, while ~18% weight loss was observed due to loss of coordinated water molecules and formate ions on the SBU up to 300 °C.¹¹⁵ A significant weight loss of ~33% is seen at ~500 °C that results from decomposition of the organic linkers in the framework.¹¹⁷ Owing to the amorphous nature of 1 min sample, it showed a steady weight loss without any distinct features common to crystalline samples. The residual material in the form of white powder obtained > 600 °C is composed of ZrO₂ that forms after decomposition of the framework.¹¹⁵

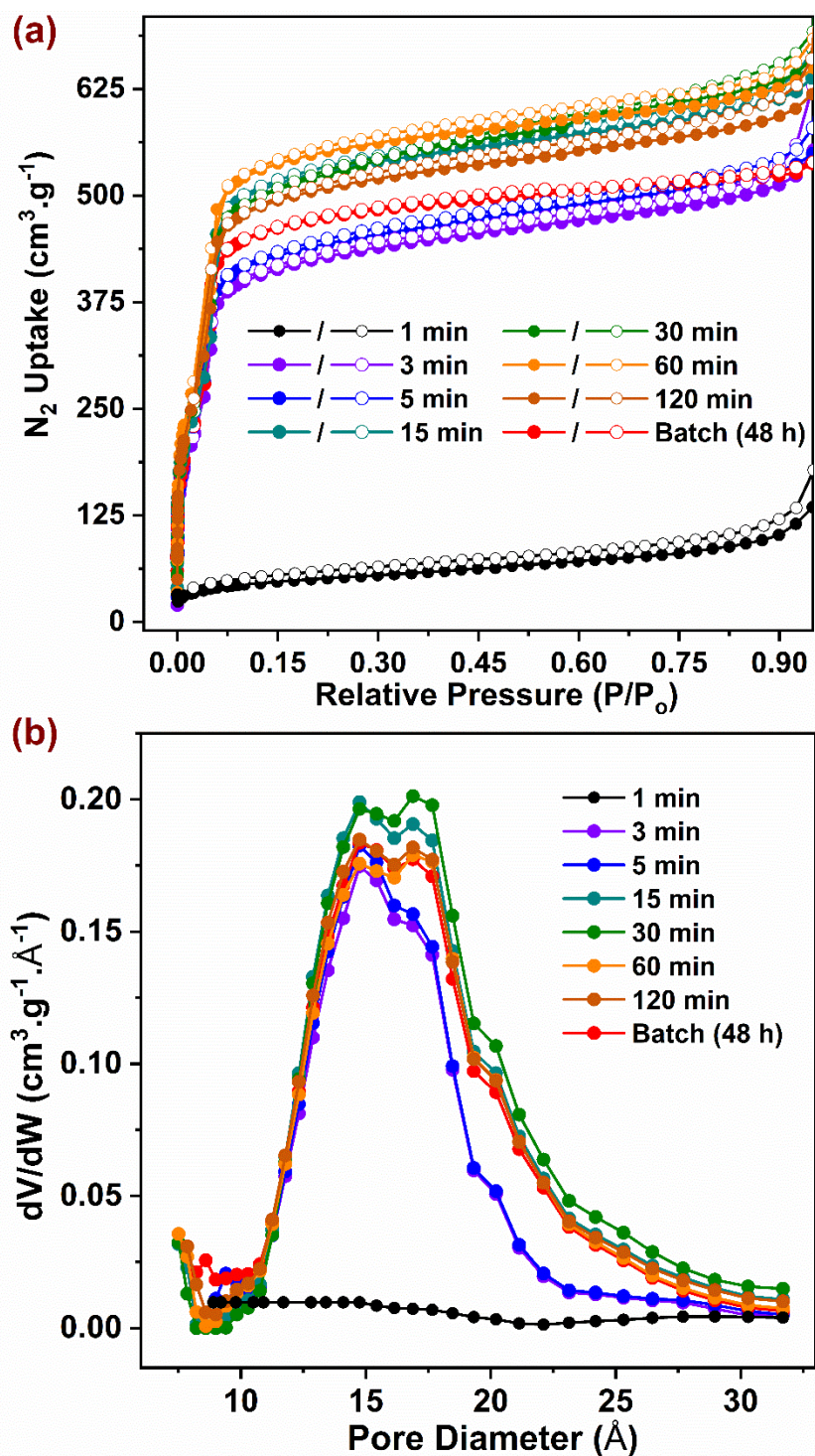


Figure 3-3 (a) N_2 adsorption (closed symbol) and desorption (open symbol) isotherm at 77 K for samples synthesized in batch and flow. (b) Pore size distribution (PSD) for all samples computed using NLDFT method.

Although most of the MOF literature focuses on reporting new structures and their use in potential applications, there is a paucity of studies that performed cost and energy analyses of the synthesis process with the goal to improve overall productivity by quantifying the cost drivers and reducing process waste.¹¹⁸⁻¹¹⁹ In a continuous manufacturing environment, comparing process parameters such as productivity ($kg_{MOF} m^{-3} day^{-1}$) with critical attributes of the synthesized product such as BET surface area ($m^2 g^{-1}$), provides a metric for tailoring the manufacturing output with the desired product quality. Figure 3-4a plots productivity and surface area for the MOF-808 samples synthesized in flow and batch as a function of residence time. If high surface areas $\sim 2000 m^2 g^{-1}$ are favored, a residence time of 15 min in flow is preferred that results in a productivity of $31,730 kg_{MOF} m^{-3} day^{-1}$. An increase in residence time beyond 15 min drastically reduces the productivity while resulting in roughly similar surface areas of the synthesized MOF. A reduction in residence time to 5 min is accompanied by lower surface area of the MOF $\sim 1600 m^2 g^{-1}$ and a corresponding increase in productivity to $95,155 kg_{MOF} m^{-3} day^{-1}$. Residence times below 3 min result in a semi-crystalline or amorphous product (Figure 3-2a) and hence were not considered. Residence times greater than 120 min result in productivities comparable to batch process making them unattractive to pursue. An effective strategy of increasing productivities in the flow reactor is accomplished by enlarging the inner diameter (ID, critical dimension of reactor tubing), which results in a quadratic dependence on volumetric flow rate ($Q \propto d^2$) – thereby increasing the precursor throughput in the reactor. An increase of tube ID by a factor of 4, from the currently used 1/16 inch (0.158 cm) to 1/4 inch (0.635 cm), increases the productivity by a factor of 16, assuming the yields are constant. However, the downside to this approach is the reduction in surface-area to volume ratio ($SA/V \propto d^{-1}$) of the tubing, which could diminish favorable heat and mass transfer characteristics.^{12, 24, 120} The key translational piece for widespread use of MOFs in revolutionary technology platforms is the ability to manufacture at desired scale with satisfactory market prices.^{12, 17} Only a handful of MOFs are commercially available with a quoted price upwards of \$30/g, making them expensive for widespread adoption.^{37, 121} For the laboratory optimized batch and flow syntheses we employed a process-based cost estimation methodology was employed to access production costs, which mimics the actual steps of synthesis (from raw materials to finished product) and determines the final cost by summing individual costs incurred in each of the steps.¹²² In order to streamline the techno-economic analysis (TEA), we only

consider production costs directly related to the MOF synthesis and ignore indirect costs and labor costs. The system boundary for the TEA, the production scenarios, the methodology for estimating process costs (materials, energy, and equipment), along with the electrical energy consumed by the process is described in Section 3.4.2 of the SI.

We performed energy balances for both batch and flow process by estimating specific enthalpy change ($kJ g_{MOF}^{-1}$), defined in terms of thermal energy input (kJ) required for heating a specific amount of the reaction mixture from room temperature (20 °C) to the reaction setpoint temperature (130 °C for Batch and 150 °C for Flow) to crystallize a gram of MOF (Figure 3-4b). Specific heat capacity c ($J kg^{-1}K^{-1}$) and density ρ ($g mL^{-1}$) for the reaction mixtures used in batch, and flow was estimated from the process modelling software ASPEN Plus V10 (Table 3-10). Heat input required only for the reaction mixture is 4-fold higher for batch synthesis compared to flow. For a biphasic-slug flow system in our flow reactor, we use a volumetric flow ratio of 2:1 for the reaction mixture to silicone oil for maximizing the amount of reaction mixture injected into the reactor without affecting the mixing characteristics in the slugs. If the energy for heating the silicone oil (continuous phase) is added to the energy required for heating the reaction mixture in flow, the total heat input for the flow process $\sim 10 kJ g_{MOF}^{-1}$ which corresponds to less than half the value for batch synthesis. The energy intensity of the process in terms of electrical energy consumed to synthesize a gram of MOF ($kWh g^{-1}$) is plotted in Figure 3-18, which accounts for the total electricity consumption in all unit operations, along with the corresponding process emissions ($kgCO_{2-eq} g^{-1}$). Since electricity is the only form of energy input required for the synthesis, process emissions originate only from the electricity grid and vary linearly as a function of energy consumed in the process. Carbon intensity of the ISO-NE electricity grid in the form of annual average GHG (greenhouse gas) emissions per kWh generated was reported to be $310 g kWh^{-1}$ in 2017.¹²³ Energy intensity of the flow synthesis compared to batch is lower by two orders of magnitude, demonstrating significant improvements in energy efficiency achieved in flow. Given the large number of functional MOFs reported in the literature, a critical assessment and optimization of manufacturing routes in a lab-scale environment serves as a prerequisite for sustainable industrial-scale synthesis paving the way for advent of low cost MOFs in commercial technologies.

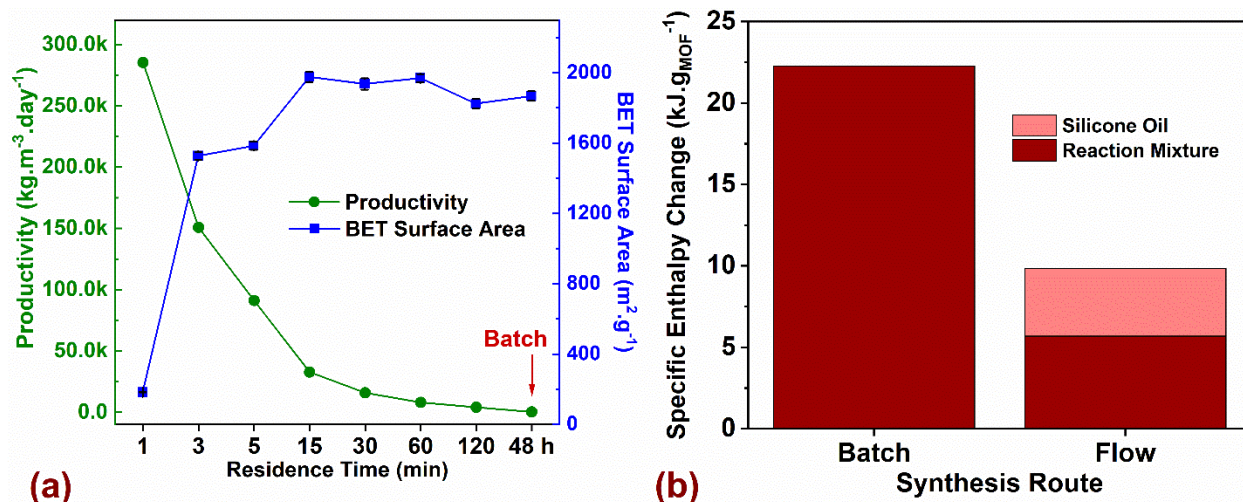


Figure 3-4 Comparison of process productivity ($kg_{MOF} m^{-3} day^{-1}$) and BET surface area ($m^2 g^{-1}$) for flow synthesized MOF-808 as a function of residence time (min) compared to batch with a reaction time of 48 h. (b) Thermal energy input required to crystallize a gram of MOF for batch and flow syntheses. Additional details on the TEA model and assumptions are listed in SI.

3.3. Conclusions

We herein report an optimized high-throughput manufacturing process using flow synthesis for the production of MOF-808 – a Zr-MOF showing remarkable hydrothermal and chemical stability featuring large micropores and open metal sites. Critical process parameters such as residence time, linker concentration and volumetric ratios of modulator and solvent were rapidly screened to map the chemical design space of MOF-808 and their influence on product attributes such as crystallinity and surface area. Optimized synthetic conditions in flow used concentrated reaction mixtures that led a reduction in the use of DMF by ~84% and formic acid by ~67% on volumetric basis – highlighting the direct benefits of flow synthesis in lowering reagent costs and a greener process. Highly crystalline monodisperse MOF-808 nanoparticles were synthesized in a residence time of 5 min in flow compared to 48 h in batch, resulting in a productivity of $95,155 kg \cdot m^{-3} \cdot day^{-1}$, which represents a record-high two order of magnitude increase than batch ($335.5 kg \cdot m^{-3} \cdot day^{-1}$). The interplay between factors such as the amount of modulator, reagent concentrations, and reaction conditions significantly affect nucleation and crystal growth rates, and should be judiciously balanced to generate desired product attributes. We report one of the first comprehensive TEA models to evaluate cost drivers and energy and mass balances involving lab-scale synthesis of MOFs. Under a continuous production environment, solvent costs dominate the

synthesis costs and a further reduction in cost structure can be achieved by minimizing the use of solvents or employing an efficient solvent recycling strategy. Minimum cost of manufacturing MOF-808 under a laboratory-demonstrated flow synthesis route was \$3/g, an order of magnitude lower compared to a handful of commercial MOFs priced upwards of \$30/g. The methodology used in the TEA is generally valid for other MOFs and highlights avenues for critical assessment and optimization of synthesis routes to manufacture MOFs at low-cost, enabling their widespread use in revolutionary technologies.

Acknowledgments:

The authors would like to thank Dr. Charles Settens for fruitful discussions related to quantification of relative crystallinity using PXRD data, Dr. Daniel Consoli for inputs on the TEA model, and Dr. Yong Zhang for technical assistance with the TEM.

3.4. Supporting Information

Synthesized samples from the flow reactor were transferred into 50 mL centrifuge tubes, washed thrice with *N,N*-dimethylformamide (DMF), and acetone. Samples were solvent exchanged with DMF for three days during which DMF was replaced every day. The DMF exchanged MOF-808 was immersed in acetone for three days during which acetone was replaced every day. The solvent-exchanged samples were vacuum dried at 22 °C for 12 h followed by activation under dynamic vacuum (120 °C for 24 h). The BET surface area and porosity of the samples was measured with N₂ adsorption measurements.

UHP N₂ gas was used to pressurize the system. Table 3-1 and Table 3-2 provide an overview of the flowrates used to obtain specific residence times and physiochemical properties of silicone oil used in flow reactions. A volumetric ratio of 1:2 Oil:Precursor was maintained to maximize the productivity of the process and operate in a stable biphasic flow regime. Higher volumetric ratio of precursor would lead to hydrodynamic failure of the reactor due to large amount of crystals clogging the tubing. Higher volume slugs also results in low mixing efficiency due to stagnation zones developed in larger slugs.

3.4.1. Materials and Methods

All reagents were commercially purchased. They are summarized below: *N,N*-dimethylformamide (99.8%, Millipore), formic acid (purity > 98%), and anhydrous methanol were obtained from EMD Millipore Chemicals. Anhydrous acetone was procured from Acros Organics. Zirconium oxychloride octahydrate ($\text{ZrOCl}_2 \cdot 8\text{H}_2\text{O}$, purity $\geq 99.5\%$), and 1,3,5-Benzenetricarboxylic acid (H_3BTC linker) was obtained from Sigma-Aldrich. Silicone oil (Dimethyl polysiloxane) for flow synthesis with the usable range of $-40\text{ }^\circ\text{C}$ to $200\text{ }^\circ\text{C}$ was procured from Alfa Aesar. The analytical tools used for materials characterization in this thesis have successfully been employed for characterizing crystallinity of nanoparticles such as diesel engine crankcase/exhaust soot,¹²⁴⁻¹³⁰ inorganic metallic species derived from lubricant/fuel ash in the diesel particulate filter,¹³¹⁻¹³⁴ and formulations used in lubricating greases for extreme-pressure applications.¹³⁵⁻¹³⁹

Synthesis of MOF-808 in Batch: Microcrystalline powder samples of MOF-808 were synthesized based on synthetic procedure reported by Jiang et al.³ H_3BTC (70 mg, 0.33 mmol) and $\text{ZrOCl}_2 \cdot 8\text{H}_2\text{O}$ (323.3 mg, 1.003 mmol) were dissolved in DMF/formic acid (15 mL/15 mL) mixture and placed in a 100 mL screw-capped glass jar, which was heated to $130\text{ }^\circ\text{C}$ for 48 h. MOF-808 precipitated as white solids that were collected by filtration and washed with DMF, and acetone; the solids were solvent-exchanged and activated as described above.

Powder X-ray diffraction (PXRD) patterns were recorded with a Bruker D8 Advance II diffractometer equipped with a $\theta/2\theta$ Bragg-Brentano geometry and Ni-filtered $\text{CuK}\alpha$ radiation ($K\alpha_1 = 1.5406\text{ \AA}$, $K\alpha_2 = 1.5444\text{ \AA}$, $K\alpha_2/K\alpha_1 = 0.5$). The tube voltage and current were 40 kV and 40 mA, respectively. Samples for PXRD were prepared by placing a thin layer of the appropriate material on a zero-background silicon crystal plate. Figure 3-6 shows the PXRD patterns for the flow-synthesized samples with varied levels of crystallinity along with background correction scheme used for measuring the relative crystallinity.

Relative Crystallinity (% RC) measurements were calculated using the HighScore Plus analysis package from Panalytical. During the course of optimization of synthesis parameters, many reaction conditions resulted in a semi-crystalline or an amorphous material. Given that the material crystallinity is an indispensable characteristic, the Equation 3-1 was used to quantify the RC of all synthesized samples. We subtracted the constant background intensity ($I_{\text{const.bkgd}}$) from the total intensity (I_{tot}) to remove substantial contributions to the signal from amorphous phases found in

semi-crystalline samples. The intensity contribution from crystalline peaks (I_{cryst}) was calculated using the corrected background, which was computed by an iterative method developed by Sonneveld et al.¹⁴⁰ that takes into account granularity of the background fitting and bending factors pertaining to the curvature.

$$\text{Relative Crystallinity (\% RC)} = 100 \times \left(\frac{\Sigma I_{\text{cryst.}}}{(\Sigma I_{\text{total}} - \Sigma I_{\text{const. bkgd}})} \right) \quad (\text{Equation 3-1})$$

A summary of the investigated MOF-808 reaction conditions for the rapid optimization of synthesis design space (in flow reactor platform) is provided in Table 3-3. Calculations for yield and productivity are described in Table 3-4 and Table 3-5. We also used the Caglioti equation to fit the FWHM data points obtained for the peaks in the XRD pattern. The Caglioti equation, described below (Equation 3-2), establishes a relationship between broadening (B) and the fitting parameters W, V, and U that are derived as an instrument response function for X-ray diffraction. The curve fit provides Lorentz and Gauss coefficients that account for crystal shape factor K and instrument broadening.

Caglioti equation:

$$B^2 = (W + V \tan \theta + U \tan^2 \theta) \quad (\text{Equation 3-2})$$

Scanning Electron Microscopy (SEM) images were acquired using Zeiss Merlin High-resolution SEM. Double coated conductive carbon tape was glued to an aluminum sample mount (or stubs, 12.7 mm diameter) to minimize charging of non-conductive MOF sample and acquire high-resolution images. Small amount of sample was transferred to the mount using a spatula and excess sample was dusted off using compressed air blown for a few seconds. Sample mounts were then sputter coated with an ultra-thin layer (~10 nm) of Au/Pd (Gold and Platinum electrode), to improve resolution of edge features on the sample, reduce charging and acquire high quality images of poorly conducting samples. The SEM operational parameters such as working distance, probe current and acceleration voltage are listed below every image acquired. Figure 3-7 shows SEM images comparing batch and flow-synthesized samples.

Transmission Electron Microscopy (TEM) images were acquired using FEI Tecnai Multipurpose Digital TEM. MOF sample was added to a glass vial containing acetone and shaken to obtain a

well-dispersed suspension. A drop or two of this suspension was added to the copper grid (5-6 nm thick and 3.05 mm wide) with a thin film of pure carbon deposited on one side (CF200-CU from Electron Microscopy Sciences). After the evaporation of acetone, the grid was placed on the sample holder and inserted in the beam column. The chamber was evacuated at $3.2\text{E-}7$ torr before the electron gun was switched on and aligned for acquiring high-resolution images. The TEM was operated at 120 kV and corrected for image aberrations using stigmator in condenser/objective lens. Figure 3-8 shows a comparison of TEM images acquired for MOF samples in batch and flow syntheses, while Figure 3-9 compares morphology of isolated crystals obtained in flow and corresponding SAED pattern. Figure 3-10 compares average size distribution of nanoparticles measured using SEM and TEM micrographs. Microcrystalline MOF-808 samples synthesized from batch and flow syntheses were imaged using a high resolution transmission electron microscope (TEM) and the corresponding crystal sizes were measured using the ImageJ software program based on a procedure reported by Hirschle et al.¹⁴¹

Nitrogen adsorption and desorption isotherms were measured by using a Quantachrome Autosorb iQ apparatus at liquid nitrogen temperature (77 K). A typical sample mass of ca. 50 mg of MOF-808 was pre-activated at 120 °C for 24 h to remove all residual solvent, before measurement. Free space correction measurements were performed using ultra-high purity He gas (UHP grade 5, 99.999% pure). Oil-free vacuum pumps were used to prevent contamination of sample or feed gases. Figure 3-12 plots the linear region of the BET equation ($0.05 < P_o < 0.15$) which satisfies the first consistency criterion of the BET theory.¹¹⁴ The data points in this region had a $R^2 > 0.997$ obtained from linear regression.

Thermogravimetric Analysis (TGA) was performed in air environment with a heating rate of 5 °C.min⁻¹ on TQA 500 of TA Instruments. Figure 3-13 provides TGA trace and derivative weight loss curves for samples synthesized in batch and flow.

3.4.2. Techno-economic Analysis (TEA)

A process-based cost estimation methodology was employed to access production costs, which mimics the actual steps of synthesis (from raw materials to finished product) and determines the final cost by summing individual costs incurred in each of the steps.¹²² In order to streamline the techno-economic analysis (TEA), we only consider production costs directly related to the MOF synthesis and ignore indirect costs and labor costs. The system boundary for the TEA showing

inputs and outputs to the model along with a simplified block diagram showing flow of materials, energy consumption, and process waste generated for each unit operation is presented in Figure 3-14. A typical lab-scale synthesis starts with dissolving reagents such as metal salt and linker in organic solvents to form the reaction mixture, which is then heated to crystallize MOF particles. The post-processing of the mixture is comprised of separating crystalline solids from the mother liquor via centrifugation, followed by multiple solvent-exchanges and activation of MOF by heating under vacuum. All steps for batch and flow syntheses remain the same except the crystallization process owing to differences in the equipment used. Process waste in the form of used solvent (*N,N*-DMF, and acetone) is generated during centrifugation and activation of the MOF; while solvent recovery and recycling is crucial for a low-cost and sustainable industrial-scale synthesis, it is not practical to implement solvent recycling for a lab-scale operation due to higher capital costs involved for setting up additional infrastructure and uncertainties in solvent purity after recycling.^{119, 142} The cost associated for executing each unit operation (e.g. crystallization, separation etc.) are added to generate the total cost of synthesis in \$/g for flow and batch syntheses (Equation 3-3). Material cost reflects the cost of raw materials (metal salt, linker, modulator, and solvents) used in the synthesis, while manufacturing costs reflect the cost of machinery amortized over equipment lifetime as well as process energy, utility costs, and routine maintenance. For a laboratory-scale synthesis, we purchased small quantities of reagents and the price quotes for each of them along with the details on the equipment used in the lab are described in Table 3-6 and Table 3-7. For an industrial scale manufacturing of MOFs, bulk purchase of reagents would be required which would result in lower cost of reagents; the inputs for the TEA model can be updated to reflect the purchase prices accordingly. We model two production scenarios to quantify cost and energy associated with lab-scale flow and batch syntheses (Figure 3-15); Scenario 1: One time synthesis – represents a typical laboratory operation where MOF is manufactured intermittently in small quantities ca. hundreds of mg scale, which is used for characterization and exploratory work, and Scenario 2: Continuous Production – representing a manufacturing environment where equipment is run continuously to achieve maximum production rates. For a meaningful comparison between the synthetic routes, we match the amount of MOF synthesized for the two processes in Scenario 1, while Scenario 2 evaluates the processes based on the same production rates on a 24 h basis. In case of flow synthesis, we choose a residence time of 5 min for modelling the TEA to compare with the batch synthesis as the baseline. Operational time

calculations for batch and flow processes are determined from mass and energy balances for the unit operations, which take into account product yield and cycle times (Table 3-8).

Cost trends for manufacturing MOF-808 in flow and batch syntheses under two scenarios are shown in Figure 3-16a. Equipment costs dominate the total cost of synthesis for both batch and flow routes in Scenario 1 while materials cost dominate the total cost for both synthetic routes in Scenario 2. Switching from an intermittent to a continuous production resembling an industrial-scale operation lowers the total synthesis cost of MOF-808 to \$11.3/g in batch and \$3/g in flow, representing an expected reduction by ~85% and ~60% respectively. The total cost of synthesis reflects the minimum cost for MOF-808 production under a typical lab-scale environment. Materials cost breakdown shown in Figure 3-16b highlights the cost of reagents used for synthesis and post-process. Lower cost of materials in flow synthesis results from the use of concentrated precursor mixtures that yield higher amount of crystalline solids on a volumetric basis of reaction mixture compared to batch. The costs originating from process solvents (DMF and acetone) that are used in post-process for separation and activation remain the same for both synthetic routes. Costs pertaining to the use of DMF and formic acid dominate the materials cost for both synthetic routes. Flow synthesis sees a dramatic reduction in the use of DMF by ~84% and formic acid by ~67% on a volumetric basis of the reaction mixture compared to batch, resulting in lower costs and a greener process, highlighting the direct benefits of using a concentrated reaction mixture. Figure 3-17 shows projections for cost savings achieved in flow by reduction in the use of DMF and formic acid as a function of MOF production on a tens of kg scale. In view of mass production, we consider bulk purchase prices for reagents (Table 3-7); these projections are achieved by extrapolating the lab-scale cost structure with a goal to quantify costs incurred in batch and flow synthesis and do not consider parameters associated with scaling-up the production such as equipment, storage space etc. Further cost reductions are possible by modifying the unit operations that can minimize the use of expensive solvents or recycling them to achieve a greener synthetic route. Given the excellent hydrothermal stability of MOF-808, modifications in the post-process by replacing the use of DMF and acetone with water for solvent-exchange before activation, considerably reduces the cost and process waste generated.¹⁴³ Using a relatively cheaper modulator such as acetic acid instead of formic acid reduces materials cost, however it could affect the pore size distribution and surface area of the solids.^{82, 93} Tradeoffs associated with cost reduction measures related to changes in the equipment, unit operations, and precursor composition should

be judiciously considered to balance the product attributes such as surface area, crystallinity with optimal cost of synthesis.

The energy intensity of the process in terms of electrical energy consumed to synthesize a gram of MOF ($kWh\ g^{-1}$) is plotted in Figure 3-18, which accounts for the total electricity consumption in all unit operations, along with the corresponding process emissions ($kgCO_{2-eq}\ g^{-1}$). Since electricity is the only form of energy input required for the synthesis, process emissions originate only from the electricity grid and vary linearly as a function of energy consumed in the process. Carbon intensity of the ISO-NE electricity grid in the form of annual average GHG (greenhouse gas) emissions per kWh generated was reported to be $310\ g\ kWh^{-1}$ in 2017.¹²³ A detailed breakdown of energy consumed in the equipment is provided in Table 3-8. Energy intensity of the flow synthesis compared to batch is lower by two orders of magnitude in scenario 1 and an order of magnitude lower in scenario 2, demonstrating significant improvements in energy efficiency achieved in flow. A primary reason for low energy intensity stems from the use of a compact heater in flow synthesis to efficiently heat the miniaturized reaction system with high SA/V ratio that results in a higher productivity, shorter residence time and minimal heat loss, unlike batch synthesis which typically uses convection ovens or heating mantles in a lab-scale environment.^{17, 25, 91} Moreover, tuning the reaction parameters to avoid the use of harsh solvothermal conditions such as high temperature and pressure will reduce capital and operating expenses.^{12, 34} Given the wide range of electricity prices ($0.07 - 0.29\ \$/kWh$) across the US,³³ lower electricity prices would further reduce the cost of synthesis. We performed a sensitivity analysis to evaluate the influence of electricity cost on the total cost of synthesis (Figure 3-19). A variation of $\pm 70\%$ of electricity cost from a base value of $\$0.12/kWh$ resulted in $\pm 9\%$ and $\pm 2\%$ variation in the total cost of batch and flow synthesis for scenario 1. In case of scenario 2, we see $\pm 0.5\%$ variation for both synthetic routes; owing to lower energy intensity achieved in flow, energy cost are relatively a small fraction of the total cost. The purpose of this TEA is to identify general trends in batch and flow processes, costs drivers, mass and energy balances, and potential pathways to curtail the synthesis costs via lower use of solvents and modification in reaction parameters. Given the large number of functional MOFs reported in the literature, a critical assessment and optimization of manufacturing routes in a lab-scale environment serves as a prerequisite for sustainable industrial-scale synthesis paving the way for advent of low cost MOFs in commercial technologies.

Silicone oil used in flow synthesis does not mix with the precursor mixture and is not considered in the materials cost matrix as it can be fully recovered and re-used without additional equipment. Electricity is the only form of energy input required for the synthesis. Average utility costs in the US were \$0.105 per kWh, however commercial utility cost for the state of Massachusetts was \$0.12 per kWh, which is considered for calculations based on price estimates from ISO-NE (Independent System Operator-New England).¹²³ About 51% of energy mix for the grid came from non-fossil fuel sources including nuclear (31%), while natural gas accounted for 48% of the fossil fuel source of the energy mix.¹⁰² Standard labor rates could vary based on manufacturing environment, however average costs for operator would be ~\$20/person/h and a supervisory person would cost ~\$35/person/h based on estimates from US bureau of labor statistics.⁶⁶ Equipment lifetime for all machinery used in the production process, the maintenance costs and consumables are obtained after consultation with corresponding OEMs (Original Equipment Manufacturers) and described in Table 3-6. Cost incurred for maintenance and consumables on most equipment over its useful life are in a range of ~15-25% of the purchase price. Equations 3-3 to 3-9 described below are considered for cost and energy accounting in the TEA model and are computed separately for flow and batch syntheses owing to differences in process yield, cycle times, and equipment used for crystallization. Definitions for all parameters used is provided in Table 3-9. For Scenario 2 as illustrated in Figure 3-15, the maximum precursor throughput in the flow reactor (1/16 inch ID) and a corresponding yield of ~80% leads to a production rate of ca. 33 g of MOF-808 in 24 h. The batch synthesis based on the recipe by Jiang et al.³ uses a 1000 mL glass jar – is scaled-up to match the production rate achieved in flow. Deviating from using 5 x 1000 mL glass jars to accommodate the precursor mixture to a single 5000 mL glass jar could result in diminished yields and a variation in induction time – MOF synthesis relies on nucleation at reactor vessel surface and changes in surface area to volume (SA/V) ratio of the vessel leads to inconsistencies.²⁴ Increasing the vessel sizes for batch synthesis also result in large gradients in heat and mass transfer limitations that affect MOF crystallinity and require re-optimization of the process parameters (temperature, induction time) and possibly modifying the heating methods.³³ Forced convection oven used in the study was Yamato DKN-402C with a capacity of 90 L and could easily hold upto 7 glass jars of 1000 mL used in scenario 2. Bulk commodity prices used in Figure 3-17 represent the cheapest option, but storage space and additional capital expenditure on

infrastructure for handling large volumes of reagents would be required to achieve ca. tens of kg production output.

$$\text{Total Cost of Synthesis } (\$.g^{-1}) = \left(\left(\frac{C_{\text{materials}} + C_{\text{energy}}}{\text{g of MOF-808 synthesized}} \right) + \left(\frac{C_{\text{operation}}}{P_{\text{MOF-808}}} \right) \right) \quad (\text{Equation 3-3})$$

$$\text{Operational Cost } (\$.day^{-1}) = \sum_{\text{All unit operations}} \left(\frac{n_{\text{machine}} \times C_{\text{machine}} \times C_{\text{Mnt. \& Cons.}}}{\text{life-time}} \right) \quad (\text{Equation 3-4})$$

$$\text{Materials Cost of Synthesis } (\$.g^{-1}) = \sum_{\text{All unit operations}} \left(\frac{C_{\text{Zr}} + C_{\text{linker}} + C_{\text{modulator}} + C_{\text{solvents}}}{\text{g of MOF-808 synthesized}} \right) \quad (\text{Equation 3-5})$$

$$\text{Total Energy Cost } (\$) = \sum_{\text{All unit operations}} (E_{\text{machine}} \times C_{\text{electricity}}) \quad (\text{Equation 3-6})$$

$$\text{Total Equipment Cost } (\$) = \sum_{\text{All unit operations}} (n_{\text{machine}} \times C_{\text{machine}} \times C_{\text{Mnt. \& Cons.}}) \quad (\text{Equation 3-7})$$

$$\text{Process Energy Intensity } (kWh.g^{-1}) = \sum_{\text{All unit operations}} \left(\frac{E_{\text{machine}}}{\text{g of MOF-808 synthesized}} \right) \quad (\text{Equation 3-8})$$

$$\text{Process Emissions } (kgCO_{2-eq}.g^{-1}) = (E_{\text{process}} \times GHG_{\text{grid}}) \quad (\text{Equation 3-9})$$

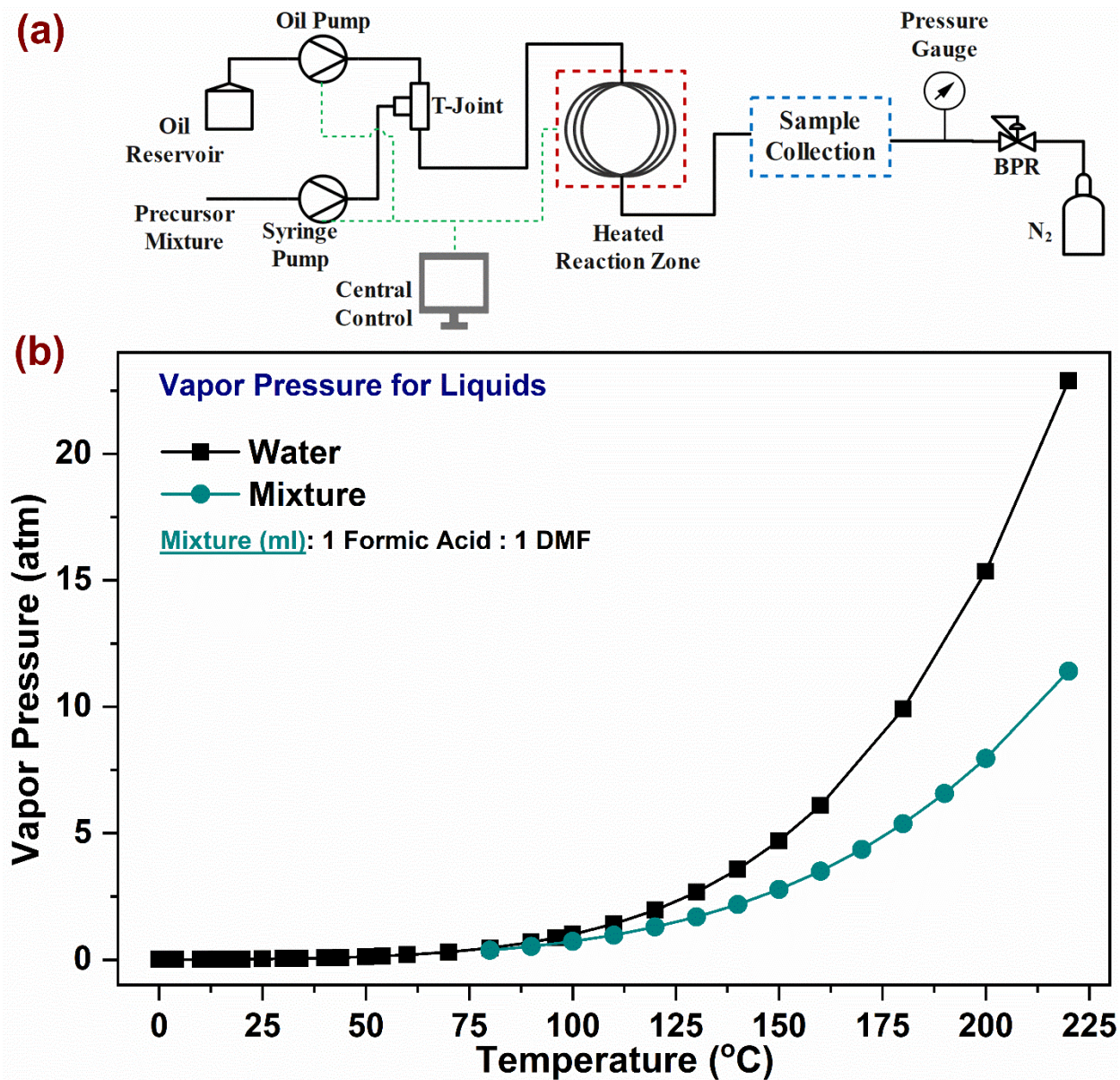


Figure 3-5 (a) Continuous flow-reactor setup used for the synthesis and optimization of MOF-808. (b) Bubble-point pressures of multiple reaction components calculated by Aspen.

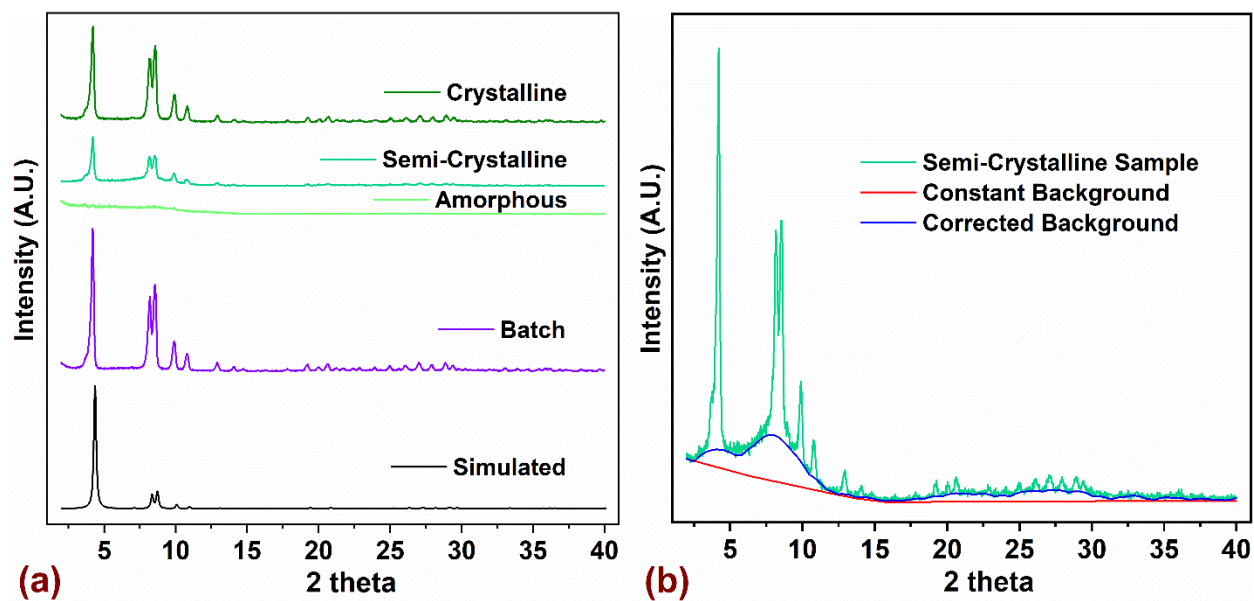


Figure 3-6 (a) PXR D patterns for MOF-808 synthesized in flow, showing different levels of crystallinity (shades of green), compared against batch sample and simulated pattern. (b) Background correction scheme used for semi-crystalline sample to quantify intensity contributions in PXR D patterns originating from crystalline phase in the sample. A hump in the low 2 theta region indicates

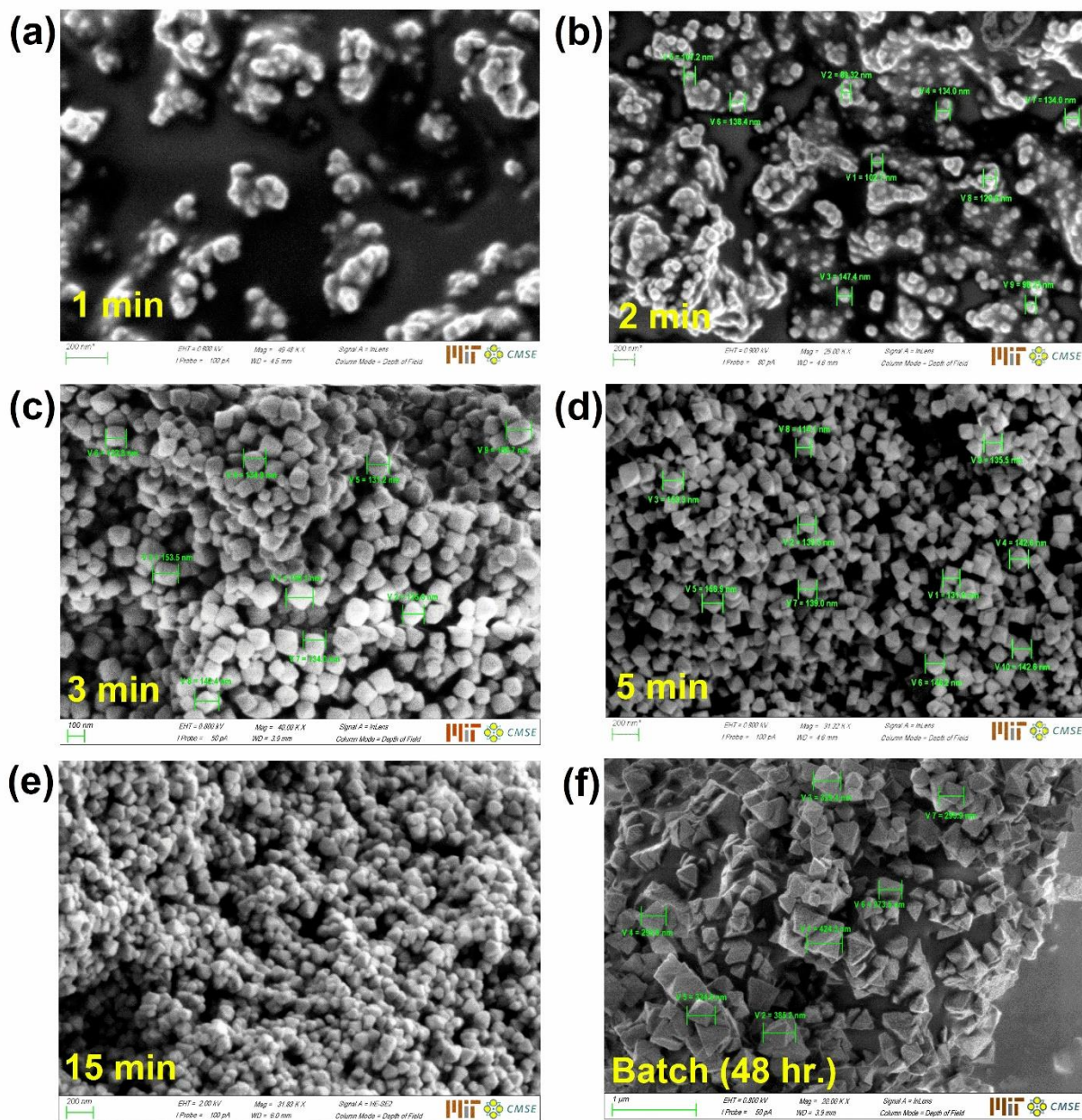


Figure 3-7 SEM images for MOF-808 synthesized in in flow (a-e), at 150 °C and short residence times (1, 2, 3, 5 and 15 min) compared to batch sample (130 °C and 48 h). Green labels on individual nanoparticles indicate average size of the solids obtained.

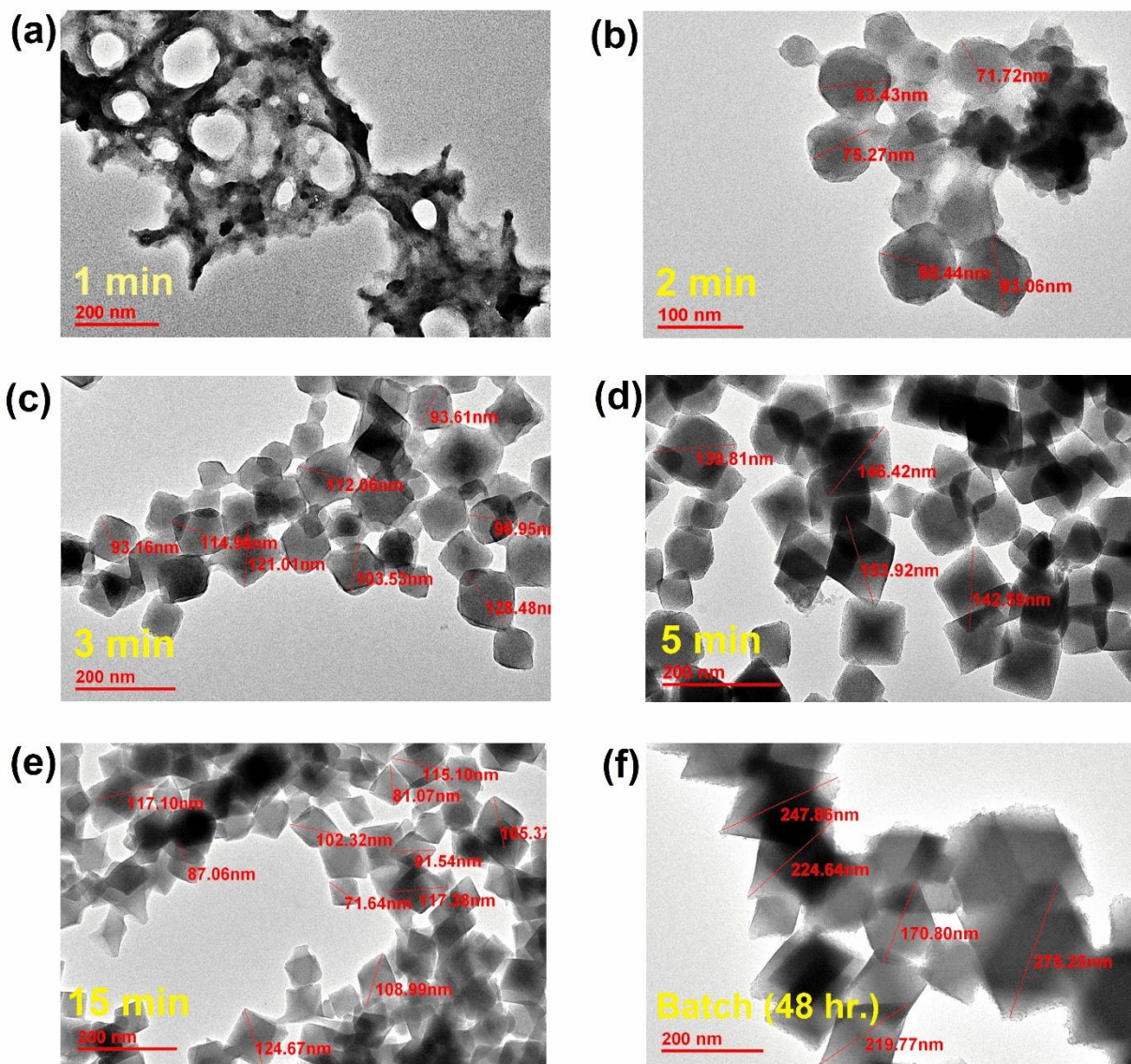


Figure 3-8 TEM images for MOF-808 synthesized in in flow (a-e), at 150 °C and short residence times (1, 2, 3, 5 and 15 min) compared to batch sample (130 °C and 48 h). Red labels on individual nanoparticles indicate average

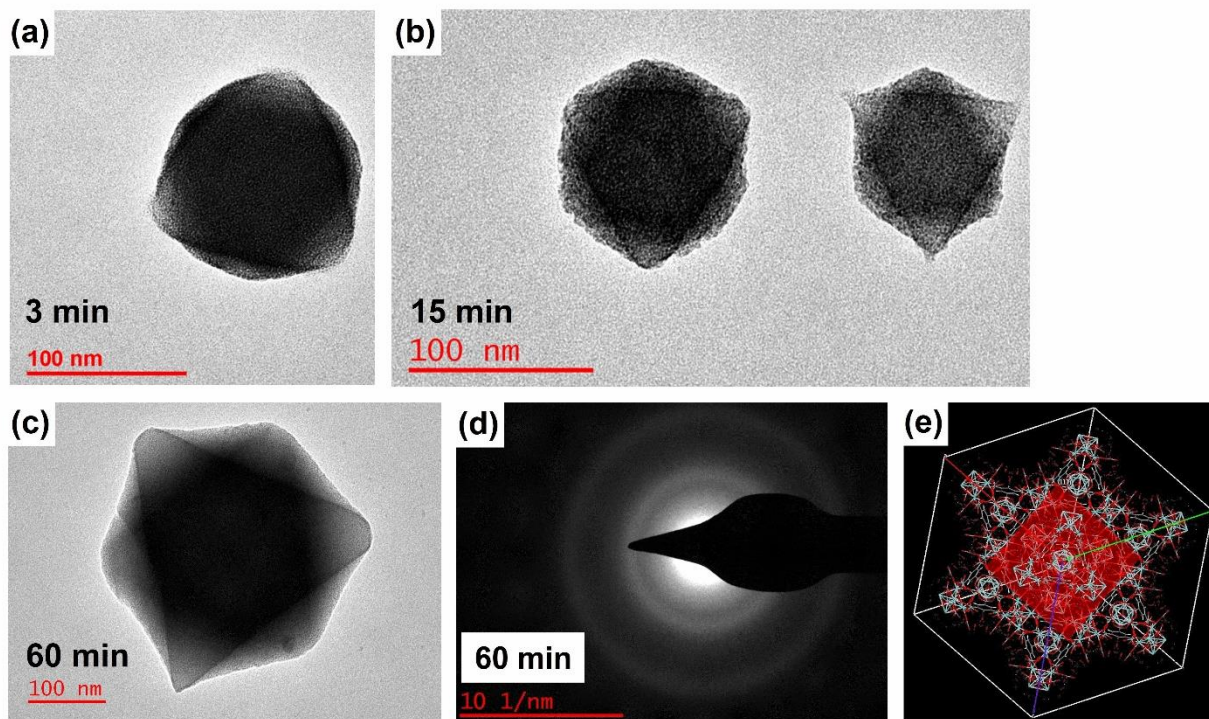


Figure 3-9 Morphology of isolated MOF-808 nanoparticles synthesized at 3, 15 and 60 min residence time in flow at 150 °C. (d) SAED (Selected Area Electron Diffraction) pattern for MOF-808 synthesized at 60 min. The diffuse concentric rings from a single nanoparticle sample in SAED could result from damage to the sample due to the electron beam in the TEM column. (e) Unit cell of MOF-808 (FCC lattice, $a = 35.076 \text{ \AA}$) viewed in (111) direction highlighted using a red plane.

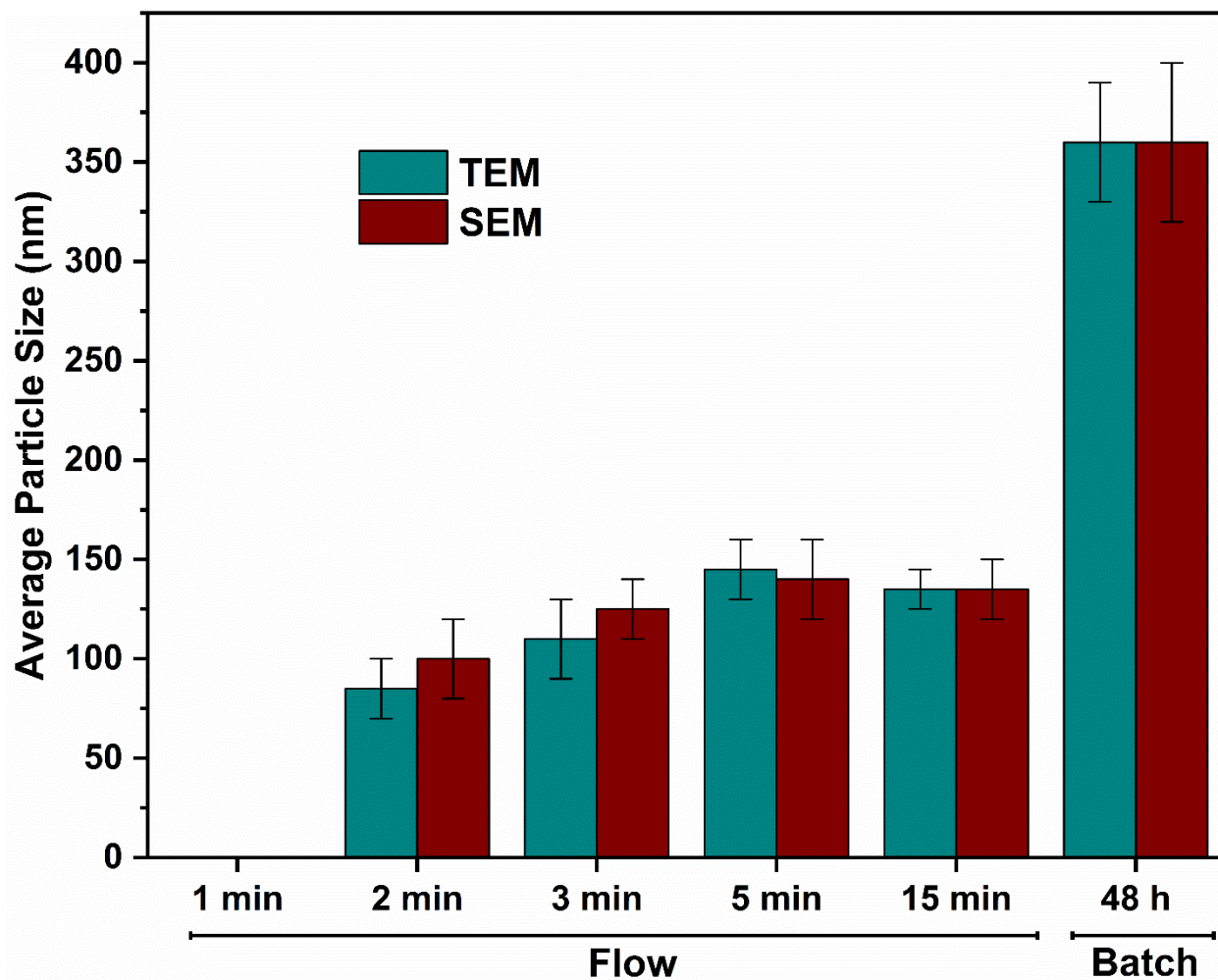


Figure 3-10 Average crystal sizes for MOF-808 nanoparticles measured from TEM and SEM images correlate well. Nearly 60 measurements were made on nanoparticles for each synthetic condition in flow and batch; their averages and corresponding error bars are reported. For the residence time of

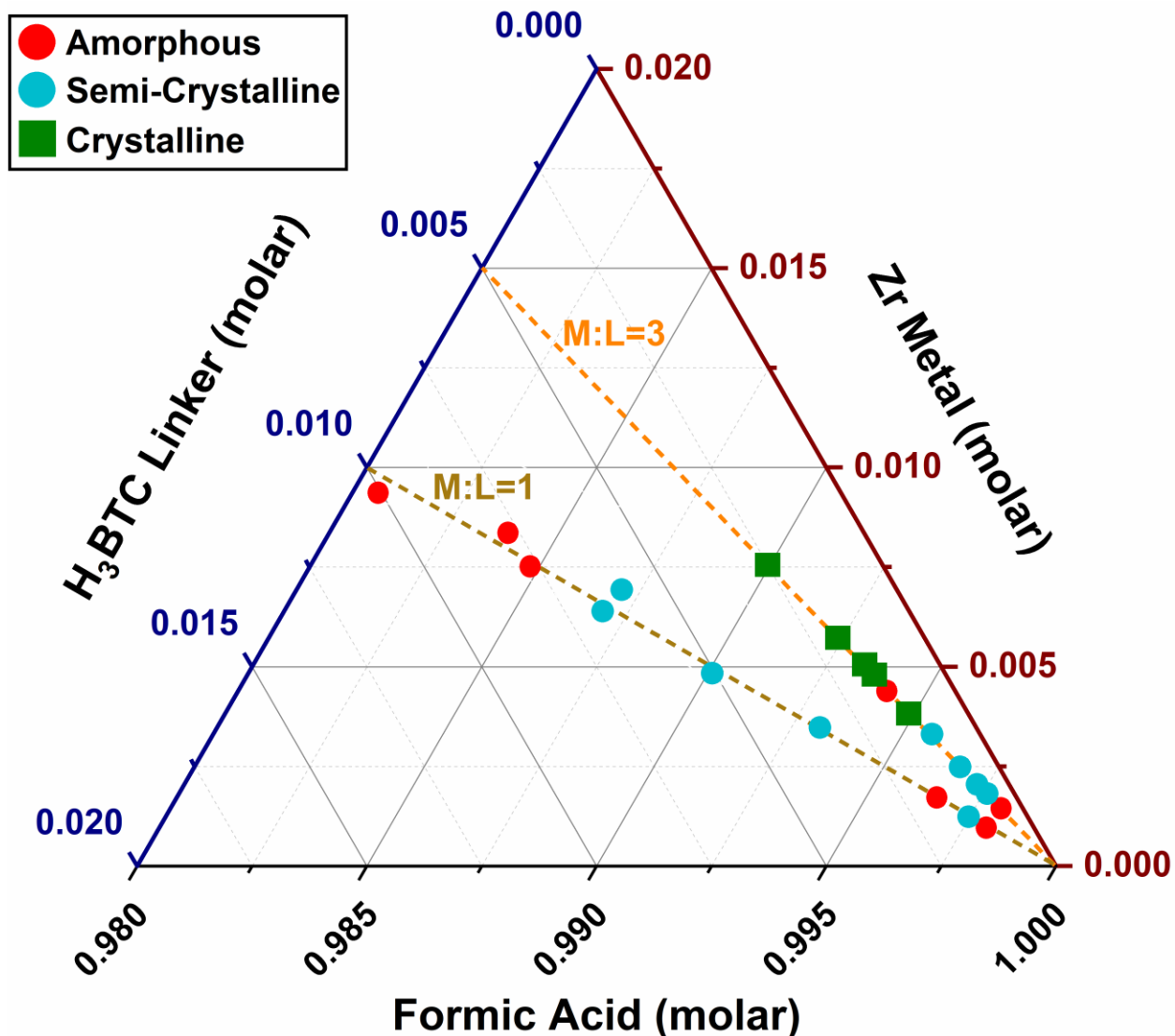


Figure 3-11 Ternary phase diagram exploring the chemical design space for MOF-808 at 150 °C and 15 min residence time. Axes for H₃BTC (Benzene-1,3,5-tricarboxylic acid) linker, Zr metal and Formic acid are in mole fractions. Synthesis compositions with a molar ratio of Metal:Linker (M:L = 1) are preferred to synthesize single crystals, while M:L = 3 is used for microcrystalline powder samples.

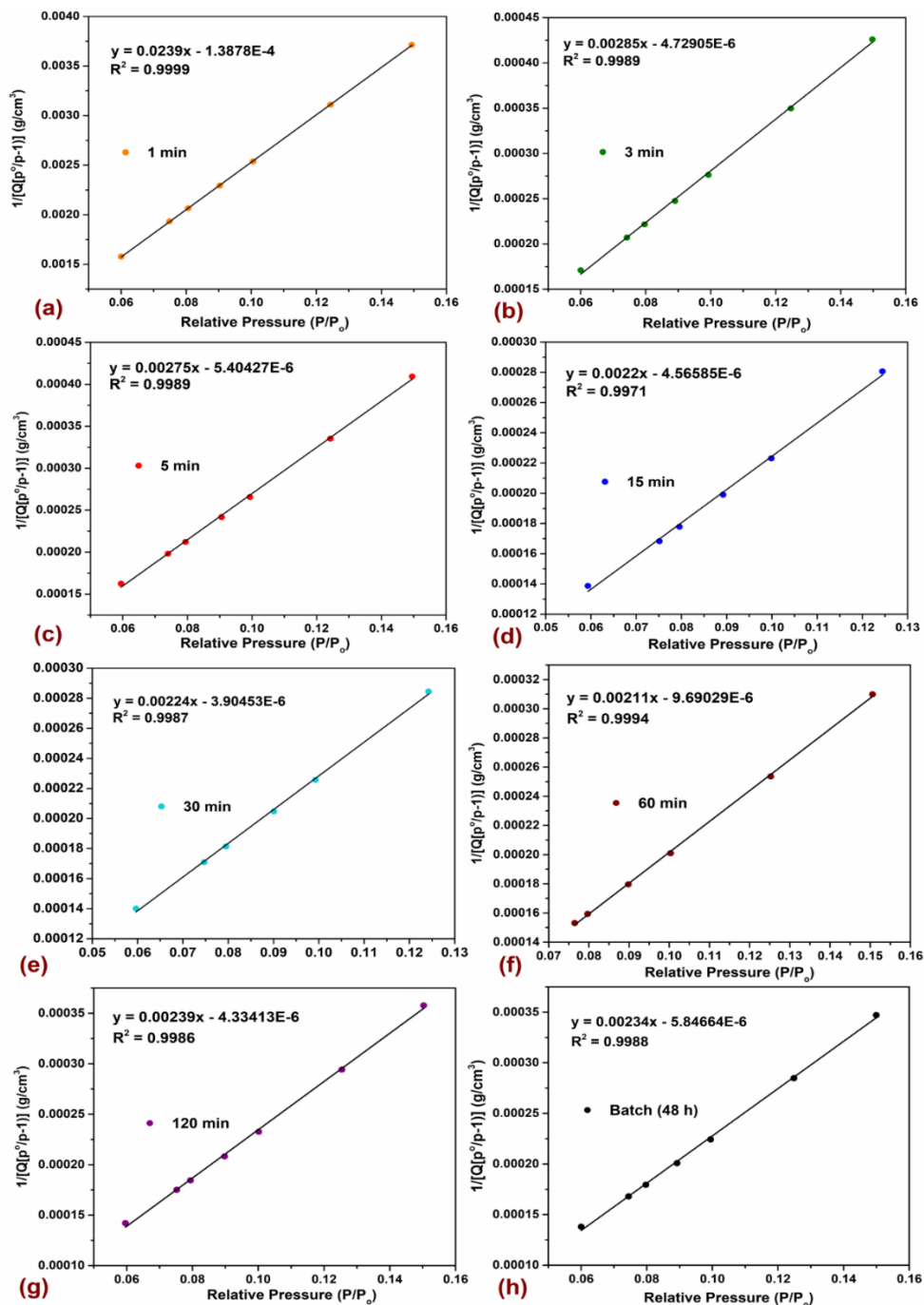


Figure 3-12 Plot of linear region of the BET equation satisfying the first criterion for application of BET theory from N₂ isotherm. Isotherm data-points lying within 0.05-0.15 P/P₀ were selected. Panel (a-g) shows curve fitting and R² values obtained from linear regression for flow-synthesized samples with residence time of 1, 3, 5, 15, 30, 60, and 120 min, while panel (h) is from batch.

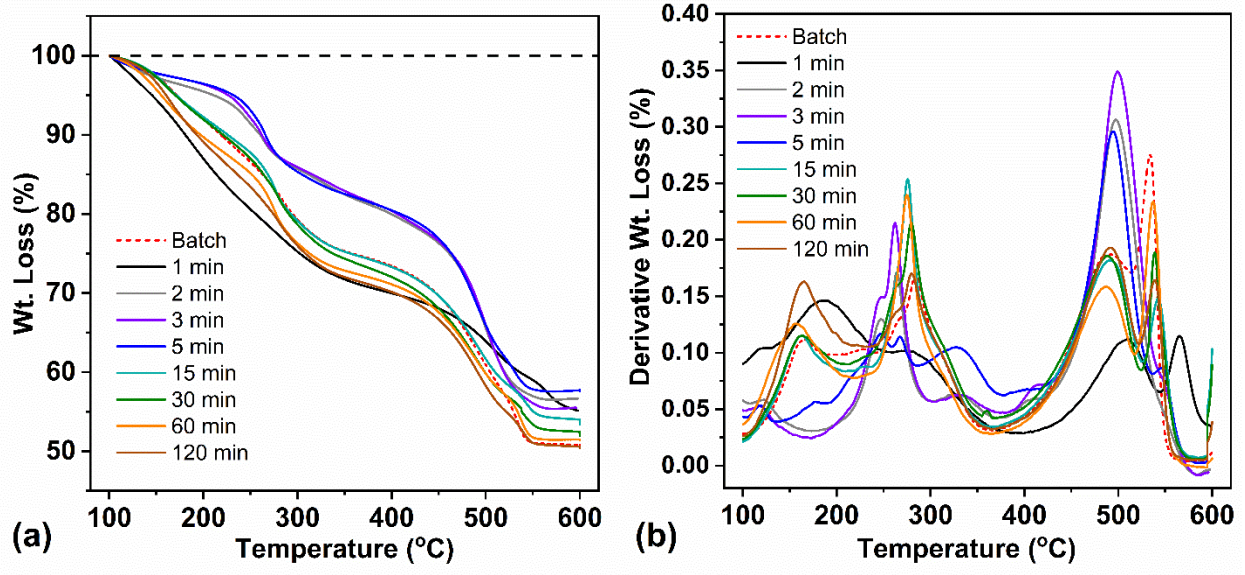


Figure 3-13 (a) TGA trace for batch and flow samples showing weight loss (%) with temperature at heating rate of $5\text{ }^{\circ}\text{C}\cdot\text{min}^{-1}$ in air. (b) Derivative weight loss for all samples indicating greatest rate of change on the weight loss curves.

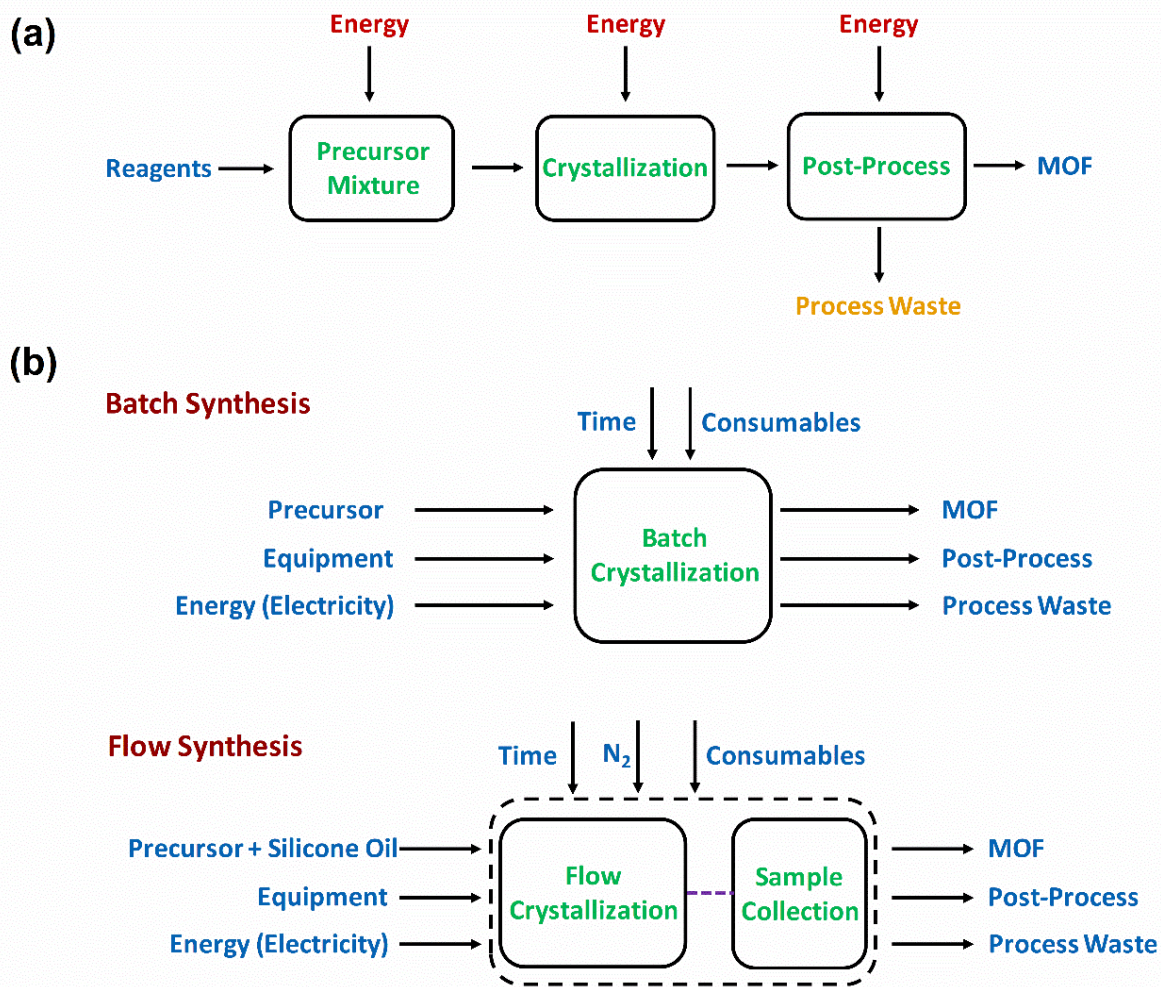


Figure 3-14 (a) Simplified block diagram for batch and flow synthesis of MOFs showing flow of materials, energy consumed and waste generation for each unit operation. (b) System boundary for the TEA model used to compare the baseline (batch synthesis) with flow synthesis. Startup/shutdown costs and associated energy consumption are considered in the model.

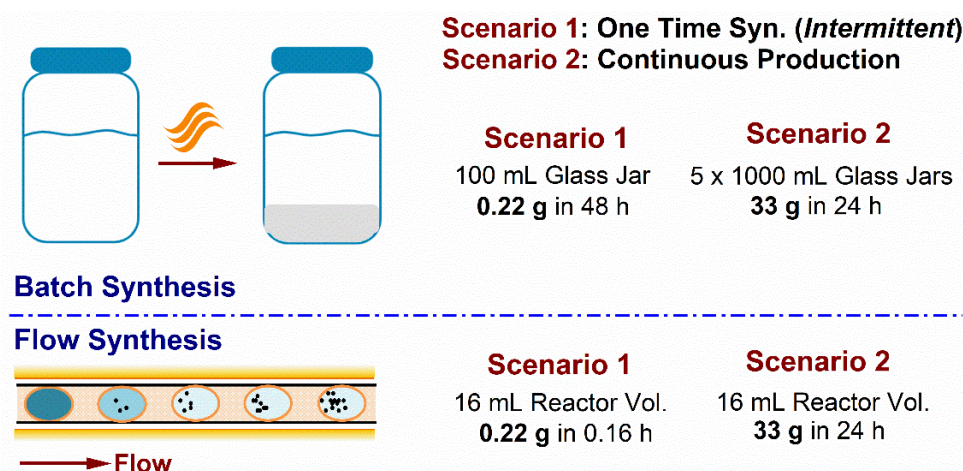


Figure 3-15 Illustration of Scenarios 1 and 2 for batch and flow syntheses that are modeled in the study. Volume of the reaction vessel required to synthesize equivalent amount of MOF in both scenarios is highlighted.

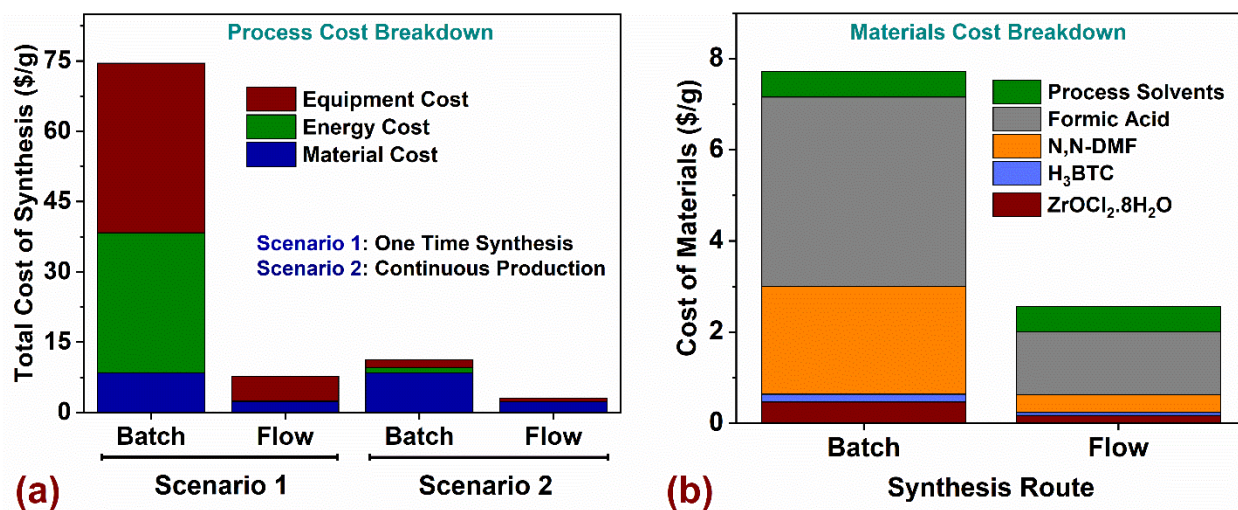


Figure 3-16 (a) Total cost of MOF synthesis for batch and flow under two scenarios modeled. The costs represent minimum cost for MOF-808 production under a typical lab-scale environment. (b) Breakdown of materials cost for batch and flow synthesis comprising of metal salt, linker, modulator and solvents.

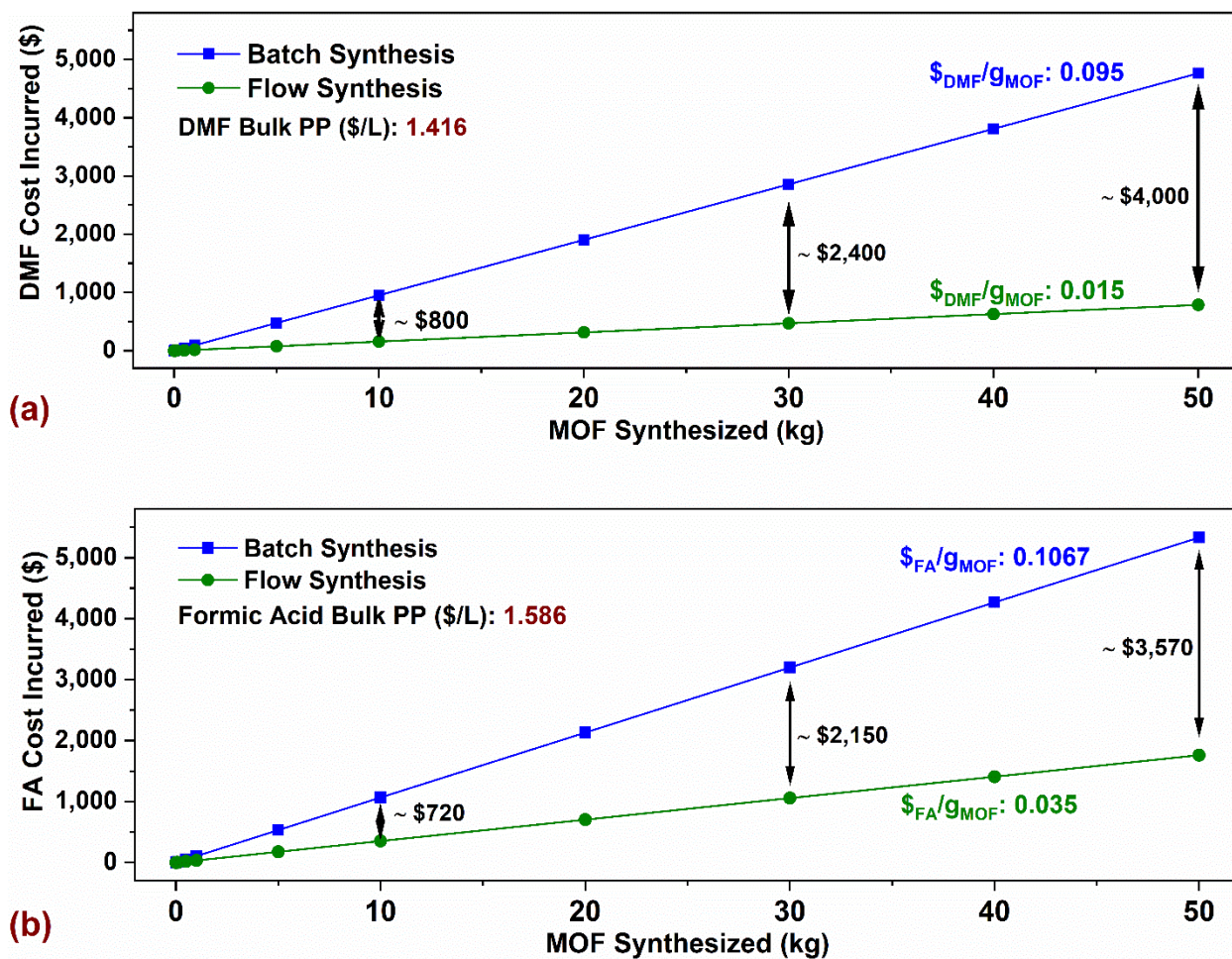


Figure 3-17 Cost incurred from the use of (a) DMF and (b) FA (Formic Acid), with scaling-up the batch and flow syntheses to manufacture MOF-808 at industrial-scale (tens of kilograms) from lab-scale (several grams), assuming constant process yields. The difference in cost between batch and flow syntheses at 10, 30 and 50 kg are highlighted. Slope of the lines represent \$ spent on DMF or FA per g_{MOF} (gram of MOF synthesized).

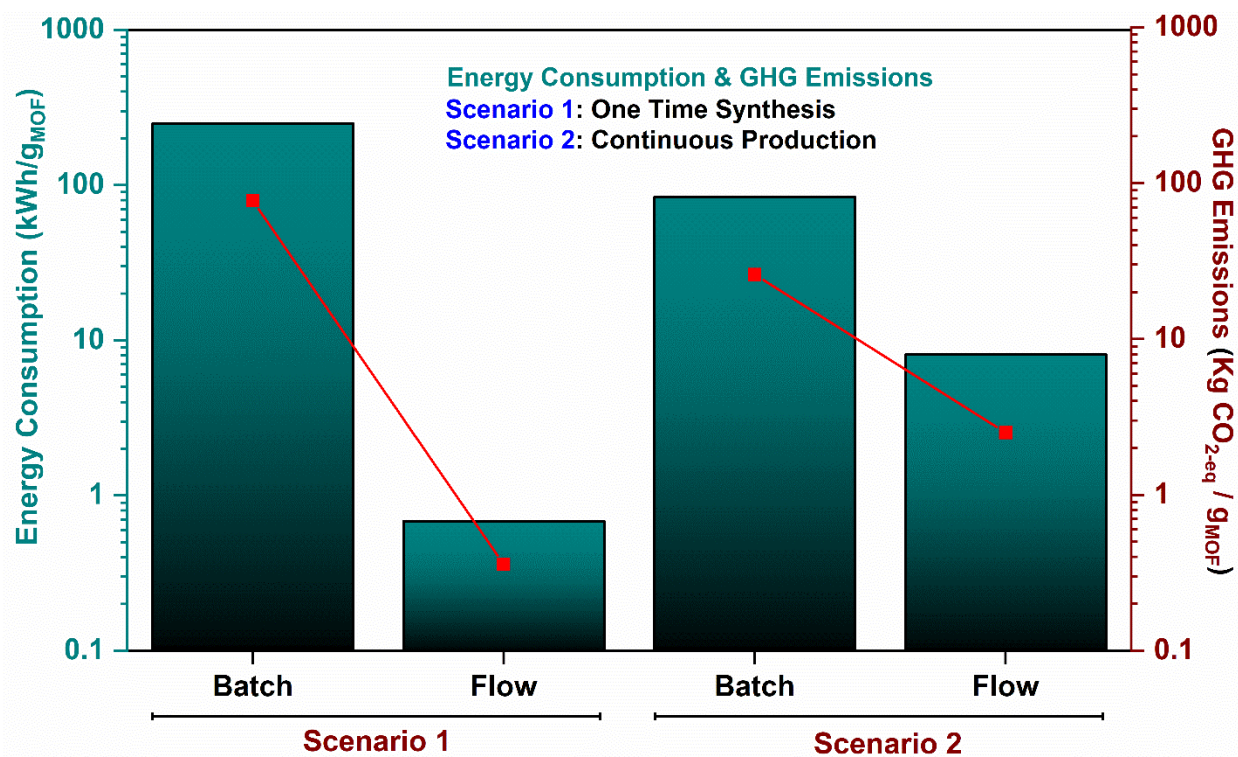


Figure 3-18 Process energy intensity ($kWh\ g^{-1}$) and corresponding process emissions ($kgCO_{2-eq}\ g^{-1}$) for batch and flow syntheses providing an overview of energy consumption and GHG emissions normalized to a gram of MOF synthesized. Additional details on the TEA model and assumptions are listed in SI.

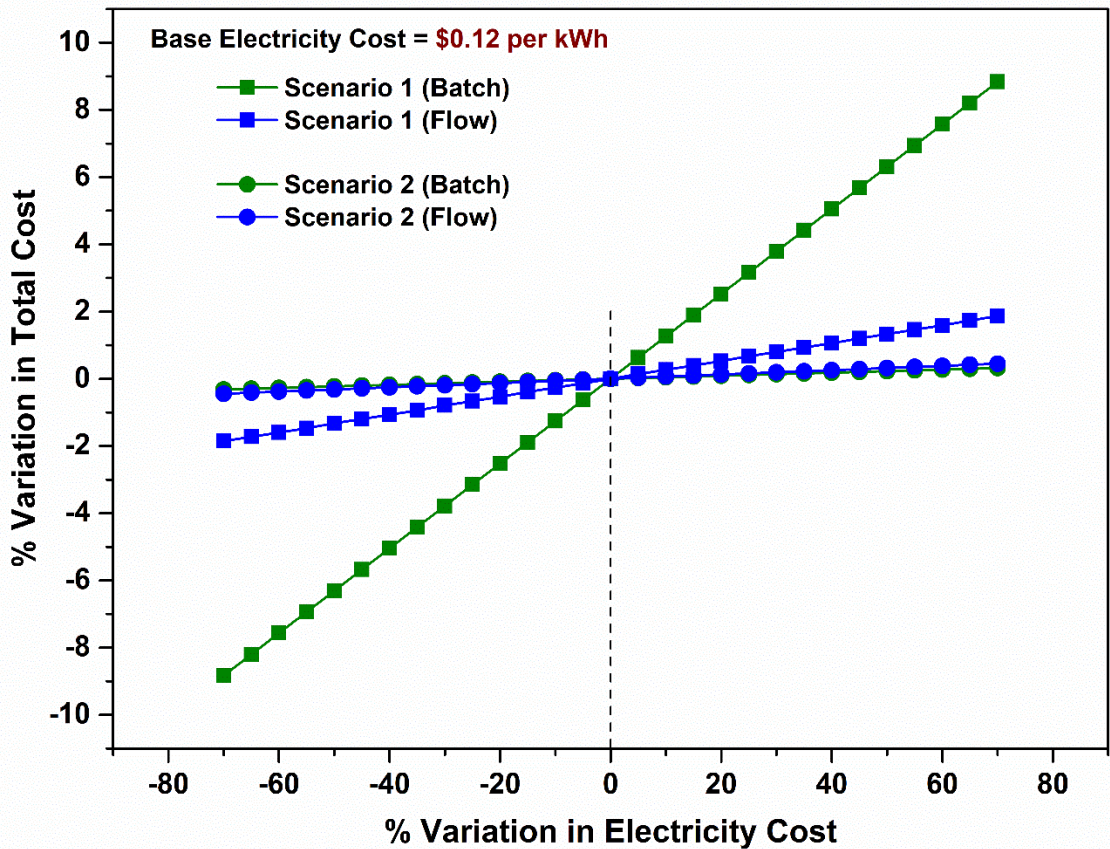


Figure 3-19 Sensitivity analysis performed to evaluate influence of electricity cost (\$/kWh) on total cost of MOF synthesis. Base electricity cost used in the analysis is \$0.12 per kWh.

Table 3-1 Residence time for multiple flow rates in a reactor volume of 16 mL. The reactor tubing had an inner diameter of 1/16 in (0.159 cm) with a heated reaction zone length of 8 m.

Total Flow Rate* (mL/min)			Residence Time		Linear Velocity
Total	Oil:Precursor (1:2)		min	hour	cm/min
	Oil	Precursor			
16.000	4.8	11.2	1	0.016	808.489
8.000	2.4	5.6	2	0.033	404.244
5.333	1.767	3.553	3	0.05	269.36
3.200	0.96	2.24	5	0.083	161.697
1.600	0.48	1.12	10	0.166	80.849
1.067	0.320	0.747	15	0.25	53.870
0.534	0.160	0.374	30	0.50	26.900
0.267	0.080	0.187	60	1.00	13.460
0.134	0.040	0.094	120	2.00	6.730

Table 3-2 Physiochemical properties of silicone oil (continuous phase) and dimensions of tubing used in the reactor for crystallization of MOF-808.

Density of Oil (@ 25°C)	855 kg/m ³
Kinematic Viscosity Of Oil (@ 25°C)	1.2E-05 m ² /s
PTFE Tubing (max operating range)	25 atm, 260 °C
T-joint (max operating range)	15 atm, 130 °C
PTFE Tubing Dimensions (in Reactor)	1/8" OD, 1/16" ID
Specific Heat Capacity (C _p) of Oil	2000 J/Kg/K
Thermal Conductivity (k) of Oil	0.135 W/m/K

Table 3-3 Summary of MOF-808 reaction conditions investigated for rapid optimization of synthesis space using the flow reactor platform at 150 °C. ‘FA:DMF’ denotes the volumetric ratio of Formic Acid to DMF used in the precursor mixture. Every reaction mixture was prepared in a fixed volume of 30 mL where volumetric ratio of FA:DMF was varied. ‘M:L’ represents molar ratio of Zr metal (in the form of ZrOCl₂.8H₂O) and H₃BTC linker (benzene-1,3,5-tricarboxylic acid, also known as Trimesic Acid). Linker concentration is varied only in precursor mixtures with M:L = 3, to probe the influence of concentrated precursor on MOF-808 crystallinity. Linker

concentration of 1 corresponds to 70 mg of H₃BTC in a 30 mL reaction mixture. Higher the concentration of precursor, lower is the ‘Acid:Metal’ molar ratio, which represents moles of Formic Acid to Zr metal in the precursor mixture. Run # 39 was the composition reported by Jiang et al.³ to synthesize MOF-808 in batch, and was used as a starting composition for optimizing flow synthesis.

Run #	FA:DMF (Vol. Ratio)	M:L (Molar Ratio)	Linker Concentration	Acid:Metal (Molar Ratio)	Res. Time (min)	% RC
1	1	3	1	396.00	15	58.66
2	1	3	1	396.00	30	68.90
3	1	3	1	396.00	60	67.38
4	1	3	1	396.00	120	73.56
5	1	3	2	198.00	15	82.69
6	1	3	2	198.00	30	81.77
7	1	3	2	198.00	60	84.00
8	1	3	2	198.00	120	81.31
9	2	3	2	264.00	15	83.35
10	2	3	2	264.00	30	81.34
11	2	3	2	264.00	60	84.36
12	2	3	2	264.00	120	84.81
13	2	3	2.5	211.00	15	86.50
14	2	3	2.5	211.00	30	83.42
15	2	3	2.5	211.00	60	86.03
16	2	3	2.5	211.00	120	83.96
17	5	3	3	220.00	15	26.43
18	5	3	3	220.00	30	23.54
19	5	3	3	220.00	60	26.56
20	5	3	3	220.00	120	22.69
21	2	3	3	176.00	15	85.89
22	2	3	3	176.00	30	85.06
23	2	3	3	176.00	60	86.15
24	2	3	3	176.00	120	86.60
25	1	1	N/A	1050.00	15	22.78
26	1	1	N/A	1050.00	30	20.73
27	1	1	N/A	1050.00	60	25.78
28	1	1	N/A	1050.00	120	34.79
29	0.25	1	N/A	53.00	15	25.45
30	0.67	1	N/A	105.00	15	21.68
31	1.5	1	N/A	158.00	15	43.06

32	4	1	N/A	210.00	15	33.07
33	1	1	N/A	132.00	2	15.16
34	1	1	N/A	132.00	5	17.39
35	1	1	N/A	132.00	15	66.80
36	1	1	N/A	132.00	30	66.57
37	1	1	N/A	132.00	60	66.03
38	1	1	N/A	132.00	120	60.62
39	1	3	1	396.00	2880	84.59
40	1	1	N/A	818.00	15	69.91
41	1	1	N/A	818.00	30	74.83
42	1	1	N/A	818.00	60	72.07
43	1	1	N/A	818.00	90	77.65
44	1	1	N/A	818.00	120	62.82
45	2	3	3	176.00	1	13.38
46	2	3	3	176.00	2	53.50
47	2	3	3	176.00	3	69.82
48	2	3	3	176.00	5	81.92
49	2	3	3	176.00	15	81.38
50	1	3	3	132.53	15	82.7
51	3	3	3	198.11	15	47.38
52	4	3	3	35.34	15	23.06
53	0.67	3	3	17.67	15	21.7
54	0.25	3	3	8.83	15	25.45
55	2	3	1	528.30	15	68.8
56	5	3	1	660.40	15	20.7
57	3	3	1	594.35	15	42.5
58	3	3	2	297.17	15	51.6
59	0.25	3	2	79.24	15	22.9
60	4	3	3	35.34	30	25.87
61	4	3	3	35.34	60	41.33
62	4	3	3	35.34	120	44.60
63	0.25	3	3	8.83	30	24.53
64	0.25	3	3	8.83	60	22.90
65	0.25	3	3	8.83	120	24.30
66	0.25	3	3	8.83	90	24.21
67	0.67	3	3	17.67	60	27.60
68	0.67	3	3	17.67	120	28.40
69	3	3	3	198.11	15	47.38
70	3	3	3	198.11	30	56.43
71	3	3	3	198.11	60	59.70

72	3	3	3	198.11	120	58.20
73	1	3	3	132.53	90	85.21
74	2	3	3	176.00	90	87.93
75	3	3	3	198.11	90	55.19
76	4	3	3	35.34	90	42.03
77	5	3	3	220.00	90	28.13

Table 3-4 Yields are calculated based on the conversion of Zr metal to MOF-808. Chemical formula for MOF-808 ($Zr_6O_4(OH)_4(BTC)_2(HCOO)_6$) has a molecular weight of 1363.8 g/mol. H₃BTC linker has a molecular weight of 210.14 g/mol. About 64.67 mg (0.2 mmol) of Zr salt was used in the precursor mixture. Below is an example calculation for yield in case of a flow synthesized sample, Run #21 in Table S3. The procedure has been adapted from Garzon-Tovar et al.¹⁶ and Furukawa et al.⁸¹

$$Yield (\%) = \left(\frac{\text{Activated Solids Obtained from Synthesis}}{\text{Solids Obtained from 100\% Zr Conversion}} \right) \times 100 \quad (\text{Equation 3-10})$$

Compound	Molar Mass	Solids Obtained for 100% Conversion of $ZrOCl_2 \cdot 8H_2O$ to MOF-808	Solids Obtained (non-activated)	Mass of Activated Solids	Yield
	g/mol	g	g	g	%
$ZrOCl_2 \cdot 8H_2O$	322.25	0.0912	0.085	0.073	80.12

Table 3-5 Calculation of process productivity ($kg_{MOF} m^{-3} day^{-1}$) for batch and flow synthesis of MOF-808 is shown in the table below. Productivity is defined as kg of solids synthesized, per m^3 of precursor mixture per day. Solids obtained for 1 and 3 min are amorphous and semi-crystalline.

$$Productivity (kg m^{-3} day^{-1}) = \frac{\text{Production Rate } \left(\frac{kg}{day}\right)}{\text{Precursor Feed Rate } \left(\frac{m^3}{h}\right) \times 24h} \quad (\text{Equation 3-11})$$

Synthesis Route	Res. Time (min)	Non-Activated Solids Obtained ($mg mL^{-1}$)	Precursor Consumed ($mL day^{-1}$)	Productivity	Yield (%)
				$kg_{MOF} m^{-3} day^{-1}$	
Flow @ 150 °C	1	17.7	16128	285465.6	~ 55
	3	29.5	5112	150804	~ 80
	5	29.5	3225.6	95155.2	~ 80
	15	29.5	1075.6	31730.2	~ 80
	30	29.5	538.5	15887.5	~ 80
	60	29.5	269.2	7943.7	~ 80
	120	29.5	135.3	3993.1	~ 80
Batch @ 130 °C	2880	0.745	450	335.5	~ 75

Table 3-6 Details of equipment used in batch and flow syntheses and calculation of operational cost of equipment (in \$/day).

Process	Equipment Description	Units	Purchase Price	Maintenance & Consumables	Equipment Life-time	Total \$	\$/day
		#	\$	\$	days		
Batch	Magnetic Stirrer	2	93.90	112.68	1825.00	225.36	0.12
	Ultrasonication	1	400.00	480.00	2190.00	480.00	0.22
	Convection Oven	1	4500.00	5400.00	2190.00	5400.00	2.47
	Pyrex Glass Jars	4	250.00	300.00	2190.00	1200.00	0.55
	Centrifuge	1	35000.00	42000.00	2555.00	42000.00	16.44
	Vacuum/Drying Oven	1	7500.00	9000.00	2555.00	9000.00	3.52
	Sample Storage, Consumables	1	600.00	720.00	1825.00	720.00	0.39
	Total Cost						59025.36

Flow	Magnetic Stirrer	2	93.90	112.68	1825.00	225.36	0.12	
	Ultrasonication	1	400.00	480.00	2190.00	480.00	0.22	
	Reactor	1	400.00	480.00	1825.00	480.00	0.26	
	Syringe Pump	1	4000.00	4800.00	3650.00	4800.00	1.32	
	SS Syringes	2	800.00	960.00	2920.00	1920.00	0.66	
	Oil Pump	1	3000.00	3600.00	2920.00	3600.00	1.23	
	Laptop	1	400.00	480.00	2190.00	480.00	0.22	
	Temp Control	1	200.00	240.00	2190.00	240.00	0.11	
	SS Sample Vials	4	190.00	228.00	1825.00	912.00	0.50	
	Tube/Fittings	1	1000.00	1200.00	2190.00	1200.00	0.55	
	Sample Storage and N ₂ Gas	1	900.00	1080.00	2190.00	1080.00	0.49	
	Centrifuge	1	35000.00	42000.00	2555.00	42000.00	16.44	
	Vacuum/Drying Oven	1	7500.00	9000.00	2555.00	9000.00	3.52	
	Total Cost						66417.36	25.64

Table 3-7 Raw material costs for reagents used in the precursor mixture and solvents. Prices reflect the cheapest rates available for purchase from EMD Millipore Chemicals, Acros Organics, and Sigma-Aldrich. Bulk purchase price in case of commodity chemicals would be cheaper than the prices mentioned below.

Reagent	Function	Price Advertised
		\$
Zirconyl Chloride Octahydrate	Zr Source	\$626 / kg
H ₃ BTC (Trimesic Acid)	Linker	\$546 / kg
<i>N,N</i> -dimethylformamide	Solvent	\$1662 / 50 L
Formic Acid	Modulator	\$755 / 10 L
Silicone Oil (Flow Synthesis)	Carrier Fluid	\$66.7 / L
Acetone	Solvent	\$20.16 / L
<i>N,N</i> -dimethylformamide (Bulk)	Solvent	\$1.41 / L
Formic Acid (Bulk)	Modulator	\$1.58 / L

Table 3-8 Energy accounting for each unit operation to synthesize MOF-808 in batch and flow process. Crystallization step is different for both processes, while rest of the operations remain the same.

Unit Operation	Process Equipment	Power Rating	Time Used	Energy Consumed	Electricity Cost	Total Cost
		W	h	kWh	\$/kWh	\$
Precursor Mixing	Magnetic Stirrer	4	0.5000	0.0018	0.120	0.0002
Crystallization (Batch) *	Forced Convection Oven	1200	48.166	57.800		6.9360
Crystallization (Flow) *	Sleeve Heater	200	0.6418	0.1284		0.0154
	Pump (Oil)	10	0.2833	0.0028		0.0003
	Syringe Pump	35	0.1166	0.0041		0.0005
	Mag. Stirrer - Syringe	4	0.1166	0.0004		0.0001
	Temp. Controller	40	0.6418	0.0257		0.0003
Computer	50	0.6418	0.0321	0.0039		
Centrifuge	Product Separation	800	0.2000	0.1600	0.0192	
Vacuum Drying Oven	Solvent Removal and Activation	3500	0.0833	0.2916	0.0350	
\$ Cost of Energy (Batch Synthesis)						6.9904
\$ Cost of Energy (Flow Synthesis)						0.0776

* Time used for Scenario 2 (continuous production) would be 24 h instead of the values mentioned in the table above.

Table 3-9 Definitions of parameters used in the techno-economic analysis.

Parameter	Unit	Definition
$C_{materials}$	\$	Total cost of materials (in all unit operations) involved in MOF synthesis.
C_{energy}	\$	Total cost of energy (in all unit operations) involved in MOF synthesis.

$C_{equipment}$	\$	Total cost of equipment (in all unit operations) involved in MOF synthesis.
$n_{machine}$	#	Number of identical machines used for the production process.
$C_{machine}$	\$	Cost of a specific machine used in the production process.
$C_{Mnt.\& Cons.}$	\$	Cost of maintenance and consumables for a specific machine.
$t_{life-time}$	days	Lifetime for a machine.
$E_{machine}$	kWh	Energy consumed by the machine (Power Rating * Usage Time).
$C_{electricity}$	\$.kWh ⁻¹	Unit cost of electricity.
C_{Zr}	\$	Cost of Zr metal salt (ZrOCl ₂ .8H ₂ O) used in synthesis.
C_{linker}	\$	Cost of H ₃ BTC linker used in synthesis.
$C_{modulator}$	\$	Cost of formic acid modulator used in synthesis.
$C_{solvents}$	\$	Cost of DMF and Acetone used in synthesis and post-process.
$E_{process}$	kWh.g ⁻¹	Energy intensity (or consumption) of the process, normalized to per g of MOF synthesized.
GHG_{grid}	kgCO ₂ -eq .kWh ⁻¹	GHG (Greenhouse Gas) emissions per kWh generation for ISO-NE grid.
$C_{operation}$	\$.day ⁻¹	Operational cost of equipment amortized over its useful lifetime.
$P_{MOF-808}$	g.day ⁻¹	Production rate of MOF-808

Table 3-10 Thermal properties of reaction mixture used in Batch and Flow synthesis.

Synthesis Route	Density of Rxn Mixture ($g\ mL^{-1}$)	Mass of Rxn Mixture (kg)	Specific Heat Capacity c ($J\ kg^{-1}K^{-1}$)	Reaction Conditions	$Q = mc\Delta T$ (kJ)
Batch (Precursor)	0.967	0.1301	1488.99	130 °C, 48 h	22.27
Flow (Precursor)	0.956	0.0318	1372.16	150 °C, 15 min	5.68
Flow (Oil)	0.963	0.0161	2000.00	150 °C, 15 min	4.17

4. Elucidating Solvothermal Crystallization of MOF-808 in a Continuous Flow Reactor and Effects of Mixing on Crystal Size Distribution

Elucidation of the crystallization pathways for MOFs allows for exploring the untapped combinatorial space of the organic and inorganic building units, creating possibilities to synthesize crystalline frameworks with desired physicochemical properties. In this chapter, we employ our continuous flow reactor to evaluate the kinetics of crystallization for Zr-based MOF-808 using time resolved powder X-ray diffraction measurements. We investigate the role of temperature and linker concentration on MOF-808 crystallization by determining the rate constants for nucleation (k_N) and growth (k_G), which are obtained from non-linear fitting of the crystallization curves with the Gualtieri model. Higher concentration of linker reduces the competitive coordination of the formate ligand (growth modulator) with the secondary building unit, thereby resulting in higher nucleation and growth rates. The activation energies obtained using Arrhenius plots for nucleation ($E_a(N)$) and growth ($E_a(G)$) are $64.7 \pm 4 \text{ kJ mol}^{-1}$ and $59.2 \pm 5 \text{ kJ mol}^{-1}$ respectively, indicating the nucleation process to be the rate-limiting step. At constant residence time, temperature and composition, higher flow velocities increase advective transport of precursor species to nucleation sites in the slugs resulting in higher average crystal sizes. A fundamental understanding of MOF-808 structural evolution would facilitate the preparation of other MOFs with tailored CSD and crystallinity as a function of synthesis parameters and reaction mixture composition.

4.1. Introduction

Metal–Organic Frameworks (MOFs) are coordination complexes consisting of organic linkers and inorganic polynuclear clusters that form two- and three-dimensional structures.¹⁴⁴ The flexibility with which the organic and inorganic units can be combined has led to the discovery of 1000's of new frameworks every year with unique properties that can be targeted for use in industrially attractive applications.¹⁴⁵ Zr-based MOFs were initially synthesized in 2008 and have demonstrated a high degree of chemical stability as well as amenability to post-synthetic modification (PSM).⁸⁰ MOF-808 was first reported by Furukawa et al,⁸¹ featuring large cavities

(diameter of 18.4 Å) and high Brunauer-Emmett-Teller (BET) surface area $\sim 2000 \text{ m}^2 \cdot \text{g}^{-1}$. The inorganic secondary building unit (SBU) in MOF-808 is comprised of a $\text{Zr}_6(\mu_3\text{-O})_4(\mu_3\text{-OH})_4(\text{CO}_2)_{12}$ referred to as Zr_6 -cluster and the organic linker comprises of benzene-1,3,5-tricarboxylic acid (H_3BTC).⁸⁰ Monocarboxylic ligands such as formate, acetate, and propionate are employed as crystal growth modulators in MOF-808 synthesis that regulate crystal size, and improve the crystallinity of the framework.^{82, 89} Although MOF-808 has been demonstrated for use in a number of industrially relevant applications such as catalysis,^{3, 83, 146} water harvesting,¹⁴⁷ heavy metal capture,⁸⁴ and arsenic removal,⁹⁴ details pertaining to kinetics of crystallization and control of the crystal size distribution (CSD) have not been reported. A thorough understanding of the self-assembly of MOF building units along with the reaction pathways to achieve precise control over the crystallization process would help in optimizing MOF synthesis to yield desired crystallinity and properties such as porosity, and defects among others.

Tailored physiochemical properties of Zr-MOFs can be achieved by coordination modulation, which uses organic ligands with a similar chemical functionality as the linker that compete for coordination sites at the SBU.^{89, 101} In the presence of a modulator, nucleation and crystal growth proceed at a reduced rate. The crystallization process requires an equilibrium between crystal formation and dissolution to allow for sufficient reorganization and defect reparation during the early stages of crystal growth.^{80, 113} In line to this, evaluating the amount of modulator, linker concentration, residence time and temperature on the extent of crystallization is imperative to achieve desired CSD, crystallinity and product yields.

The use of microfluidic flow reactors offers the ability to explore a wide range of synthetic parameters in a short amount of time with minimal consumption of reagents making them ideal to extract kinetic information.¹⁴⁸⁻¹⁵⁰ Here, we use a biphasic liquid–liquid slug flow in our reactor to perform continuous microbatch MOF crystallization. In-situ diffraction techniques such as energy dispersive X-ray diffraction (EDXRD)¹⁵¹⁻¹⁵³ and small angle X-ray scattering (SAXS)¹⁵⁴⁻¹⁵⁵ are commonly used to study kinetics of MOF crystallization. They entail the use of a heating apparatus for the reaction mixture, which is loaded into a vial (analogous to a batch reactor) and placed in the X-ray beam path to monitor the evolution of diffraction peaks as a function of time. Although in-situ diffraction measurements allow for a better temporal resolution compared to individual samples synthesized at various residence times to study the evolution of crystallinity, the influence

of parameters such as mixing of reagents, shear rates, and flow-induced molecular transport on nucleation and growth kinetics can only be studied in a continuous flow reactor. Here, we report the kinetics of crystallization for MOF-808 using a continuous flow reactor. Time-resolved crystallization study was performed by synthesizing MOF samples at desired residence times and powder X-ray diffraction (PXRD) was employed to monitor the extent of crystallization by integrating the area under prominent Bragg peaks. We investigate the role of temperature and linker concentration on rate constants of nucleation and growth that are obtained by non-linear fitting of the crystallization curves with the Gualtieri model. The rate constants were used to calculate activation energies using Arrhenius plots; the activation energy for nucleation was higher than crystal growth, implying nucleation to be the rate-limiting step. Finally, we report the use of flow rates and volume of the precursor slugs as additional tools for tuning the CSD (Crystal Size Distribution) of MOFs while achieving a narrow size distribution. Our work presented in this study elucidates the influence of synthesis conditions along with the role of reactor operational parameters to achieve crystalline MOFs with tailored CSD.

4.2. Results and Discussion

A continuous flow reactor operating in biphasic liquid–liquid slug flow regime offers the ability for precise control of RTD (residence time distribution) by eliminating the velocity differences across the channel as seen in a plug flow reactor.¹⁵⁶ In our flow reactor, silicone oil is used as an immiscible continuous phase as it preferentially wets the PTFE reactor tubing and encapsulates the slugs (μL droplets) of the dispersed phase containing the MOF precursors. Importantly, the miniaturization of the reaction system reduces diffusion lengths, aids in rapid mixing of reagents, enables fast heat and mass transport, along with seamless control of RTD (order of milliseconds), all critical elements to monitor nucleation and crystallization events. As the precursor slugs traverse the heated reaction zone, crystallization reactions give rise to viable nucleation sites that emerge from short-range crystalline order, proceeding to grain growth, and culminating into MOF crystals. The schematic for the flow reactor is illustrated in Figure 4-5 of the supporting information and details pertaining to reactor components and operation are provided in our previous work.¹⁰² In order to collect a large number of samples to perform this time-resolved crystallization study, we developed a rapid sampler module connected to the outlet of the flow reactor (Figure 4-6), which facilitates easy sampling by quenching the reactions at desired residence times. MOF solids collected at the reactor outlet are filtered and washed twice with *N,N*-

dimethylformamide (DMF) followed by acetone, before characterization with powder X-ray diffraction (PXRD). Figure 4-7 shows the PXRD pattern along with Miller indices of the prominent peaks for MOF-808. The evolution of crystallinity as a function of time is monitored using the parameter termed extent of crystallization ($\alpha(t)$), which is the ratio of integrated intensity $I(t)$ of a prominent peak at any residence time t to the maximum intensity I_{max} of the peak obtained after complete crystallization (Equation 4-1). For MOF-808, integration of peak area corresponding to the reflections from (400) was chosen to calculate $\alpha(t)$ as there are no overlapping peaks or any pre- or post-edge features, which could increase the error while obtaining area under the peak. The crystallization curves ($\alpha(t)$ vs. t) obtained at 110 °C and 150 °C are shown in Figure 4-8. After a short induction time, long-range crystalline order could be detected and the reflections from 400 gained intensity until they reached their respective maxima beyond which there was no change in $I(t)$. Since the crystallization curves obtained from Bragg reflections of two planes (400) and (331) are superimposable, the presence of preferred orientation of crystals influencing the integrated peak area can be excluded (Figure 4-8).¹⁵⁷ Unlike batch reactors used for in-situ diffraction experiments that intrinsically operate in a transient mode, flow reactors allow studies of the crystallization process at a steady state with precise control over temperature and residence time, thereby enabling time-resolved crystallization studies for any MOF of interest.

$$\alpha(t) = \frac{I(t)}{I_{max}} \dots \text{(Equation 4-1)}$$

The crystallization behavior of MOFs strongly depends on reaction conditions such as temperature, residence time, concentration of reactants and the type of solvents employed.¹⁵⁸⁻¹⁵⁹ In order to gain insights into solvothermal crystallization of MOF-808, we assessed the role of temperature and linker concentration in the reaction mixture. The crystallization curves obtained from MOF syntheses at four different temperatures (110 °C, 120 °C, 130 °C, and 150 °C) in the continuous flow reactor are shown in Figure 4-1a, while the curves from four different linker concentrations (1X, 2X, 2.5X, and 3X) are shown in Figure 4-1b. The linker concentration of 1X in the reaction mixture corresponds to 0.33 mmol of benzene-1,3,5-tricarboxylic acid (H₃BTC) based on the synthesis procedure reported by Jiang et al.³ The composition of 2X corresponds to a 2-fold increase of linker concentration in the reaction mixture with other parameters held constant; additional details pertaining to reaction mixture composition are provided in Table 4-5 and Section 4.4.2 of the SI. The linker concentration used for all the crystallization curves in Figure 1a was

3X, while a reaction temperature of 150 °C was used for all conditions explored in Figure 4-1b. The kinetic evaluation of crystallization curves was performed by fitting the data (closed symbols) in Figure 4-1 with the Gualtieri model—derived for heterogeneous crystallization of a solid from a liquid by Gualtieri.¹⁶⁰ The Gualtieri model (Equation 4-2) is well-suited for evaluating solution-mediated transformation reactions and allows for differentiation of nucleation and crystal growth by treating them as individual processes compared to the commonly used Avrami–Erofeev (AE) model which was developed for solid state processes.^{105, 153} The Gualtieri expression relates the extent of crystallization $\alpha(t)$ as a function of residence time t , the rate constant of growth k_G , the fitting parameters a and b , along with the dimensionality of crystal growth n which was set to 3 for MOF-808 as it crystallizes in $Fd-3m$ space group (cubic crystal system).^{3, 158, 161} The fitting parameters a and b are used to calculate the probability of nucleation P_N , which is described later in the study. The rate constant for nucleation k_N is calculated from the fitting parameter ($k_N = 1/a$). The induction time (t_0) defined as the period during which no crystalline products are observed, was shorter for synthesis at higher temperatures; for instance t_0 is 5 min at 110 °C which reduces to 1 min at 150 °C. Furthermore, the residence times for complete crystallization t_f at $\alpha(t) = 1$ were shorter at higher temperatures (5 min at 150 °C, increasing to ~60 min at 110 °C). Table 4-6 summarizes t_0 and t_f for all reaction conditions explored in the study. The kinetic parameters obtained by fitting the Gualtieri model to the crystallization curves obtained at different temperatures along with R^2 values are summarized in Table 4-1. The values for both k_G and k_N increase with temperature as expected for a reactive-crystallization process.¹⁶² At each temperature, $k_N < k_G$ implying that the nucleation is slower than crystal growth and the rate-limiting step. All k values increase by an order of magnitude as the temperature increases from 110 °C to 150 °C.

Similarly, the reactions carried out with variation in linker concentration (Figure 4-1b) provide insight into the coordination modulation mechanism for MOF-808.

Table 4-2 summarizes the kinetic parameters obtained for reaction conditions with varying linker concentration at 150 °C. A higher linker concentration in the reaction mixture enhances the linker coordination with the SBU by reducing the competitive coordination of the formate ligand, leading to an increase in the reaction rates. For a 3X linker concentration the molar ratio of formic acid to Zr metal (Acid: Metal) is 176, while a 1X linker concentration results in a molar ratio of 528.3

indicating higher competition by the formate ligand for coordination with the SBU (Table 4-5). Lower reaction rates with higher Acid:Metal ratio translates to lower rates for self-assembly process of MOFs.¹⁶³ The induction time t_0 is 8 min for 1X concentration which reduces to 1 min for the 3X condition. The residence times for complete crystallization were shorter at higher concentrations (5 min at 3X, 40 min at 2.5X, 45 min at 2X and 60 min at 1X). The values for k_G and k_N increase with linker concentration, which is in line with the concept of coordination modulation.^{80, 101} Larger amounts of modulator (formic acid) in the reaction mixture lead to slower nucleation rates, k_N , resulting in fewer nucleation sites that grow at a decreased growth rate k_G for all reaction conditions, $k_N < k_G$ implying the nucleation step to be rate limiting. The k values for both nucleation and growth increase by an order of magnitude as the linker concentration is increased from 1X to 3X. We also use the AE expression (Equation 4-6 and Section 4.4.2 in SI) as a second model to fit the crystallization curves. The curve fitting for the extent of crystallization $\alpha(t)$ is shown in Figure 4-9 and Figure 4-10 for different temperatures and linker concentrations respectively. The kinetic parameters such as the overall rate constant k and the Avrami exponent n_{AE} are tabulated in Table 4-7 and Table 4-8. The values for n_{AE} in the range of 0.6 to 1 are characteristic for a first order reaction mechanism and suggest that crystallization is controlled by the formation of nucleation sites.^{105, 153, 164} The k values obtained from the AE model are of the same order of magnitude compared to the Gualtieri model and increase by more than 5-fold with temperature (110 °C to 150 °C) and 8-fold with linker concentration (1X to 3X).

$$\alpha(t) = \frac{1}{1 + e^{\frac{-(t-a)}{b}}} [1 - e^{-(k_G \cdot t)^n}] \dots \text{(Equation 4-2)}$$

Table 4-1 Kinetic parameters obtained by fitting the crystallization curves obtained at four different temperatures using the Gualtieri model. The linker concentration for all conditions was 3X.

Temperature (°C)	<i>a</i>	<i>b</i>	<i>n</i>	<i>k_G</i> (min ⁻¹)	<i>k_N</i> (min ⁻¹)	<i>R</i> ²
110	23.87	19.44	3	0.070	0.041	0.991
120	17.29	12.43	3	0.089	0.057	0.998
130	9.26	6.81	3	0.163	0.107	0.996
150	3.69	1.78	3	0.382	0.271	0.998

Table 4-2 Kinetic parameters obtained by fitting the crystallization curves obtained at four different linker concentrations using the Gualtieri model. The reaction temperature for all conditions was held at 150 °C.

Linker Concentration	<i>a</i>	<i>b</i>	<i>n</i>	<i>k_G</i> (min ⁻¹)	<i>k_N</i> (min ⁻¹)	<i>R</i> ²
1X	18.07	9.2	3	0.078	0.055	0.999
2X	12.49	7.32	3	0.167	0.080	0.996
2.5X	12.16	6.34	3	0.238	0.082	0.996
3X	3.69	1.78	3	0.382	0.271	0.998

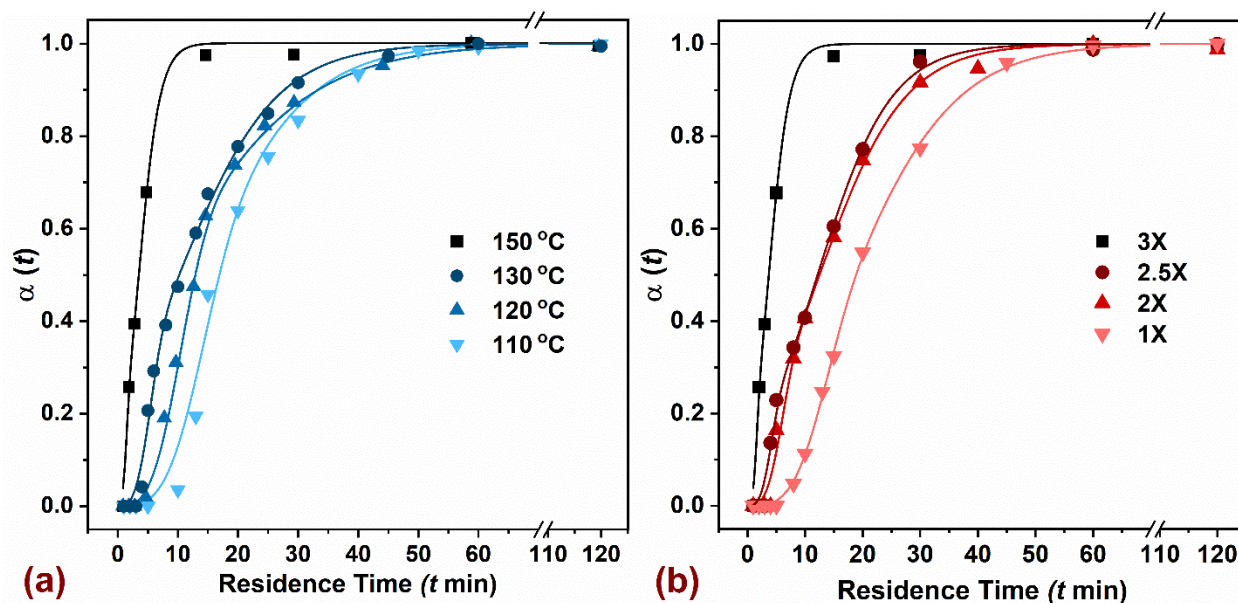


Figure 4-1 Extent of crystallization $\alpha(t)$ plotted against time t (closed symbols) and the corresponding Gualtieri fitting (solid curves) to investigate (a) influence of reaction temperature (110 °C to 150 °C) at 3X linker concentration, and (b) influence of linker concentration (1X to 3X) at 150 °C on the rates of crystallization.

The crystallization process of MOFs proceeds via two steps, nucleation of discrete particles followed by the crystal growth process, which is typically monitored by diffraction measurements and has a S-shaped curve.¹⁶⁵ The nucleation sites in the reaction mixture are not directly visible in the diffraction experiments and are estimated by the Gualtieri model by defining the probability of nucleation P_N (Equation 4-3). The expression for P_N has a Gaussian distribution of probability for the total number of nuclei N present at time t while the fitting parameter a gives the position of the top of the Gaussian peak (maximum rate of nucleation), and the parameter b is the variance of the peak describing the distribution of the probability with time.^{153, 160} The plot of P_N versus t (blue curve) for the crystallization curve obtained at 130 °C and 3X linker concentration is shown in Figure 4-2. Nucleation can be seen to extend well into the crystal growth regime and follows a Gaussian distribution to estimate the presence of viable nucleation sites at time t . The probability of nucleation for different temperatures and linker concentration is shown in Figure 4-11 and Figure 4-12 respectively. An increase in temperature leads to a faster nucleation rate with an earlier maximum as indicated by the values of fitting parameter a , while P_N becomes negligible toward the end of the crystal growth regime ($\alpha(t) > 0.9$). The maximum rate of nucleation occurs at ~ 24

min at 110 °C, which reduces to ~4 min at 150 °C. Similarly, an increase in the linker concentration also reduces the time at which maximum nucleation rate occurs, ~18 min at 1X reducing to ~4 min at 3X concentration. Since nucleation rates are strongly dependent on the level of supersaturation of the reaction mixture, an increase in the linker concentration achieves higher nucleation rates at lower residence times.¹⁶⁶

$$P_N = \frac{dN}{dt} = e^{-\left(\frac{(t-a)^2}{2b^2}\right)} \dots \text{(Equation 4-3)}$$

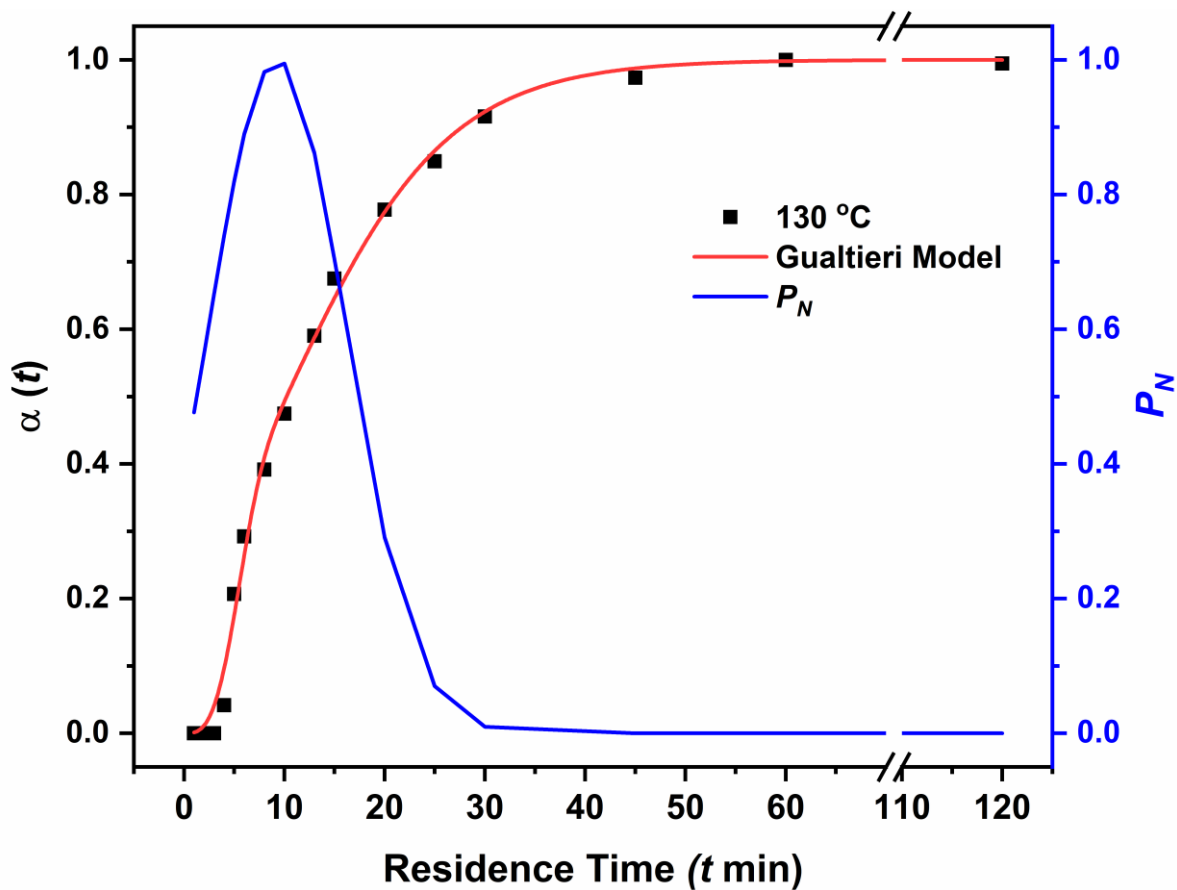


Figure 4-2 Extent of crystallization $\alpha(t)$ plotted against time t (closed symbol) and the corresponding Gaultieri fitting (red curve) as well as probability of nucleation P_N (blue curve). The crystallization curve was obtained at 130 °C with a linker concentration of 3X.

The rate constants for nucleation k_N and growth k_G obtained by fitting the crystallization curves with the Gualtieri model allow for calculation of corresponding activation energies $E_A(N)$ and $E_A(G)$ for nucleation and growth respectively. The activation energies are calculated by fitting the linearized Arrhenius expressions (Equation 4-4 and 4-5) to the Arrhenius plots ($\ln k$ vs. $1/T$) shown in Figure 4-3. The Arrhenius expression correlates the rate constant k with the pre-exponential factor A , reaction temperature T , the universal gas constant R and the activation energy E_A . The values for $E_A(N)$ and $E_A(G)$ determined by the slopes of the linear regression are $64.7 \pm 4 \text{ kJ} \cdot \text{mol}^{-1}$ and $59.2 \pm 5 \text{ kJ} \cdot \text{mol}^{-1}$ respectively (Table 4-3). A slightly higher activation energy calculated for $E_A(N)$ implies nucleation being the rate-limiting step for MOF-808. The values for both activation energies do not deviate much from each other and are fairly close the values reported by Zahn et al.¹⁰¹ for MOF-801 ($71 \pm 3 \text{ kJ} \cdot \text{mol}^{-1}$ for $E_A(N)$ and $66 \pm 6 \text{ kJ} \cdot \text{mol}^{-1}$ $E_A(G)$). They hypothesized that both energies reflect the same chemical reaction that is the exchange of modulator ligand on the Zr_6 -cluster (SBU), which would not be influenced by the size of the growing entity—either a small nucleation site or a larger crystal. MOF-801 also known as the Zr-fumarate MOF uses similar reagents in the reaction mixture (Zr salt, *N,N*-DMF, formic acid and Fumaric acid as the linker) compared to MOF-808. The activation energy calculated from the AE model using the overall rate constant k was $57.3 \pm 4 \text{ kJ} \cdot \text{mol}^{-1}$ which is in close agreement with the values obtained from the Gualtieri model (Figure 4-13). In general, the calculated activation energies for MOF-808 are of the same order of magnitude compared to the values reported for other MOFs such as HKUST-1,¹⁵¹ ZIF-8,¹⁶⁷ and UiO-66¹⁵² (Table 4-9).

$$k_N = Ae^{-\left(\frac{E_a(N)}{RT}\right)} \rightarrow \ln k_N = \ln A - \frac{E_a(N)}{RT} \dots \text{(Equation 4-4)}$$

$$k_G = Ae^{-\left(\frac{E_a(G)}{RT}\right)} \rightarrow \ln k_G = \ln A - \frac{E_a(G)}{RT} \dots \text{(Equation 4-5)}$$

Table 4-3 Activation energies for nucleation and growth obtained from Arrhenius plots for k_N and k_G . The linker concentration for all conditions was 3X.

Temperature (°C)	k_N (min^{-1})	k_G (min^{-1})	$E_A(N)$ ($\text{kJ} \cdot \text{mol}^{-1}$)	$E_A(G)$ ($\text{kJ} \cdot \text{mol}^{-1}$)	R^2
110	0.041	0.070			0.991
120	0.057	0.089	64.7 ± 4	59.2 ± 5	(Nucleation)
130	0.107	0.163			0.984
150	0.271	0.382			(Growth)

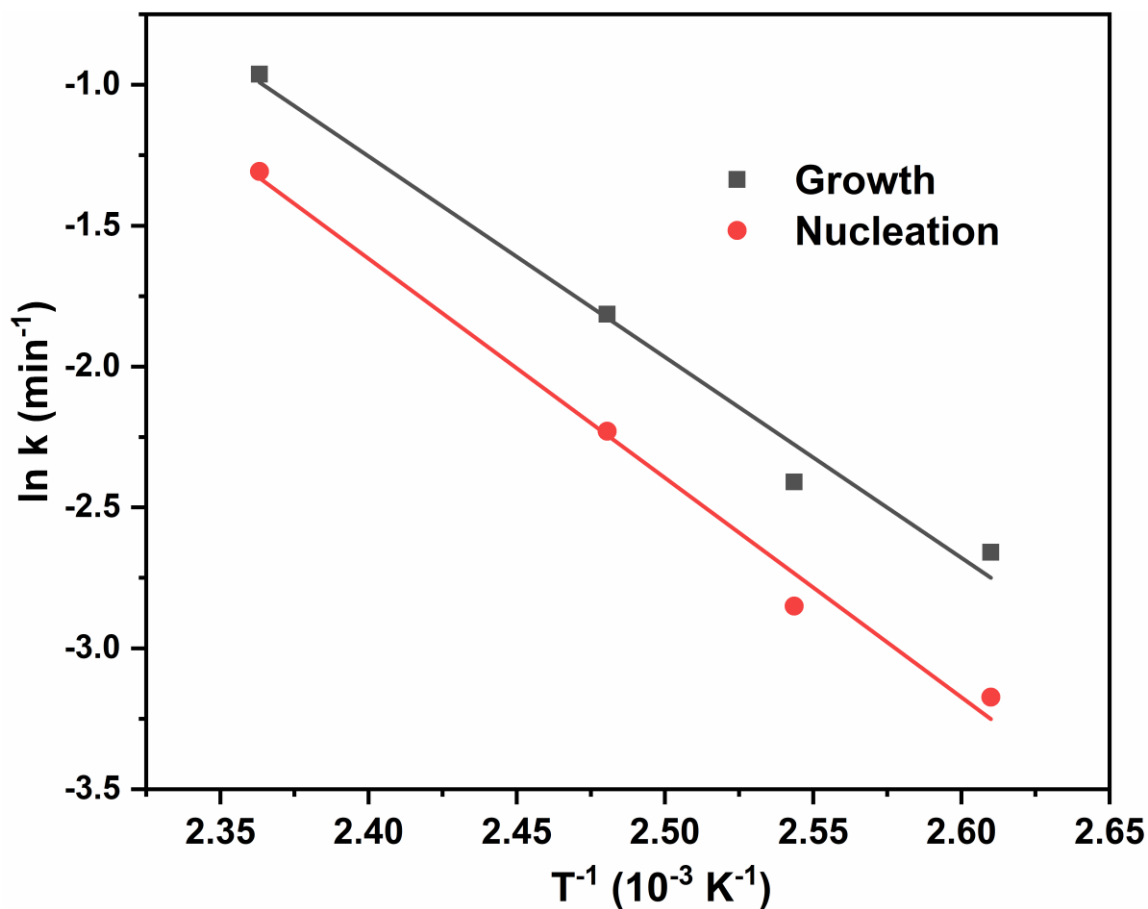


Figure 4-3 Arrhenius plots for the temperature-dependent rate constants of nucleation (red circles) and growth (grey squares) obtained from evaluation of the Gualtieri model.

Slug-flow crystallizers have recently been used to perform cooling crystallization,¹⁶⁸⁻¹⁷⁰ reactive crystallization¹⁷¹⁻¹⁷³ and anti-solvent crystallization¹⁷⁴⁻¹⁷⁵ as they provide many degrees of freedom for control of crystal size distribution (CSD), morphology, and reproducibility, along with benefits of an easier scale-up and higher process productivity. Achieving reproducible and narrow CSD is desirable for manufacturing crystalline materials with desired physiochemical characteristics, which simplifies the downstream processing steps and enhances bioavailability for drugs.¹⁷⁶ In this study, we use our flow reactor to examine the effects of flow rate and volume of the MOF precursor (reaction mixture) contained in the slugs on CSD of MOF-808. We investigated five different biphasic slug flow configurations achieved by varying the ratio of volumetric flow rates for the silicone oil (continuous phase) and the precursor (dispersed phase). All the conditions explored had a residence time of 15 min at a temperature of 150 °C and a 3X linker concentration in the reaction mixture which ensured completion of the crystallization process $\alpha(t) = 1$ (Figure 4-1a and Table 4-6). Figure 4-4a provides a schematic for these configurations wherein a biphasic slug-flow in a 16 mL reactor for 1:1 ‘Oil:Precursor’ was achieved with a flow rate of 0.53 mL/min for both the phases, while 1:10 configuration was achieved with a flow rate of 0.097 mL/min for Oil and 0.97 mL/min for the Precursor phase (Table 4-10). The ‘Precursor Only’ condition was used to study the effects of mixing patterns encountered in a single-phase flow in a PFR compared to the biphasic slug-flow regime. We studied the effects of flow rate on CSD by varying the length of the reactor tubing with the same inner diameter (1/16 inch), while maintaining a constant residence time of 15 min (Figure 4-4b and Table 4-9). Microcrystalline MOF-808 samples synthesized from all reactor configurations were imaged using a high resolution TEM (Transmission Electron Microscope) and the corresponding crystal sizes were measured using the ImageJ software program based on a procedure reported by Hirschle et al.¹⁴¹ (Figure 4-14, Figure 4-15, and Figure 4-16). Average crystal sizes shown in Figure 4-4c are obtained from measurements of ~500 nanoparticles for every biphasic slug-flow configuration from three different reactors, while the error bars correspond to one standard deviation. Interestingly, the average crystal sizes had a positive correlation with an increase in the total flow rate while maintaining a residence time of 15 min for all conditions. For instance, a total flow rate of 0.334 mL/min in a 5 mL reactor resulted in average crystal sizes of ~105 nm, while a total flow rate of 1.067 mL/min in a 16 mL reactor resulted in crystal sizes of ~180 nm. However, there was no change in CSD with variations of biphasic slug-flow configurations pertaining to the volumetric

flow ratios of ‘Oil:Precursor’ across all reactors. Similar observations can be made for the single-phase flow condition (Precursor Only) which also results in an increase in average crystal sizes with higher flow rates. Figure 4-4d shows CSD trends for the Precursor Only condition with the mean sizes being ~105 nm for the 5 mL reactor, ~140 nm for 9 mL reactor, and ~180 nm for 16 mL reactor. The CSD trends for all the biphasic slug-flow configurations are provided in Figure 4-14, Figure 4-15, and Figure 4-16. To our knowledge, this is the first comprehensive study that explores the use of flow rates and volume of the precursor slugs as additional tools for tuning the crystal sizes of MOFs while achieving a narrow size distribution.

The variation in CSD as a function of total flow rates can be explained by considering the mixing effects in the precursor slugs moving through a millifluidic channel. Each precursor slug is a well-mixed microbatch reactor where mixing of reagents occur over the order of milliseconds and is accomplished by chaotic advection, which originates from recirculating flow patterns inside the slug.¹⁷⁷ Song et al.¹⁷⁸ provided a scaling argument for estimating the characteristic mixing time t_{mix} as a function of the dimensionless Péclet number Pe (Equation 4-8 to 4-10 and Section 4.4.3 of SI). An increase in the flow rate results in higher rate of advective transport for reagents leading to a larger Pe and a smaller t_{mix} (Table 4-11). For instance, to achieve a residence time of 15 min in a 16 mL reactor, the total flow rate of 1.067 mL/min results in a Pe of 14,180. On similar lines, the Pe in a 9 mL and 5 mL reactor are 7,166 and 4,440 respectively. Higher Pe enhances flow-mediated transport of precursor species to the nucleation sites in the precursor slugs, which accelerates the crystal growth rates leading to a faster consumption of reagents in the slug.¹⁷⁹ Since the reaction mixture composition for all conditions explored remained constant (3X linker concentration), the nucleation rate J , which strongly depends on the level of supersaturation S remains the same (Equation 4-10). As the precursor slugs enter the heated reaction zone of the flow reactor, the nucleation rate would be similar across all reactor configurations, however higher flow rates to achieve the same residence time of 15 min leads to a larger Pe and consequently higher crystal growth rates. Since the reaction mixture is compartmentalized in individual slugs, higher crystal growth rates result in a simultaneous reduction in the nucleation rate owing to lower levels of supersaturation upon faster consumption of reagents. This phenomenon can be used to elucidate the CSD trends evident in our flow reactor as a function of total flow rates and offers a simpler control for manipulating the crystal sizes without requiring complicated experimental setup for supersaturation control, non-monotonic temperature profiles among others.

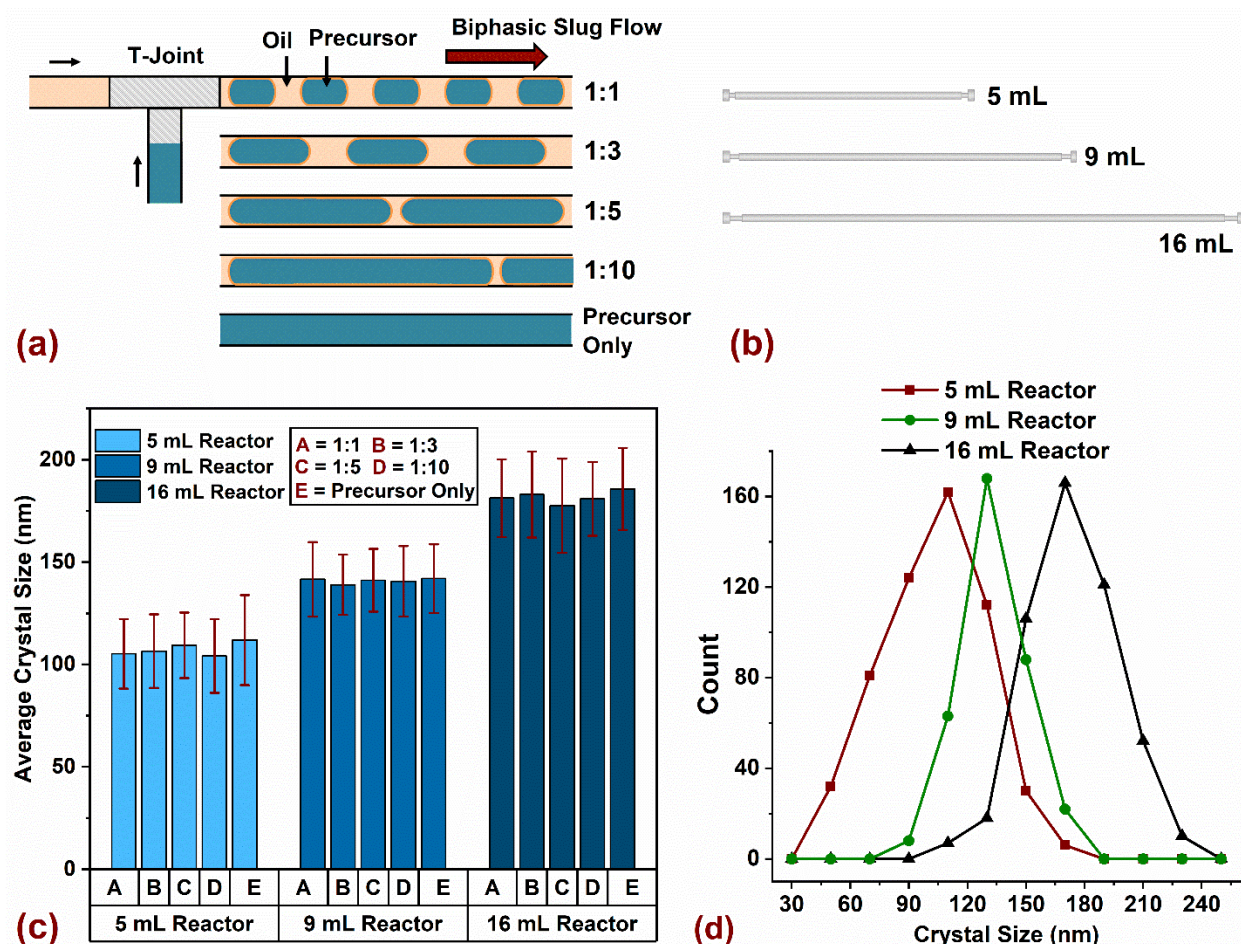


Figure 4-4 (a) Schematic representation of biphasic liquid-liquid slug flow at different volumetric ratios of silicone oil (continuous phase) and the precursor or reaction mixture (dispersed phase), generated using a T-joint. (b) Illustration of three different reactor configurations used in the study with same tube ID (1/16 inch or 1.58 mm). (c) Average crystal sizes obtained from 5 mL, 9 mL, and 16 mL reactors along with error bars representing one standard deviation for all volumetric ratios of ‘Oil:Precursor’. (d) CSD as a function of reactor volume for the single-phase flow condition (Precursor Only).

4.3. Conclusions

In this chapter, we investigated kinetics of crystallization for Zr-based MOF-808 using a continuous flow reactor. The rate constants for nucleation k_N and growth k_G were obtained by non-linear fitting of crystallization curves with the Gualtieri model, which is well suited for evaluating solution-mediated transformation reactions. The values for both k_N and k_G increased by more than 5-fold with temperature (110 °C to 150 °C) and with linker concentration in the

reaction mixture (1X to 3X). For all reaction conditions explored, $k_N < k_G$ implying that the nucleation process is slower than crystal growth and the rate-limiting step. Activation energies for nucleation $E_A(N)$ and growth $E_A(G)$ determined from Arrhenius plots were $64.7 \pm 4 \text{ kJ.mol}^{-1}$ and $59.2 \pm 5 \text{ kJ.mol}^{-1}$ respectively, while the activation energy calculated from the AE model using the overall rate constant k was $57.3 \pm 4 \text{ kJ.mol}^{-1}$ which is in close agreement with the Gualtieri model. Our study provides the first account for the use of flow rates in the reactor as a simpler tool for tuning the crystal sizes of MOFs with a narrow distribution. Average crystal sizes of ~ 105 nm were achieved in a 5 mL reactor, ~ 140 nm in a 9 mL reactor, and ~ 180 nm in a 16 mL reactor. For a constant residence time across all reactor configurations, an increase in the flow rate enhances flow-mediated transport of precursor species to the nucleation sites, thereby accelerating the crystal growth, accompanied by a simultaneous reduction in the nucleation rate due to faster consumption of reagents—the phenomenon responsible for CSD trends seen in our flow reactor. The results presented in this work allow for a better understanding of nucleation and crystal growth kinetics of self-assembled porous frameworks along with additional degrees of control offered by flow reactors to synthesize MOFs with desired physiochemical properties for real-world applications.

Acknowledgements:

The authors would like to thank Dr. Yong Zhang for technical assistance with TEM and Dr. Shuai Yuan for fruitful discussions on crystallization kinetics of Zr-based MOFs.

4.4. Supporting Information

The flow reactor platform used in this study was built using components that were available commercially along with a few custom-built modules to achieve fast heat transfer, isothermal temperature distribution in the reaction zone, optimal mixing, and fast sampling. Detailed descriptions of liquid handling modules, fluidic connections and the crystallizer apparatus are provided in our previous study.¹⁰² Figure 4-5 provides a schematic for the setup and calculations for bubble-point pressure to maintain stable reactor operation. Flow synthesis was performed at a minimum pressure of 4 atm for all synthesis conditions (with reaction temperature of 110 °C – 150

°C) to avoid formation of gas bubbles that may deleteriously affect the durability of reactor tubing and the MOF crystallization process. A rapid sampler module was custom-built for the flow reactor platform that can collect multiple samples in a short period. Figure 4-6 provides a schematic for the module and describes its operation. The ability to collect multiple samples synthesized under identical reaction conditions as well as fast collection of samples synthesized under a wide range of operating conditions makes the setup ideal to obtain crystallization kinetics data. Synthesized samples were transferred into 50 mL centrifuge tubes, washed once with hexane, twice with *N,N*-dimethylformamide (DMF) and twice with acetone before characterization. UHP N₂ gas was used to pressurize the system. Table S1 provides an overview of the flowrates and residence times used for a 16 mL reactor volume.

4.4.1. Materials and Methods

All reagents were commercially purchased. They are summarized below: *N,N*-dimethylformamide (99.8%, Millipore), and formic acid (purity > 98%), were obtained from EMD Millipore Chemicals. Anhydrous acetone was procured from Acros Organics. Zirconium oxychloride octahydrate (ZrOCl₂·8H₂O, purity ≥ 99.5%), and 1,3,5-Benzenetricarboxylic acid (H₃BTC linker) was obtained from Sigma-Aldrich. Silicone oil (Dimethyl Polysiloxane) for flow synthesis was procured from Alfa Aesar (#A1272822) and had an operating range of -40 °C to 200 °C with a flash point of >270 °C.

Synthesis of MOF-808 in Batch: Microcrystalline powder samples of MOF-808 were synthesized based on a synthesis procedure reported by Jiang et al.³ H₃BTC (70 mg, 0.33 mmol) and ZrOCl₂·8H₂O (323.3 mg, 1.003 mmol) were dissolved in DMF/formic acid (15 mL/15 mL) mixture and placed in a 100 mL screw-capped glass jar, which was heated to 130 °C for 48 h. MOF-808 precipitated as white solids that were collected by filtration and washed with *N,N*-DMF, and acetone.

Powder X-ray diffraction (PXRD) patterns were recorded with a Bruker D8 Advance II diffractometer equipped with a $\theta/2\theta$ Bragg-Brentano geometry and Ni-filtered CuK α radiation ($K\alpha_1 = 1.5406 \text{ \AA}$, $K\alpha_2 = 1.5444 \text{ \AA}$, $K\alpha_2/K\alpha_1 = 0.5$). The tube voltage and current were 40 kV and 40 mA, respectively. Samples for PXRD were prepared by placing a thin layer of the appropriate material on a zero-background silicon crystal plate, which was rotated at 15 rpm.

Transmission Electron Microscopy (TEM) images were acquired using FEI Tecnai Multipurpose Digital TEM. The MOF sample was added to a glass vial containing acetone and shaken to obtain a well-dispersed suspension. A drop or two of this suspension was added to the copper grid (5-6 nm thick and 3.05 mm wide) with a thin film of pure carbon deposited on one side (CF200-CU from Electron Microscopy Sciences). After evaporation of acetone, the grid was placed on the TEM sample holder and inserted in the beam column. The chamber was evacuated at 3.2×10^{-7} torr before the electron gun was switched on and aligned for acquiring high-resolution images. The TEM was operated at 120 kV and corrected for image aberrations using stigmator in condenser/objective lens. Figure 4-14, Figure 4-15, and Figure 4-16 show a comparison of TEM images acquired for microcrystalline MOF-808 samples in three different flow reactors (5 mL, 9 mL, and 16 mL) and five configurations for biphasic slug flow for all reactors.

Non-linear least-squares curve fitting was performed using OriginLab 9.1 software program. The NLFit tool was used to model user-defined expressions (Gualtieri and Avrami-Erofeev) for fitting the crystallization curves. The independent and dependent variables along with fitting parameters were defined, while the constants such as the growth dimension ($n = 3$) was fixed. The tool estimates initial values for the parameters before the fitting commences. Fitting can be performed either by using ‘one iteration’ at a time or ‘fit until converged’ options. The rate constants and fitting parameters obtained are tabulated and used to interpret kinetics of nucleation, growth and calculate corresponding activation energies.

4.4.2. Evaluation of Kinetic Data with Avrami–Erofeev Model

The Avrami–Erofeev (AE) expression is described in Equation 4-6. The AE model correlates the extent of crystallization $\alpha(t)$ with residence time t , the overall rate constant k , and the Avrami exponent n_{AE} . The AE expression is used to describe the kinetics of solid-state transformation reactions at constant temperature.¹⁸⁰ The transformations generally follow a characteristic S-shaped growth curve wherein the transformation rates are slow at the beginning followed by an exponential increase and culminate with a plateau region indicating completion of the process. Millange et al.^{151, 181} emphasized the limitations in interpreting the kinetic parameters obtained by the AE model and proposed the use of Gualtieri model for solution-mediated transformation reactions, which would be more suited to study the kinetics of MOF crystallization. Since the AE

model does not separate the rate constants for nucleation and growth, the interpretation of the overall rate constant k becomes difficult and carries uncertainties.

$$\alpha(t) = [1 - e^{-(k \cdot t)^{n_{AE}}}] \dots \text{(Equation 4-6)}$$

Activation energy is calculated from the overall rate constant k at different temperatures (110 °C to 150 °C) by fitting the Arrhenius expression (Equation 4-7) to the Arrhenius plot (Figure 4-13). Activation energy obtained from the AE model is $57.3 \pm 4 \text{ kJ.mol}^{-1}$ with R^2 (Coefficient of Determination) value of 0.991.

$$k = Ae^{-\left(\frac{E_a}{RT}\right)} \rightarrow \ln k = \ln A - \frac{E_a}{RT} \dots \text{(Equation 4-7)}$$

4.4.3. Influence of Mixing Effects on CSD

The mixing mechanism inside the droplets (precursor slugs) is complex and originates from fully developed recirculating flow patterns due to the shear stress near the tube wall. The fluid inside the slug is stretched, folded and reoriented continuously as the droplet travels in the serpentine reactor tubing.⁷⁰ The characteristic mixing time t_{mix} originating from chaotic mixing in the droplets scales as a function of Pe (Equation 4-8).¹⁷⁸ a is the length of the slug ($\sim 10 \text{ mm}$), w is the channel width or tube diameter (1.58 mm), U is the linear flow velocity, and D is the diffusion coefficient. For a first order approximation of D in liquids, we used a value of $10^{-9} \text{ m}^2\text{s}^{-1}$ reported by Liu et al.¹⁸²

$$t_{mix} \sim \left(\frac{aw}{U}\right) \log(Pe) \dots \text{(Equation 4-8)}$$

$$Pe = \left(\frac{wU}{D}\right) = \frac{\text{Advective Transport Rate}}{\text{Diffusive Transport Rate}} \dots \text{(Equation 4-9)}$$

$$J \propto \exp\left(\frac{-C}{(\ln S)^2}\right) \dots \text{(Equation 4-10)}$$

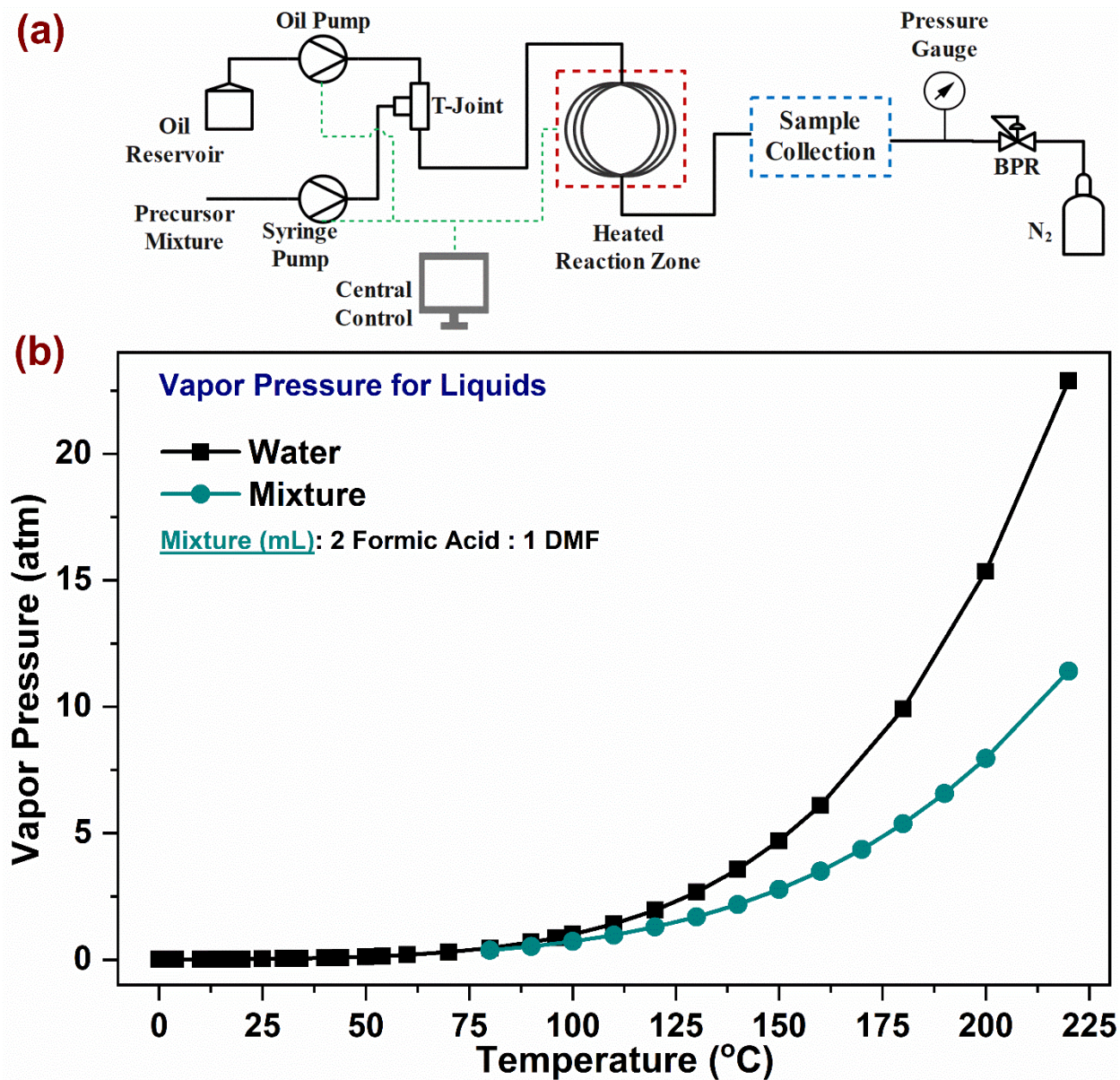


Figure 4-5 (a) The schematic for the flow reactor setup used for crystallization of MOF-808. (b) Bubble-point pressures of multiple reaction components calculated by Aspen.

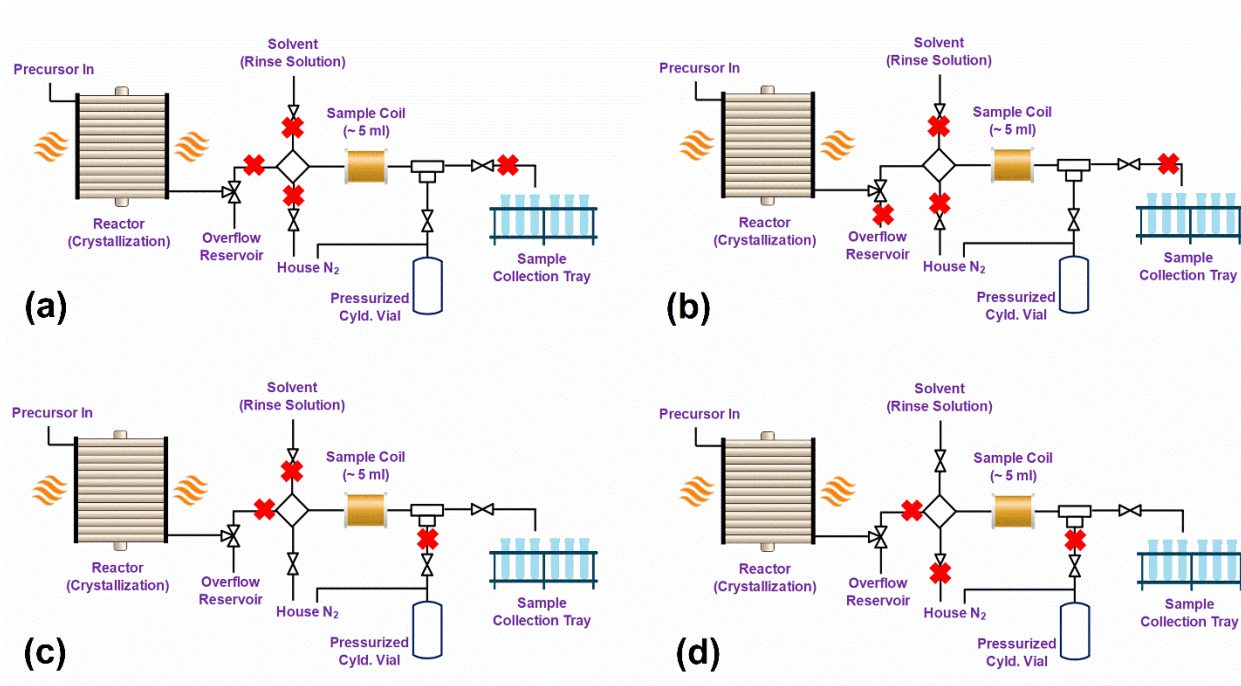


Figure 4-6 Simplified schematic of the rapid sampler module (sample collection) illustrating different modes of operation. The cross symbol (X) implies a closed valve for the flow of reagents. (a) Reaction mixture containing MOF-808 crystals exiting the reactor after crystallization, bypassing the module and flowing into an overflow reservoir. (b) Reaction mixture being collected in the sample coil (~5 mL volume). (c) Pressurized N₂ gas used for evacuation of reaction mixture out of the sample coil, which is collected in an external vessel (50 mL centrifuge tube) for separation of solids and characterization. (d) Solvent (hexane) is injected in the sample coil for rinsing before collecting the next sample.

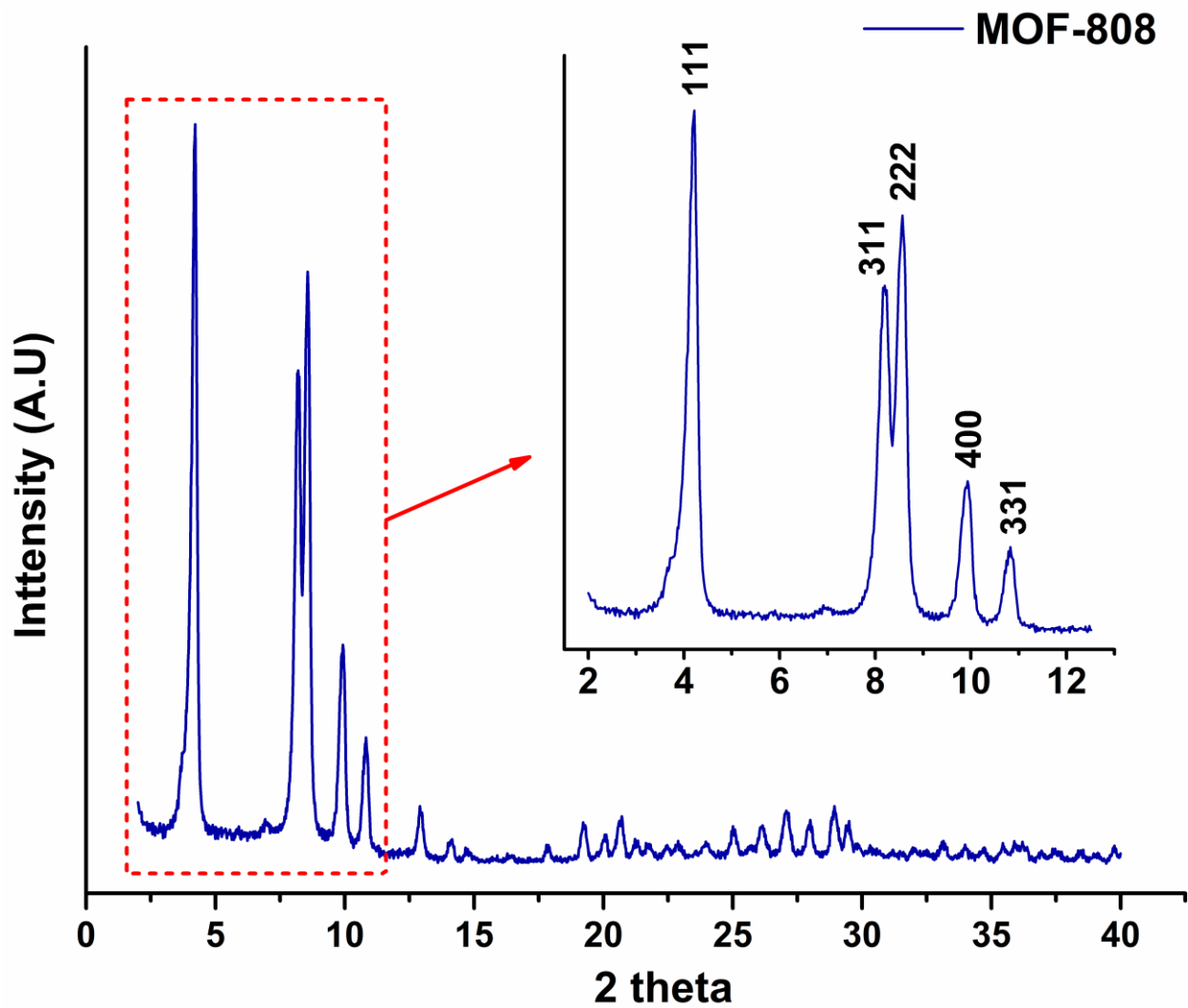


Figure 4-7 Powder XRD pattern for MOF-808 showing miller indices for prominent peaks below 12° 2 theta. Area under the curve for peaks corresponding to the plane (400) is monitored as a function of time to generate extent of crystallization $\alpha(t)$ curves for specific reaction conditions.

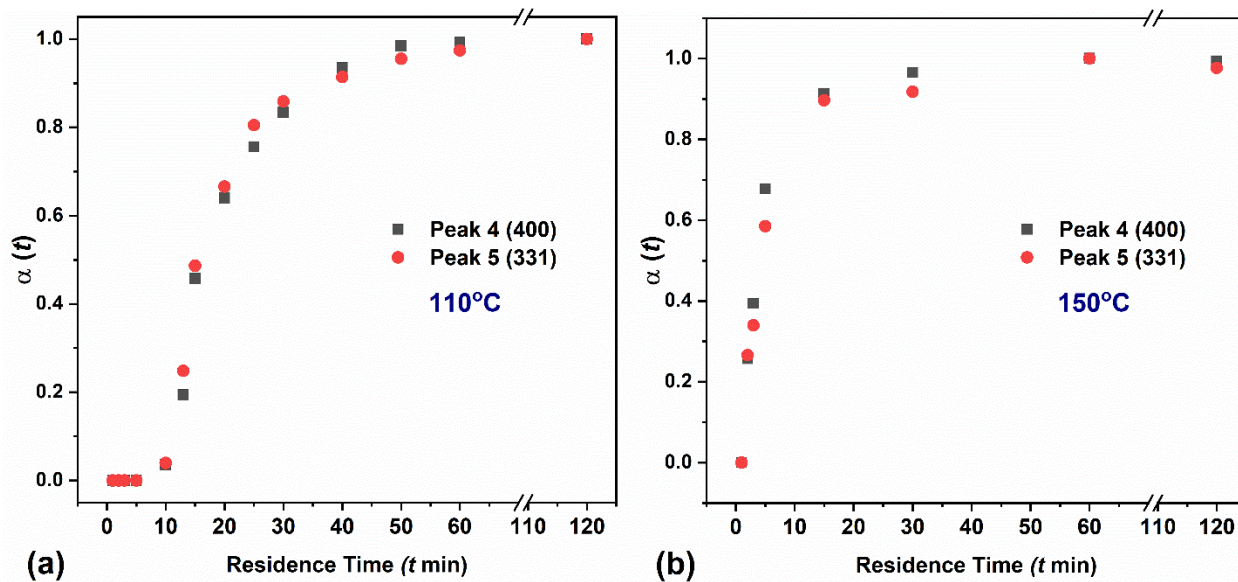


Figure 4-8 Superimposition of extent of crystallization $\alpha(t)$ plotted against time t , obtained from integration of area under the curve for peaks corresponding to reflections from 400 and 331 planes respectively, at (a) 110 °C and (b) 150 °C.

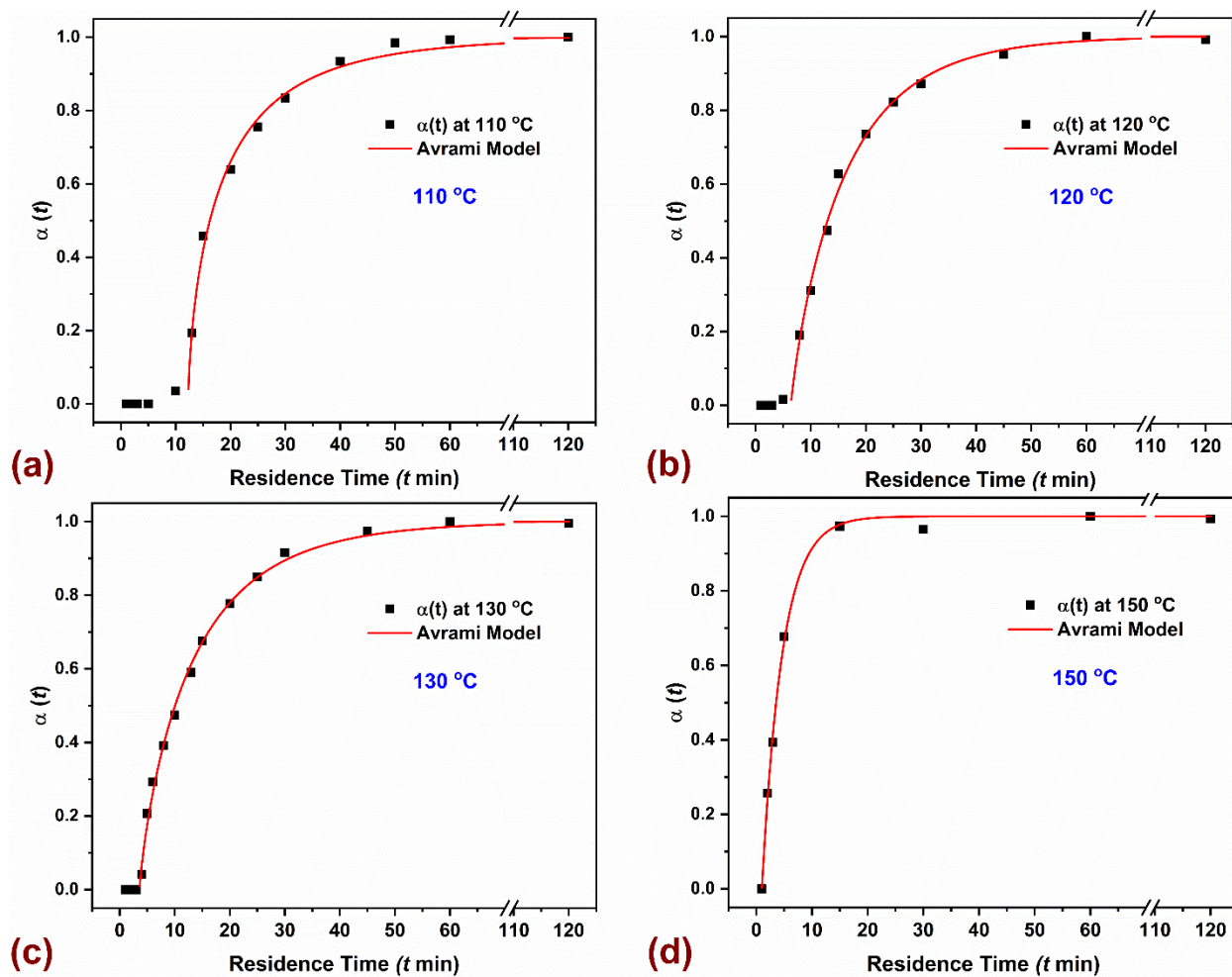


Figure 4-9 Extent of crystallization $\alpha(t)$ plotted against time t (closed symbols) and the corresponding AE fitting (red curves) at (a) 110 °C, (b) 120 °C, (c) 130 °C, and (d) 150 °C. The reaction mixture for all conditions has a 3X linker concentration.

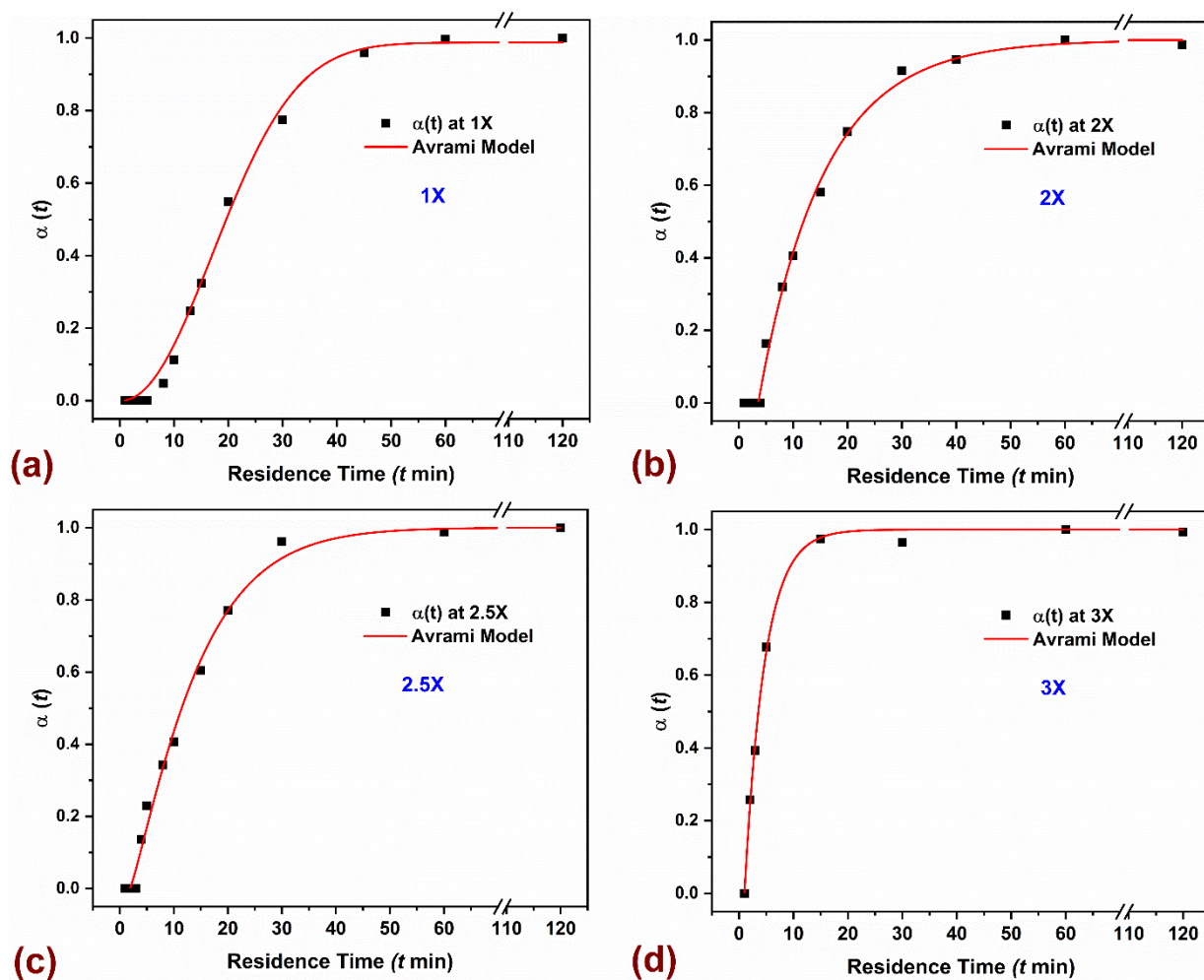


Figure 4-10 Extent of crystallization $\alpha(t)$ plotted against time t (closed symbols) and the corresponding AE fitting (red curves) at a linker concentration of (a) 1X, (b) 2X, (c) 2.5X, and (d) 3X. The reaction temperature for all conditions was held constant at 150 °C.

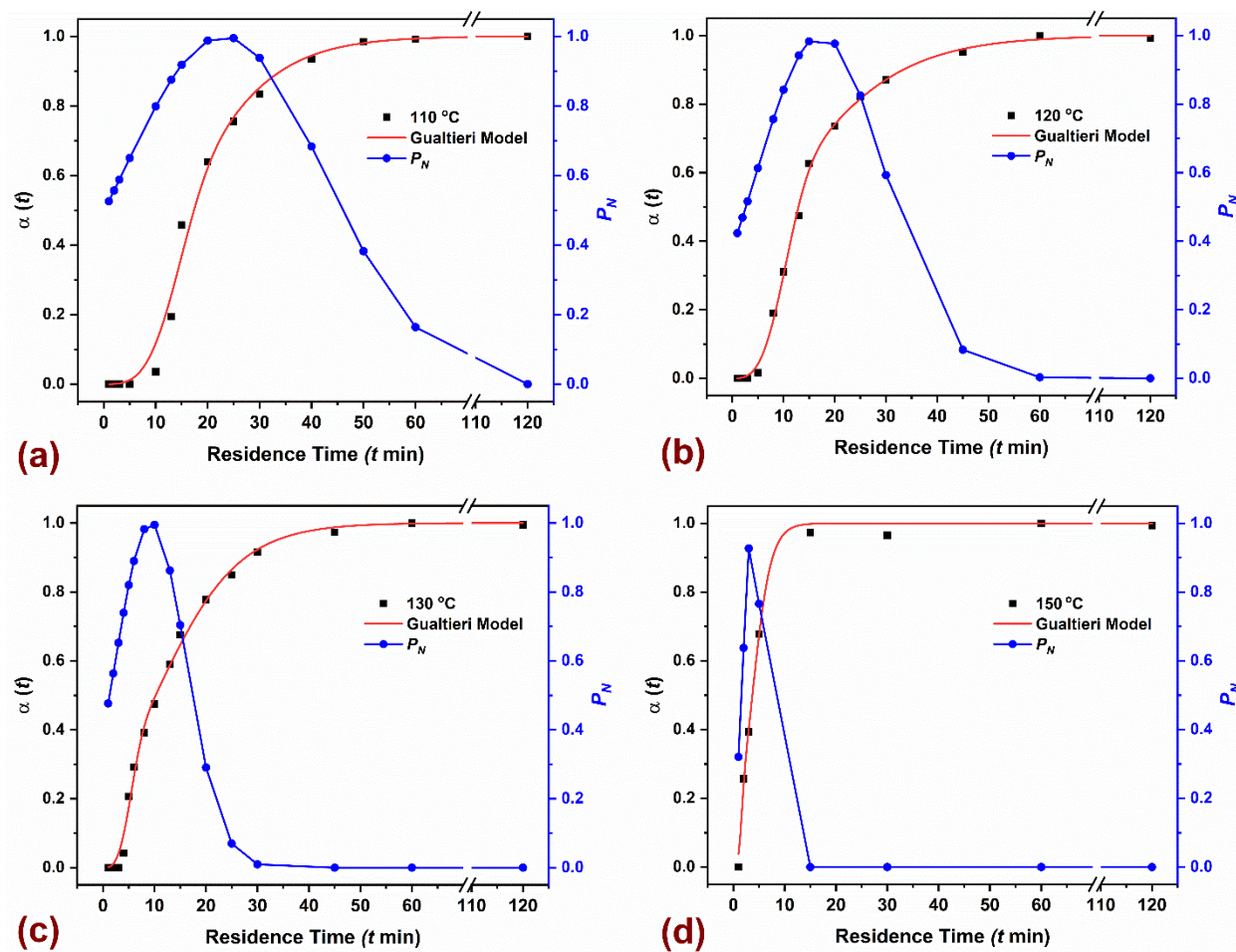


Figure 4-11 Extent of crystallization $\alpha(t)$ plotted against time t (closed symbols) and the corresponding Gaultieri fitting (red curves) as well as the probability of nucleation P_N (blue curves) at (a) 110 °C, (b) 120 °C, (c) 130 °C, and (d) 150 °C. The reaction mixture for all conditions has a 3X linker concentration.

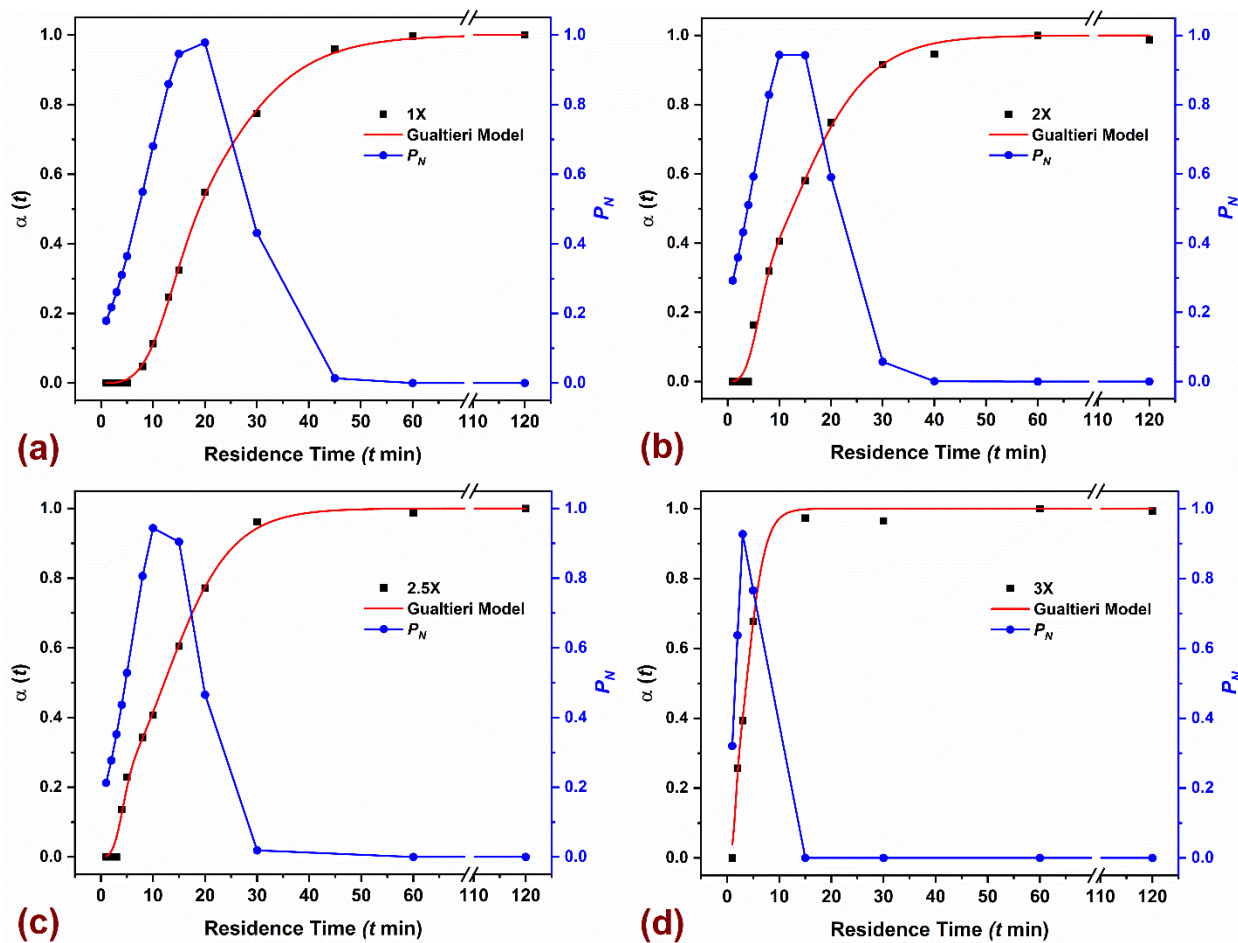


Figure 4-12 Extent of crystallization $\alpha(t)$ plotted against time t (closed symbols) and the corresponding Gaultieri fitting (red curves) as well as the probability of nucleation P_N (blue curves) at a linker concentration of (a) 1X, (b) 2X, (c) 2.5X, and (d) 3X. The reaction temperature for all conditions was held constant at 150 °C.

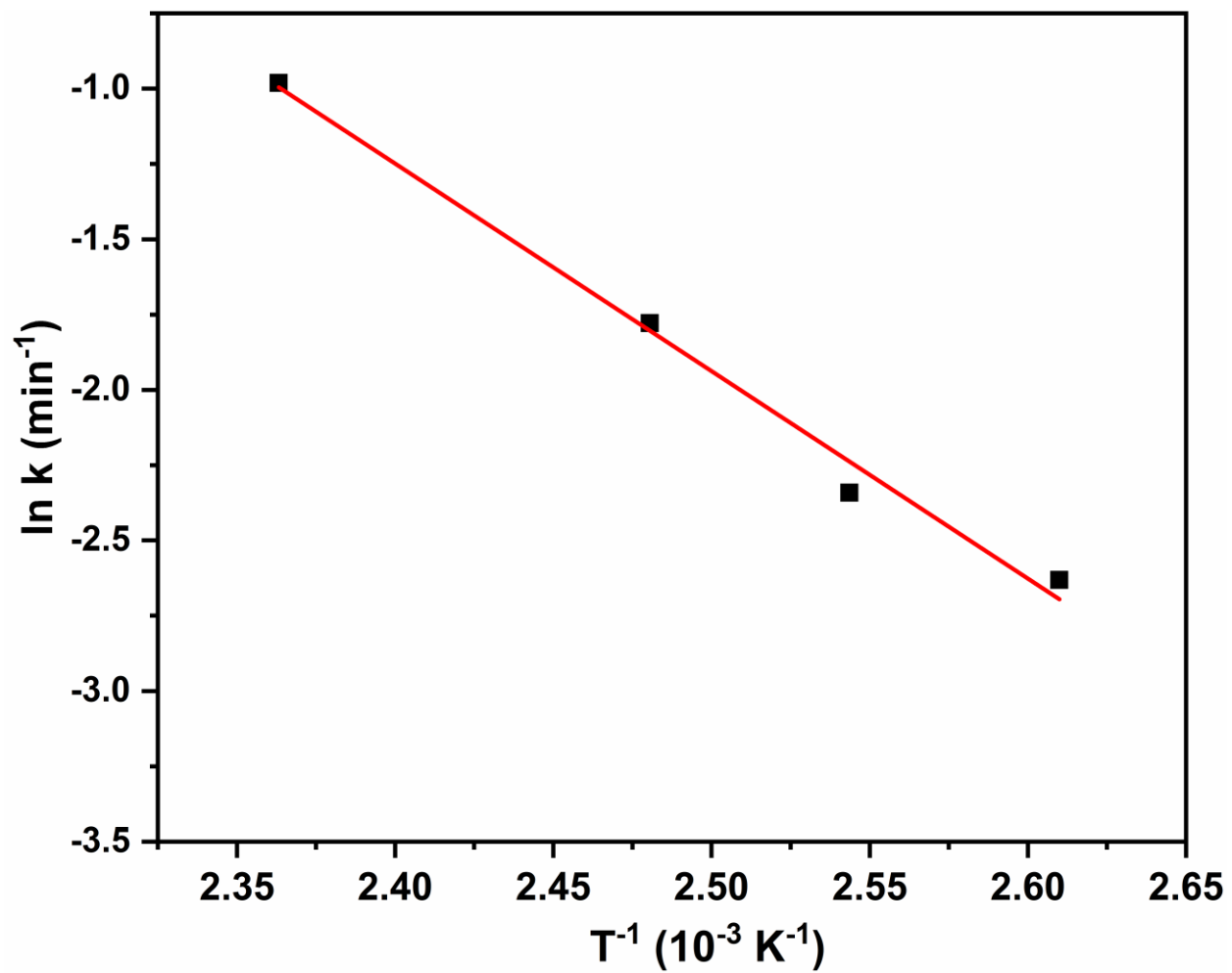


Figure 4-13 Arrhenius plots for the temperature-dependent rate constants (black squares) obtained from evaluation of the AE model.

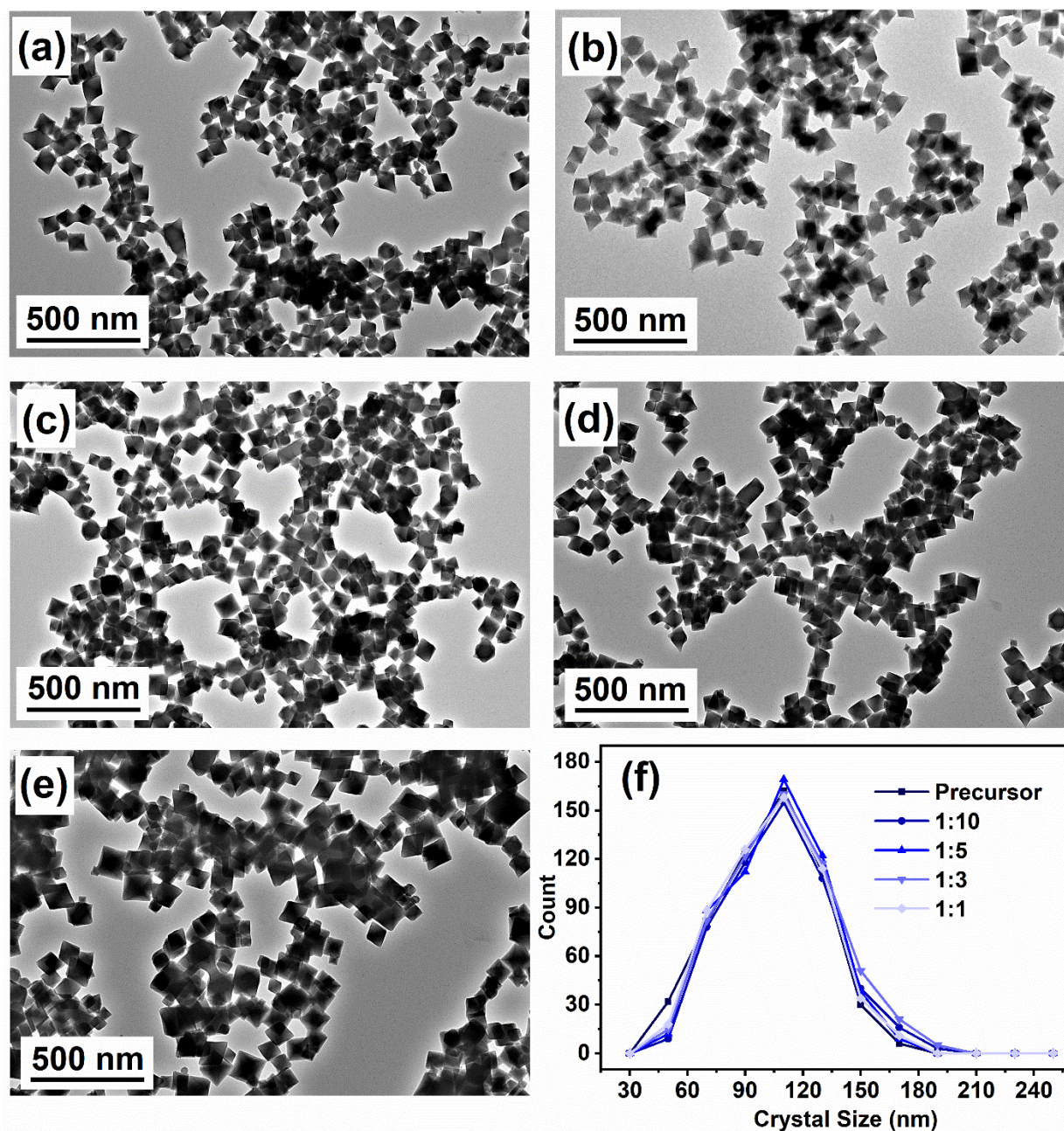


Figure 4-14 TEM images for MOF-808 synthesized in a 5 mL flow reactor (at 150 °C, 15 min residence time and 3X linker concentration), using volumetric flow ratios of ‘Oil:Precursor’ (a) 1:1, (b) 1:3, (c) 1:5, (d) 1:10, and (e) Precursor Only. (f) A line histogram of CSD obtained from TEM measurements for all biphasic slug-flow configurations.

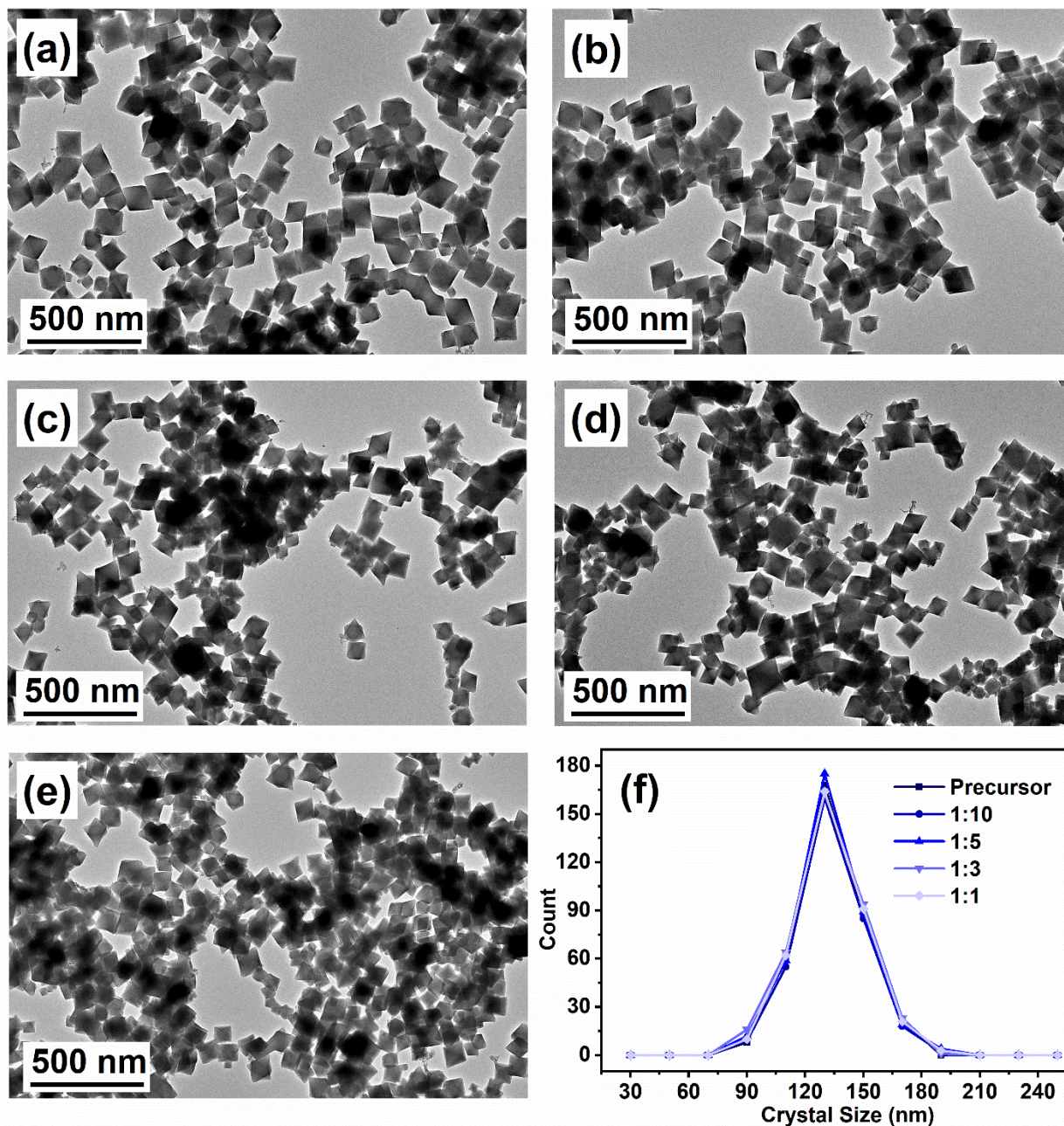


Figure 4-15 TEM images for MOF-808 synthesized in a 9 mL flow reactor (at 150 °C, 15 min residence time and 3X linker concentration), using volumetric flow ratios of ‘Oil:Precursor’ (a) 1:1, (b) 1:3, (c) 1:5, (d) 1:10, and (e) Precursor Only. (f) A line histogram of CSD obtained from TEM measurements for all biphasic slug-flow configurations.

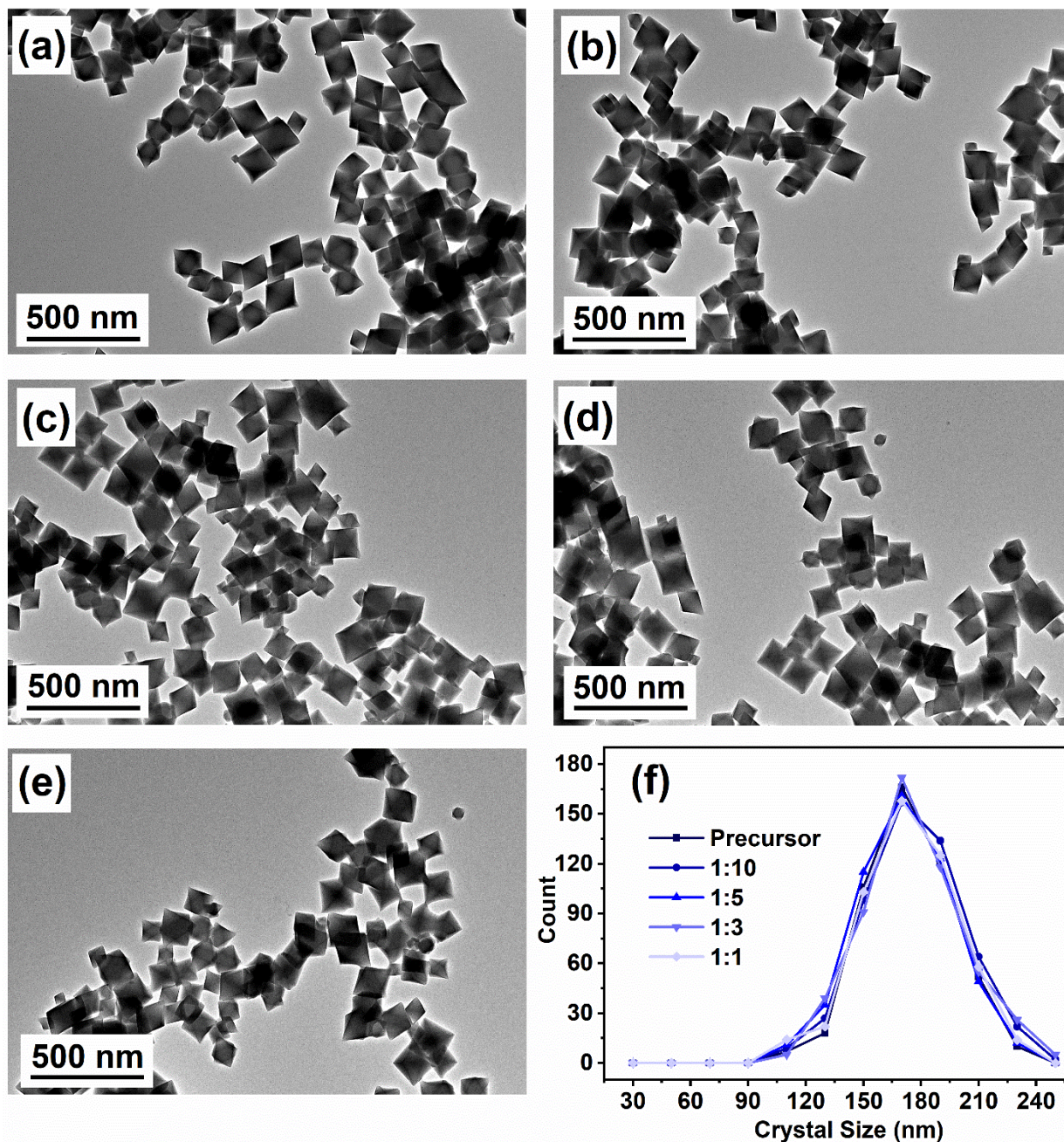


Figure 4-16 TEM images for MOF-808 synthesized in a 16 mL flow reactor (at 150 °C, 15 min residence time and 3X linker concentration), using volumetric flow ratios of ‘Oil:Precursor’ (a) 1:1, (b) 1:3, (c) 1:5, (d) 1:10, and (e) Precursor Only. (f) A line histogram of CSD obtained from TEM measurements for all biphasic slug-flow configurations.

Table 4-4 Residence time and corresponding flow rates in a reactor with 16 mL volume. The reactor tubing had an inner diameter of 1/16 in (0.159 cm) and a length of ~8 m for the heated reaction zone.

	Total Flow Rate (mL/min)		Residence Time	Linear Velocity
	Oil:Precursor (1:1)			
	Oil	Precursor	min	cm/min
16.00	8	8	1	808.48
8.00	4	4	2	404.24
5.33	2.66	2.66	3	269.36
3.20	1.6	1.6	5	161.69
2.00	1	1	8	101.01
1.60	0.8	0.8	10	80.84
1.06	0.53	0.53	15	53.87
0.80	0.4	0.4	20	40.40
0.53	0.26	0.26	30	26.90
0.35	0.17	0.17	45	17.67
0.26	0.13	0.13	60	13.46
0.13	0.06	0.06	120	6.73

Table 4-5 Summary of MOF-808 reaction mixture compositions investigated for evaluating kinetic parameters. ‘FA:DMF’ denotes the volumetric ratio of Formic Acid to DMF used in the reaction mixture. Every reaction mixture was prepared in a fixed volume of 30 mL. ‘M:L’ represents molar ratio of Zr metal ($\text{ZrOCl}_2 \cdot 8\text{H}_2\text{O}$) and H_3BTC linker (benzene-1,3,5-tricarboxylic acid, also known as Trimesic Acid) and was held constant across all compositions ($\text{M:L} = 3$). Four different temperatures and linker concentrations are evaluated to probe their effect on extent of crystallization $\alpha(t)$ of MOF-808. Linker concentration of 1X corresponds to 70 mg (0.33 mmol) of H_3BTC dissolved in a 30 mL reaction mixture of Formic Acid and DMF in a 2:1 volumetric ratio. Linker concentration of 2X would correspond to a 2-fold increase in the linker concentration of the 30 mL reaction mixture volume with a M:L ratio of 3 maintained constant. Higher the concentration of precursors (metal salt and linker), lower is the ‘Acid:Metal’ molar ratio, which represents moles of Formic Acid modulator to Zr metal in the reaction mixture.

Sl. No.	FA:DMF (Vol. Ratio)	M:L (Molar Ratio)	Linker Concentration	Acid:Metal (Molar Ratio)	Temperature (°C)
Fig. 1a					
1	2	3	3X	176.0	110
2	2	3	3X	176.0	120
3	2	3	3X	176.0	130
4	2	3	3X	176.0	150
Fig. 1b					
5	2	3	1X	528.3	150
6	2	3	2X	264.0	150
7	2	3	2.5X	211.0	150
8	2	3	3X	176.0	150

Table 4-6 Values for the induction time t_o and residence time for complete crystallization t_f for all the reaction conditions explored in the study.

Temperature (°C)	t_o (min)	t_f (min)
110	5	60
120	4	55
130	3	45
150	1	5
Linker Concentration	t_o (min)	t_f (min)
1X	8	60
2X	4	45
2.5X	3	40
3X	1	5

Table 4-7 Kinetic parameters obtained by fitting the crystallization curves at four different temperatures using the AE model. The linker concentration for all conditions explored was 3X.

Temperature (°C)	n_{AE}	k (min ⁻¹)	R^2
110	0.661	0.072	0.992
120	0.891	0.096	0.996
130	0.835	0.169	0.998
150	1.003	0.375	0.995

Table 4-8 Kinetic parameters obtained by fitting the crystallization curves at four different linker concentrations using the AE model. The reaction temperature for all conditions explored was held at 150 °C.

Linker Concentration	n_{AE}	k (min^{-1})	R^2
1X	0.812	0.043	0.997
2X	0.979	0.083	0.998
2.5X	0.987	0.169	0.998
3X	1.003	0.375	0.995

Table 4-9 Activation energies of nucleation $E_A(N)$ and crystal growth $E_A(G)$ reported for other MOFs in the literature compared to MOF-808 (this study).

Temperature (°C)	$E_A(N)$ $kJ.mol^{-1}$	$E_A(G)$ $kJ.mol^{-1}$	Reference
MOF-808	64.7	59.2	Current Work
MOF-801	71	66	Zahn et al. ¹⁰¹
HKUST-1	72	64	Millange et al. ¹⁵¹
ZIF-8	69	72	Cravillon et al. ¹⁶⁷
UiO-66	46	39	Ragon et al. ¹⁵²

Table 4-10 Residence times and corresponding flow rates for the Oil and Precursor phase in three different flow reactor volumes investigated in the study.

Flow Reactor Volume (mL)			5 mL Reactor	9 mL Reactor	16 mL Reactor
Residence Time (min)			15	15	15
Linear Velocity (mm/s)			2.811	4.536	8.981
Volumetric Flow Rates (mL/min)	Total	mL/min	0.334	0.600	1.067
	Oil:Precursor (1:1)	Oil	0.167	0.300	0.533
		Precursor	0.167	0.300	0.533
	Oil:Precursor (1:3)	Oil	0.084	0.150	0.267
		Precursor	0.251	0.450	0.800
	Oil:Precursor (1:5)	Oil	0.056	0.100	0.178
Precursor		0.278	0.500	0.889	
Oil:Precursor (1:10)	Oil	0.030	0.055	0.097	
	Precursor	0.304	0.545	0.970	
Precursor Only	Oil	0.000	0.000	0.000	
	Precursor	0.334	0.600	1.067	

Table 4-11 Values for dimensionless Péclet number Pe calculated as a function of total flow rates for three different reactor configurations. The characteristic mixing times t_{mix} are estimated based on a scaling argument (Eqn. S3) for the 1:1 Oil:Precursor biphasic slug flow configuration.

Flow Reactor Volume (mL)	5 mL Reactor	9 mL Reactor	16 mL Reactor
Residence Time (min)	15	15	15
Reactor Tube ID (mm)	1.58	1.58	1.58
Linear Velocity (mm/s)	2.811	4.536	8.981
Total Flow Rate (mL/min)	0.334	0.6	1.067
Pe	4,440	7,166	14,180
t_{mix} for 1:1 'Oil:Precursor' Flow (ms)	20.5	13.4	7.304

5. Accelerated synthesis of Ni₂Cl₂(BTDD) metal–organic framework in a continuous flow reactor for atmospheric water capture

Adapted with permission from “Bagi, S., Wright, A. M., Oppenheim, J., Dincă, M., & Román-Leshkov, Y. (2021). Accelerated Synthesis of a Ni₂Cl₂(BTDD) Metal–Organic Framework in a Continuous Flow Reactor for Atmospheric Water Capture. *ACS Sustainable Chemistry & Engineering*, 9(11), 3996-4003”.¹⁰² Copyright 2021 American Chemical Society.

Atmospheric water capture (AWC) has tremendous potential to address global shortage of clean drinking water. The Ni₂Cl₂(BTDD) metal–organic framework (MOF) has shown optimal water sorption performance under low relative humidity conditions, but its potentially high production costs stemming in part from its lengthy multi-day synthesis has hindered wide-spread implementation. As with most traditional MOF syntheses, the original synthesis of Ni₂Cl₂(BTDD) involves batch reactors that have intrinsic inefficiencies impacting productivity during scale-up. In this chapter, we report a continuous manufacturing process for Ni₂Cl₂(BTDD) that can achieve higher yields, reduced solvent use, and drastically faster crystallization times compared to the batch process. Optimization of the synthesis space in the flow reactor as a function of residence time, temperature, and solvent volume yields 50% and 40% reductions in methanol and hydrochloric acid consumption by volume, respectively, with a simultaneous 3-fold increase in productivity (defined in units of $kg_{MOF} m^{-3} day^{-1}$). A computational fluid dynamics (CFD) model was developed to quantitate productivity enhancements in the flow reactor based on improved heat-transfer rates, larger surface-area to volume ratios, and effective residence times. This work adds critical facets to the growing body of research suggesting that the synthesis of MOFs in flow reactors offers unique opportunities for reducing production costs.

5.1. Introduction

Most of the arid and semi-arid regions in the world do not have access to potable water. This problem will worsen due to increasing global water demand for both personal and industrial use, a growing global population, and desertification of fertile areas through over-farming and climate

change, eventually leading to a projected water deficit of almost 2000 billion m³ by 2030.¹⁸³⁻¹⁸⁴ In areas with relative humidity (RH) below ca. 30%, water harvesting relies on capital- and energy-intensive processes, such as dewing or sea-water desalination supplemented with a complex distribution infrastructure of pipelines.¹⁸⁵⁻¹⁸⁶ Atmospheric water capture (AWC) offers an alternative solution given that the atmosphere holds nearly 1.3×10^{16} L of water—a value representing ca. 0.3% of the global fresh water supply.¹⁸⁷⁻¹⁸⁸ However, performing direct water capture from the atmosphere in areas with low RH (<30%) in an energy-efficient manner requires new sorbent materials. The ideal AWC sorbent material requires physical properties such as large gravimetric capacities, steep water uptake characteristics in a narrow RH range, and complete water release with minimal temperature swings over thousands of cycles.

Metal-organic frameworks (MOFs) fulfill many, if not all of these requirements. MOFs are crystalline coordination lattices consisting of multitopic organic linkers and inorganic polynuclear clusters forming highly ordered 2D and 3D structures.¹⁸⁹ One class of MOFs that is attractive for AWC applications feature coordinatively unsaturated open metal sites that serve as nucleation sites for water adsorption.⁶³ Recently, Dincă and coworkers¹⁹⁰⁻¹⁹² demonstrated that the M₂Cl₂(BTDD) (M = Co, Ni; H₂BTDD = bis(1H-1,2,3-triazolo[4,5-*b*],[4',5'-*i*])dibenzo[1,4]dioxin) family of MOFs, which feature hexagonal pores decorated with open metal sites, are particularly well-suited for direct water capture from simulated atmosphere. In particular, the Ni analog exhibits an exceptional gravimetric water uptake capacity of 1.07 g·g⁻¹ at a relative humidity (RH) of 35%. The energy efficiency of water capture and release from Ni₂Cl₂(BTDD) was optimized by matching the pore size to the critical diameter for water capillary condensation and minimizing adsorption/desorption hysteresis.¹⁹³⁻¹⁹⁴ While more expensive compared to other sorbents, such as silica gel and zeolites, MOFs are topologically diverse with tunable properties, making them ideally suited for water-capture applications.⁷²

Despite its superior water uptake performance, scaling-up the manufacturing of Ni₂Cl₂(BTDD) remains prohibitively expensive due to long reaction times and excess use of solvents required for precursor dilution in the reaction mixture. For example, the synthesis of 1 g of Ni₂Cl₂(BTDD) requires dissolving 1.808 g of NiCl₂·6H₂O and 0.912 g of the organic ligand H₂BTDD in a solvent mixture comprising 800 mL of *N,N*-dimethylformamide (*N,N*-DMF), 800 mL of methanol (CH₃OH), and 512 mL of aqueous hydrochloric acid (HCl, 37 wt.%), followed by heating at 100

°C for 48 hours in a batch reactor to generate crystalline solids with ca. 75% yield. Slow crystallization times coupled with high solvent-to-solid ratios severely limit productivity, and this problem is exacerbated during scale-up due to the inherent challenges associated with increasing the size of batch reactors.⁹⁰ These inefficiencies result in higher costs and considerable capital and operating expenditures to produce the quantities needed for industrial AWC applications.^{25, 64} It is therefore imperative to identify approaches that minimize synthesis costs through reduced use of solvents, increasing yields, and increasing process productivity for all MOFs, and for Ni₂Cl₂(BTDD) in particular.

The use of flow chemistry to achieve product intensification by improving heat and mass transfer, decreasing the use of solvents, and improving scalability through parallelization has transformed many disciplines, including polymer chemistry,²⁶ organic synthesis,²⁷⁻²⁹ and photochemistry.³⁰ Numerous studies over the past decade have demonstrated the feasibility of synthesizing MOFs in flow,^{17, 195-202} however, the influence of synthetic parameters on product crystallinity and scale-up strategies for high-throughput manufacturing by considering the transport processes have not been explored thoroughly. Here, we investigate the use of flow reactors for the accelerated synthesis of Ni₂Cl₂(BTDD) under mild solvothermal conditions. Specifically, we use a biphasic liquid-liquid slug flow pattern to perform continuous microbatch MOF crystallization resulting in drastic increases in manufacturing productivity compared to batch processes. Computational fluid dynamics (CFD) calculations were used to quantitate productivity enhancements in the flow reactor based on improved heat-transfer rates, larger surface-area to volume ratios, and effective residence times. This information was used to model a scale-up scenario for producing 1 kg of Ni₂Cl₂(BTDD) per month, providing estimates for supply-chain logistics and equipment sizing. This work demonstrates synthesis in flow enables manufacturing MOFs for AWC with significantly reduced materials costs and increased productivity compared to batch.

5.2. Results and Discussion

Continuous MOF crystallization studies were performed in a flow reactor shown schematically in Figure 5-1. The injection module consists of a syringe pump and positive displacement piston pump for introducing the precursor mixture and silicone oil, respectively. The reactor module is composed of PTFE tubing held together using an aluminum core and jacket that is inserted into an electrically heated furnace allowing for nearly isothermal operation with fast heat transfer. A back-

pressure regulator maintains the reactor operating pressure at a value higher than the bubble-point pressure of the reaction mixture. The MOF precursor mixture is injected into a continuous stream of silicone oil using a T-junction forming a segmented biphasic slug flow. Silicone oil was used because it preferentially wets the hydrophobic surface of the PTFE tubing, thereby producing a continuous phase for the MOF precursor mixture to travel as discrete, uniformly spaced droplets within the tube. In our flow reactor, the slug generation process is associated with the dynamic pressure profile existing at the T-junction when two immiscible fluids are simultaneously introduced in the stream. When the stream of first phase is flowing through the junction, the flow of the second phase is obstructed due to immiscibility of the two phases, resulting in pressure build up. When the pressure reaches a critical point, the first phase is driven back from the T-junction shearing off the droplet into the stream, generating a slug. This alternated cyclic build-up and release of pressure is responsible for the segmentation of the liquids allowing reproducible slug lengths.^{97, 120}

Each slug is equivalent to a well-mixed micro-batch reactor, where the interfacial properties between the two phases, such as surface tension and viscosity, control the shape and fluid dynamic properties of the droplet. Accordingly, in order to maintain a stable biphasic slug flow, the surface tension between the precursor and continuous phase should be lower than the surface tension between precursor and walls of reactor tubing.⁶⁵ Within each droplet, complete mixing of reagents is achieved through chaotic advection, where repeated folding and stretching of fluid layers accelerates diffusive mixing.^{98, 203} Importantly, compartmentalizing the MOF precursor in microliter volume droplets results in high surface area to volume (SA/V) ratios, which translates to shorter diffusion length scales for heat and mass transport processes. The slugs undergo a step-function change from room temperature to reaction set-point temperature upon entering the heated reaction zone. Precise temperature control is critical for manipulating the kinetics of nucleation, short-range crystalline ordering, and crystal growth.⁹⁹ Consequently, the flow system affords rapid mixing of reagents, near perfect step changes in temperature profiles, and precise control of residence times, all critical elements to accelerate nucleation and crystallization events.^{32, 65} Importantly, this flow reactor setup supports a wide operational window to control the steady-state evolution of the product crystallinity by varying reaction conditions, including residence time (minutes to days) and temperature (up to 250 °C at a working pressure of 25 atm). Additional details pertaining to flow reactor components, operational windows, volumetric flow rates, and

residence times are summarized in Figure 5-5 and Figure 5-6 as well as Table 5-1 and Table 5-2 of the Supporting Information (SI).

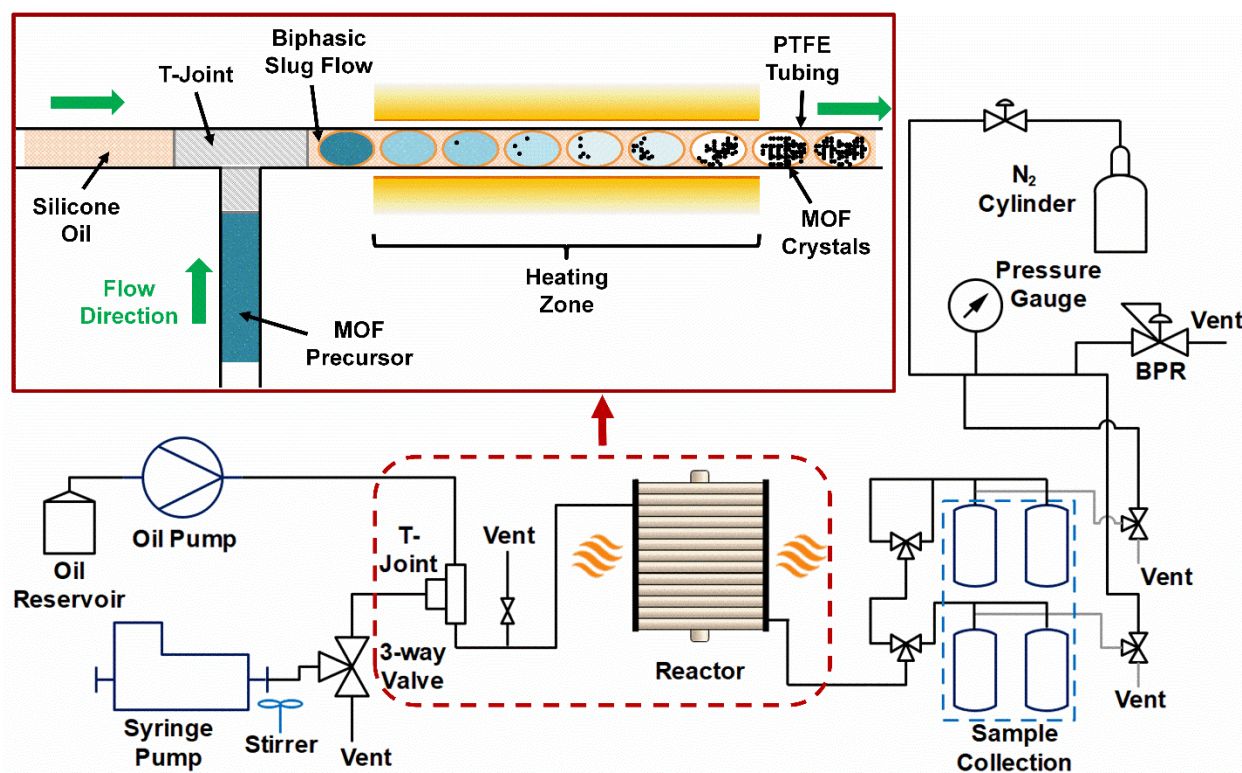


Figure 5-1 Schematic for the modular flow synthesis platform. Inset picture with red boundaries illustrates the phenomenological model of crystallization using a biphasic slug flow generated from two immiscible fluids in a T-junction.

Unlike batch reactors that intrinsically operate in a transient mode, flow reactors allow investigating processes at steady-state with precise control over temperature and residence time.²⁵ These features enable performing time-resolved crystallization studies in a single experimental run. Figure 5-2 shows a map of the $\text{Ni}_2\text{Cl}_2(\text{BTDD})$ synthesis space where the effects of changing solvent ratio, residence time, and temperature on product crystallinity were investigated. The relative crystallinity (RC), determined from a ratio of intensity contributions originating from the crystalline phase calculated using an iterative background correction method to the total intensity from the PXRD patterns (Equation 5-1 and Figure 5-7 provide additional details), was used to define the amount of crystalline product per experiment.¹⁴⁰ Accordingly, a value of 100% RC corresponded to the highest yield of crystalline $\text{Ni}_2\text{Cl}_2(\text{BTDD})$, a value of >80% RC was classified

as “crystalline”, a value in the $30\% \leq RC \leq 80\%$ range was classified as “semi-crystalline”, and RC values $< 30\%$ were classified as “amorphous”. Residence time and reaction temperature were varied in a range of 15-240 min and 120-150 °C, respectively, based on synthesis parameters previously reported in the literature.^{12, 17, 24, 195-197, 202, 204} Optimal Ni₂Cl₂(BTDD) crystallinity values were obtained for a reaction temperature of 140 °C and residence times between 30 and 60 min (Figure 5-2a). Temperatures above 150 °C resulted in linker degradation, while reactions below 120 °C failed to crystallize the MOF in the specified range of residence times. Note that residence times greater than 240 min were not investigated as they resulted in a lower process productivity (by a factor of 4 compared to flow conditions optimized at 60 min), making it unattractive compared to the batch process.

Flow reactors can usually operate at higher concentrations provided reagents remain in solution—an advantage in the current scenario for using concentrated precursor mixture to increase productivity while maintaining similar yields.¹¹⁰⁻¹¹¹ Figure 5-2b plots the results of varying the volumetric ratio of solvents (CH₃OH and HCl normalized to DMF) at 140 °C with a residence time of 60 min. Solvent composition was optimized starting from the recipe used in batch (1:1:0.64 volumetric ratio for DMF, CH₃OH and HCl) and lowering HCl content by 10%, 40%, and 60% and CH₃OH by 25% and 50%. Interestingly, the solvent composition used in batch synthesis (labelled ‘Batch Optimized’ in Figure 5-2b) resulted in amorphous residue in flow synthesis. The highest amount of crystalline solids in flow reactor was obtained with a volumetric ratio of DMF:CH₃OH:HCl = 1:0.5:0.38 (labelled ‘Flow Optimized’ in Figure 5-2b). These values represent a decrease in CH₃OH and HCl volume by 50% and 40%, respectively, compared to the optimized batch composition. Additionally, we performed three batch syntheses at 100°C, 120°C, and 140°C with a crystallization time of 48 hours using the ‘flow optimized’ starting composition. These results are compared to the samples synthesized in flow reactor under optimal conditions (140°C, 1 h) using PXRD, N₂ adsorption, and water-uptake measurements (Figure 5-8 and Table 5-5). The BET surface area for batch samples steadily increased from 1795 m²/g to 1944 m²/g, as a function of reaction temperature (100°C to 140°C), while the gravimetric water uptake capacity steadily increased from 0.91 g/g to 0.98 g/g at 92% RH. The corresponding % RC values (Table 5-5) confirm an increase in crystallinity with higher temperature for batch samples, while flow synthesized samples exhibited the highest crystallinity of all synthetic conditions. Importantly, no solids are formed in batch syntheses after 1 h of crystallization. Taken together, these data

demonstrate that the flow system can access unique synthetic conditions leading to $\text{Ni}_2\text{Cl}_2(\text{BTDD})$ with a higher surface area and water-uptake, accompanied by a simultaneous reduction of solvents used and a lower residence time. We therefore conclude that the flow synthesis of $\text{Ni}_2\text{Cl}_2(\text{BTDD})$ is advantageous in every aspect compared to batch synthesis.

In deprotonation modulation, the amount of modulator (HCl) has to be tuned in the reaction mixture based on the synthesis route and reaction conditions such as temperature, and residence time. Under identical solvothermal conditions, reducing the amount of modulator (HCl) accelerates the MOF formation process leading to a product with lower crystallinity, while an increase in modulator lowers crystallization rates of MOF thereby requiring longer residence times for crystal growth. Owing to small system dimensions and large surface-area to volume ratio in flow reactor that leads to fast heat transfer, the heating profiles achieved are different compared to the batch reactor, which typically sees large gradients in heat and mass transfer. This is the primary reason for batch and flow syntheses exhibiting different reaction conditions (temperature, time, and composition) that are optimal to synthesize crystalline product. The amount of DMF could not be changed as it was maintained at the solubility limit of the H_2BTDD ligand in the precursor mixture. The metal salt and the ligand had a molar ratio of 2.2 (to keep a 10% stoichiometric metal excess) in all synthetic conditions explored in the design space. The yield obtained in batch and flow syntheses were ~75% and ~80% respectively (Table 5-6) and are calculated based on the conversion of the limiting reagent (H_2BTDD ligand) into $\text{Ni}_2\text{Cl}_2(\text{BTDD})$. The maximum productivity achieved in the batch synthesis was $0.245 \text{ kg}_{\text{MOF}} \text{ m}^{-3} \text{ day}^{-1}$ while flow synthesis resulted in $0.765 \text{ kg}_{\text{MOF}} \text{ m}^{-3} \text{ day}^{-1}$, representing a 3-fold productivity increase (Table 5-7). Flow synthesis productivity slightly decreases to $0.509 \text{ kg}_{\text{MOF}} \text{ m}^{-3} \text{ day}^{-1}$ if we take into account the silicone oil along with reaction mixture in our calculation. The standard engineering productivities based on reactor volume rather than volume of reaction mixture translates to $0.0643 \text{ kg}_{\text{MOF}} \text{ m}^{-3} \text{ day}^{-1}$ for batch and $12.24 \text{ kg}_{\text{MOF}} \text{ m}^{-3} \text{ day}^{-1}$ for flow, representing a two order of magnitude (~190 times) higher productivity achieved in flow (Table 5-7).

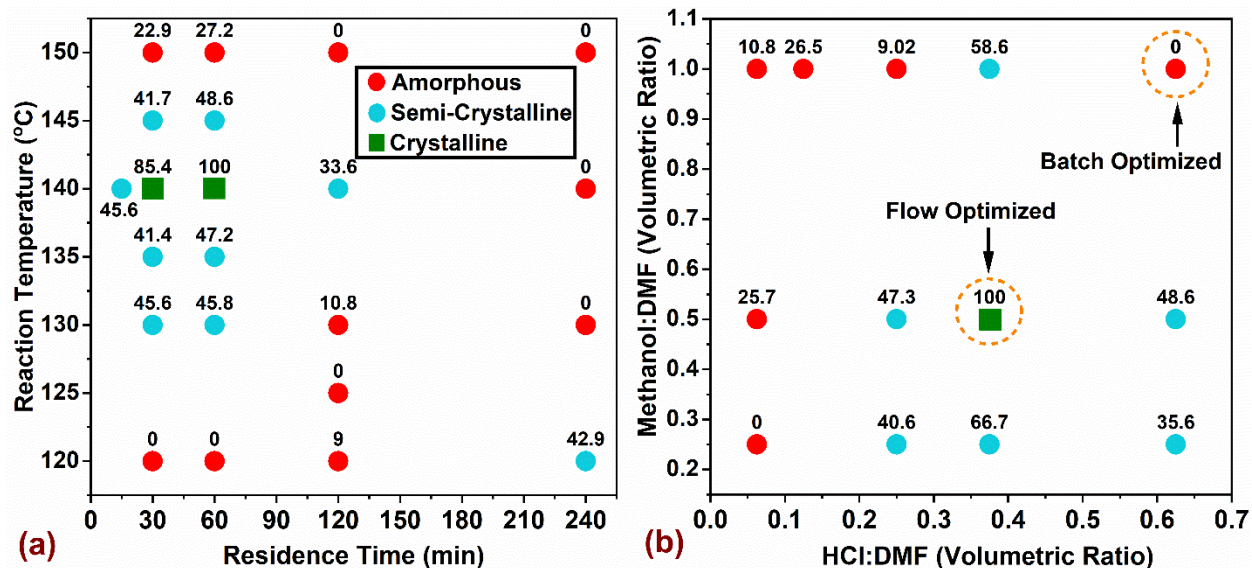


Figure 5-2 Map of synthesis space investigated for $\text{Ni}_2\text{Cl}_2(\text{BTDD})$ using flow synthesis varying (a) reaction temperature and residence time; and (b) volumetric ratios of Methanol:DMF and HCl:DMF solvents at a fixed temperature of 140 °C and 60 min residence time. Labels represent relative crystallinity in percentages (% RC), which were quantified by the intensity contribution in powder X-ray diffraction (PXRD) patterns originating from crystalline phase in the samples. The metal:ligand (M:L) molar ratio was maintained at 2.2 in all cases.

Samples synthesized in flow at optimal reaction conditions were characterized using powder X-Ray diffraction (PXRD), N_2 adsorption, scanning electron microscopy (SEM), transmission electron microscopy (TEM), and water uptake measurements, and were compared with samples synthesized in batch. Figure 3a compares the reflections from PXRD patterns for $\text{Ni}_2\text{Cl}_2(\text{BTDD})$ synthesized in flow and batch along with simulated pattern from the computational model, confirming the single-phase nature of the flow synthesized microcrystalline powder sample. The permanent porosity of activated samples synthesized using batch and flow method was studied using N_2 adsorption isotherms at 77 K (Figure 5-3b). The activated samples exhibit a Type IV isotherm, as is expected for mesoporous materials. To satisfy the first criteria of the BET equation¹¹⁴, isotherm data was fit to the 0.05-0.15 P/P_0 range, yielding values of 1837 $\text{m}^2\cdot\text{g}^{-1}$ and 2157 $\text{m}^2\cdot\text{g}^{-1}$ for batch and flow samples, respectively. Water vapor adsorption isotherms were measured at 298 K for the activated samples (Figure 5-3c). Both batch and flow samples exhibit Type IV isotherms with a steep uptake step at approximately 0.28 P/P_0 , which is equivalent to 28%

RH. At 92% RH, the total water uptake for batch and flow samples is 1.06 g.g⁻¹ and 1.14 g.g⁻¹ respectively. Ni₂Cl₂(BTDD) crystallizes in the $R\bar{3}m$ space group (trigonal crystal system) with an olive green needle-shaped morphology of microcrystals confirmed by the SEM image in Figure 5-3d, identical to previously reported structure.²⁰⁵⁻²⁰⁶ Samples synthesized in batch and flow are compared in Figure 5-9 using high-magnification SEM images, while Figure 5-10 and Figure 5-11 provide high-resolution TEM images. Synthesis of Ni₂Cl₂(BTDD) in flow maintains similar crystallinity, pore size, and water-uptake characteristics compared to batch synthesis, while reducing volume of solvents used in the precursor mixture and improved productivity of the process.

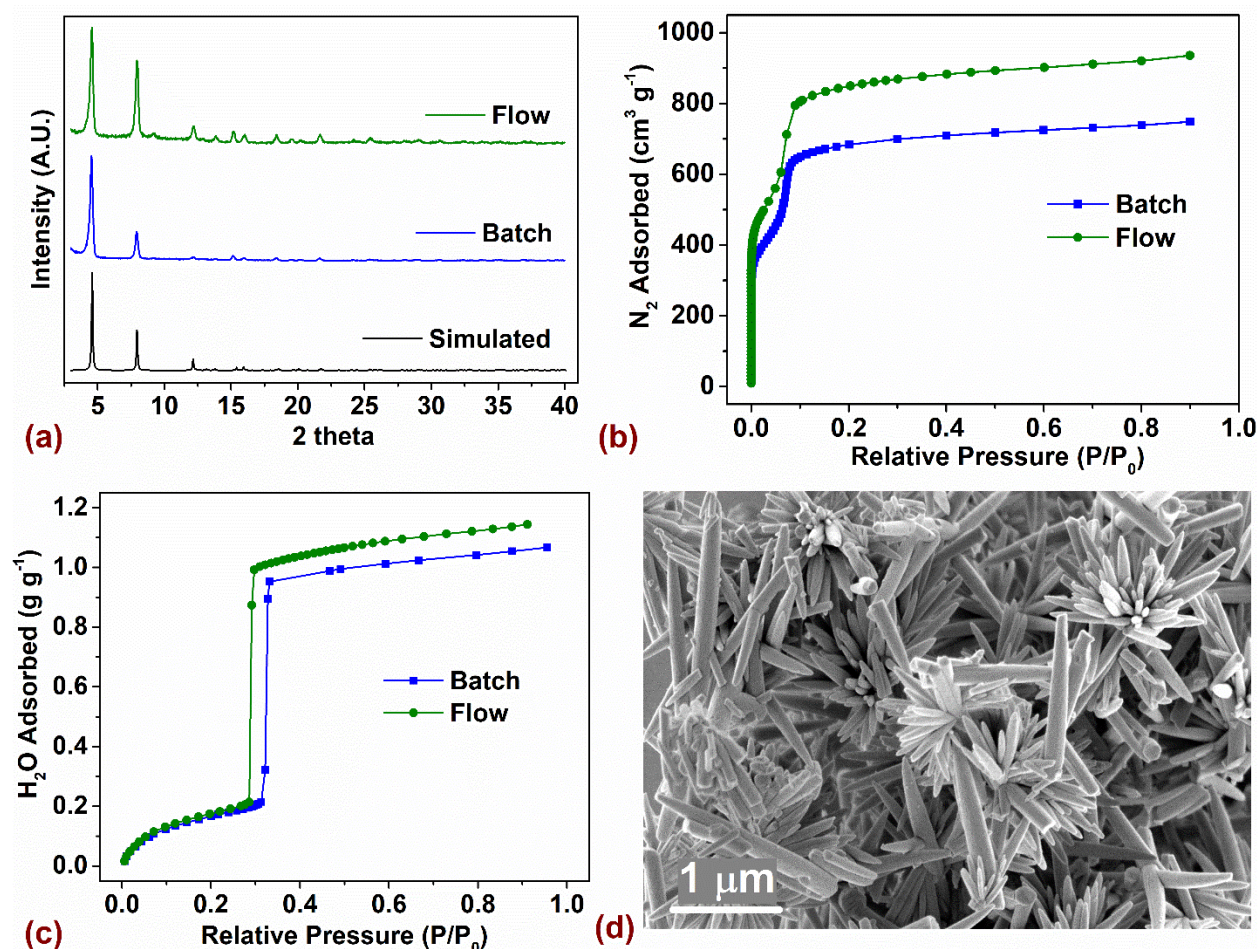


Figure 5-3 Characterization of Ni₂Cl₂(BTDD) synthesized at optimal flow reaction conditions using (a) PXRD patterns, (b) N₂ adsorption isotherm at 77 K, (c) water vapor adsorption isotherm at 298 K, and (d) SEM image.

Although a large number of studies exist on novel MOF structures and their potential applications, there is a paucity of reports on the scale-up of MOF syntheses.^{12, 24, 40, 207} The key translation piece for the use of MOFs in revolutionary technology platforms is the ability to manufacture at desired scale, purity and satisfy the market price requirements.¹⁷ The design of scaled-up flow reactors as a manufacturing system involves appropriate sizing of reactor equipment (such as pumps, reactor tubing configuration, heating furnace and sample collection strategy) and lowering crystallization time by optimization of synthetic conditions for higher throughput.²⁰⁸ Although parallelization offers a simple method of linear productivity scale-up by increasing the number of reactors, it requires a complex network of fluid flow distribution and control devices.³³ Alternatively, throughput can be increased by enlarging the inner diameter (ID) of the reactor tubing, which results in quadratic dependence on volumetric flow rate ($Q \propto d^2$). An increase in tube ID by a factor of 4, from 1/16 inch (0.158 cm) to 1/4 inch (0.635 cm), increases the productivity by a factor of 16, assuming the yields are constant. However, the downside to this approach is the reduction in surface-area to volume ratio ($SA/V \propto d^{-1}$) of the tubing, which could decrease the efficiency of heat transfer processes.^{12, 24, 120} From an operational standpoint, the propensity for hydrodynamic failure due to clogging of synthesized solids in the tube is indirectly proportional to the tube ID.⁶⁴ Accordingly, we modeled a scale-up scheme by enlarging the tube ID using the COMSOL Multiphysics® platform to compute variation in heat transfer rates and growth of thermal boundary layers as a function of tube ID. The reactor is modelled as a 2D axisymmetric geometry and a coupled heat transfer and fluid flow problem is solved under non-isothermal interface. Axial temperature profiles for different tube IDs as a function of the precursor position from reactor inlet as it traverses the heated reaction zone are shown in Figure 5-4a, while gradients in temperature near the entrance region of reaction zone and evolution of thermal boundary layers as a function of tube ID are illustrated in Figure 5-4b. The variation in heat transfer rates induces deviation in effective residence time (τ_{eff}), which is defined as the ratio of time spent by precursor at setpoint temperature in the reaction zone to the desired residence time. It was found that tube IDs below 3/8 inch have >90% τ_{eff} , while further increasing the tube ID results in poorer heat and mass transfer characteristics compared to those typically seen in batch reactor (Figure 5-14). Thus, owing to short diffusion length scales and high SA/V for tube IDs below 3/8 inch (0.952 cm), the fluid exhibits a near step-function change in the temperature from room temperature to the reaction temperature. The reactor tubing was modeled with uniform wall temperatures to characterize

developing thermal boundary layers radially inward to the tube axis. The boundary layer thickness increases along the length of the tube and gradually fills the entire flow section. The distance from inlet to the region of boundary layer convergence is defined as thermal entrance length (L_T), beyond which there is no radial gradient in temperature.²⁰⁹⁻²¹⁰ The L_T for a 1/16 inch reactor is 2.1 cm, while a 1 inch reactor has L_T of ~5200 cm—a three order of magnitude increase when operated at same reaction conditions (140 °C and 60 min res time). Owing to small system dimensions in case of 1/16 inch (radius of 0.079 cm), boundary layers quickly develop resulting in fast heat transfer characteristics and a high τ_{eff} . Details on meshing sequence and modelling parameters are summarized in Figure 5-12 and Figure 5-13, and Table 5-2.

Tradeoffs associated with enlarging reactor tubes for higher production rate while losing benefits of small system dimension in the flow reactor must be judiciously considered before scaling-up the system.²¹¹ Computing MOF production rates and consumption of reagents with an increase in the tube ID is important from a standpoint of logistical planning while operating in a continuous manufacturing environment. A target scenario for synthesizing 1 kg of $\text{Ni}_2\text{Cl}_2(\text{BTDD})$ per month with continuous operation was evaluated and presented in Figure 5-15 and Table 5-3; additional assumptions are described in section 3 of the Supporting Information. Based on our heat transfer models, in order to maintain favorable heat and mass transfer characteristics, the reactor configuration must have a maximum ID of 3/8 inch. However, this configuration can only achieve ~0.21 kg_{MOF} per month, while the reactor with 1/16 inch ID used in the current study synthesizes ~0.00587 kg_{MOF} per month, two orders of magnitude lower. A resourceful strategy in this case would be using a combinatorial approach of increasing tube ID to an extent where heat transfer characteristics are retained, and parallelization of such reactor units, ensuring higher production rates. Estimates presented in Figure 5-15a require using 5 identical reactor units of 3/8 inch ID operated in parallel to achieve the target production scenario of 1 kg of $\text{Ni}_2\text{Cl}_2(\text{BTDD})$ per month. Traditional batch synthesis procedure employs 1000 mL glass bottle, producing 260 mg of $\text{Ni}_2\text{Cl}_2(\text{BTDD})$ from 528 mL of reaction mixture heated at 100 °C for 48 h. Scaling-up the synthesis to manufacture 1 kg of $\text{Ni}_2\text{Cl}_2(\text{BTDD})$ would involve using ca. 3847 bottles of 1000 mL capacity, each containing ca. 528 mL of reaction mixture. From an operational standpoint, replacing 3847 bottles of 1 L capacity with one large volume reactor vessel, for example 3500 L vessel with ~58% of its volume filled would be ideal, however it may require re-optimization of reaction conditions due to their poor translation with change in batch reactor volume.²⁴ Section 5.4.2 in SI provides

additional details on production scenarios. The flexibility and modular configuration of flow reactors opens pathways for cost-efficient and industrial scale manufacturing of novel MOFs.

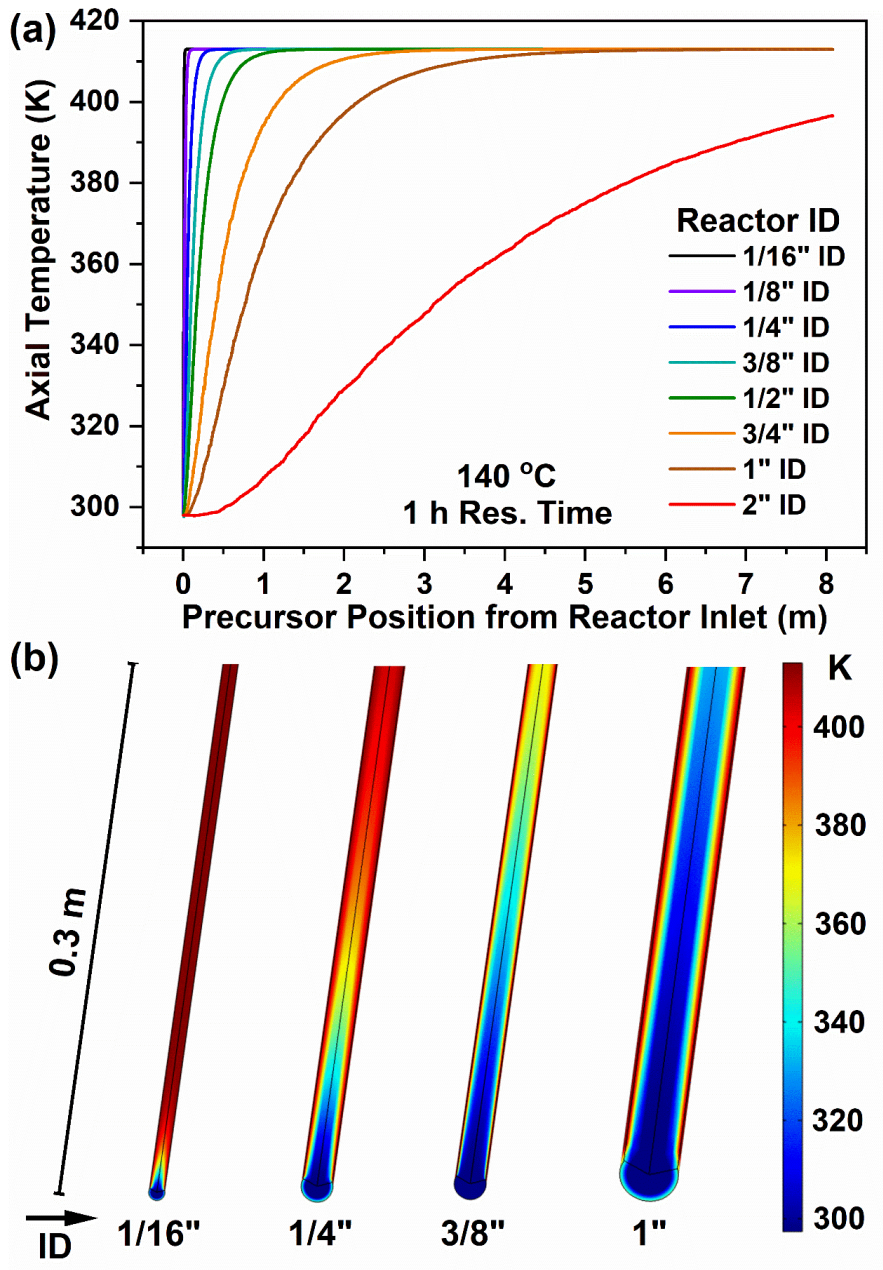


Figure 5-4 (a) Axial temperature profile along the length of reactor tube plotted against position of the precursor slug from reactor inlet. (b) Three dimensional (3D) slice plots at the entrance region of flow reactor showing both the temperature gradient and the growth of thermal boundary

layers in the heated reaction zone as a function of tube ID. Outer diameter and tube wall is held at 140 °C and fluid flow has linear velocity of 13.4 cm/min to achieve residence time of 60 min (8 m reactor tube length).

5.3. Conclusions

An optimized flow synthesis procedure permits the accelerated manufacturing of Ni₂Cl₂(BTDD)—a strong candidate for adsorption-based atmospheric water capture platforms. Process parameters such as residence time, reaction temperature, and solvent quantity were optimized by mapping the chemical synthesis space of Ni₂Cl₂(BTDD). Ideal synthesis conditions in flow resulted in reduced methanol and hydrochloric acid volumes in the precursor mixture by 50% and 40% respectively, while achieving threefold increase in productivity compared to batch synthesis. Tradeoffs associated with using larger tube sizes on process productivity and deteriorating heat transfer properties were evaluated using a CFD model. These results represent a critical advance towards realizing a sustainable and scalable manufacturing route for Ni₂Cl₂(BTDD) and provide a potential blueprint for the production of other azolate-based, water-stable MOFs that may impact atmospheric water generation technologies and other applications requiring water stability and high porosity.

Acknowledgements:

S.B. and Y.R-L., thank the U.S. Department of Energy, Office of Basic Energy Sciences under Award No. DE-SC0016214 for support. The authors would like to thank Dr. Charles Settens for fruitful discussion related to quantification of relative crystallinity using PXRD data and Dr. Yong Zhang for technical assistance with TEM

5.4. Supporting Information

5.4.1. Materials and Methods

All reagents except H₂BTDD ligand are commercially purchased: NiCl₂•6H₂O (Strem Chemicals), HCl (32-35%, BDH – VWR Analytic), Methanol (99.9%, VWR), N,N-dimethylformamide (99.8%, Millipore). H₂BTDD ligand was synthesized as described in previous literature.^{191, 212-214} Reagents for ligand synthesis are summarized: 1-chloro-2,4-dinitrobenzene (99%, TCI), Catechol

(99%, Sigma-Aldrich), K_2CO_3 (99%, Sigma-Aldrich), Sn Powder (150 micron, 99.5%, Sigma-Aldrich), diethyl ether (99%, Sigma-Aldrich), Trimethylsilyl bromide (97%, Sigma-Aldrich), Acetone (ACS grade, Macron Chemical), Fuming HNO_3 (90% min, Macron), H_2SO_4 (95-98%, BDH Chemicals), Acetic Acid (ACS grade, VWR BDH Chemicals), $NaNO_2$ (98%, Alfa Aesar), Ethanol (200 proof, Koptec), KOH (ACS grade, BDH chemicals), CsF (99%, Beantown Chemicals) were used as received. Benzene (ACS grade, EMD) was purged with argon, and subjected to three freeze-pump-thaw cycles before bringing into a nitrogen-filled glovebox and stored over 3 Å molecular sieves.

Synthesis of $Ni_2Cl_2(BTDD)$ in Batch: In a typical synthesis, 228 mg H_2BTDD (0.75 mmol) was dissolved in 200 mL N,N-Dimethylformamide (DMF) in a 1000 mL Pyrex glass bottle by stirring and heating to approximately 100 °C. The clear solution was then cooled to room temperature. In a separate 500 mL bottle, 1.9 mmol (2.2 eq.) metal chloride hydrate was dissolved in a solution of 200 ml methanol and 128 mL of 37 wt. % hydrochloric acid. The clear solutions were added to a 1000 mL Pyrex glass bottle (~53% filled), capped, and heated to 100 °C in an oven for 48 h. The reaction mixtures were removed from the oven and filtered to collect the solids followed by washing with DMF and methanol. For approximately 100 mg of $Ni_2Cl_2(BTDD)$, solvent exchange is carried out using 30 mL of DMF thrice and 30 mL of methanol thrice, followed by Soxhlet extraction with 100 mL methanol for approximately 48 h. Samples from the batch and flow were activated under dynamic vacuum at 100 °C for 24 h.

Powder X-ray diffraction (PXRD) patterns were recorded with a Bruker D8 Advance II diffractometer equipped with a $\theta/2\theta$ Bragg-Brentano geometry and Ni-filtered $CuK\alpha$ radiation ($K\alpha_1 = 1.5406 \text{ \AA}$, $K\alpha_2 = 1.5444 \text{ \AA}$, $K\alpha_2/K\alpha_1 = 0.5$). The tube voltage and current were 40 kV and 40 mA, respectively. Samples for PXRD were prepared by placing a thin layer of the appropriate material on a zero-background silicon crystal plate. Figure 5-7 (a, b) shows the PXRD of the synthesized samples with different crystallinity along with background correction scheme used for measuring the relative crystallinity.

Relative Crystallinity (% RC) measurements were calculated using the HighScore Plus analysis package from Panalytical. During the course of optimization of synthesis parameters, many reaction conditions resulted in a semi-crystalline or an amorphous sample. Given that the material crystallinity is an indispensable characteristic, the Equation 5-1 was used to quantify the RC of all

synthesized samples. We subtracted the constant background intensity ($I_{\text{const.bkgd}}$) from the total intensity (I_{tot}) to remove substantial contributions to the signal from amorphous phases found in semi-crystalline samples. The intensity contribution from crystalline peaks (I_{cryst}) was calculated using the corrected background, which was computed by an iterative method developed by Sonneveld et al.¹⁴⁰ that takes into account granularity of the background fitting and bending factors pertaining to the curvature.

$$\text{Relative Crystallinity (\% RC)} = 100 \times \left(\frac{\sum I_{\text{cryst.}}}{(\sum I_{\text{total}} - \sum I_{\text{const. bkgd}})} \right) \quad (\text{Equation 5-1})$$

A summary of the investigated $\text{Ni}_2\text{Cl}_2(\text{BTDD})$ reaction conditions for the rapid optimization of synthesis design space (in flow reactor platform) is provided in Table 5-4. Calculations for yield and productivity are described in Table 5-5 and Table 5-6. We also used the Caglioti equation to fit the FWHM data points obtained for the peaks in the XRD pattern. The Caglioti equation, described below (Equation 5-2), establishes a relationship between broadening (B) and the fitting parameters W, V, and U that are derived as an instrument response function for X-ray diffraction. The curve fit provides Lorentz and Gauss coefficients that account for crystal shape factor K and instrument broadening.

Caglioti equation:

$$B^2 = (W + V \tan \theta + U \tan^2 \theta) \quad (\text{Equation 5-2})$$

Nitrogen adsorption isotherms were measured by a volumetric method using a Micromeritics ASAP 2020 gas sorption analyzer. A typical sample of ca. 40 mg of metal-organic framework, pre-activated at 100°C to remove all residual solvent, was transferred in an Ar filled glovebox to a pre-weighed analysis tube. The tube with sample inside was weighed again to determine the mass of the sample. The tube was capped with a Micromeritics TranSeal, brought out of the glovebox, and transferred to the analysis port of the gas sorption analyzer. Free space correction measurements were performed using ultra-high purity He gas (UHP grade 5, 99.999% pure). Nitrogen isotherms were measured using UHP grade nitrogen. All nitrogen analyses were performed using a liquid nitrogen bath at 77 K. Oil-free vacuum pumps were used to prevent contamination of sample or feed gases.

Water vapor adsorption and desorption isotherms were measured by a volumetric method using a Micromeritics ASAP 2020 gas sorption analyzer with a vapor dose option and a heated manifold. A typical sample of ca. 40 mg of metal-organic framework, pre-activated at 100°C to remove all residual solvent, was transferred in an Ar filled glovebox to a pre-weighed analysis tube. The tube with sample inside was weighed again to determine the mass of the sample. The tube was capped with a Micromeritics TranSeal, brought out of the glovebox, and transferred to the analysis port of the gas sorption analyzer. Free space correction measurements were performed using ultra-high purity He gas (UHP grade 5, 99.999% pure). Water vapor adsorption isotherms were measured using Milli-Q water. The water was degassed on the ASAP 2020 manifold prior to measurement. All water analyses were performed using water-bath held at constant temperature with a recirculating chiller. The manifold was held 10 °C above the temperature of the sample water bath, and the vapor dosing tube was held 15 °C above the temperature of the sample water bath. Oil-free vacuum pumps were used to prevent contamination of sample or feed gases.

Scanning Electron Microscopy (SEM) images were acquired using Zeiss Merlin High-resolution SEM. Double coated conductive carbon tape was glued to an aluminum sample mount (or stubs, 12.7 mm diameter) to minimize charging of non-conductive MOF sample and acquire high-resolution images. Small amount of sample was transferred to the mount using a spatula and excess sample was dusted off using compressed air blown for a few seconds. Sample mounts were then sputter coated with an ultra-thin layer (~10 nm) of Au/Pd (Gold and Platinum electrode), to improve resolution of edge features on the sample, reduce charging and acquire high quality images of poorly conducting samples. The SEM was operated at a working distance of 4.9 mm, probe current of 100 pA and acceleration voltage of 2 kV. Images were acquired for both batch and flow synthesized samples at three different magnifications (8 kX, 20 kX and 60 kX). Figure 5-8 shows SEM images comparing batch and flow-synthesized samples.

Transmission Electron Microscopy (TEM) images were acquired using FEI Tecnai Multipurpose Digital TEM. MOF sample was added to a glass vial containing acetone and shaken to obtain a well-dispersed suspension. A drop or two of this suspension was added to the copper grid (5-6 nm thick and 3.05 mm wide) with a thin film of pure carbon deposited on one side (CF200-CU from Electron Microscopy Sciences). After the evaporation of acetone, the grid was placed on the sample holder and inserted in the beam column. The chamber was evacuated at 3.2×10^{-7} torr before

the electron gun was switched on and aligned for acquiring high-resolution images. The TEM was operated at 120 kV and corrected for image aberrations using stigmator in condenser/objective lens. Figure 5-10 and Figure 5-11 show a comparison of TEM images acquired for MOF samples in batch and flow mode.

5.4.2. Synthesis Scale-up

Scale-up calculations are presented for the scenarios associated with the enlargement of the reactor tube inner diameter (ID) as a strategy to achieve higher throughput. COMSOL Multiphysics platform was used to calculate changes in heat transfer and flow dynamics associated with increase in the ID of the tubing. The reactor tubing was modeled as a 2D axisymmetric geometry with varying diameters from 1/16 in (0.159 cm) to 2 in (5.08 cm), and a constant length of 8 m in the crystallizer (heated reaction zone of the tubing). To achieve a residence time of 60 min, a linear velocity of 13.4 cm/min and total flow rate of 0.267 mL/min was used. A coupled heat transfer and fluid flow problem is solved using the nonisothermal flow interface. Laminar Flow (SPF) and Heat Transfer in Fluids (HT) modules are employed and boundary conditions at the inlet, outlet, for fluid flow and heat transfer are specified. All cases engaged physics-controlled meshing sequence, which ensures there were no void regions in the computational domain or overlap in neighboring elements. The meshing sequence also resulted in low computational time and cost, while maintaining sufficient resolution with desired accuracy. Axisymmetric models with single phase flow regime cannot be used to investigate true temperature profile of reagents in biphasic slug flows. Thermal properties of individual components such as tube wall, the silicone oil phase, and the dispersed MOF precursor phase must be considered in the model and are analogous to electrical resistances in a circuit. Concerning reaction driven crystallization processes, reaction rate (r), and reaction enthalpy (ΔH_R) must be considered in the model, which strongly influence local temperature of reagents as they traverse along the heated reaction zone.^{34, 215} Another important parameter to be considered for reactor design is the adiabatic temperature rise (ΔT_{ad}), which is the maximum temperature rise in the flow reactor without any heat transfer.^{33, 204} It takes into account reaction enthalpy, initial concentration of reagents, conversion of reagent in the reaction, specific heat capacity of reagents. These parameters could significantly change based on the reaction probed in flow synthesis. Table 5-2 provides physiochemical properties of the continuous phase used for modelling and Figure 5-12 illustrates variation in meshing sequence

associated with changes in the reactor tube ID. Figure 5-13 is a 2D plot visualizing evolution of thermal boundary layers in radial direction—outer diameter to tube axis, for different tube IDs.

Scaling-up the flow reactor platform would require appropriate sizing of pumping equipment, sample containers and associated components—Figure 5-13 provides estimated flow rates used to achieve a residence time of 60 min (in a reactor tubing of 8 m) with different tube IDs. It is also essential to calculate the consumption of reagents while scaling-up the flow reactor platform; the data helps plan the logistics for executing a target production rate in a continuous manufacturing environment (for example, to manufacture 1 kg of MOF per month; a month is 30 days). Volumetric flow rates of Oil:Precursor are in a 1:2 ratio, leading to a precursor flow rate of 0.187 mL/min in a 1/16 in reactor tubing to achieve 60 min residence time. Figure 5-14 and Table 5-3 shows multiple scale-up scenarios for different reactor IDs. All calculated values were based on a constant yield of 80% and a productivity of $0.765 \text{ kg}_{\text{MOF}} \text{ m}^{-3} \text{ day}^{-1}$ (kg of MOF synthesized per m^3 of precursor mixture per day). Using a parallelization scheme, we estimated the required numbers of parallel reactors with identical configurations to achieve the target production rate of 1 kg of MOF synthesized per month. Based on the batch synthesis procedure described in section 2, we would synthesize 260 mg of $\text{Ni}_2\text{Cl}_2(\text{BTDD})$ from 528 mL of reaction mixture heated at 100 °C in a 1000 mL glass bottle for 48 h (a productivity of $0.245 \text{ kg}_{\text{MOF}} \text{ m}^{-3} \text{ day}^{-1}$). In order to generate 1 kg of $\text{Ni}_2\text{Cl}_2(\text{BTDD})$ in batch, we would need $\sim 3,847$ glass bottles of 1000 mL capacity, each containing 528 mL of reaction mixture. Using a larger volume batch reactor could require re-optimization of synthesis conditions and may result in diminished yields.²⁴

For evaluating engineering productivities based on the volume of reactor vessel, we present the following analysis comparing batch and flow reactors operated for a period of 1 month (30 days). A part of the calculation for production rates from parallelized configurations of flow reactors is described in Figure 5-15. One flow reactor of 1/16 inch ID with a 16 mL reactor volume generates 5.87 g per month and if we operate 6 identical flow reactors, the production rate of $\text{Ni}_2\text{Cl}_2(\text{BTDD})$ would be 35.253 g per month. On similar lines, one batch reactor with a 1000 mL volume generates 1.929 g per month when they are renewed every 48 hour for a month; operating 6 identical batch reactors results in 11.575 g per month. However, batch reactors need a downtime of ~ 3 -6 h in between consecutive runs; assuming a 6 h downtime between runs, each synthesis cycle lasts for 54 h, producing 1.714 g per month and 6 identical reactors results in 10.288 g per month. We

consider 30 days per month for calculations. The resulting productivities based on the amount of MOF synthesized per volume of reactor per month are:

- Flow synthesis: $367.21 \text{ kg}_{\text{MOF}} \text{ m}^{-3} \text{ month}^{-1}$
- Batch synthesis: $1.929 \text{ kg}_{\text{MOF}} \text{ m}^{-3} \text{ month}^{-1}$
- Batch synthesis (with downtime): $1.714 \text{ kg}_{\text{MOF}} \text{ m}^{-3} \text{ month}^{-1}$

It is necessary to correlate the productivities obtained from batch and flow syntheses to the amount of MOF required for use in an AWC device, which helps evaluate the efficacy of syntheses routes to fulfill real-world demands. For instance, the AWC device presented by Hanikel et al.⁵⁸ uses Al based MOF-303 operating at 10-40% RH and was able to deliver 1.3 L of water per kg of MOF for a 24 hour harvesting cycle. MOF-303 has a gravimetric water uptake capacity of 0.3 g/g (g of water per g of MOF) at a P/P_o of 0.4 and the device used ~430 g of MOF. Replacing MOF-303 with Ni₂Cl₂(BTDD) in the device would increase the water delivered per cycle at least by a factor of 2. From the production scenario described in Figure 5-15, operating 5 reactors with a 3/8" ID helps achieve a production target of 1 kg Ni₂Cl₂(BTDD) per month. The MOF produced per month would operationalize two water capture devices of the same configuration described by Hanikel et al.⁵⁸ for generating potable water using solar energy. It is worth noting that the water harvesting capacity (per capture cycle) of sorbent-based water capture devices is still fairly low compared to other atmospheric water capture techniques such as fog capture or dewing, but in arid and semi-arid areas with RH lower than 60%, sorbent-based water capture is the most efficient route to capture water vapor and convert it to potable water.^{57, 187, 216}

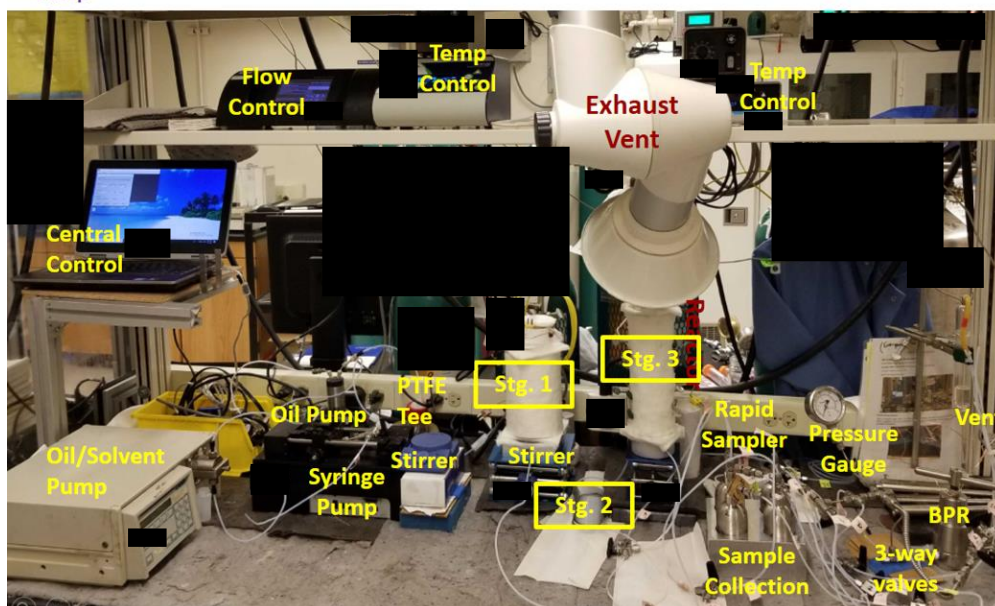
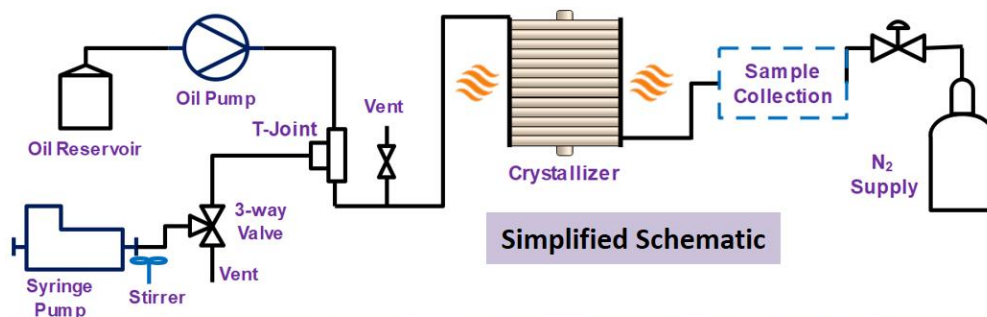


Figure 5-5 Continuous flow-reactor setup used for synthesis and optimization.

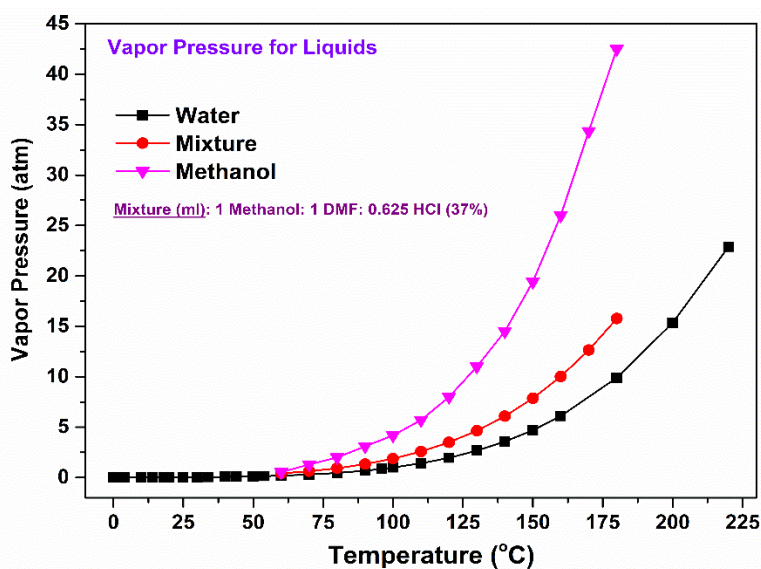


Figure 5-6 Bubble-point pressures of multiple components calculated by Aspen.

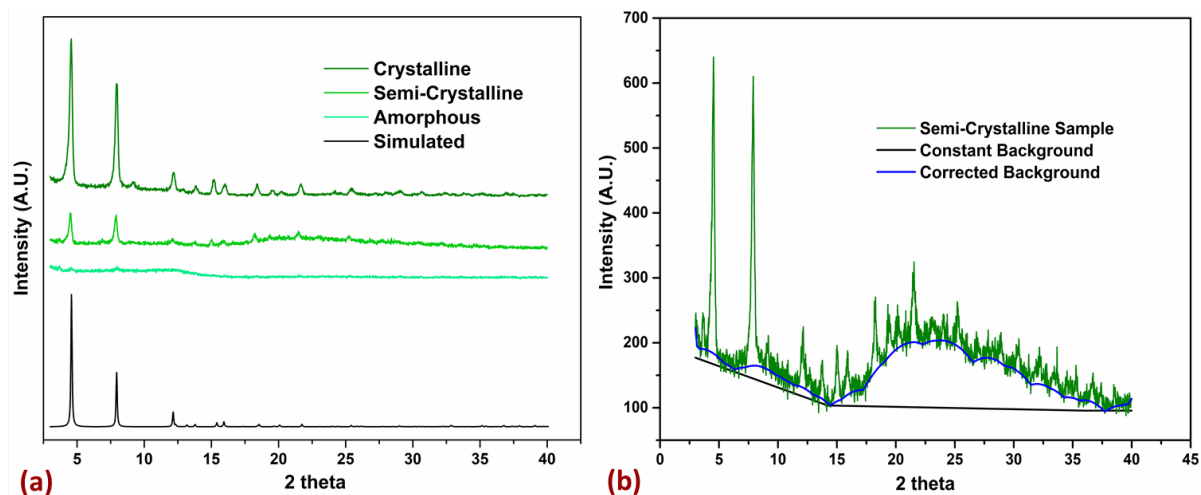


Figure 5-7 (a) PXR D patterns of $\text{Ni}_2\text{Cl}_2(\text{BTDD})$ obtained at different flow syntheses conditions showing varied levels of crystallinity, compared against simulated pattern. (b) Background correction scheme used to quantify intensity contributions from crystalline domains in the sample.

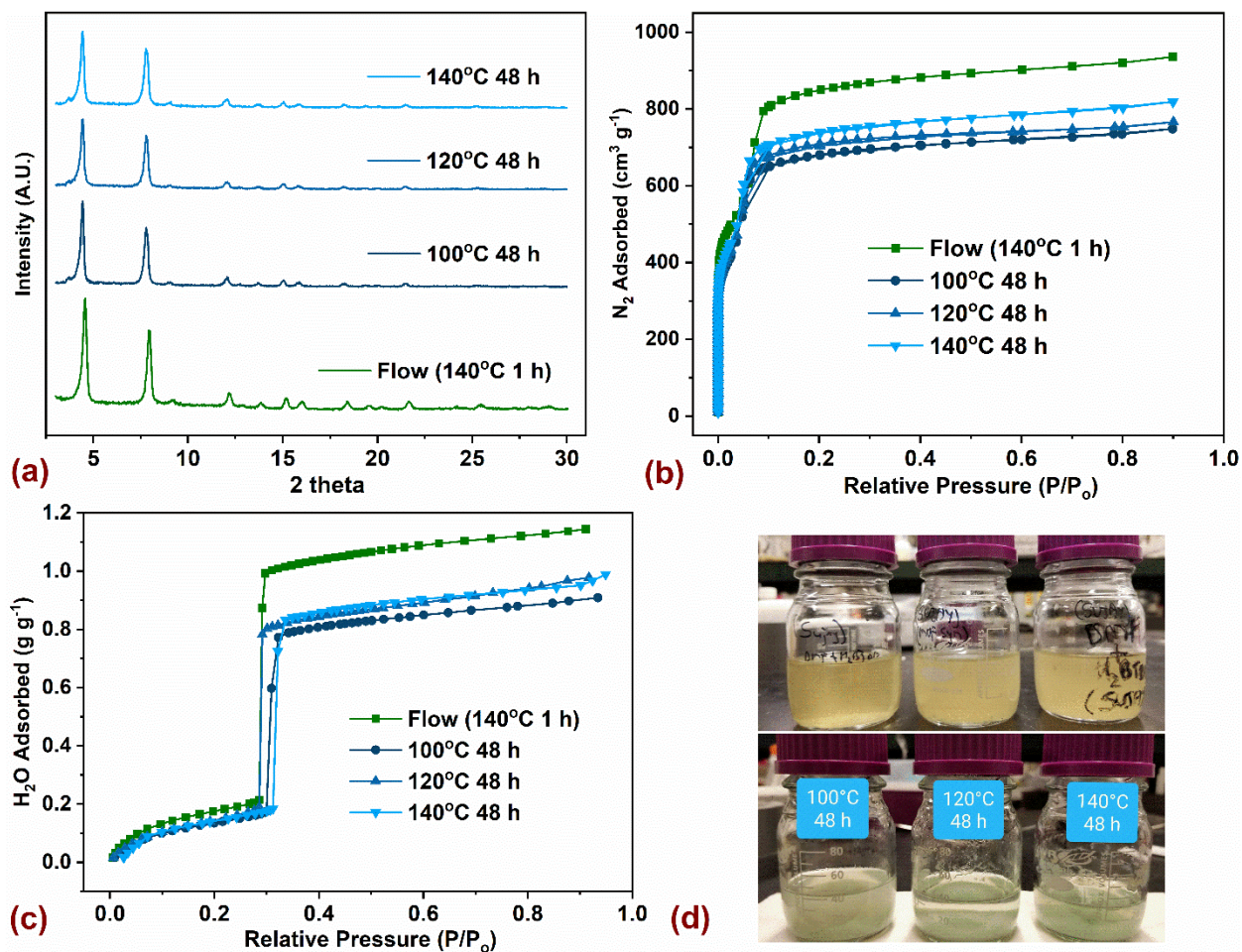


Figure 5-8 Characterization of $\text{Ni}_2\text{Cl}_2(\text{BTDD})$ synthesized at three different batch conditions (100°C, 120°C, 140°C at 48 hour) and their comparison with the ‘flow optimized’ condition (140°C and 1 hour). The volumetric ratio of “DMF:CH₃OH:HCl = 1:0.5:0.38” was used for all synthetic conditions which corresponds to the reaction mixture composition optimized in the flow reactor. (a) PXRD patterns, (b) N₂ adsorption isotherm at 77 K, (c) water vapor adsorption isotherm at 298 K, and (d) Batch samples (pre- and post-synthesis) in a 120 mL Pyrex glass bottle.

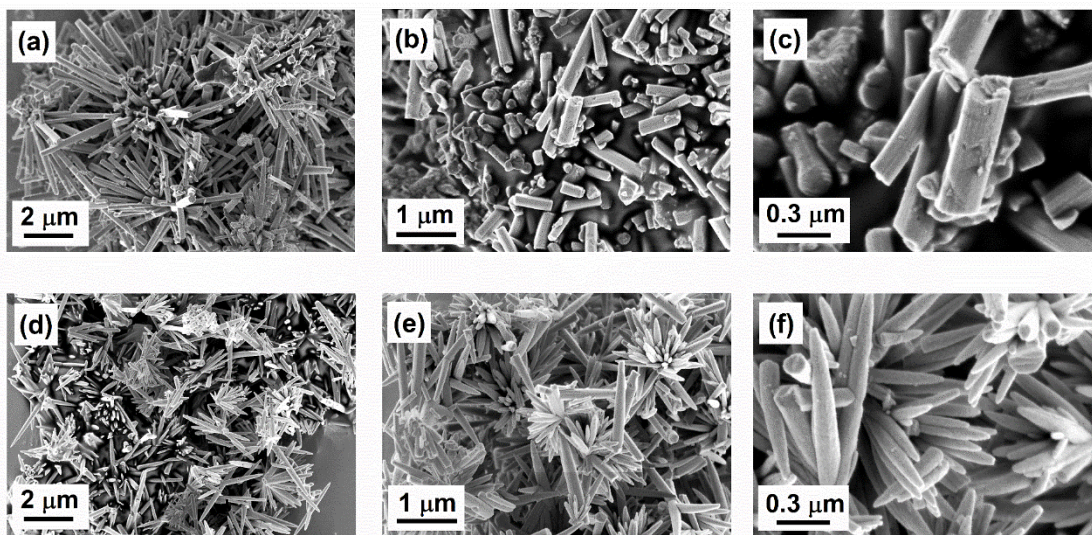


Figure 5-9 SEM images of $\text{Ni}_2\text{Cl}_2(\text{BTDD})$ synthesized in batch (a-c) and flow (d-f).

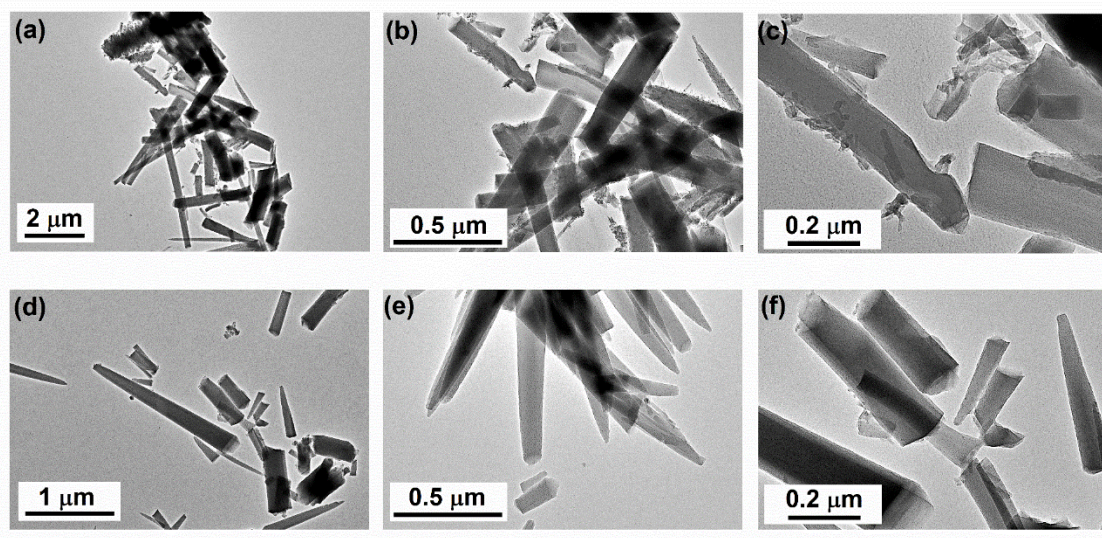


Figure 5-10 TEM images of $\text{Ni}_2\text{Cl}_2(\text{BTDD})$ synthesized in batch (a-c) and flow (d-f).

Flow Synthesis

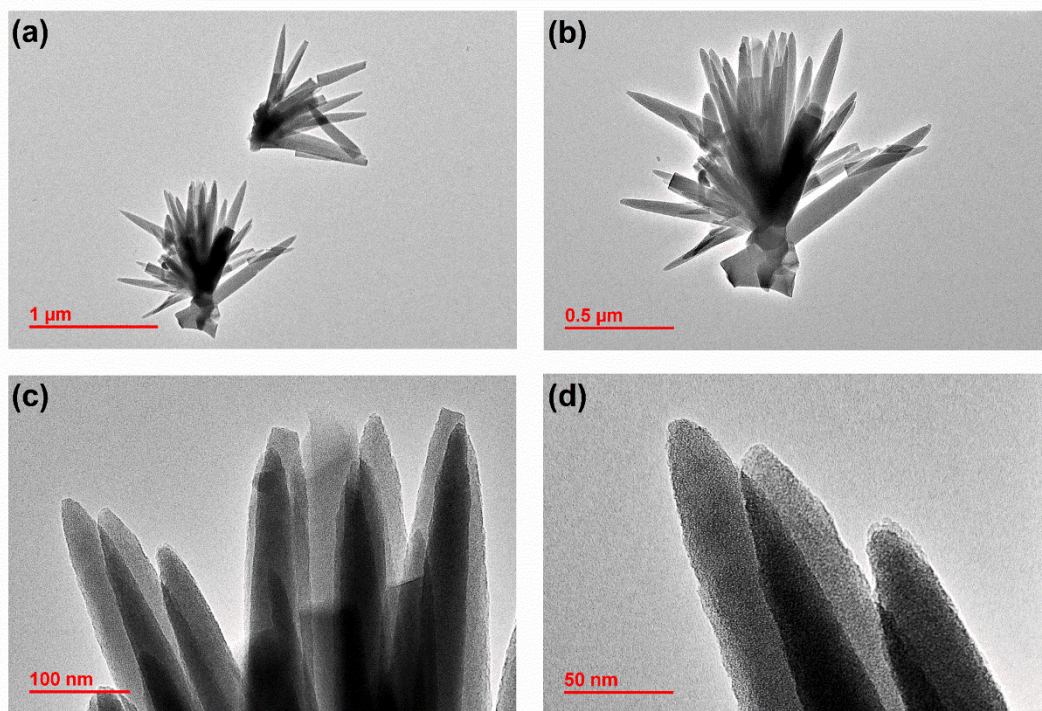


Figure 5-11 TEM images of $\text{Ni}_2\text{Cl}_2(\text{BTDD})$ synthesized in flow showing a “bouquet of crystals”. Higher resolution images (c-d) show needle-like crystal morphology.

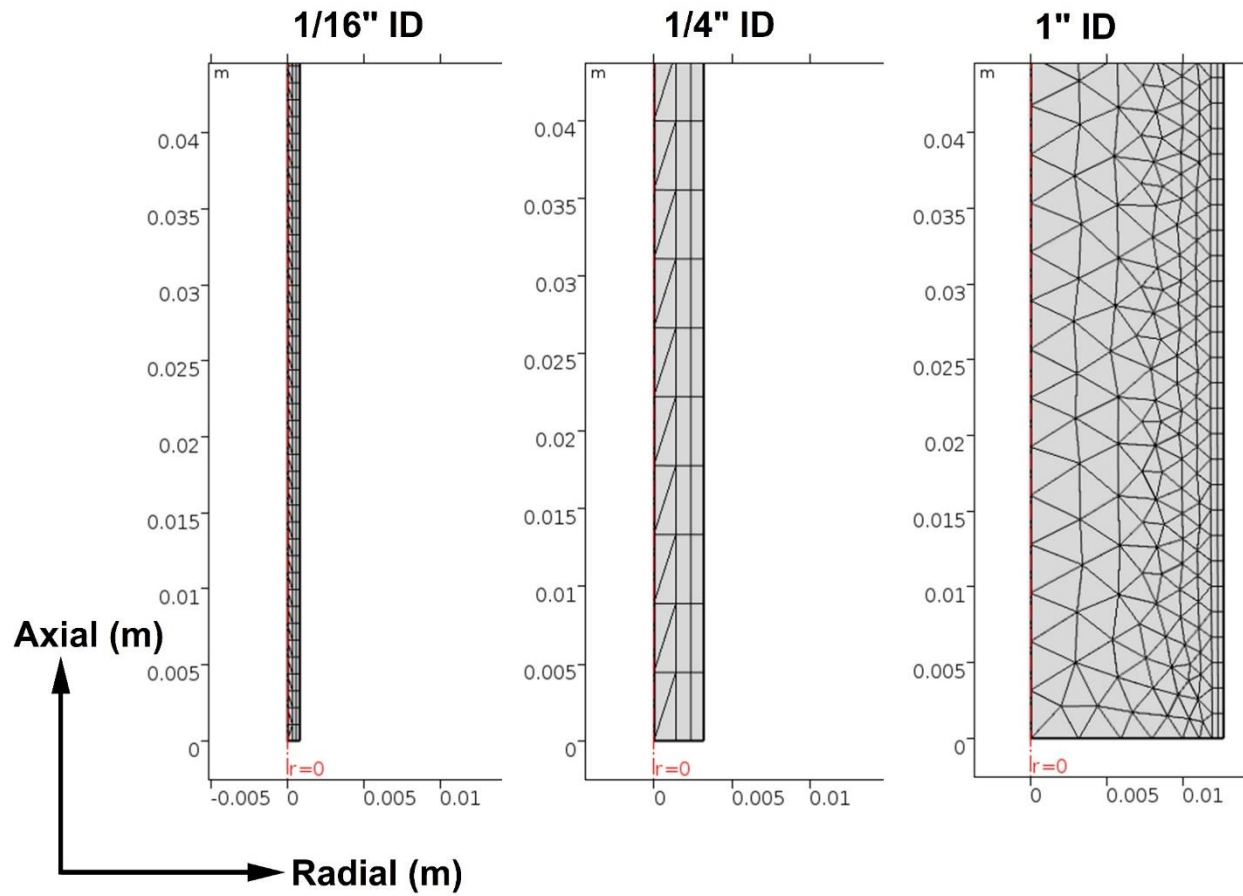


Figure 5-12 Physics-controlled meshing sequences with different tube diameters to model fluid flow and non-isothermal heat transfer using the COMSOL Multiphysics platform.

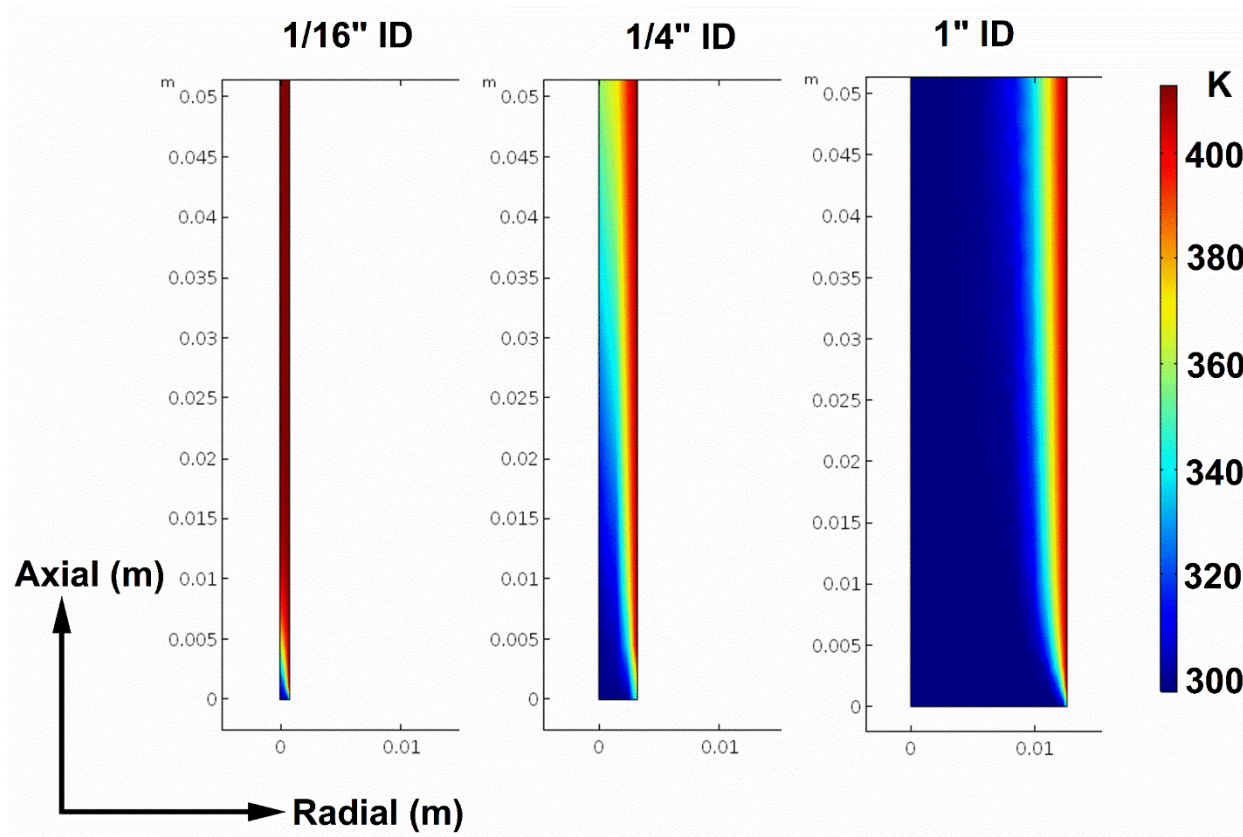


Figure 5-13 2D plots showing the growth of the thermal boundary layers (radially inward toward tube axis @ $r=0$) for different tube IDs. Tube wall is held at 140 °C and fluid flow had linear velocity of 13.4 cm/min to achieve residence time of 60 min (~ 8 m reactor tube length).

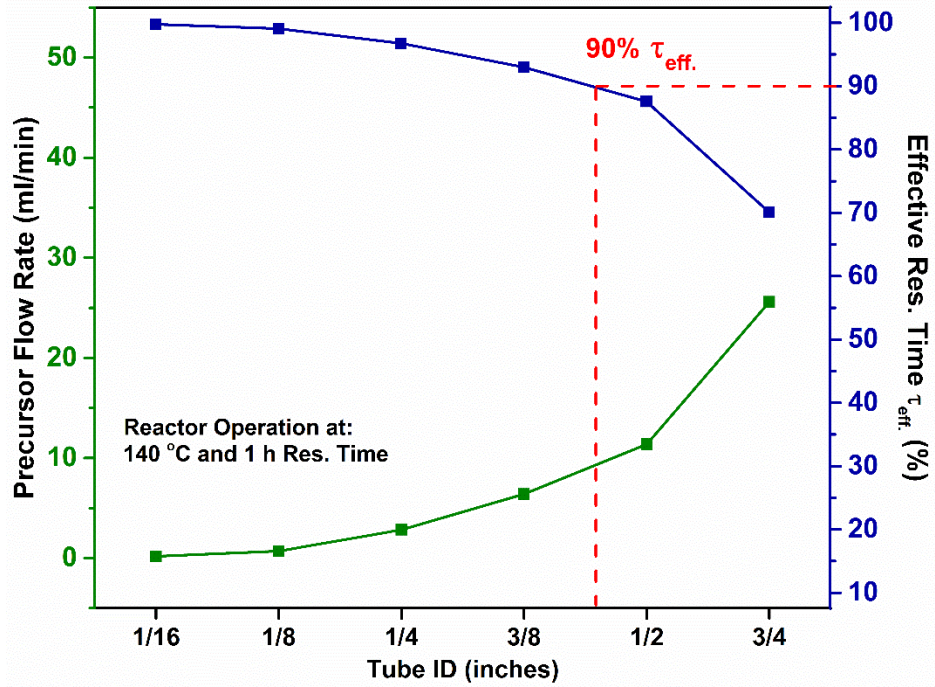


Figure 5-14 Variation in precursor flow rate as a function of reactor tube ID. Effective residence time (τ_{eff}) decreases with reactor tube ID and is $> 90\%$ for tube IDs below $\frac{3}{8}$ inch.

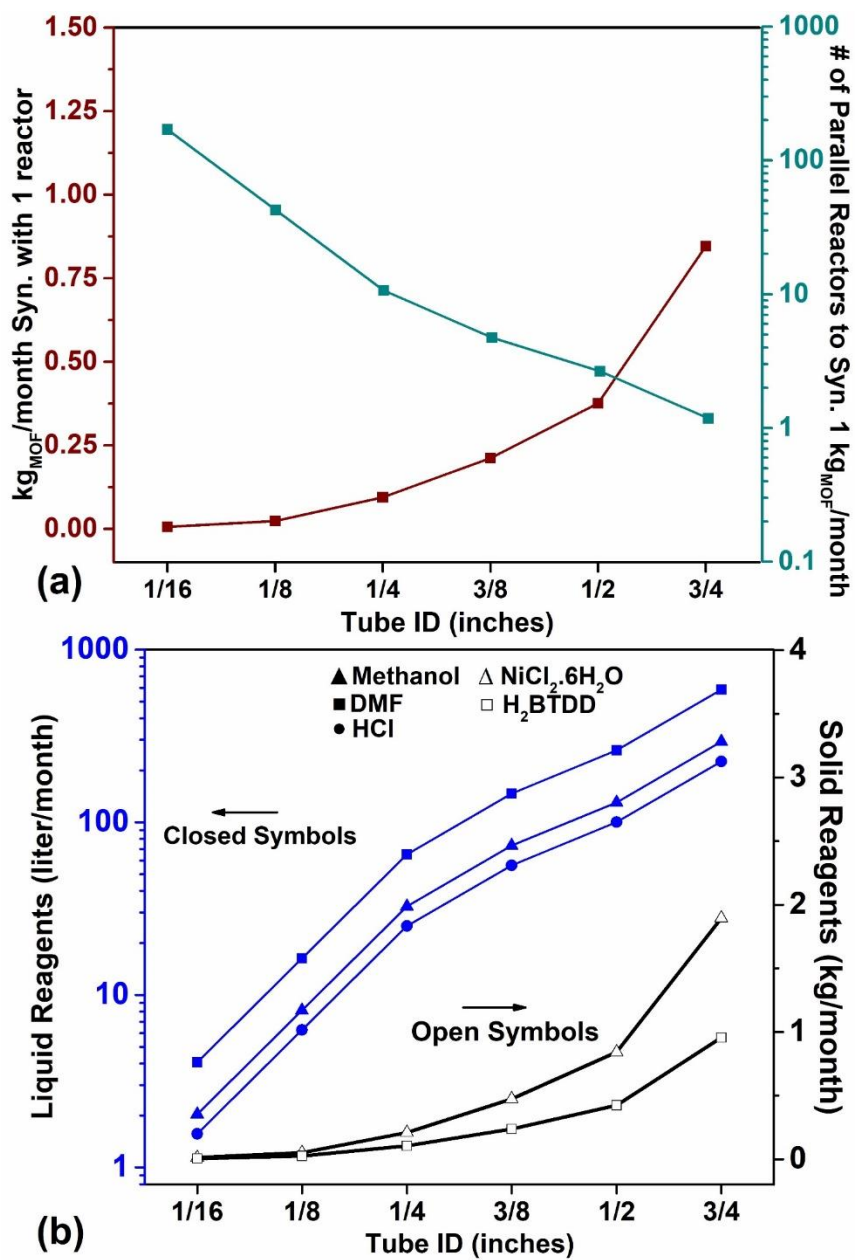


Figure 5-15 (a) Production output as a function of reactor tube ID and parallelization scenarios to achieve 1 kg of Ni₂Cl₂(BTDD) per month. We consider 30 days per month for calculations. (b) Solid and liquid reagents consumed per month based on the chosen reactor configuration. All cases assumed 80% yield and a productivity of 0.765 kg_{MOF} m⁻³ day⁻¹.

Table 5-1 Residence time for multiple flow rates in a reactor volume of 16 mL. The reactor tubing had an inner diameter of 1/16 in (0.159 cm) with a heated reaction zone length of 8 m.

Total Flow Rate* (mL/min)			Residence Time		Linear Velocity
Total	Oil:Precursor (1:2)		min	hour	cm/min
	Oil	Precursor			
1.067	0.320	0.747	15	0.25	53.870
0.534	0.160	0.374	30	0.50	26.900
0.267	0.080	0.187	60	1.00	13.460
0.134	0.040	0.094	120	2.00	6.730
0.067	0.020	0.047	240	4.00	3.360

Table 5-2 Physiochemical properties of silicone oil (continuous phase) and dimensions of tubing used in the reactor for crystallization of Ni₂Cl₂(BTDD).

Density of Oil (@ 25 °C)	855 kg/m ³
Kinematic Viscosity Of Oil (@ 25 °C)	1.2E-05 m ² /s
PTFE Tubing (max operating range)	370 psi, 260 °C
T-joint (max operating range)	225 psi, 130 °C
PTFE Tubing Dimensions (in)	1/8" OD, 1/16" ID
Specific Heat Capacity (C _p) of Oil	2000 J/Kg/K
Thermal Conductivity (k) of Oil	0.135 W/m/K

Table 5-3 Data for Figure 5-15 that evaluates scale-up scenarios by enlarging the reactor inner diameter. All the values assume 80% process yield and a productivity of $0.765 \text{ kg}_{\text{MOF}} \text{ m}^{-3} \text{ day}^{-1}$. Flow rates reported are for precursor only (volumetric flow ratio of 1:2 for Oil:Precursor was maintained). Changes in the reagents consumption due to variation in the reaction conditions were considered in the calculations. Silicone oil is immiscible with the reaction mixture and can be reused in the synthesis.

Tube ID (in)	Precursor Flow Rate (Q)		MOF Production		DMF	HCl	CH ₃ OH	NiCl ₂ .6H ₂ O	H ₂ BTDD
	mL / min	mL/day	mg/day	kg/month	liter/month (consumed)			kg/month (consumed)	
0.062	0.2	256.1	195.9	0.01	4.08	1.57	2.03	0.01	0.01
0.125	0.7	1024.1	783.4	0.02	16.31	6.26	8.15	0.05	0.03
0.250	2.8	4096.2	3133.6	0.09	65.23	25.05	32.61	0.21	0.11
0.375	6.4	9216.6	7050.6	0.21	146.76	56.35	73.38	0.47	0.23
0.500	11.4	16384.9	12534.5	0.38	260.90	100.18	130.45	0.84	0.42
0.750	25.6	36866.2	28202.6	0.85	587.04	225.42	293.52	1.89	0.95

Error! Not a valid link.

Table 5-4 Summary of Ni₂Cl₂(BTDD) reaction conditions investigated for rapid optimization of synthesis space using the flow reactor platform. Amount of DMF, and molar ratio of metal to

ligand (M:L) was constant in all cases. ‘HCl:DMF’ and ‘CH₃OH:DMF’ ratios denote the volumetric ratio of hydrochloric acid to DMF and methanol to DMF used in the precursor mixture. Run # 38, 39 are duplicates of Run # 22 and 23 to show reproducibility. Molar ratio of ‘Acid:Metal’ represents moles of HCl to Ni metal in the precursor mixture.

Run #	Reaction Conditions		Volumetric Ratio		Molar Ratio		Rel. Cryst.
	Res. Time (min)	Temp. (°C)	HCl:DMF	CH ₃ OH:DMF	M:L	Acid:Metal	% RC
1	120	120	0.062	1.00	2.2	216.35	32.9
2	120	130	0.062	1.00	2.2	216.35	10.9
3	240	130	0.125	1.00	2.2	432.71	0.0
4	120	120	0.25	1.00	2.2	865.42	9.0
5	120	140	0.25	1.00	2.2	865.42	0.0
6	240	140	0.25	1.00	2.2	865.42	0.0
7	30	150	0.125	1.00	2.2	432.71	26.6
8	60	140	0.625	1.00	2.2	2163.54	0.0
9	60	150	0.625	1.00	2.2	2163.54	0.0
10	120	140	0.625	1.00	2.2	2163.54	0.0
11	240	120	0.375	0.50	2.2	1298.12	43.0
12	60	140	0.625	1.00	2.2	2163.54	0.0
13	30	150	0.625	1.00	2.2	2163.54	0.0
14	240	120	0.625	1.00	2.2	2163.54	73.0
15	120	130	0.375	1.00	2.2	1298.12	0.0
16	60	130	0.375	0.50	2.2	1298.12	0.0
17	60	120	0.375	0.50	2.2	1298.12	0.0
18	30	120	0.375	0.50	2.2	1298.12	0.0
19	30	140	0.375	1.00	2.2	1298.12	58.6
20	30	145	0.375	1.00	2.2	1298.12	0.0
21	30	135	0.375	1.00	2.2	1298.12	41.4
22	30	140	0.375	0.50	2.2	1298.12	85.4

23	60	140	0.375	0.50	2.2	1298.12	100.0
24	120	140	0.375	0.50	2.2	1298.12	33.6
25	120	140	0.375	0.50	2.2	1298.12	28.0
26	60	150	0.375	0.50	2.2	1298.12	27.2
27	30	150	0.375	0.50	2.2	1298.12	34.9
28	120	120	0.375	0.50	2.2	1298.12	28.3
29	120	130	0.375	0.50	2.2	1298.12	44.9
30	30	140	0.375	0.25	2.2	1298.12	66.7
31	60	140	0.375	0.25	2.2	1298.12	62.9
32	120	140	0.375	0.25	2.2	1298.12	48.5
33	30	150	0.375	0.50	2.2	1298.12	22.9
34	120	120	0.375	0.25	2.2	1298.12	56.0
35	30	140	0.250	0.25	2.2	865.42	40.6
36	60	140	0.250	0.25	2.2	865.42	33.1
37	60	130	0.250	0.25	2.2	865.42	45.8
38	30	140	0.375	0.50	2.2	1298.12	87.7
39	60	140	0.375	0.50	2.2	1298.12	100.0
40	30	130	0.062	0.50	2.2	216.35	45.7
41	120	150	0.062	0.25	2.2	216.35	0.0
42	60	135	0.250	0.50	2.2	865.42	47.3
43	60	145	0.625	0.50	2.2	2163.54	48.6
44	15	140	0.625	0.25	2.2	2163.54	45.7
45	120	125	0.375	0.50	2.2	1298.12	0.0
46	240	150	0.375	0.50	2.2	1298.12	0.0
47	120	120	0.375	0.50	2.2	1298.12	9.0
48	30	145	0.375	0.50	2.2	1298.12	41.7
Batch	2880	100	0.625	1.00	2.2	2163.54	92.7

Table 5-5 BET surface areas and corresponding % RC (Relative Crystallinity) for batch and flow samples presented in Figure 5-8.

Sample ID	Surface Area (m ² /g)	% RC
Batch (100°C 48 h)	1795 ± 18	69.6
Batch (120°C 48 h)	1871 ± 16	75.3
Batch (140°C 48 h)	1944 ± 20	78.4
Flow (140°C 1 h)	2157 ± 17	100

Table 5-6 Yields were calculated based on the conversion of the limiting reagent (H₂BTDD ligand) into Ni₂Cl₂(BTDD). A factor of 80% is used for mass retained after activation as we expect to lose 10-30% of mass (from solids obtained after synthesis) when activated, due to removal of water and other solvents from pores of Ni₂Cl₂(BTDD).

$$Yield (\%) = \left(\frac{\text{Solids Obtained from Synthesis}}{\text{Solids Obtained from 100\% H}_2\text{BTDD Conversion}} \right) \times \left(\frac{80}{100} \right) \times 100 \quad (\text{Equation 5-3})$$

Precursor Component		Molar Mass	Initial Amount in Precursor		Solids Obtained for 100% H ₂ BTDD Conversion to Ni ₂ Cl ₂ (BTDD)	Actual Solids Obtained (non-activated)	Yield (activated)
			mg	mol			
H ₂ BTDD	Linker	266.2	51	1.915e-4	86.68	86.25	79.6
Ni ₂ Cl ₂ (BTDD)	MOF	452.5					

Table 5-7 Process productivity for the batch and flow synthesis of Ni₂Cl₂(BTDD) using volume of reaction mixture.

$$Productivity (kg_{MOF} m^{-3} day^{-1}) = \frac{\text{Production Rate } (\frac{kg}{day})}{\text{Precursor Feed Rate } (\frac{m^3}{h}) \times 24h} \quad (\text{Equation 5-4})$$

Synthesis Route	Res. Time (min)	Flow Rate (mL min ⁻¹)	Activated	Precursor consumed per day (mL day ⁻¹)	Productivity* (mg _{MOF} mL ⁻³ day ⁻¹) or (kg _{MOF} m ⁻³ day ⁻¹)	Yield (%)
			Solids Obtained (mg day ⁻¹)			
Flow @140 °C	60	0.178	195.85	256.1	0.765	~ 80
Batch @100 °C	2880	N/A	64.31	262.5	0.245	~ 75

*Productivity was calculated based on Equation 5-4.

Flow synthesis results in a 3-fold higher productivity compared to batch.

Table 5-8 Process productivity for the batch and flow synthesis of Ni₂Cl₂(BTDD) using volume of reactor.

$$Productivity_{Reactor Vol.} (kg_{MOF} m^{-3} day^{-1}) = \frac{\text{Production Rate } (\frac{kg}{day})}{\text{Volume of Reactor}} \quad (\text{Equation 5-5})$$

Synthesis Route	Res. Time (min)	Flow Rate (mL min ⁻¹)	Activated	Reactor Volume (mL)	Productivity** (mg _{MOF} mL ⁻³ day ⁻¹) or (kg _{MOF} m ⁻³ day ⁻¹)	Yield (%)
			Solids Obtained (mg day ⁻¹)			
Flow @140 °C	60	0.178	195.85	16	12.24	~ 80
Batch @100 °C	2880	N/A	64.31	1000	0.064	~ 75

**Productivity is calculated based on Equation 5-5.

Flow synthesis results in a 2 order of magnitude (~190 times) higher productivity compared to batch.

6. A Compact Device for Practical Atmospheric Water Harvesting

In this chapter, a novel concept for a compact and affordable sorbent-based atmospheric water harvesting (AWH) device is presented. The device is capable of on-demand generation of water using low-grade energy such as sunlight and targeted for use by remote communities as well as the lucrative outdoor- & adventure-sports market. We rigorously follow the product design methodology to develop a theoretical framework and detailed designs aided by computational modelling that help evaluate operational feasibility of the device. The MOF (Metal–Organic Framework) recently reported by the Dincă group at MIT ($Ni_2Cl_2(BTDD)$) and its synthesis optimized in our previous study¹⁰² has shown unprecedented levels of gravimetric water uptake (82% water by wt. below 30% RH), is used for calculating performance metrics of the AWH device termed as the ‘MOTTLE’. For reduced manufacturing costs, the MOTTLE uses commercially available construction materials such as Aluminum, PMMA, and borosilicate glass, which are durable, light-weight and improve overall device productivity owing to better thermal conductivity and high IR transmissivity. The device consists of two modules, a moisture battery and an external enclosure (or a condenser). The moisture battery functions as a reservoir of water-vapor and is judiciously designed to ensure maximum water yield per uptake/release cycle coupled with the ability to seamlessly run multiple cycles during day- and night-time operation. The estimated productivity (L/kg/day) of our device is similar to the existing bulky prototypes despite being an order of magnitude lighter in weight and a smaller footprint (reduced by 5X). We strongly believe that a compact design for AWH device coupled with low-cost manufacturing would be key for widespread deployment and a successful commercial product.

6.1. Introduction and Motivation

Most of the arid and semi-arid regions in the world do not have access to potable water. This problem will worsen due to increasing global water demand for both personal and industrial use, a growing global population, and desertification of fertile areas through over-farming and climate change, eventually leading to a projected water deficit of almost 2000 billion m³ by 2030.^{184, 217} Our planet does not lack water, however most of the water is either too salty or locked in ice. Energy-intensive methods such as desalination produce relatively cheap fresh water, however it

requires a distribution infrastructure and a large capital cost.²¹⁸ Water-vapor in the atmosphere is another fresh water resource which holds ~10% of all fresh water in lakes on earth and is ubiquitously present across the planet.²¹⁹ Developing a low-cost and energy-efficient process for capture and conversion of water-vapor to potable water would be key in solving water shortages faced in arid and semi-arid areas. Current atmospheric water harvesters (AWH) function by dewing (chilling air below its dew point) or by distilling water absorbed in concentrated brine, both of which are energy-intensive processes and are not viable options for use in remote locations with no energy-access.²²⁰ For water capture below 50% RH, the AWH should operate with a sorbent material that can uptake and release water-vapor with minimum energy requirements and powered by abundantly available low-grade energy sources such as sunlight. The ideal AWH sorbent material requires physical properties such as large gravimetric capacities, steep water uptake characteristics in a narrow RH range, and complete water release with minimal temperature swings over thousands of cycles. Metal-organic frameworks (MOFs) fulfill many, if not all of these requirements. MOFs are crystalline coordination lattices consisting of multitopic organic linkers and inorganic polynuclear clusters forming highly ordered 2D and 3D structures.⁴⁰

A handful of recent studies^{57-58, 221} have presented prototype AWH devices that use MOFs as sorbents for water capture and operate using abundantly available solar energy. For instance, Hanikel et al.⁵⁸ used Al based MOF-303 in AWH device operating at 10-40% RH, which was able to deliver 1.3 L of water per kg of MOF for a 24-hour harvesting cycle. The productivity of the device expressed in terms of L of water per kg of MOF per day was 1.3 L/kg/day. The device was bulky (~12 kg) and had a large footprint (110x110x40 cm). The device also used external battery power for heating the MOF bed (for quicker regeneration) as well as a fan for faster saturation of MOF in order to accommodate multiple water capture cycles for a 24 hour period; these operational attributes combined with low water yields make the existing AWH devices unattractive for widespread deployment. We present a concept for a compact AWH device that can operate seamlessly during day- and night-time, with similar water yields rivaling the bulky counterparts described in previous publications. The device can generate water in remote locations on-demand using sunlight-during the day and low-grade heat source such as a candle or cigarette lighter during night-time. The device weighs ~1.1 kg with a foot-print of Ø11x26 cm (similar to a 1-2 L water bottle) and is constructed from commercially available materials such as Aluminum, PMMA, glass etc. The device is targeted for use by remote communities as well as the lucrative outdoor- &

adventure-sports market, wherein the goal is to ensure fast generation of water using a compact ‘bottle shaped’ device in areas with no access to potable water.

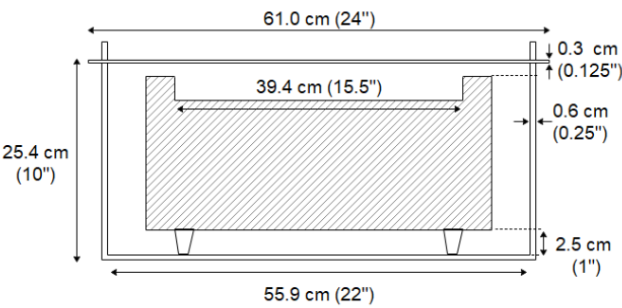

Although the field of MOF-based AWH devices is relatively new and in an exploratory phase, two major bottlenecks in deployment of these devices are: **1)** Low water yield from bulky devices, and **2)** High cost of sorbent. Manufacturing cost of sorbents can be lowered by choosing MOFs whose starting materials are low-cost and commercially available. We strongly believe that a compact design for AWH device coupled with low cost of manufacturing would be key for widespread deployment and a successful commercial product.

6.2. Results and Discussion

The overarching goal of this chapter is to present a novel concept for a compact and affordable AWH device capable of on-demand generation of water using solar energy in an arid or semi-arid environment. Our device uses a coating comprised of MOF along with a binding agent (such as Polysiloxane or graphite) as the active material for sorption, hence the device is referred to as the ‘MOTTLE’ (MOF-based Water Capture Bottle). For the purposes of evaluating performance metrics of the MOTTLE, we use the stellar MOF termed $Ni_2Cl_2(BTDD)$, which delivers a gravimetric uptake capacity of 0.82 g/g (g of water per g of MOF) below 30% RH.⁶² **Table 6-1** summarizes key features of MOTTLE compared to existing AWH devices.

Table 6-1 Comparing key attributes of existing AWH device and the MOTTLE

Key Characteristic	Previous Prototype ⁵⁷	MOTTLE
Device Size (cm)	61x61x26 (device) and 91x91x31 (enclosure)	Ø11x26
Approx. device weight (kg)	~ 12	~ 1.1
MOF/Binder loading	450 g (MOF-303) + 150 g (Graphite)	174 g $Ni_2Cl_2(BTDD)$ + 58 g (Siloxane Binder)
Multiple AWH cycles (24 hours)	Yes (Extra battery, heater, fan)	Yes
Water Yield per AWH cycle and Device Productivity	0.175 L/kg (<i>MOF-303</i>) and 1.3 L/kg/day	0.82 L/kg ($Ni_2Cl_2(BTDD)$)
Construction Materials	PMMA, PS Foam, Wood, Al	PMMA, Al, Glass

Modularity	No	Yes (Standalone Water Bottle)
Schematic of the Device		

We followed a systematic product design methodology during the course of concept generation, detailed design and understanding the value proposition of the product. The following technical section is divided into two segments: **1) Device operation during day- and night-time, 2) Computational Models, and 3) Device fabrication and assembly.**

6.2.1. Device Operation

The MOTTLE comprises of two main modules, the moisture battery, which holds the MOF coating, and an external case that encloses the battery. The moisture battery comprises of an aluminum base-plate with 78 threaded circular holes (2.84 mm ID) which accommodate threaded aluminum rods (203 mm long). The Al rods comprise of 1.5 mm thick sorbent coating (MOF + binder). The moisture battery is designed to hold 312 cm³ of sorbent, equaling 174 g of MOF along with 58 g of binding agent (3:1 ratio by mass). The resulting powder particle density is 0.74 g/cm³ (Equation 1), which is the ideal value for moisture transfer.²¹⁹ The geometry of the battery was chosen to facilitate max sorbent loading with a large surface-to-volume ratio in order to facilitate faster heat and mass transport processes. The Al components in the battery are light-weight, and durable with good thermal properties compared to the stainless steel counterparts. The external case is made from clear PMMA (Polymethyl methacrylate) which has a high melting point (160°C), highly IR transparent, and shatter-resistant.⁵⁷ The inner diameter of the enclosure holds a solar heat pipe (1.5 mm thick borosilicate glass) coated with a solar absorptive layer that ensures efficient absorption of incident solar radiation and transfer of heat to the moisture battery, which facilitates faster release of moisture accelerating the water-vapor release cycle. The outer walls of

the PMMA enclosure act as the condenser and provides surface for heat transfer with the surroundings. The enclosure has an annular cavity (460 mL) which stores the condensed water that can be collected for use after the release cycle is complete. **Figure 6-1** and **Figure 6-2** provide schematics for the moisture battery and the external case (condenser) module.

$$\rho_{Sorbent} = \frac{m_{Sorbent}}{\frac{m_{MOF}}{\rho_{MOF}} + \frac{m_{binder}}{\rho_{binder}}} = \frac{500 \text{ g}}{\frac{375 \text{ g}}{0.7 \text{ g.cm}^{-3}} + \frac{125 \text{ g}}{0.9 \text{ g.cm}^{-3}}} = 0.741 \text{ g.cm}^{-3} \dots \text{(Equation 6-1)}$$

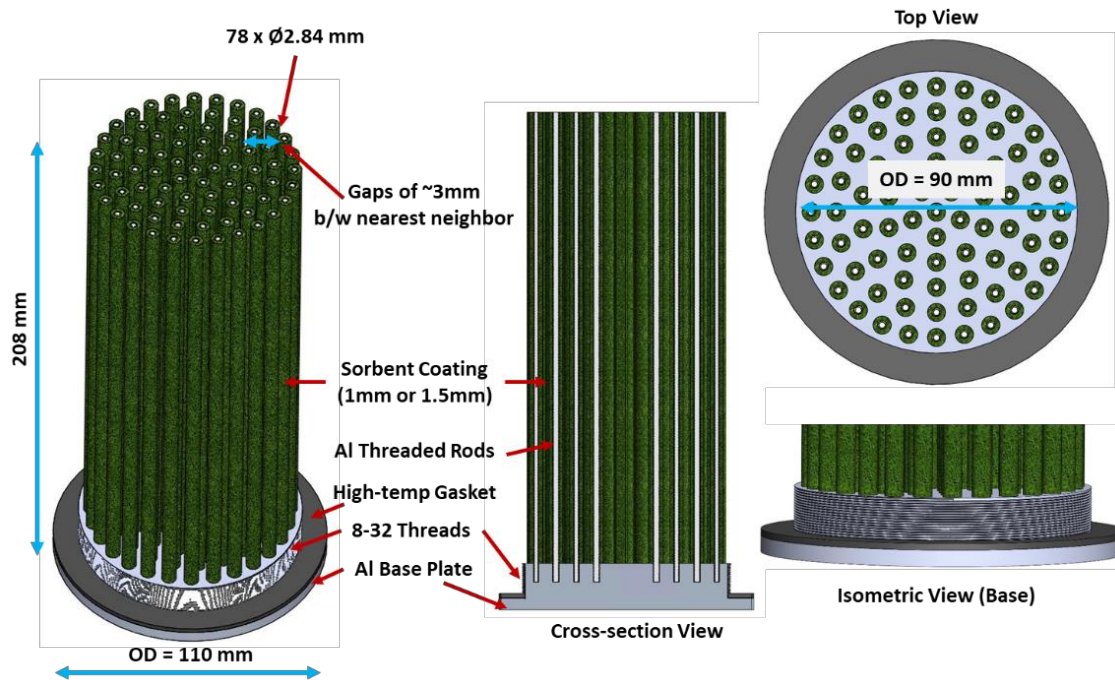


Figure 6-1 Moisture Battery with sorbent coating

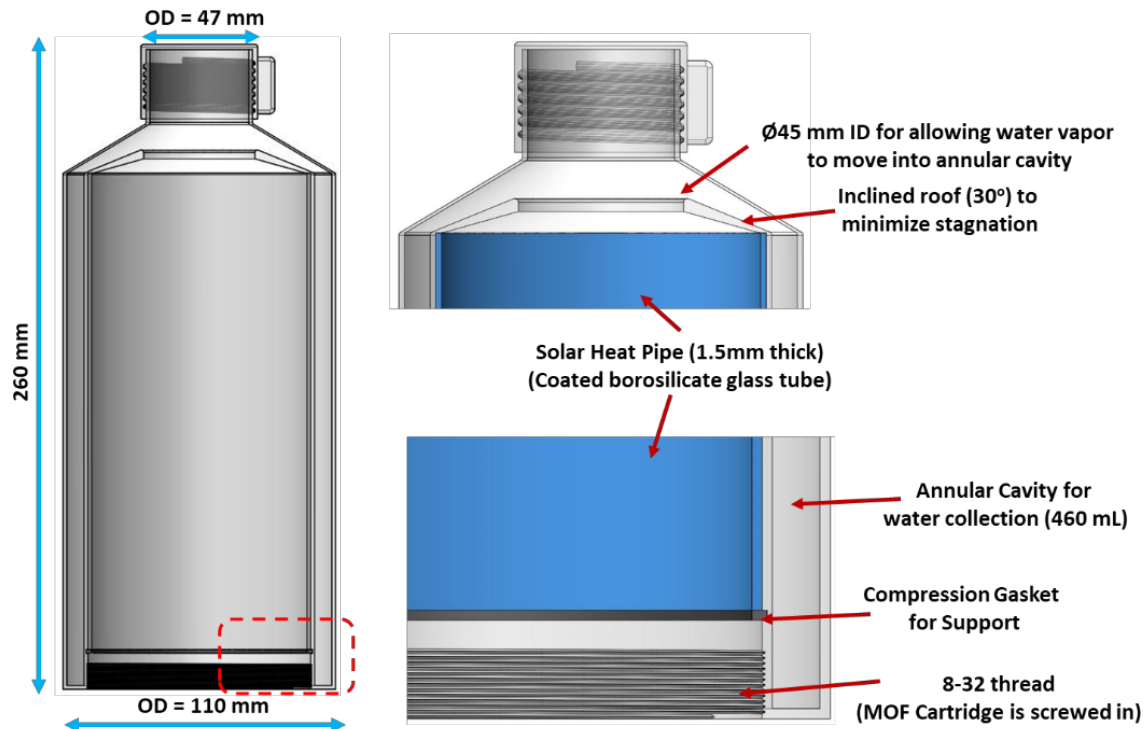


Figure 6-2 External case or enclosure (condenser).

The water harvesting cycle (WHC) for the MOTTLE is similar to the existing sorbent-based AWH devices. **Figure 6-3** shows the WHC comprising of capture and release cycles. The capture cycle starts with exposure of unsaturated MOF battery to ambient air, wherein MOF adsorbs the water-vapor in the pores. The saturation of the MOF at a given RH can be estimated from the water adsorption isotherms; large uptake values at low RH can be achieved in hydrolytically stable MOFs with large pore volumes and hydrophilic pore environments.²²² The saturated MOF battery is inserted into the external case and locked using 8-32 screw threads provided at the bottom of the Al base-plate. During day-time operation, exposure to sunlight heats up the battery leading to release of water-vapor. The hot humid air is subsequently cooled down when it comes in contact with the outer wall of the external case (or condenser module), in our case by ambient cooling, to its dew point that results in liquefied water collected in the annular cavity of the external case. The collecting cycle (i.e. release of water-vapor and condensation) continues in the MOTTLE until the MOF is unsaturated. The unsaturated moisture battery is now unscrewed from the external case and exposed to ambient air to saturate it with water-vapor and the next water harvesting cycle continues.

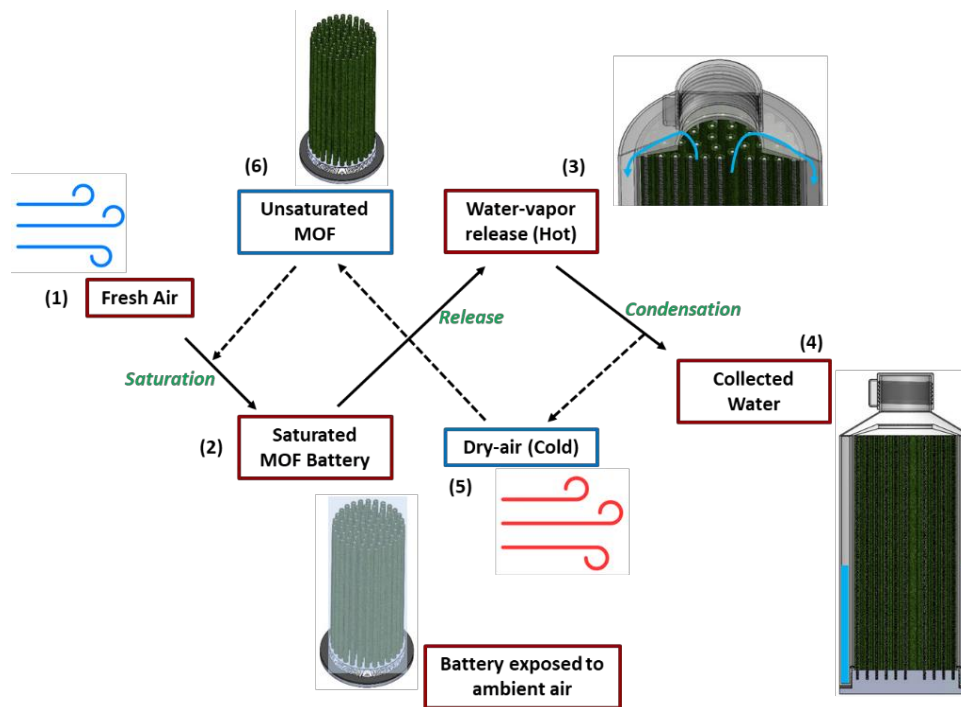


Figure 6-3 Water harvesting cycle (WHC) composed of water-vapor capture and release cycles. Solid arrows indicate saturation of MOF battery and release of vapor when heated, which condenses to water collected in the external case. Dotted arrows indicate exposure of unsaturated MOF battery to fresh ambient air for adsorbing atmospheric water-vapor.

Existing AWH devices^{57, 221} that only rely on sunlight for operation are limited to one WHC per day; however these devices can be equipped with a solar panel to power an electric heater, and a fan to speed up the cycles that can improve the productivity of the device, but make the overall process economically unattractive.⁶² In order for our MOTTLE to seamlessly continue water production during night-time, the WHC can be initiated using low-grade heat sources such as a candle or a cigarette lighter which are compact and can be easily carried by the user, unlike a bulky solar panel that powers a heater and a fan. During night-time operation of the MOTTLE, the heat source is applied to the Al base-plate of the moisture battery which results in temperatures ranging from 120°C closer to the base-plate to 60°C at the far end of the battery in 20 min. Additional details on the heat-transfer model using a heat-source are provided later in the chapter, while modelling heat-transfer using ambient sunlight is no covered in the present work. The external heat sources should be carefully chosen to achieve temperatures below 150°C in the battery to facilitate faster harvesting cycles without degrading the MOF structure.⁵ Previous studies^{57, 219, 221}

have demonstrated that heating MOFs upto 70°C is sufficient for release of water-vapor. The external case made from PMMA (acting as a thermal insulator) is not heated and exposed to ambient air (ideally 15°C-30°C), which creates a temperature gradient of > 40°C in the MOTTLE; this temperature difference is sufficient to create high humidity ratio (> 94% RH) required to condense large quantities of water. **Figure 6-4** illustrates day- and night-time operation of MOTTLE using sunlight & external heat sources.

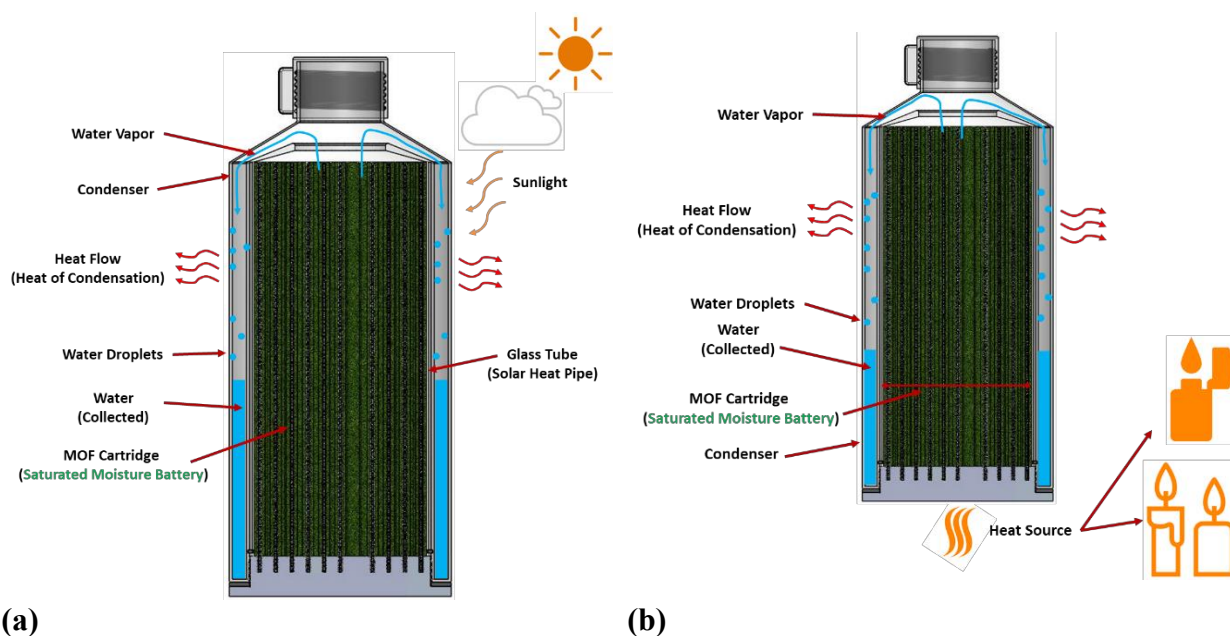


Figure 6-4 (a) Day-time operation of MOTTLE and (b) Night-time operation of MOTTLE

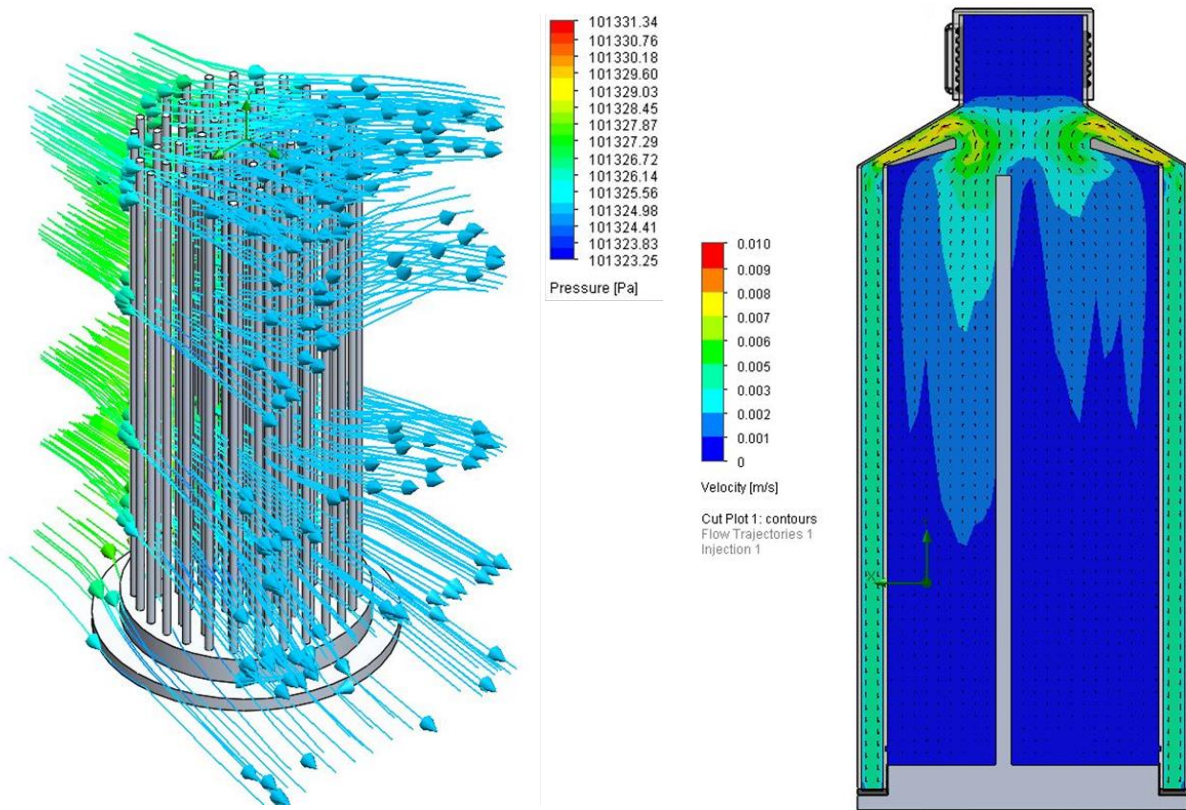
The compact design of MOTTLE limits the total amount of MOF loading in the battery, which in turn reduces the water yield per harvest cycle. However, faster harvest cycles can essentially result in a similar or better productivity (liters of water per kg of MOF per day) compared to existing AWH prototype devices. Accurate modelling of WHC in a device is complicated as it depends on *material properties* (uptake capacity, pore sizes, adsorption enthalpy, hysteresis etc.) and *component-level properties* (packing porosities, MOF layer thickness, vapor transport, inter/intra-crystalline diffusivities, thermal conductivity etc.).²¹⁶ Logan et al.²²² evaluated adsorption/desorption kinetics for a few water stable MOFs by cycling them from 30-70% RH. They found Zr based MOF-808 with an uptake capacity of 0.7 g/g, completes an uptake/release cycle in 120 min for a 1 mm layer thickness resulting in a productivity of 8.66 L/kg/day, while a 2 mm layer thickness of MOF completed the uptake/release cycle in 220 min. We present a case below for estimating productivities in our MOTTLE. If we use a 1.5 mm thick MOF-808 coating

(~184 g of total MOF loading) and assume 180 min for completing a single uptake/release cycle using low grade heat source (not sunlight)—then a continuous operation of 24 h would result in a productivity of ~1.04 L/kg/day—fairly close to the values reported by Fathieh et al.⁵⁷ The efficiency of the collection cycle determined in the ratio of mass of collected water to the mass of MOF used in the battery is usually dependent on the MOF used and the temperature difference between the battery and condenser module. Fathieh et al. reported the collection cycle efficiencies to be above 75% for MOF-801, MOF-303 and Zeolite 13K, which translates to >75% of the moisture released is converted to drinkable water in the condenser. This represents a significant improvement achieved by a compact device over its bulky counterparts. If $\text{Ni}_2\text{Cl}_2(\text{BTDD})$ is used assuming other factors remain the same the productivity is ~1.2 L/kg/day owing higher gravimetric uptake capacities and steep uptake at 30% RH.⁶¹

Our design philosophy for the MOTTLE closely follows the recommendations by LaPotin et al.²¹⁶ which describe strategies to minimize resistance to heat transfer and improve vapor transport in the battery as well as in the internal voids of the device, that help improve productivity parameters. Sorption kinetics of the moisture battery depend on intra-crystalline diffusion (within the adsorbent crystals) and inter-crystalline diffusion (within the bed/coating). While smaller crystals can lead to faster sorption kinetics within the crystals, it inevitably increases the resistance in a packed layer at high packing densities. Layer thickness of the sorbent has to be optimized for a given MOF/binder as inter- and intra-crystalline vapor transport are interrelated. In our device, for $\text{Ni}_2\text{Cl}_2(\text{BTDD})$ MOF, a 1 mm layer thickness results in 103 g of MOF loading, while 1.5 mm thickness results in 174 g of total loading which significantly improves the water yield per cycle. For thickness beyond 2 mm, the total sorbent loading would be >230 g which further improves the water yield per cycle (L/kg), however inter-crystalline transport resistance starts to dominate leading to longer cycle times thereby reducing the device productivity (L/kg/day). Owing to low thermal conductivities exhibited by MOFs (usually 0.4-1 W/(m.K)), increasing the sorbent layer thickness inadvertently increases the length of thermal transport thereby delaying the cycle time.²²³ Tradeoffs associated with choosing the specific MOF, coating thickness, & surface area-to-volume ratio should be judiciously considered in order improve device productivity.

6.2.2. Computational Models

Operational feasibility of the MOTTLE was evaluated using CFD (SOLIDWORKS) and heat-transfer (COMSOL) models to refine the concept before prototyping and real-world tests. Flow simulation package in SOLIDWORKS characterizes fluid flow patterns in internal voids as well as over external features, which help understand vapor transport during release cycle in the device cavities and pressure/velocity gradients in the moisture battery that is exposed to ambient air during saturation.



(a) **Figure 6-5** (a) Pressure gradients over moisture battery when exposed to ambient air (6 mph wind speed) at 50% RH and 298 K. (b) Cross-section of MOTTLE showing velocity field in cavities, when water-vapor is released at 40 mg/s.

During the saturation phase, the moisture battery has to be disassembled from the device and exposed to ambient air. **Figure 6-5a** illustrates pressure gradients over the moisture battery when exposed to ambient air at 6 mph wind speed conditions, 298 K and 50% RH, which constitute

pleasant weather conditions. No significant pressure drop is predicted around the Al rods, thus ensuring easy access of ambient air to the MOF coating. In our MOTTLE, a total loading of 174 g of $\text{Ni}_2\text{Cl}_2(\text{BTDD})$ MOF (1.5 mm thick coating), would require 355 L of air at 50% RH for complete saturation; hence its necessary to allow easy access of air to all Al rods for quicker saturation. During the release cycle, water-vapor should be quickly transported to the outer walls of the external case without any stagnation zones; **Figure 6-5b** illustrate velocity fields existing in the internal cavities of the MOTTLE during the release cycle. The water-vapor release rate considered in the model was 40 mg/s (144 mL per hour), which represents the time taken for completing one release cycle. The region adjacent to the bottom of the battery sees lower velocities during the earlier stages of release cycle, however no stagnation zones exist in the internal cavities except in the region adjoining the bottle cap.

It is crucial to model the temperature distribution achieved in a MOF coated Al rod (as a function of the rod length), using off-grid heat sources such as a candle or cigarette lighter during night-time operation. This data helps us understand the operational feasibility of the device when using low-grade and compact heat sources. Models to evaluate radiation heat transfer using sunlight are not considered in the current work. We assume a simplified model of the moisture battery, wherein we consider one MOF coated Al rod that is heated using a cigarette lighter (**Figure 6-6**), while thermal properties for materials are provided in **Table 6-2**. The heat flux from a cigarette lighter is estimated to be 63 kW/m^2 , which is applied at the bottom of the base-plate.²²⁴ We can approximate the base-plate as a collector of heat, which is then transferred to the individual rods; the heating power available per rod is calculated to be $\sim 5 \text{ W}$ (Equation 6-2). The Al rod is modeled as a 2D axisymmetric geometry and solved using 'heat transfer in solids' module in COMSOL. A convective heat loss boundary condition ($h = 5 \text{ W}/(\text{m}^2\cdot\text{K})$) is applied for the outer edges of the MOF coating, while the heat input is applied to the base of the rod. **Figure 6-7** shows temperature distribution in the rod using a 3D slice-plot. Temperatures in the range of 59°C - 120°C are achieved and sufficient for quick release of water-vapor.²²¹ We determined that it took ~ 15 min for temperature to equilibrate in the rod based on the time-dependent studies conducted. Shorter the time taken to reach set-point temperatures, quicker is the water-vapor release cycle that helps improve device productivity parameters.

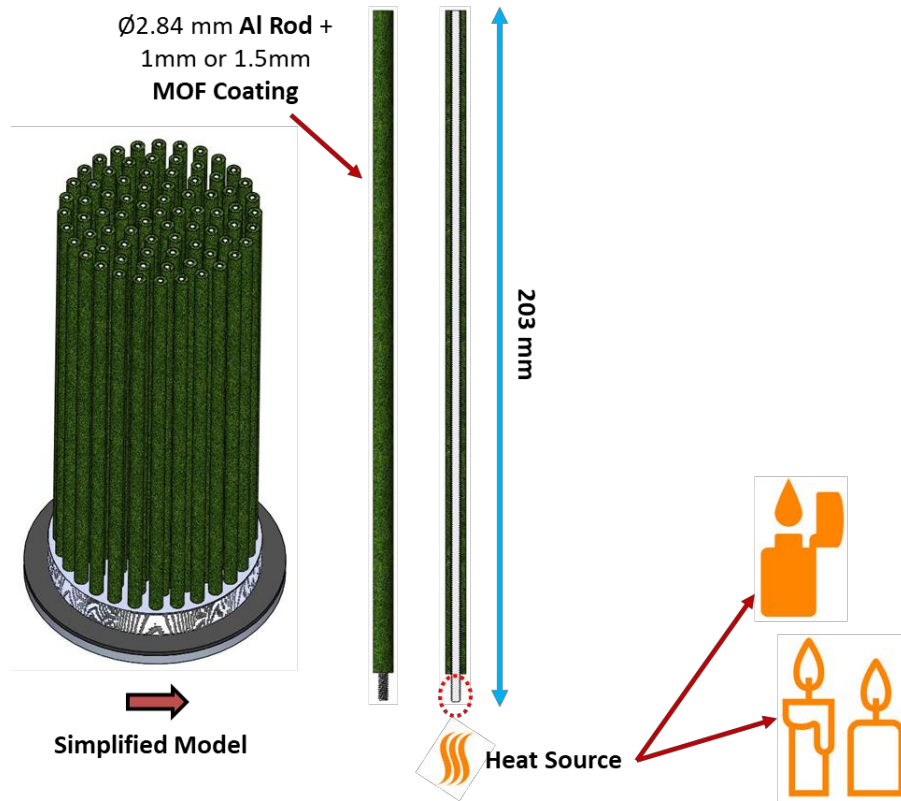


Figure 6-6 A simplified heat transfer model for estimating temperature distribution in the MOF coated Al rod

Table 6-2 Thermal properties for Al and MOF/Binder coating used in the model.

Material	Heat Capacity (C_p)	Thermal Conductivity	Density
Aluminum	900 J/(kg.K)	238 W/(m.K)	2700 kg/m ³
MOF + Binder	850 J/(kg.K)	0.5 W/(m.K)	1100 kg/m ³

Calculation for power input (W) available per Al rod

$$Power_{Rod} = \frac{Area_{Base-Plate} \times (Heat\ flux)}{\#\ of\ rods} \dots \text{(Equation 6-2)}$$

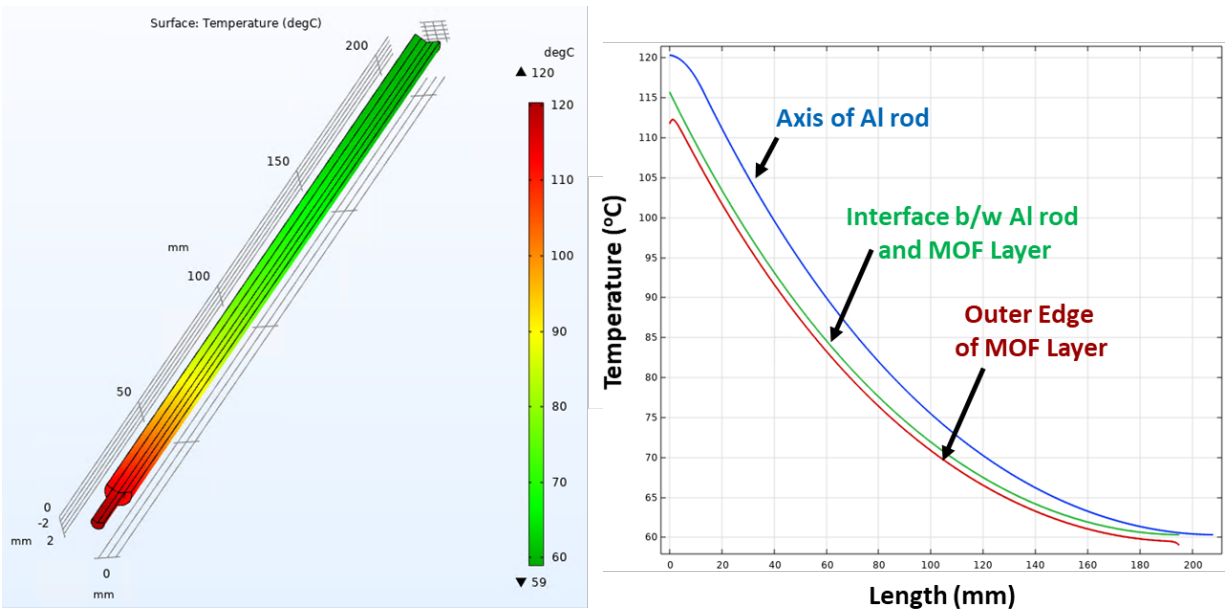


Figure 6-7 3D slice-plot showing temperature distribution in an Al rod with 1.5 mm MOF coating

6.2.3. Device Fabrication and Assembly

In order to fulfill the vision of a lost-cost and sturdy device, the MOTTLE uses commercially available construction materials such as Aluminum, PMMA, and borosilicate glass, which are durable and improve performance parameters such as better thermal conductivity, improved mass transport, and high IR transmissivity. The external case made from PMMA has a 1.5 mm uniform thickness and can be injection molded by 3rd party bottle manufacturers. The cap enclosing the case is also made from PMMA with SP400 finish and L-8 thread specification (ASTM D2911), offering a leak-proof configuration to prevent loss of water-vapor escaping the device during release cycle. The bottom part of the external case has 8-32 thread specified wherein the moisture battery can be inserted and locked by screwing into the case. The inner wall of the external case has a solar heat pipe (1.5 mm thick, 190 mm long borosilicate glass), whose inner diameter is coated with a solar absorptive paint (Pyromark 2500) which absorbs incident solar energy and efficiently transfers it to the moisture battery during the day-time water-vapor release cycles. Solar heat tubes are commonly used in solar water-heaters and often result in temperature ranges of 55°C-90°C on a clear day.²²⁵ The heat pipe is locked in place using a compression gasket located at the bottom of the external case. The external case has an inclined roof (30°) connected to Ø45 mm opening that leads to the annular cavity (460 mL), where condensed water is collected. This

design ensures efficient transport of water-vapor released by the MOF layers that are located on the outer periphery of the battery.

The moisture battery functions as a reservoir for storing water-vapor into the porous sorbent and releases the vapor when sorbent is heated. The skeletal framework of the battery is made from low-cost 6061 Al alloy which is widely used to make light-weight & durable components that can be easily machined. Al also offers high thermal conductivity (205 W/(m.K)) resulting in fast heat transfer that accelerates the water-vapor release cycles improving overall device productivity (L/kg/day). The inner diameter ($\text{Ø}90$ mm) of the base-plate is 13 mm thick and has 8-32 threads (8 mm of threaded length) machined on the circumference that locks the battery into the external case. The base-plate has 78 threaded holes (4-40 threads, 8 mm deep) which can accommodate $\text{Ø}2.84$ mm Al rods (203 mm long). The base-plate has a 5 mm thick flange of $\text{Ø}110$ mm, on top of which a high temperature gasket can be inserted. The gasket sits at the interface between external case and the battery, preventing any damage to the PMMA case during high temperature exposure of the base-plate. The MIT central machine shop would be employed to machine the base-plate, while threaded Al rods and gasket are commercially available. The sorbent coating process will be developed based on existing studies^{56, 226} and implemented for the MOTTLE. The base-plate with the threaded rods will be dip-coated using a slurry of MOF and the binding agent, followed by heating it at 120°C for 2 h to remove water and the volatile contents of the binder. The process will be repeated 3 times to get a 1.5mm thick coating on the Al rods. The threads provide additional support for the coating and act as fins to increase the rate of heat transfer during the release cycle.

7. Conclusions and Outlook

7.1. Conclusions

This thesis focuses on developing a continuous flow reactor platform for energy- and cost-efficient synthesis of porous materials (MOFs and Zeolites), which have been demonstrated for use in numerous applications such as atmospheric water capture, catalysis, gas storage, carbon capture, separation, ion exchange, sensors etc. Although flow reactors were used for accelerated synthesis of MOFs over the past decade, most of these studies employ a PTFE or a steel tubing immersed in an oil bath (or a sand bath) that is heated using a hot plate as the heated reaction zone. These setups are relatively easy to setup for a laboratory-scale synthesis, however they suffer from large gradients in temperature distribution in the bath, which could affect crystallization reactions along with the physicochemical properties of the synthesized product. Moreover, scaling-up the flow reactor by enlargement of the tube ID or via parallelization of reactors cannot be achieved using a temperature bath for a pilot-plant scale or industrial scale manufacturing. The flow reactor platform presented in this work is designed to offer precise control of temperature, pressure along with the capability to process reaction mixtures with a wide range of pH, viscosity, and density. Traditionally used batch reactors for solvothermal synthesis of MOFs suffer from intrinsic inefficiencies related to poor heat and mass transfer, which affect their scalability and product quality. The reactor is compact and can be easily scaled-up based on the desired production target for a specific MOF or a zeolite. The use of commercially available bulk materials such as Aluminum, PTFE tubing and high-temperature insulation ensured low cost for building the reactor. The flow reactor helped with process intensification of MOF synthesis along with fast screening of the chemical reaction space parameters, thereby lowering the time required for optimization of synthesis, lower use of solvents and improved process productivity.

My work began with exploring the synthesis pathways for Zr-based MOFs, such as MOF-808 in the continuous flow reactor. MOF-808 has demonstrated to have an outstanding hydrothermal and chemical stability with a potential for post-synthetic modification, thereby making it a promising candidate for use in catalysis, adsorption, separation, drug delivery and others. MOF-808 features coordinatively unsaturated open metal sites at the Zr-oxo cluster (SBU) and large cavities $\sim 18.4 \text{ \AA}$ along with the BET surface area of $2000 \text{ m}^2/\text{g}$ – all the necessary aspects for their use in

applications such as methane-to-methanol conversion, broad-spectrum heavy metal trap among others. The batch synthesis for MOF-808 involves heating the reaction mixture at 130 °C for 48 h leading to lower process productivities. Critical process parameters such as residence time, linker concentration and volumetric ratios of modulator and solvent were rapidly screened to map the chemical design space of MOF-808 and their influence on product attributes such as crystallinity and surface area. Optimized synthetic conditions in flow used concentrated reaction mixtures that led a reduction in the use of DMF by ~84% and formic acid by ~67% on volumetric basis – highlighting the direct benefits of flow synthesis in lowering reagent costs and a greener process. Highly crystalline monodisperse MOF-808 nanoparticles were synthesized in a residence time of 5 min in flow compared to 48 h in batch, resulting in a productivity of $95,155 \text{ kg}\cdot\text{m}^{-3}\cdot\text{day}^{-1}$, which represents a record-high two order of magnitude increase than batch ($335.5 \text{ kg}\cdot\text{m}^{-3}\cdot\text{day}^{-1}$). The interplay between factors such as the amount of modulator, reagent concentrations, and reaction conditions significantly affect nucleation and crystal growth rates, and should be judiciously balanced to generate desired product attributes. We also report one of the first comprehensive techno-economic analysis (TEA) to evaluate cost drivers and energy and mass balances involving lab-scale synthesis of MOFs. Under a continuous production environment, solvent costs dominate the synthesis costs and a further reduction in cost structure can be achieved by minimizing the use of solvents or employing an efficient solvent recycling strategy. Minimum cost of manufacturing MOF-808 under a laboratory-demonstrated flow synthesis route was \$3/g, an order of magnitude lower compared to a handful of commercial MOFs priced upwards of \$30/g. The methodology used in the TEA is generally valid for other MOFs and highlights avenues for critical assessment and optimization of synthesis routes to manufacture MOFs at low-cost, enabling their widespread use in revolutionary technologies.

Following the optimization of MOF-808 in the flow reactor, it was necessary to understand the kinetics of crystallization that would help in achieving tailored physicochemical properties of the MOF for real-world applications. The use of microfluidic flow reactors offers the ability to explore a wide range of synthetic parameters in a short amount of time with minimal consumption of reagents making them ideal to extract kinetic information. We developed a rapid sampler module in-house that is attached to the reactor outlet facilitating easy collection of large number of samples by quenching the reactions at any residence time. The rate constants for nucleation k_N and growth k_G were obtained by non-linear fitting of crystallization curves with the Gualtieri model, which is

well suited for evaluating solution-mediated transformation reactions. The crystallization curves monitor evolution of crystallinity with time and are generated by integration of peak area corresponding to Bragg reflections from (400). The values for rate constants both k_N and k_G increased by more than 5-fold with temperature (110 °C to 150 °C) and with linker concentration in the reaction mixture (1X to 3X). For all reaction conditions explored, $k_N < k_G$ implying that the nucleation process is slower than crystal growth and the rate-limiting step. The nucleation sites in the reaction mixture are not directly visible in the diffraction experiments and are estimated by the Gualtieri model by defining the probability of nucleation P_N (total number of nuclei N present at time t). Activation energies for nucleation $E_A(N)$ and growth $E_A(G)$ determined from Arrhenius plots were $64.7 \pm 4 \text{ kJ.mol}^{-1}$ and $59.2 \pm 5 \text{ kJ.mol}^{-1}$ respectively, while the activation energy calculated from the Avrami-Erofeev model using the overall rate constant k was $57.3 \pm 4 \text{ kJ.mol}^{-1}$ which is in close agreement with the Gualtieri model. My work provides the first account for the use of flow rates in the reactor as a simpler tool for tuning the crystal sizes of MOFs with a narrow distribution. Average crystal sizes of ~105 nm were achieved in a 5 mL reactor, ~140 nm in a 9 mL reactor, and ~180 nm in a 16 mL reactor. For a constant residence time across all reactor configurations, an increase in the flow rate enhances flow-mediated transport of precursor species to the nucleation sites, thereby accelerating the crystal growth, accompanied by a simultaneous reduction in the nucleation rate due to faster consumption of reagents—the phenomenon responsible for CSD trends seen in our flow reactor. The results presented in this work allow for a better understanding of nucleation and crystal growth kinetics of self-assembled porous frameworks along with additional degrees of control offered by flow reactors to synthesize MOFs with desired physiochemical properties for real-world applications.

Building on the process intensification achieved in the flow reactor, we then focused on using the reactor platform to address imminent challenges such as global shortage of clean drinking water. In dry climates (RH<50%), atmospheric water capture (AWC) offers an alternative solution given that the atmosphere holds nearly 1.3×10^{16} L of water: a value representing ca. 0.3% of the global fresh water supply. The ideal AWC sorbent material must have large gravimetric capacities, steep water uptake characteristics in a narrow RH range, and complete water release with minimal temperature swings over thousands of cycles. Among a wide list of sorbent materials, the $\text{Ni}_2\text{Cl}_2(\text{BTDD})$ MOF has shown optimal water sorption performance under low relative humidity conditions, but its potentially high production costs, stemming in part from its lengthy multiday

batch synthesis, has hindered widespread implementation. We developed a continuous manufacturing process for $\text{Ni}_2\text{Cl}_2(\text{BTDD})$ that can achieve higher yields, reduce solvent use (by 50% on volumetric basis), and drastically faster crystallization times (1 hour) in comparison to the batch process (48 hour) – leading to a 3-fold increase in process productivity ($\text{kg}_{\text{MOF}}/\text{m}^3/\text{day}$). We developed CFD models to evaluate trade-offs associated with the enlargement of reactor tubes for higher production rate while losing the benefits of small system dimensions in the flow reactor must be judiciously considered before scale-up of the system. A target scenario for synthesizing 1 kg of $\text{Ni}_2\text{Cl}_2(\text{BTDD})$ per month with continuous operation was assessed. The heat transfer models suggested the use of 5 identical reactors of 3/8" ID operated in parallel to achieve the production target. The traditional batch synthesis procedure employs a 1000 mL glass bottle, producing 260 mg of $\text{Ni}_2\text{Cl}_2(\text{BTDD})$ from 528 mL of reaction mixture heated at 100 °C for 48 h. A scale-up of the synthesis to manufacture 1 kg of $\text{Ni}_2\text{Cl}_2(\text{BTDD})$ would involve the usage of ca. 3847 bottles of 1000 mL capacity, each containing ca. 528 mL of reaction mixture. From an operational standpoint, replacing 3847 bottles of 1 L capacity with one large volume reactor vessel, for example, a 3500 L vessel with ~58% of its volume filled would be ideal; however, it may require re-optimization of reaction conditions due to their poor translation with change in batch reactor volume. This work adds critical facets to the growing body of research suggesting that the synthesis of MOFs in flow reactors offers unique opportunities to reduce production costs and offers easier pathways for scaling-up the manufacturing of MOFs.

7.2. Outlook and Future Work

Continuous flow reactors have been emerging as new paradigm for high-throughput synthesis of ordered porous materials. As demonstrated by this work, the flow platform is promising for large-scale production of MOFs, which would enable their use in industrial applications. Current global market size of MOFs is ~\$70 million as of 2019 and is expected to grow at 34% CAGR until 2024 (~\$410 million). There are ca. ~10's of MOFs which exhibit excellent hydrothermal and chemical stability under desired operational conditions, which would be outstanding candidates for applications such as high API loading in drug delivery devices, CO_2 separation and storage, low pressure CH_4 storage in automotive applications, energy-efficient heat pumps, harvesting fresh drinking water from atmosphere and others. A handful of MOFs are commercially available with a quoted market price of >\$30/g, while any successful application would require MOF prices to be lower than \$0.2/g. Based on our techno-economic model, ~80-85% of the synthesis cost

originate from the raw materials such as solvents, and organic linkers, while ~15% of the cost originates from energy & equipment cost. We have successfully synthesized and optimized a few industrially relevant MOFs (MOF-808, Ni₂Cl₂(BTDD), HKUST-1, MFU-4l, V-MIL-101, and MIL-100 (Fe)), resulting in reduced amount of solvents, with improved yield, shorter crystallization times and improved process productivity. We firmly believe that the use of flow-reactors for scaled-up production of promising MOF candidates would lead to reduced synthesis costs aiding their quicker adoption in industrial applications. The key translation piece for the use of MOFs in revolutionary industrial applications is the ability to manufacture at desired scale, purity and satisfy the market price requirements.

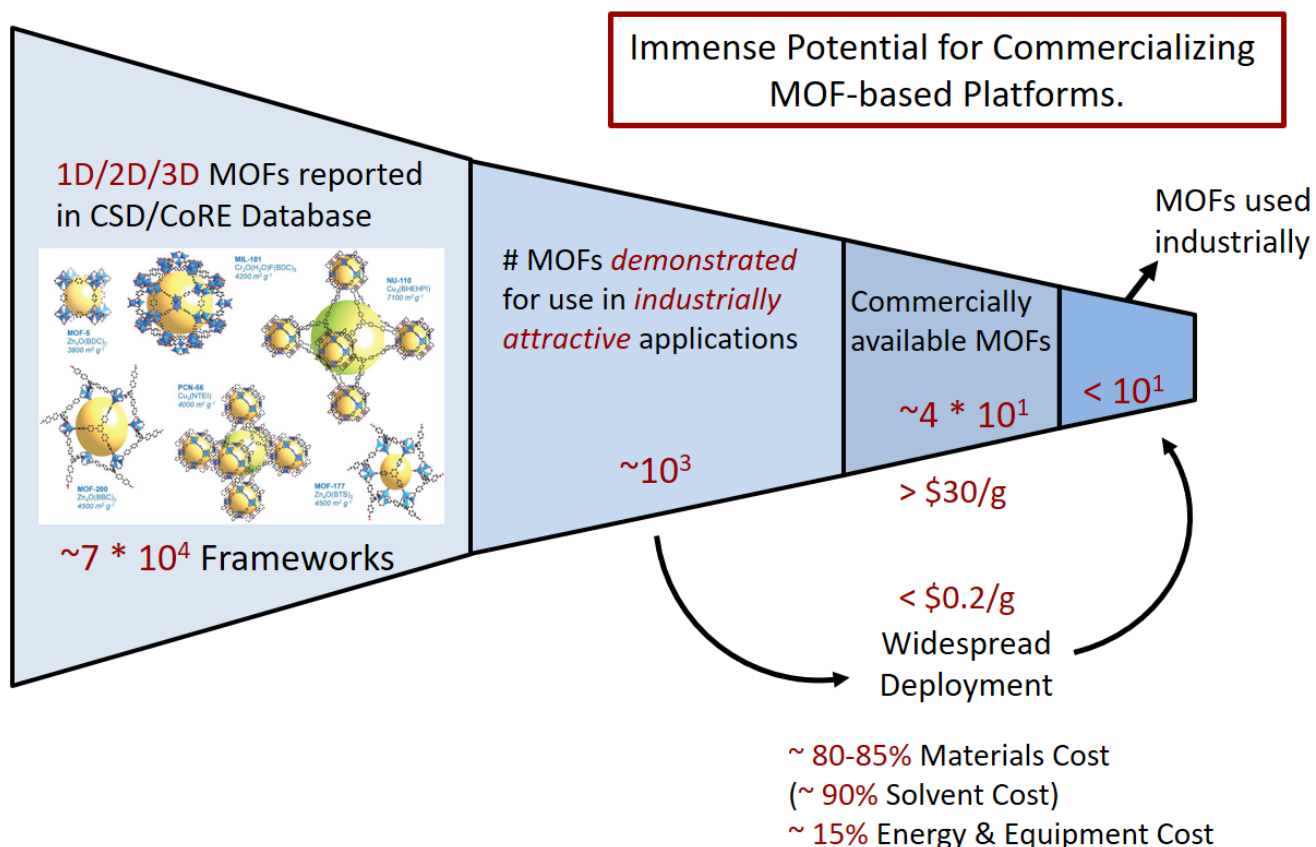


Figure 7-1 The current landscape for MOF-based industrial applications and the immense potential for widespread deployment of MOFs with reduced synthesis costs.

7.2.1. Future Work

Building upon this thesis, the future work can be divided into three main parts.

- Automation of the reactor platform: The laboratory-scale flow reactor developed in this thesis is a semi-automated platform which can be used as a ‘proof of concept’ to develop a fully automated bench-top version in the future. The functional blocks of the automated platform are highlighted in Figure 2-11. The automated version could also incorporate machine learning and AI modules, which can substantially reduce the necessary information gathering and the manual effort required from the operator to synthesize a specific MOF/zeolite. The platform would comprise of reagents preloaded into cartridge or vessels, connected to compact reactors for crystallization. The product can be separated from supernatant downstream followed by solvent exchange and activation. The robotic platform for flow synthesis of organic compounds developed by Jensen and co-workers^{28, 227} could serve as a conceptual model for our automated platform. We can think of our platform being analogous to an automatic espresso machine that can customize the size of the beverage, the coffee beans used, and the type of drink (cortado, latte, americano, macchiato) among others. The automation of the platform is more of an engineering or a product design challenge as it involves integration of the robotic and electronic components (previously developed) into the existing flow platform.
- Scaling-up of the flow reactor: Although the progress in using flow reactors for process intensification of MOF synthesis is exciting, the full potential of the continuous flow reactors can be realized upon their successful scale-up for industrial scale production. There are a few examples of scaling-up the flow reactors for improved process productivity of the liquid phase reactions in the pharmaceutical industry,²¹¹ however, there are no case-studies for using flow reactors to perform solid forming reactions. The issue of solids (formed during crystallization reactions) clogging the tubes of the flow reactor is one of the most common reasons why scaling-up of the PFR and their implementation for industrial scale production has been slow. The lab-scale flow reactor (1/16” tube ID) did not suffer from any clogging issues during MOF crystallization; it is often hard to predict if a scaled-up flow system (upto 1/2” tube ID) would suffer from any hydrodynamic failure owing to clogging of solids. For zeolite synthesis, many of the gels injected into the reactor did clog the tubes irrespective of a single-phase flow or a biphasic slug-flow regime. Most industrial crystallization processes employ CSTRs and batch reactors for large-scale production (metric tons scale) of solid forming reactions.

- Compact device for AWC (MOTTLE): The novel design presented in this thesis for a compact sorbent-based AWC device needs to be validated for its real-world performance. The current design can be further refined using computational models for evaluating the productivity using only sunlight as a heat source for regeneration. The prototypes can be built relatively easily and tested in a lab environment using off-grid heat sources (candle, cigarette lighter or something similar). Testing for the device performance in sunlight can be accomplished on campus especially on the rooftops of #3 or #66 along with sensors for measuring temperature, RH, water generated, solar insolation among others. The optimized device could cost in a range of \$50–\$80 per unit and can be attractive for the outdoors/recreational market along with communities living in remote areas with no easy access to drinking water supply.

References

1. Yaghi, O. M.; Kalmutzki, M. J.; Diercks, C. S., *Introduction to Reticular Chemistry*. 2019. doi:10.1002/9783527821099.
2. Kalmutzki, M. J.; Hanikel, N.; Yaghi, O. M., Secondary building units as the turning point in the development of the reticular chemistry of MOFs. *Sci Adv* **2018**, *4* (10). doi:10.1126/sciadv.aat9180.
3. Jiang, J.; Gándara, F.; Zhang, Y.-B.; Na, K.; Yaghi, O. M.; Klemperer, W. G., Superacidity in Sulfated Metal–Organic Framework-808. *J Am Chem Soc* **2014**, *136* (37), 12844-12847. doi:10.1021/ja507119n.
4. Rosi, N. L., Hydrogen Storage in Microporous Metal–Organic Frameworks. *Science* **2003**, *300* (5622), 1127-1129. doi:10.1126/science.1083440.
5. Howarth, A. J.; Liu, Y.; Li, P.; Li, Z.; Wang, T. C.; Hupp, J. T.; Farha, O. K., Chemical, thermal and mechanical stabilities of metal–organic frameworks. *Nature Reviews Materials* **2016**, *1* (3). doi:10.1038/natrevmats.2015.18.
6. Devic, T.; Serre, C., High valence 3p and transition metal based MOFs. *Chem. Soc. Rev.* **2014**, *43* (16), 6097-6115. doi:10.1039/c4cs00081a.
7. Kalmutzki, M. J.; Diercks, C. S.; Yaghi, O. M., Metal–Organic Frameworks for Water Harvesting from Air. *Advanced Materials* **2018**, *30* (37). doi:10.1002/adma.201704304.
8. Chen, T.-H.; Popov, I.; Zenasni, O.; Daugulis, O.; Miljanić, O. Š., Superhydrophobic perfluorinated metal–organic frameworks. *Chem Commun* **2013**, *49* (61). doi:10.1039/c3cc41564c.
9. Nguyen, J. G.; Cohen, S. M., Moisture-Resistant and Superhydrophobic Metal–Organic Frameworks Obtained via Postsynthetic Modification. *J Am Chem Soc* **2010**, *132* (13), 4560-4561. doi:10.1021/ja100900c.
10. Konstas, K.; Osl, T.; Yang, Y.; Batten, M.; Burke, N.; Hill, A. J.; Hill, M. R., Methane storage in metal organic frameworks. *Journal of Materials Chemistry* **2012**, *22* (33). doi:10.1039/c2jm32719h.
11. Boot-Handford, M. E.; Abanades, J. C.; Anthony, E. J.; Blunt, M. J.; Brandani, S.; Mac Dowell, N.; Fernández, J. R.; Ferrari, M.-C.; Gross, R.; Hallett, J. P.; Haszeldine, R. S.; Heptonstall, P.; Lyngfelt, A.; Makuch, Z.; Mangano, E.; Porter, R. T. J.; Pourkashanian, M.; Rochelle, G. T.; Shah, N.; Yao, J. G.; Fennell, P. S., Carbon capture and storage update. *Energy Environ. Sci.* **2014**, *7* (1), 130-189. doi:10.1039/c3ee42350f.
12. Dunne, P. W.; Lester, E.; Walton, R. I., Towards scalable and controlled synthesis of metal-organic framework materials using continuous flow reactors. *React Chem Eng* **2016**, *1* (4), 352-360. doi:10.1039/c6re00107f.
13. Möhle, S.; Zirbes, M.; Rodrigo, E.; Gieshoff, T.; Wiebe, A.; Waldvogel, S. R., Modern Electrochemical Aspects for the Synthesis of Value-Added Organic Products. *Angewandte Chemie International Edition* **2018**, *57* (21), 6018-6041. doi:10.1002/anie.201712732.
14. Mueller, U.; Schubert, M.; Teich, F.; Puetter, H.; Schierle-Arndt, K.; Pastré, J., Metal–organic frameworks—prospective industrial applications. *J. Mater. Chem.* **2006**, *16* (7), 626-636. doi:10.1039/b511962f.

15. Zhang, X.; Wan, K.; Subramanian, P.; Xu, M.; Luo, J.; Fransaer, J., Electrochemical deposition of metal–organic framework films and their applications. *Journal of Materials Chemistry A* **2020**, *8* (16), 7569–7587. doi:10.1039/d0ta00406e.
16. Garzon-Tovar, L.; Cano-Sarabia, M.; Carne-Sanchez, A.; Carbonell, C.; Imaz, I.; MasPOCH, D., A spray-drying continuous-flow method for simultaneous synthesis and shaping of microspherical high nuclearity MOF beads. *React Chem Eng* **2016**, *1* (5), 533–539. doi:10.1039/c6re00065g.
17. Rubio-Martinez, M.; Avci-Camur, C.; Thornton, A. W.; Imaz, I.; MasPOCH, D.; Hill, M. R., New synthetic routes towards MOF production at scale. *Chemical Society Reviews* **2017**, *46* (11), 3453–3480. doi:10.1039/c7cs00109f.
18. Wang, Z.; Li, Z.; Ng, M.; Milner, P. J., Rapid mechanochemical synthesis of metal–organic frameworks using exogenous organic base. *Dalton T* **2020**, *49* (45), 16238–16244. doi:10.1039/d0dt01240h.
19. Stolle, A.; Szuppa, T.; Leonhardt, S. E. S.; Ondruschka, B., Ball milling in organic synthesis: solutions and challenges. *Chemical Society Reviews* **2011**, *40* (5). doi:10.1039/c0cs00195c.
20. Zhang, R.; Tao, C.-A.; Chen, R.; Wu, L.; Zou, X.; Wang, J., Ultrafast Synthesis of Ni-MOF in One Minute by Ball Milling. *Nanomaterials* **2018**, *8* (12). doi:10.3390/nano8121067.
21. Friščić, T.; Reid, D. G.; Halasz, I.; Stein, R. S.; Dinnebier, R. E.; Duer, M. J., Ion- and Liquid-Assisted Grinding: Improved Mechanochemical Synthesis of Metal-Organic Frameworks Reveals Salt Inclusion and Anion Templating. *Angewandte Chemie International Edition* **2010**, *49* (4), 712–715. doi:10.1002/anie.200906583.
22. Howard, J. L.; Sagatov, Y.; Repousseau, L.; Schotten, C.; Browne, D. L., Controlling reactivity through liquid assisted grinding: the curious case of mechanochemical fluorination. *Green Chem* **2017**, *19* (12), 2798–2802. doi:10.1039/c6gc03139k.
23. Titi, H. M.; Do, J.-L.; Howarth, A. J.; Nagapudi, K.; Friščić, T., Simple, scalable mechanosynthesis of metal–organic frameworks using liquid-assisted resonant acoustic mixing (LA-RAM). *Chem Sci* **2020**, *11* (29), 7578–7584. doi:10.1039/d0sc00333f.
24. Rubio-Martinez, M.; Hadley, T. D.; Batten, M. P.; Constanti-Carey, K.; Barton, T.; Marley, D.; Monch, A.; Lim, K. S.; Hill, M. R., Scalability of Continuous Flow Production of Metal-Organic Frameworks. *Chemsuschem* **2016**, *9* (9), 938–941. doi:10.1002/cssc.201501684.
25. Liu, Z. D.; Zhu, J.; Wakihara, T.; Okubo, T., Ultrafast synthesis of zeolites: breakthrough, progress and perspective. *Inorg Chem Front* **2019**, *6* (1), 14–31. doi:10.1039/c8qi00939b.
26. Steinbacher, J. L.; McQuade, D. T., Polymer chemistry in flow: New polymers, beads, capsules, and fibers. *J Polym Sci Pol Chem* **2006**, *44* (22), 6505–6533. doi:10.1002/pola.21630.
27. Kim, H.; Nagaki, A.; Yoshida, J., A flow-microreactor approach to protecting-group-free synthesis using organolithium compounds. *Nat Commun* **2011**, *2*. doi:ARTN 264 10.1038/ncomms1264.
28. Adamo, A.; Beingessner, R. L.; Behnam, M.; Chen, J.; Jamison, T. F.; Jensen, K. F.; Monbaliu, J. C. M.; Myerson, A. S.; Revalor, E. M.; Snead, D. R.; Stelzer, T.; Weeranoppanant, N.; Wong, S. Y.; Zhang, P., On-demand continuous-flow production of

- pharmaceuticals in a compact, reconfigurable system. *Science* **2016**, 352 (6281), 61-67. doi:10.1126/science.aaf1337.
29. Yoshida, J. I.; Kim, H.; Nagaki, A., Green and Sustainable Chemical Synthesis Using Flow Microreactors. *Chemsuschem* **2011**, 4 (3), 331-340. doi:10.1002/cssc.201000271.
30. Pieber, B.; Shalom, M.; Antonietti, M.; Seeberger, P. H.; Gilmore, K., Continuous Heterogeneous Photocatalysis in Serial Micro-Batch Reactors. *Angew Chem Int Edit* **2018**, 57 (31), 9976-9979. doi:10.1002/anie.201712568.
31. Cummings, M. A.; Haaf, M.; McQuade, D. T.; Steinbacher, J.; Poe, S. L.; Moy, R., Precipitate forming reactions in a simplified microfluidic device. *Abstr Pap Am Chem S* **2006**, 231.
32. Gunther, A.; Jensen, K. F., Multiphase microfluidics: from flow characteristics to chemical and materials synthesis. *Lab Chip* **2006**, 6 (12), 1487-1503. doi:10.1039/b609851g.
33. Zhang, J.; Wang, K.; Teixeira, A. R.; Jensen, K. F.; Luo, G., Design and Scaling Up of Microchemical Systems: A Review. *Annual Review of Chemical and Biomolecular Engineering* **2017**, 8 (1), 285-305. doi:10.1146/annurev-chembioeng-060816-101443.
34. Kockmann, N.; Roberge, D. M., Harsh Reaction Conditions in Continuous-Flow Microreactors for Pharmaceutical Production. *Chemical Engineering & Technology* **2009**, 32 (11), 1682-1694. doi:10.1002/ceat.200900355.
35. Murray, P. M.; Bellany, F.; Benhamou, L.; Bučar, D.-K.; Tabor, A. B.; Sheppard, T. D., The application of design of experiments (DoE) reaction optimisation and solvent selection in the development of new synthetic chemistry. *Organic & Biomolecular Chemistry* **2016**, 14 (8), 2373-2384. doi:10.1039/c5ob01892g.
36. McKinstry, C.; Cathcart, R. J.; Cussen, E. J.; Fletcher, A. J.; Patwardhan, S. V.; Sefcik, J., Scalable continuous solvothermal synthesis of metal organic framework (MOF-5) crystals. *Chem Eng J* **2016**, 285, 718-725. doi:10.1016/j.cej.2015.10.023.
37. Basolite Pricing. Sigma–Aldrich. <https://www.sigmaaldrich.com/materials-science/material-science-products.html?TablePage=103996366> Accessed May 14, 2020. doi:<https://www.sigmaaldrich.com/materials-science/material-science-products.html?TablePage=103996366>.
38. Liu, J.; Chen, L.; Cui, H.; Zhang, J.; Zhang, L.; Su, C.-Y., Applications of metal–organic frameworks in heterogeneous supramolecular catalysis. *Chem. Soc. Rev.* **2014**, 43 (16), 6011-6061. doi:10.1039/c4cs00094c.
39. Scott, A. Semiconductor industry to begin using MOFs. <https://cen.acs.org/articles/95/i32/Semiconductor-industry-begin-using-MOFs.html> (accessed 08 June 2021).
40. Furukawa, H.; Cordova, K. E.; O'Keeffe, M.; Yaghi, O. M., The Chemistry and Applications of Metal-Organic Frameworks. *Science* **2013**, 341 (6149), 974-+. doi:10.1126/science.1230444.
41. Li, H.; Wang, K.; Sun, Y.; Lollar, C. T.; Li, J.; Zhou, H.-C., Recent advances in gas storage and separation using metal–organic frameworks. *Materials Today* **2018**, 21 (2), 108-121. doi:10.1016/j.mattod.2017.07.006.
42. Li, H.; Li, L.; Lin, R.-B.; Zhou, W.; Zhang, Z.; Xiang, S.; Chen, B., Porous metal-organic frameworks for gas storage and separation: Status and challenges. *EnergyChem* **2019**, 1 (1). doi:10.1016/j.enchem.2019.100006.

43. Pettinari, C.; Marchetti, F.; Mosca, N.; Tosi, G.; Drozdov, A., Application of metal – organic frameworks. *Polymer International* **2017**, *66* (6), 731-744. doi:10.1002/pi.5315.
44. Chen, L.; Zhang, X.; Cheng, X.; Xie, Z.; Kuang, Q.; Zheng, L., The function of metal–organic frameworks in the application of MOF-based composites. *Nanoscale Advances* **2020**, *2* (7), 2628-2647. doi:10.1039/d0na00184h.
45. Yap, M. H.; Fow, K. L.; Chen, G. Z., Synthesis and applications of MOF-derived porous nanostructures. *Green Energy & Environment* **2017**, *2* (3), 218-245. doi:10.1016/j.gee.2017.05.003.
46. Sakamaki, Y.; Tsuji, M.; Heidrick, Z.; Watson, O.; Durchman, J.; Salmon, C.; Burgin, S. R.; Beyzavi, M. H., Preparation and Applications of Metal–Organic Frameworks (MOFs): A Laboratory Activity and Demonstration for High School and/or Undergraduate Students. *Journal of Chemical Education* **2020**, *97* (4), 1109-1116. doi:10.1021/acs.jchemed.9b01166.
47. Grande, C. A.; Rodrigues, A. E., Layered Vacuum Pressure-Swing Adsorption for Biogas Upgrading. *Ind Eng Chem Res* **2007**, *46* (23), 7844-7848. doi:10.1021/ie070942d.
48. Peterson, G. W.; DeCoste, J. B.; Glover, T. G.; Huang, Y.; Jasuja, H.; Walton, K. S., Effects of pelletization pressure on the physical and chemical properties of the metal–organic frameworks Cu₃(BTC)₂ and UiO-66. *Micropor Mesopor Mat* **2013**, *179*, 48-53. doi:10.1016/j.micromeso.2013.02.025.
49. Bazer-Bachi, D.; Assié, L.; Lecocq, V.; Harbuzaru, B.; Falk, V., Towards industrial use of metal-organic framework: Impact of shaping on the MOF properties. *Powder Technology* **2014**, *255*, 52-59. doi:10.1016/j.powtec.2013.09.013.
50. Tagliabue, M.; Rizzo, C.; Millini, R.; Dietzel, P. D. C.; Blom, R.; Zanardi, S., Methane storage on CPO-27-Ni pellets. *Journal of Porous Materials* **2010**, *18* (3), 289-296. doi:10.1007/s10934-010-9378-0.
51. Moreira, M. A.; Santos, J. C.; Ferreira, A. F. P.; Loureiro, J. M.; Ragon, F.; Horcajada, P.; Shim, K.-E.; Hwang, Y.-K.; Lee, U. H.; Chang, J.-S.; Serre, C.; Rodrigues, A. E., Reverse Shape Selectivity in the Liquid-Phase Adsorption of Xylene Isomers in Zirconium Terephthalate MOF UiO-66. *Langmuir* **2012**, *28* (13), 5715-5723. doi:10.1021/la3004118.
52. Küsgens, P.; Zgaverdea, A.; Fritz, H.-G.; Siegle, S.; Kaskel, S., Metal-Organic Frameworks in Monolithic Structures. *Journal of the American Ceramic Society* **2010**, *93* (9), 2476-2479. doi:10.1111/j.1551-2916.2010.03824.x.
53. Ren, J.; Segakweng, T.; Langmi, H. W.; North, B. C.; Mathe, M., Ni foam-immobilized MIL-101(Cr) nanocrystals toward system integration for hydrogen storage. *Journal of Alloys and Compounds* **2015**, *645*, S170-S173. doi:10.1016/j.jallcom.2015.01.083.
54. Pinto, M. L.; Dias, S.; Pires, J., Composite MOF Foams: The Example of UiO-66/Polyurethane. *Acs Appl Mater Inter* **2013**, *5* (7), 2360-2363. doi:10.1021/am303089g.
55. Chen, Y.; Huang, X.; Zhang, S.; Li, S.; Cao, S.; Pei, X.; Zhou, J.; Feng, X.; Wang, B., Shaping of Metal–Organic Frameworks: From Fluid to Shaped Bodies and Robust Foams. *J Am Chem Soc* **2016**, *138* (34), 10810-10813. doi:10.1021/jacs.6b06959.
56. Kummer, H.; Jeremias, F.; Warlo, A.; Fuldner, G.; Fröhlich, D.; Janiak, C.; Gläser, R.; Henninger, S. K., A Functional Full-Scale Heat Exchanger Coated with Aluminum

- Fumarate Metal–Organic Framework for Adsorption Heat Transformation. *Ind Eng Chem Res* **2017**, *56* (29), 8393-8398. doi:10.1021/acs.iecr.7b00106.
57. Fathieh, F.; Kalmutzki, M. J.; Kapustin, E. A.; Waller, P. J.; Yang, J.; Yaghi, O. M., Practical water production from desert air. *Sci Adv* **2018**, *4* (6). doi:10.1126/sciadv.aat3198.
58. Hanikel, N.; Prévot, M. S.; Fathieh, F.; Kapustin, E. A.; Lyu, H.; Wang, H.; Diercks, N. J.; Glover, T. G.; Yaghi, O. M., Rapid Cycling and Exceptional Yield in a Metal–Organic Framework Water Harvester. *ACS Central Science* **2019**, *5* (10), 1699-1706. doi:10.1021/acscentsci.9b00745.
59. Cychosz Struckhoff, K.; Thommes, M.; Sarkisov, L., On the Universality of Capillary Condensation and Adsorption Hysteresis Phenomena in Ordered and Crystalline Mesoporous Materials. *Advanced Materials Interfaces* **2020**, *7* (12). doi:10.1002/admi.202000184.
60. Canivet, J.; Fateeva, A.; Guo, Y.; Coasne, B.; Farrusseng, D., Water adsorption in MOFs: fundamentals and applications. *Chem. Soc. Rev.* **2014**, *43* (16), 5594-5617. doi:10.1039/c4cs00078a.
61. Rieth, A. J.; Yang, S.; Wang, E. N.; Dincă, M., Record Atmospheric Fresh Water Capture and Heat Transfer with a Material Operating at the Water Uptake Reversibility Limit. *ACS Central Science* **2017**, *3* (6), 668-672. doi:10.1021/acscentsci.7b00186.
62. Rieth, A. J.; Tulchinsky, Y.; Dincă, M., High and Reversible Ammonia Uptake in Mesoporous Azolate Metal–Organic Frameworks with Open Mn, Co, and Ni Sites. *J Am Chem Soc* **2016**, *138* (30), 9401-9404. doi:10.1021/jacs.6b05723.
63. Wright, A. M.; Rieth, A. J.; Yang, S.; Wang, E. N.; Dincă, M., Precise control of pore hydrophilicity enabled by post-synthetic cation exchange in metal–organic frameworks. *Chem Sci* **2018**, *9* (15), 3856-3859. doi:10.1039/c8sc00112j.
64. Liu, Z. D.; Zhu, J.; Peng, C.; Wakihara, T.; Okubo, T., Continuous flow synthesis of ordered porous materials: from zeolites to metal-organic frameworks and mesoporous silica. *React Chem Eng* **2019**, *4* (10), 1699-1720. doi:10.1039/c9re00142e.
65. Song, H.; Chen, D. L.; Ismagilov, R. F., Reactions in droplets in microfluidic channels. *Angew Chem Int Edit* **2006**, *45* (44), 7336-7356. doi:10.1002/anie.200601554.
66. Stroock, A. D., Chaotic Mixer for Microchannels. *Science* **2002**, *295* (5555), 647-651. doi:10.1126/science.1066238.
67. Ghaini, A.; Mescher, A.; Agar, D. W., Hydrodynamic studies of liquid–liquid slug flows in circular microchannels. *Chem Eng Sci* **2011**, *66* (6), 1168-1178. doi:10.1016/j.ces.2010.12.033.
68. Shui, L.; Eijkel, J. C. T.; van den Berg, A., Multiphase flow in microfluidic systems – Control and applications of droplets and interfaces. *Advances in Colloid and Interface Science* **2007**, *133* (1), 35-49. doi:10.1016/j.cis.2007.03.001.
69. Günther, A.; Jensen, K. F., Multiphase microfluidics: from flow characteristics to chemical and materials synthesis. *Lab Chip* **2006**, *6* (12), 1487-1503. doi:10.1039/b609851g.
70. Wang, J.; Wang, J.; Feng, L.; Lin, T., Fluid mixing in droplet-based microfluidics with a serpentine microchannel. *RSC Advances* **2015**, *5* (126), 104138-104144. doi:10.1039/c5ra21181f.

71. Bai, Y.; Dou, Y.; Xie, L.-H.; Rutledge, W.; Li, J.-R.; Zhou, H.-C., Zr-based metal–organic frameworks: design, synthesis, structure, and applications. *Chemical Society Reviews* **2016**, *45* (8), 2327–2367. doi:10.1039/c5cs00837a.
72. Zhou, H. C.; Long, J. R.; Yaghi, O. M., Introduction to Metal-Organic Frameworks. *Chem Rev* **2012**, *112* (2), 673–674. doi:10.1021/cr300014x.
73. Hendon, C. H.; Rieth, A. J.; Korzynski, M. D.; Dinca, M., Grand Challenges and Future Opportunities for Metal-Organic Frameworks. *Accs Central Sci* **2017**, *3* (6), 554–563. doi:10.1021/acscentsci.7b00197.
74. Lin, K. S.; Adhikari, A. K.; Ku, C. N.; Chiang, C. L.; Kuo, H., Synthesis and characterization of porous HKUST-1 metal organic frameworks for hydrogen storage. *Int J Hydrogen Energ* **2012**, *37* (18), 13865–13871. doi:10.1016/j.ijhydene.2012.04.105.
75. Chen, W.; Wu, C. S., Synthesis, functionalization, and applications of metal-organic frameworks in biomedicine. *Dalton T* **2018**, *47* (7), 2114–2133. doi:10.1039/c7dt04116k.
76. Horcajada, P.; Gref, R.; Baati, T.; Allan, P. K.; Maurin, G.; Couvreur, P.; Ferey, G.; Morris, R. E.; Serre, C., Metal-Organic Frameworks in Biomedicine. *Chem Rev* **2012**, *112* (2), 1232–1268. doi:10.1021/cr200256v.
77. Lee, J.; Farha, O. K.; Roberts, J.; Scheidt, K. A.; Nguyen, S. T.; Hupp, J. T., Metal-organic framework materials as catalysts. *Chem Soc Rev* **2009**, *38* (5), 1450–1459. doi:10.1039/b807080f.
78. Yuan, S.; Li, Y.; Peng, J.; Questell-Santiago, Y. M.; Akkiraju, K.; Giordano, L.; Zheng, D. J.; Bagi, S.; Román-Leshkov, Y.; Shao-Horn, Y., Conversion of Methane into Liquid Fuels—Bridging Thermal Catalysis with Electrocatalysis. *Advanced Energy Materials* **2020**, *10* (40). doi:10.1002/aenm.202002154.
79. Moghadam, P. Z.; Li, A.; Wiggin, S. B.; Tao, A.; Maloney, A. G. P.; Wood, P. A.; Ward, S. C.; Fairen-Jimenez, D., Development of a Cambridge Structural Database Subset: A Collection of Metal–Organic Frameworks for Past, Present, and Future. *Chem Mater* **2017**, *29* (7), 2618–2625. doi:10.1021/acs.chemmater.7b00441.
80. Yuan, S.; Feng, L.; Wang, K.; Pang, J.; Bosch, M.; Lollar, C.; Sun, Y.; Qin, J.; Yang, X.; Zhang, P.; Wang, Q.; Zou, L.; Zhang, Y.; Zhang, L.; Fang, Y.; Li, J.; Zhou, H.-C., Stable Metal-Organic Frameworks: Design, Synthesis, and Applications. *Advanced Materials* **2018**, *30* (37). doi:10.1002/adma.201704303.
81. Furukawa, H.; Gandara, F.; Zhang, Y. B.; Jiang, J. C.; Queen, W. L.; Hudson, M. R.; Yaghi, O. M., Water Adsorption in Porous Metal-Organic Frameworks and Related Materials. *J Am Chem Soc* **2014**, *136* (11), 4369–4381. doi:10.1021/ja500330a.
82. Liang, W.; Chevreau, H.; Ragon, F.; Southon, P. D.; Peterson, V. K.; D'Alessandro, D. M., Tuning pore size in a zirconium–tricarboxylate metal–organic framework. *CrystEngComm* **2014**, *16* (29), 6530–6533. doi:10.1039/c4ce01031k.
83. Baek, J.; Rungtaweevoranit, B.; Pei, X.; Park, M.; Fakra, S. C.; Liu, Y.-S.; Matheu, R.; Alshimri, S. A.; Alshehri, S.; Trickett, C. A.; Somorjai, G. A.; Yaghi, O. M., Bioinspired Metal–Organic Framework Catalysts for Selective Methane Oxidation to Methanol. *J Am Chem Soc* **2018**, *140* (51), 18208–18216. doi:10.1021/jacs.8b11525.
84. Peng, Y.; Huang, H.; Zhang, Y.; Kang, C.; Chen, S.; Song, L.; Liu, D.; Zhong, C., A versatile MOF-based trap for heavy metal ion capture and dispersion. *Nat Commun* **2018**, *9* (1). doi:10.1038/s41467-017-02600-2.

85. Efome, J. E.; Rana, D.; Matsuura, T.; Lan, C. Q., Metal–organic frameworks supported on nanofibers to remove heavy metals. *Journal of Materials Chemistry A* **2018**, *6* (10), 4550-4555. doi:10.1039/c7ta10428f.
86. Trickett, C. A.; Osborn Popp, T. M.; Su, J.; Yan, C.; Weisberg, J.; Huq, A.; Urban, P.; Jiang, J.; Kalmutzki, M. J.; Liu, Q.; Baek, J.; Head-Gordon, M. P.; Somorjai, G. A.; Reimer, J. A.; Yaghi, O. M., Identification of the strong Brønsted acid site in a metal–organic framework solid acid catalyst. *Nature Chemistry* **2018**, *11* (2), 170-176. doi:10.1038/s41557-018-0171-z.
87. Zheng, H.-Q.; Liu, C.-Y.; Zeng, X.-Y.; Chen, J.; Lü, J.; Lin, R.-G.; Cao, R.; Lin, Z.-J.; Su, J.-W., MOF-808: A Metal–Organic Framework with Intrinsic Peroxidase-Like Catalytic Activity at Neutral pH for Colorimetric Biosensing. *Inorganic Chemistry* **2018**, *57* (15), 9096-9104. doi:10.1021/acs.inorgchem.8b01097.
88. Rojas-Buzo, S.; García-García, P.; Corma, A., Zr-MOF-808@MCM-41 catalyzed phosgene-free synthesis of polyurethane precursors. *Catalysis Science & Technology* **2019**, *9* (1), 146-156. doi:10.1039/c8cy02235f.
89. Schaate, A.; Roy, P.; Godt, A.; Lippke, J.; Waltz, F.; Wiebcke, M.; Behrens, P., Modulated Synthesis of Zr-Based Metal-Organic Frameworks: From Nano to Single Crystals. *Chemistry - A European Journal* **2011**, *17* (24), 6643-6651. doi:10.1002/chem.201003211.
90. Monsalve-Bravo, G. M.; Moscoso-Vasquez, H. M.; Alvarez, H., Scaleup of Batch Reactors Using Phenomenological-Based Models. *Ind Eng Chem Res* **2014**, *53* (22), 9439-9453. doi:10.1021/ie500587r.
91. Fitzpatrick, D. E.; Ley, S. V., Engineering chemistry: integrating batch and flow reactions on a single, automated reactor platform. *React Chem Eng* **2016**, *1* (6), 629-635. doi:10.1039/c6re00160b.
92. Bayliss, P. A.; Ibarra, I. A.; Pérez, E.; Yang, S.; Tang, C. C.; Poliakoff, M.; Schröder, M., Synthesis of metal–organic frameworks by continuous flow. *Green Chem.* **2014**, *16* (8), 3796-3802. doi:10.1039/c4gc00313f.
93. Reinsch, H.; Waitschat, S.; Chavan, S. M.; Lillerud, K. P.; Stock, N., A Facile “Green” Route for Scalable Batch Production and Continuous Synthesis of Zirconium MOFs. *Eur J Inorg Chem* **2016**, *2016* (27), 4490-4498. doi:10.1002/ejic.201600295.
94. Li, Z.-Q.; Yang, J.-C.; Sui, K.-W.; Yin, N., Facile synthesis of metal-organic framework MOF-808 for arsenic removal. *Materials Letters* **2015**, *160*, 412-414. doi:10.1016/j.matlet.2015.08.004.
95. Wang, Y.; Li, L.; Yan, L.; Cao, L.; Dai, P.; Gu, X.; Zhao, X., Continuous synthesis for zirconium metal-organic frameworks with high quality and productivity via microdroplet flow reaction. *Chinese Chemical Letters* **2018**, *29* (6), 849-853. doi:10.1016/j.ccllet.2017.09.057.
96. Faustini, M.; Kim, J.; Jeong, G. Y.; Kim, J. Y.; Moon, H. R.; Ahn, W. S.; Kim, D. P., Microfluidic Approach toward Continuous and Ultrafast Synthesis of Metal-Organic Framework Crystals and Hetero Structures in Confined Microdroplets. *J Am Chem Soc* **2013**, *135* (39), 14619-14626. doi:10.1021/ja4039642.
97. Kashid, M. N.; Agar, D. W., Hydrodynamics of liquid-liquid slug flow capillary microreactor: Flow regimes, slug size and pressure drop. *Chem Eng J* **2007**, *131* (1-3), 1-13. doi:10.1016/j.cej.2006.11.020.

98. Ufer, A.; Mendorf, M.; Ghaini, A.; Agar, D. W., Liquid-Liquid Slug Flow Capillary Microreactor. *Chemical Engineering & Technology* **2011**, *34* (3), 353-360. doi:10.1002/ceat.201000334.
99. Patterson, J. P.; Abellan, P.; Denny, M. S.; Park, C.; Browning, N. D.; Cohen, S. M.; Evans, J. E.; Gianneschi, N. C., Observing the Growth of Metal-Organic Frameworks by in Situ Liquid Cell Transmission Electron Microscopy. *J Am Chem Soc* **2015**, *137* (23), 7322-7328. doi:10.1021/jacs.5b00817.
100. Shi, H.-h.; Xiao, Y.; Ferguson, S.; Huang, X.; Wang, N.; Hao, H.-x., Progress of crystallization in microfluidic devices. *Lab on a Chip* **2017**, *17* (13), 2167-2185. doi:10.1039/c6lc01225f.
101. Zahn, G.; Zerner, P.; Lippke, J.; Kempf, F. L.; Lilienthal, S.; Schröder, C. A.; Schneider, A. M.; Behrens, P., Insight into the mechanism of modulated syntheses: in situ synchrotron diffraction studies on the formation of Zr-fumarate MOF. *CrystEngComm* **2014**, *16* (39), 9198-9207. doi:10.1039/c4ce01095g.
102. Bagi, S.; Wright, A. M.; Oppenheim, J.; Dincă, M.; Román-Leshkov, Y., Accelerated Synthesis of a Ni₂Cl₂(BTDD) Metal–Organic Framework in a Continuous Flow Reactor for Atmospheric Water Capture. *ACS Sustainable Chemistry & Engineering* **2021**, *9* (11), 3996-4003. doi:10.1021/acssuschemeng.0c07055.
103. Hartmann, M.; Machoke, A. G.; Schwieger, W., Catalytic test reactions for the evaluation of hierarchical zeolites. *Chemical Society Reviews* **2016**, *45* (12), 3313-3330. doi:10.1039/c5cs00935a.
104. Sindoro, M.; Yanai, N.; Jee, A.-Y.; Granick, S., Colloidal-Sized Metal–Organic Frameworks: Synthesis and Applications. *Accounts of Chemical Research* **2013**, *47* (2), 459-469. doi:10.1021/ar400151n.
105. Moh, P. Y.; Brenda, M.; Anderson, M. W.; Attfield, M. P., Crystallisation of solvothermally synthesised ZIF-8 investigated at the bulk, single crystal and surface level. *CrystEngComm* **2013**, *15* (45). doi:10.1039/c3ce40943k.
106. Bowden, G.; Pichler, B.; Maurer, A., Optimization of the copper mediated [F-18]radiofluorination (CMRF) of arylstannane precursors using a "design of experiments" (DoE) approach. *J Labelled Compd Rad* **2019**, *62*, S339-S340.
107. Bowden, G. D.; Pichler, B. J.; Maurer, A., A Design of Experiments (DoE) Approach Accelerates the Optimization of Copper-Mediated F-18-Fluorination Reactions of Arylstannanes. *Sci Rep-Uk* **2019**, *9*. doi:ARTN 11370
10.1038/s41598-019-47846-6.
108. Weissman, S. A.; Anderson, N. G., Design of experiments (DoE) and process optimization. A review of recent publications. *Org Process Res Dev* **2015**, *19* (11), 1605-1633.
109. Murray, P. M.; Bellany, F.; Benhamou, L.; Bucar, D. K.; Tabor, A. B.; Sheppard, T. D., The application of design of experiments (DoE) reaction optimisation and solvent selection in the development of new synthetic chemistry. *Org Biomol Chem* **2016**, *14* (8), 2373-2384. doi:10.1039/c5ob01892g.
110. Tummala, S.; Ramirez, A.; Srivastava, S.; Hallow, D. M., DEVELOPMENT OF DESIGN SPACE FOR REACTION STEPS: APPROACHES AND CASE STUDIES FOR IMPURITY CONTROL. *Chemical Engineering in the Pharmaceutical Industry: Active Pharmaceutical Ingredients* **2019**, 1091-1122.

111. Illg, T.; Lob, P.; Hessel, V., Flow chemistry using milli- and microstructured reactors-From conventional to novel process windows. *Bioorgan Med Chem* **2010**, *18* (11), 3707-3719. doi:10.1016/j.bmc.2010.03.073.
112. Thommes, M.; Kaneko, K.; Neimark, A. V.; Olivier, J. P.; Rodriguez-Reinoso, F.; Rouquerol, J.; Sing, K. S. W., Physisorption of gases, with special reference to the evaluation of surface area and pore size distribution (IUPAC Technical Report). *Pure and Applied Chemistry* **2015**, *87* (9-10), 1051-1069. doi:10.1515/pac-2014-1117.
113. Wei, R.; Gaggioli, C. A.; Li, G.; Islamoglu, T.; Zhang, Z.; Yu, P.; Farha, O. K.; Cramer, C. J.; Gagliardi, L.; Yang, D.; Gates, B. C., Tuning the Properties of Zr₆O₈ Nodes in the Metal Organic Framework UiO-66 by Selection of Node-Bound Ligands and Linkers. *Chem Mater* **2019**, *31* (5), 1655-1663. doi:10.1021/acs.chemmater.8b05037.
114. Gómez-Gualdrón, D. A.; Moghadam, P. Z.; Hupp, J. T.; Farha, O. K.; Snurr, R. Q., Application of Consistency Criteria To Calculate BET Areas of Micro- And Mesoporous Metal–Organic Frameworks. *J Am Chem Soc* **2015**, *138* (1), 215-224. doi:10.1021/jacs.5b10266.
115. Liu, H.; Zhang, Z.; Tang, J.; Fei, Z.; Liu, Q.; Chen, X.; Cui, M.; Qiao, X., Quest for pore size effect on the catalytic property of defect-engineered MOF-808-SO₄ in the addition reaction of isobutylene with ethylene glycol. *Journal of Solid State Chemistry* **2019**, *269*, 9-15. doi:10.1016/j.jssc.2018.07.030.
116. Jia, C. M.; Cirujano, F. G.; Bueken, B.; Claes, B.; Jonckheere, D.; Van Geem, K. M.; De Vos, D., Geminal Coordinatively Unsaturated Sites on MOF-808 for the Selective Uptake of Phenolics from a Real Bio-Oil Mixture. *Chemsuschem* **2019**, *12* (6), 1256-1266. doi:10.1002/cssc.201802692.
117. Valenzano, L.; Civalleri, B.; Chavan, S.; Bordiga, S.; Nilsen, M. H.; Jakobsen, S.; Lillerud, K. P.; Lamberti, C., Disclosing the Complex Structure of UiO-66 Metal Organic Framework: A Synergic Combination of Experiment and Theory. *Chem Mater* **2011**, *23* (7), 1700-1718. doi:10.1021/cm1022882.
118. Benaskar, F.; Ben-Abdelmoumen, A.; Patil, N. G.; Rebrov, E. V.; Meuldijk, J.; Hulshof, L. A.; Hessel, V.; Krtshil, U.; Schouten, J. C., Cost Analysis for a Continuously Operated Fine Chemicals Production Plant at 10 Kg/Day Using a Combination of Microprocessing and Microwave Heating. *Journal of Flow Chemistry* **2011**, *1* (2), 74-89. doi:10.1556/jfchem.2011.00015.
119. DeSantis, D.; Mason, J. A.; James, B. D.; Houchins, C.; Long, J. R.; Veenstra, M., Techno-economic Analysis of Metal–Organic Frameworks for Hydrogen and Natural Gas Storage. *Energy & Fuels* **2017**, *31* (2), 2024-2032. doi:10.1021/acs.energyfuels.6b02510.
120. Ghaini, A.; Mescher, A.; Agar, D. W., Hydrodynamic studies of liquid-liquid slug flows in circular microchannels. *Chem Eng Sci* **2011**, *66* (6), 1168-1178. doi:10.1016/j.ces.2010.12.033.
121. Schoenecker, P. M.; Belancik, G. A.; Grabicka, B. E.; Walton, K. S., Kinetics study and crystallization process design for scale-up of UiO-66-NH₂ synthesis. *AIChE Journal* **2013**, *59* (4), 1255-1262. doi:10.1002/aic.13901.
122. Smart, C.; Reese, G.; Adams, L.; Batchelor, A.; Redrick, A., Process-Based Cost Modeling. *Journal of Parametrics* **2011**, *26* (1), 79-100. doi:10.1080/10157891.2007.10462279.
123. ISO New England Air Emissions Report. https://www.iso-ne.com/static-assets/documents/2019/04/2017_emissions_report.pdf Accessed May 22, 2020.

124. Kamp, C. J.; Bagi, S. D., Advanced analytical methods for the study of lubricant-derived ash and associated impacts on engine aftertreatment components. In *SAE Technical Paper Series*, 2019. doi:10.4271/2019-01-2293.
125. Sharma, V.; Bagi, S.; Patel, M.; Aderniran, O.; Aswath, P. B., Structure and Chemistry of Soot and Its Role in Wear of Diesel Engines. *Tribology Online* **2016**, *11* (5), 551-555. doi:10.2474/trol.11.551.
126. Sharma, V.; Bagi, S.; Patel, M.; Aderniran, O.; Aswath, P. B., Influence of Engine Age on Morphology and Chemistry of Diesel Soot Extracted from Crankcase Oil. *Energy & Fuels* **2016**, *30* (3), 2276-2284. doi:10.1021/acs.energyfuels.5b02512.
127. Bagi, S.; Sharma, V.; Aswath, P. B., Role of dispersant on soot-induced wear in Cummins ISB engine test. *Carbon* **2018**, *136*, 395-408. doi:10.1016/j.carbon.2018.04.066.
128. Vyavhare, K.; Bagi, S.; Patel, M.; Aswath, P. B., Impact of Diesel Engine Oil Additives–Soot Interactions on Physiochemical, Oxidation, and Wear Characteristics of Soot. *Energy & Fuels* **2019**, *33* (5), 4515-4530. doi:10.1021/acs.energyfuels.8b03841.
129. Bagi, S.; Kamp, C. J.; Sharma, V.; Aswath, P. B., Multiscale characterization of exhaust and crankcase soot extracted from heavy-duty diesel engine and implications for DPF ash. *Fuel* **2020**, 282. doi:10.1016/j.fuel.2020.118878.
130. Bagi, S.; Sharma, V.; Patel, M.; Aswath, P. B., Effects of Diesel Soot Composition and Accumulated Vehicle Mileage on Soot Oxidation Characteristics. *Energy & Fuels* **2016**, *30* (10), 8479-8490. doi:10.1021/acs.energyfuels.6b01304.
131. Bagi, S.; Singh, N.; Andrew, R., Investigation into Ash from Field Returned DPF Units: Composition, Distribution, Cleaning Ability and DPF Performance Recovery. In *SAE Technical Paper Series*, 2016. doi:10.4271/2016-01-0928.
132. Kamp, C. J.; Bagi, S.; Wang, Y., Phenomenological Investigations of Mid-Channel Ash Deposit Formation and Characteristics in Diesel Particulate Filters. In *SAE Technical Paper Series*, 2019. doi:10.4271/2019-01-0973.
133. Bagi, S.; Bowker, R.; Andrew, R., Understanding Chemical Composition and Phase Transitions of Ash from Field Returned DPF Units and Their Correlation with Filter Operating Conditions. *SAE International Journal of Fuels and Lubricants* **2016**, *9* (1), 239-259. doi:10.4271/2016-01-0898.
134. Kamp, C. J.; Zhang, S.; Bagi, S.; Wong, V.; Monahan, G.; Sappok, A.; Wang, Y., Ash Permeability Determination in the Diesel Particulate Filter from Ultra-High Resolution 3D X-Ray Imaging and Image-Based Direct Numerical Simulations. *SAE International Journal of Fuels and Lubricants* **2017**, *10* (2), 608-618. doi:10.4271/2017-01-0927.
135. Shah, A.; Bagi, S.; Aswath, P., Wear and Friction of Greases Containing Organic and Inorganic Sulfur Carriers. *Tribology Online* **2017**, *12* (4), 162-170. doi:10.2474/trol.12.162.
136. Vyavhare, K.; Bagi, S.; Pichumani, P. S.; Sharma, V.; Aswath, P. B., Chemical and physical properties of tribofilms formed by the interaction of ashless dithiophosphate anti-wear additives. *Lubrication Science* **2021**, *33* (4), 188-200. doi:10.1002/lis.1537.
137. Bagi, S.; Vyavhare, K.; Aswath, P. B., Tribological characteristics of greases with and without metallo-organic friction-modifiers. *Tribology - Materials, Surfaces & Interfaces* **2018**, *12* (4), 223-236. doi:10.1080/17515831.2018.1542790.

138. Bagi, S.; Aswath, P., Mechanism of Friction and Wear in MoS₂ and ZDDP/F-PTFE Greases under Spectrum Loading Conditions. *Lubricants* **2015**, *3* (4), 687-711. doi:10.3390/lubricants3040687.
139. Bagi, S. D.; Aswath, P. B., Role of MoS₂ morphology on wear and friction under spectrum loading conditions. *Lubrication Science* **2015**, *27* (7), 429-449. doi:10.1002/lis.1296.
140. Sonneveld, E. J.; Visser, J. W., Automatic Collection of Powder Data from Photographs. *J Appl Crystallogr* **1975**, *8* (Feb1), 1-7. doi:10.1107/S0021889875009417.
141. Hirschle, P.; Preiß, T.; Auras, F.; Pick, A.; Völkner, J.; Valdepérez, D.; Witte, G.; Parak, W. J.; Rädler, J. O.; Wuttke, S., Exploration of MOF nanoparticle sizes using various physical characterization methods – is what you measure what you get? *Crystengcomm* **2016**, *18* (23), 4359-4368. doi:10.1039/c6ce00198j.
142. Jimenez-Gonzalez, C. n.; Curzons, A. D.; Constable, D. J. C.; Cunningham, V. L., Expanding GSK's Solvent Selection Guide? application of life cycle assessment to enhance solvent selections. *Clean Technologies and Environmental Policy* **2004**, *7* (1), 42-50. doi:10.1007/s10098-004-0245-z.
143. Kalinovsky, Y.; Cooper, N. J.; Main, M. J.; Holder, S. J.; Blight, B. A., Microwave-assisted activation and modulator removal in zirconium MOFs for buffer-free CWA hydrolysis. *Dalton T* **2017**, *46* (45), 15704-15709. doi:10.1039/c7dt03616g.
144. Rowsell, J. L. C.; Yaghi, O. M., Metal-organic frameworks: a new class of porous materials. *Micropor Mesopor Mat* **2004**, *73* (1-2), 3-14. doi:10.1016/j.micromeso.2004.03.034.
145. Furukawa, H.; Cordova, K. E.; O'Keeffe, M.; Yaghi, O. M., The Chemistry and Applications of Metal-Organic Frameworks. *Science* **2013**, *341* (6149). doi:10.1126/science.1230444.
146. Jiang, J.; Yaghi, O. M., Brønsted Acidity in Metal–Organic Frameworks. *Chem Rev* **2015**, *115* (14), 6966-6997. doi:10.1021/acs.chemrev.5b00221.
147. Logan, M. W.; Langevin, S.; Xia, Z. Y., Reversible Atmospheric Water Harvesting Using Metal-Organic Frameworks. *Sci Rep-Uk* **2020**, *10* (1). doi:ARTN 1492
10.1038/s41598-020-58405-9.
148. Alvarez, A. J.; Myerson, A. S., Continuous Plug Flow Crystallization of Pharmaceutical Compounds. *Crystal Growth & Design* **2010**, *10* (5), 2219-2228. doi:10.1021/cg901496s.
149. Stelzer, T.; Lakerveld, R.; Myerson, A. S., CHAPTER 7. Process Intensification in Continuous Crystallization. In *The Handbook of Continuous Crystallization*, 2020; pp 266-320. doi:10.1039/9781788013581-00266.
150. Chen, D. L.; Gerdt, C. J.; Ismagilov, R. F., Using Microfluidics to Observe the Effect of Mixing on Nucleation of Protein Crystals. *J Am Chem Soc* **2005**, *127* (27), 9672-9673. doi:10.1021/ja052279v.
151. Millange, F.; El Osta, R.; Medina, M. E.; Walton, R. I., A time-resolved diffraction study of a window of stability in the synthesis of a copper carboxylate metal–organic framework. *Crystengcomm* **2011**, *13* (1), 103-108. doi:10.1039/c0ce00530d.
152. Ragon, F.; Horcajada, P.; Chevreau, H.; Hwang, Y. K.; Lee, U. H.; Miller, S. R.; Devic, T.; Chang, J.-S.; Serre, C., In Situ Energy-Dispersive X-ray Diffraction for the

Synthesis Optimization and Scale-up of the Porous Zirconium Terephthalate UiO-66. *Inorg Chem* **2014**, *53* (5), 2491-2500. doi:10.1021/ic402514n.

153. Reinsch, H.; Stock, N., Formation and characterisation of Mn-MIL-100. *Crystengcomm* **2013**, *15* (3), 544-550. doi:10.1039/c2ce26436f.

154. Cravillon, J.; Schröder, C. A.; Nayuk, R.; Gummel, J.; Huber, K.; Wiebcke, M., Fast Nucleation and Growth of ZIF-8 Nanocrystals Monitored by Time-Resolved In Situ Small-Angle and Wide-Angle X-Ray Scattering. *Angewandte Chemie International Edition* **2011**, *50* (35), 8067-8071. doi:10.1002/anie.201102071.

155. Stavitski, E.; Goesten, M.; Juan-Alcañiz, J.; Martinez-Joaristi, A.; Serra-Crespo, P.; Petukhov, A. V.; Gascon, J.; Kapteijn, F., Kinetic Control of Metal-Organic Framework Crystallization Investigated by Time-Resolved In Situ X-Ray Scattering. *Angewandte Chemie International Edition* **2011**, *50* (41), 9624-9628. doi:10.1002/anie.201101757.

156. Liu, Z.; Zhu, J.; Peng, C.; Wakihara, T.; Okubo, T., Continuous flow synthesis of ordered porous materials: from zeolites to metal-organic frameworks and mesoporous silica. *React Chem Eng* **2019**, *4* (10), 1699-1720. doi:10.1039/c9re00142e.

157. Ahnfeldt, T.; Stock, N., Synthesis of isorecticular CAU-1 compounds: effects of linker and heating methods on the kinetics of the synthesis. *Crystengcomm* **2012**, *14* (2), 505-511. doi:10.1039/c1ce05956d.

158. Rowsell, J. L. C.; Yaghi, O. M., Metal-organic frameworks: a new class of porous materials. *Micropor Mesopor Mat* **2004**, *73* (1-2), 3-14. doi:10.1016/j.micromeso.2004.03.034.

159. Hausdorf, S.; Wagler, J.; Moßig, R.; Mertens, F. O. R. L., Proton and Water Activity-Controlled Structure Formation in Zinc Carboxylate-Based Metal Organic Frameworks. *The Journal of Physical Chemistry A* **2008**, *112* (33), 7567-7576. doi:10.1021/jp7110633.

160. Gualtieri, A. F., Synthesis of sodium zeolites from a natural halloysite. *Physics and Chemistry of Minerals* **2001**, *28* (10), 719-728. doi:10.1007/s002690100197.

161. Furukawa, H.; Gándara, F.; Zhang, Y.-B.; Jiang, J.; Queen, W. L.; Hudson, M. R.; Yaghi, O. M., Water Adsorption in Porous Metal-Organic Frameworks and Related Materials. *J Am Chem Soc* **2014**, *136* (11), 4369-4381. doi:10.1021/ja500330a.

162. McDonald, M. A.; Salami, H.; Harris, P. R.; Lagerman, C. E.; Yang, X.; Bommarius, A. S.; Grover, M. A.; Rousseau, R. W., Reactive crystallization: a review. *React Chem Eng* **2021**, *6* (3), 364-400. doi:10.1039/d0re00272k.

163. Forgan, R. S., Modulated self-assembly of metal-organic frameworks. *Chem Sci* **2020**, *11* (18), 4546-4562. doi:10.1039/d0sc01356k.

164. Venna, S. R.; Jasinski, J. B.; Carreon, M. A., Structural Evolution of Zeolitic Imidazolate Framework-8. *J Am Chem Soc* **2010**, *132* (51), 18030-18033. doi:10.1021/ja109268m.

165. Grand, J.; Awala, H.; Mintova, S., Mechanism of zeolites crystal growth: new findings and open questions. *Crystengcomm* **2016**, *18* (5), 650-664. doi:10.1039/c5ce02286j.

166. McGinty, J.; Yazdanpanah, N.; Price, C.; ter Horst, J. H.; Sefcik, J., CHAPTER 1. Nucleation and Crystal Growth in Continuous Crystallization. In *The Handbook of Continuous Crystallization*, 2020; pp 1-50. doi:10.1039/9781788013581-00001.

167. Cravillon, J.; Schröder, C. A.; Bux, H.; Rothkirch, A.; Caro, J.; Wiebcke, M., Formate modulated solvothermal synthesis of ZIF-8 investigated using time-resolved in

- situ X-ray diffraction and scanning electron microscopy. *Crystengcomm* **2012**, *14* (2), 492-498. doi:10.1039/c1ce06002c.
168. Jiang, M.; Papageorgiou, C. D.; Waetzig, J.; Hardy, A.; Langston, M.; Braatz, R. D., Indirect Ultrasonication in Continuous Slug-Flow Crystallization. *Crystal Growth & Design* **2015**, *15* (5), 2486-2492. doi:10.1021/acs.cgd.5b00263.
169. Jiang, M.; Zhu, Z.; Jimenez, E.; Papageorgiou, C. D.; Waetzig, J.; Hardy, A.; Langston, M.; Braatz, R. D., Continuous-Flow Tubular Crystallization in Slugs Spontaneously Induced by Hydrodynamics. *Crystal Growth & Design* **2014**, *14* (2), 851-860. doi:10.1021/cg401715e.
170. Rimez, B.; Debuysschère, R.; Conté, J.; Lecomte-Norrand, E.; Gourdon, C.; Cognet, P.; Scheid, B., Continuous-Flow Tubular Crystallization To Discriminate between Two Competing Crystal Polymorphs. 1. Cooling Crystallization. *Crystal Growth & Design* **2018**, *18* (11), 6431-6439. doi:10.1021/acs.cgd.8b00928.
171. Neugebauer, P.; Khinast, J. G., Continuous Crystallization of Proteins in a Tubular Plug-Flow Crystallizer. *Crystal Growth & Design* **2015**, *15* (3), 1089-1095. doi:10.1021/cg501359h.
172. Rubio-Martinez, M.; Hadley, T. D.; Batten, M. P.; Constanti-Carey, K.; Barton, T.; Marley, D.; Mönch, A.; Lim, K.-S.; Hill, M. R., Scalability of Continuous Flow Production of Metal-Organic Frameworks. *Chemsuschem* **2016**, *9* (9), 938-941. doi:10.1002/cssc.201501684.
173. Vacassy, R.; Lemaître, J.; Hofmann, H.; Gerlings, J. H., Calcium carbonate precipitation using new segmented flow tubular reactor. *Aiche J* **2000**, *46* (6), 1241-1252. doi:10.1002/aic.690460616.
174. Hussain, M. N.; Jordens, J.; John, J. J.; Braeken, L.; Van Gerven, T., Enhancing pharmaceutical crystallization in a flow crystallizer with ultrasound: Anti-solvent crystallization. *Ultrasonics Sonochemistry* **2019**, *59*. doi:10.1016/j.ultsonch.2019.104743.
175. Pal, S.; Madane, K.; Kulkarni, A. A., Antisolvent based precipitation: Batch, capillary flow reactor and impinging jet reactor. *Chem Eng J* **2019**, *369*, 1161-1171. doi:10.1016/j.cej.2019.03.107.
176. Rossi, D.; Jamshidi, R.; Saffari, N.; Kuhn, S.; Gavriilidis, A.; Mazzei, L., Continuous-Flow Sonocrystallization in Droplet-Based Microfluidics. *Crystal Growth & Design* **2015**, *15* (11), 5519-5529. doi:10.1021/acs.cgd.5b01153.
177. Song, H.; Chen, D. L.; Ismagilov, R. F., Reactions in Droplets in Microfluidic Channels. *Angewandte Chemie International Edition* **2006**, *45* (44), 7336-7356. doi:10.1002/anie.200601554.
178. Song, H.; Bringer, M. R.; Tice, J. D.; Gerds, C. J.; Ismagilov, R. F., Experimental test of scaling of mixing by chaotic advection in droplets moving through microfluidic channels. *Applied Physics Letters* **2003**, *83* (22), 4664-4666. doi:10.1063/1.1630378.
179. Mura, F.; Zaccone, A., Effects of shear flow on phase nucleation and crystallization. *Physical Review E* **2016**, *93* (4). doi:10.1103/PhysRevE.93.042803.
180. Pang, Y.; Sun, D.; Gu, Q.; Chou, K.-C.; Wang, X.; Li, Q., Comprehensive Determination of Kinetic Parameters in Solid-State Phase Transitions: An Extended Johnson–Mehl–Avrami–Kolomogorov Model with Analytical Solutions. *Crystal Growth & Design* **2016**, *16* (4), 2404-2415. doi:10.1021/acs.cgd.6b00187.
181. Millange, F.; Medina, M. I.; Guillou, N.; Férey, G.; Golden, K. M.; Walton, R. I., Time-Resolved In Situ Diffraction Study of the Solvothermal Crystallization of Some

- Prototypical Metal-Organic Frameworks. *Angewandte Chemie International Edition* **2010**, 49 (4), 763-766. doi:10.1002/anie.200905627.
182. Liu, X. Diffusion in Liquids: Equilibrium Molecular Simulations and Predictive Engineering Models. TU Delft, 2013. doi:10.4233/uuid:239b19f7-59d0-47b3-a3e3-dd1aeb19701f.
183. Wang, S. B.; Peng, Y. L., Natural zeolites as effective adsorbents in water and wastewater treatment. *Chem Eng J* **2010**, 156 (1), 11-24. doi:10.1016/j.cej.2009.10.029.
184. Rieth, A. J.; Dincă, M., Moisture Farming with Metal-Organic Frameworks. *Chem* **2017**, 2 (6), 757-759. doi:10.1016/j.chempr.2017.05.017.
185. Jenkins, B.; Gilbert, R.; Nelson, J. The 2030 Water Resources Group: Collaboration and Country Leadership to Strengthen Water Security 2017. <https://www.hks.harvard.edu/sites/default/files/2030%20WRG%20final.pdf>.
186. Jenkins, B. R., Decision Making for Sustainability. *Glob Iss Water Pol* **2018**, 19, 377-430. doi:10.1007/978-94-024-1213-0_12.
187. Kim, H.; Yang, S.; Rao, S. R.; Narayanan, S.; Kapustin, E. A.; Furukawa, H.; Umans, A. S.; Yaghi, O. M.; Wang, E. N., Water harvesting from air with metal-organic frameworks powered by natural sunlight. *Science* **2017**, 356 (6336), 430-432. doi:10.1126/science.aam8743.
188. Schneider, S. H., *Encyclopedia of climate and weather*. Oxford University Press: 2011; Vol. 1. doi:10.1093/acref/9780199765324.001.0001.
189. Wei, R. P.; Gaggioli, C. A.; Li, G. Z.; Islamoglu, T.; Zhang, Z. X.; Yu, P.; Farha, O. K.; Cramer, C. J.; Gagliardi, L.; Yang, D.; Gates, B. C., Tuning the Properties of Zr₆O₈ Nodes in the Metal Organic Framework UiO-66 by Selection of Node-Bound Ligands and Linkers. *Chem Mater* **2019**, 31 (5), 1655-1663. doi:10.1021/acs.chemmater.8b05037.
190. Rieth, A. J.; Hunter, K. M.; Dinca, M.; Paesani, F., Hydrogen bonding structure of confined water templated by a metal-organic framework with open metal sites. *Nat Commun* **2019**, 10. doi:10.1038/s41467-019-12751-z.
191. Rieth, A. J.; Wright, A. M.; Skorupskii, G.; Mancuso, J. L.; Hendon, C. H.; Dinca, M., Record-Setting Sorbents for Reversible Water Uptake by Systematic Anion Exchanges in Metal-Organic Frameworks. *J Am Chem Soc* **2019**, 141 (35), 13858-13866. doi:10.1021/jacs.9b06246.
192. Rieth, A. J.; Yang, S.; Wang, E. N.; Dinca, M., Record Atmospheric Fresh Water Capture and Heat Transfer with a Material Operating at the Water Uptake Reversibility Limit. *Acs Central Sci* **2017**, 3 (6), 668-672. doi:10.1021/acscentsci.7b00186.
193. Canivet, J.; Bonnefoy, J.; Daniel, C.; Legrand, A.; Coasne, B.; Farrusseng, D., Structure-property relationships of water adsorption in metal-organic frameworks. *New J Chem* **2014**, 38 (7), 3102-3111. doi:10.1039/c4nj00076e.
194. Coasne, B.; Gubbins, K. E.; Pellenq, R. J. M., Temperature effect on adsorption/desorption isotherms for a simple fluid confined within various nanopores. *Adsorption* **2005**, 11, 289-294. doi:DOI 10.1007/s10450-005-5939-y.
195. Batten, M. P.; Rubio-Martinez, M.; Hadley, T.; Carey, K. C.; Lim, K. S.; Polyzos, A.; Hill, M. R., Continuous flow production of metal-organic frameworks. *Curr Opin Chem Eng* **2015**, 8, 55-59. doi:10.1016/j.coche.2015.02.001.
196. Reinsch, H.; Waitschat, S.; Chavan, S. M.; Lillerud, K. P.; Stock, N., A Facile "Green" Route for Scalable Batch Production and Continuous Synthesis of Zirconium MOFs. *Eur J Inorg Chem* **2016**, (27), 4490-4498. doi:10.1002/ejic.201600295.

197. Waitschat, S.; Wharmby, M. T.; Stock, N., Flow-synthesis of carboxylate and phosphonate based metal-organic frameworks under non-solvothermal reaction conditions. *Dalton T* **2015**, 44 (24), 11235-11240. doi:10.1039/c5dt01100k.
198. Albuquerque, G. H.; Fitzmorris, R. C.; Ahmadi, M.; Wannemacher, N.; Thallapally, P. K.; McGrail, B. P.; Herman, G. S., Gas-liquid segmented flow microwave-assisted synthesis of MOF-74(Ni) under moderate pressures. *Crystengcomm* **2015**, 17 (29), 5502-5510. doi:10.1039/c5ce00848d.
199. Rasmussen, E. G.; Kramlich, J.; Novosselov, I. V., Scalable Continuous Flow Metal-Organic Framework (MOF) Synthesis Using Supercritical CO₂. *Acs Sustain Chem Eng* **2020**, 8 (26), 9680-9689. doi:10.1021/acssuschemeng.0c01429.
200. Gao, H.; Luan, Y.; Chaikittikul, K.; Dong, W.; Li, J.; Zhang, X.; Jia, D.; Yang, M.; Wang, G., A Facile in Situ Self-Assembly Strategy for Large-Scale Fabrication of CHS@MOF Yolk/Shell Structure and Its Catalytic Application in a Flow System. *Acs Appl Mater Inter* **2015**, 7 (8), 4667-4674. doi:10.1021/am508079j.
201. He, B.; Sadiq, M. M.; Batten, M. P.; Suzuki, K.; Rubio-Martinez, M.; Gardiner, J.; Hill, M. R., Continuous Flow Synthesis of a Zr Magnetic Framework Composite for Post-Combustion CO₂ Capture. *Chemistry – A European Journal* **2019**, 25 (57), 13184-13188. doi:10.1002/chem.201902560.
202. Bayliss, P. A.; Ibarra, I. A.; Perez, E.; Yang, S. H.; Tang, C. C.; Poliakoff, M.; Schroder, M., Synthesis of metal-organic frameworks by continuous flow. *Green Chem* **2014**, 16 (8), 3796-3802. doi:10.1039/c4gc00313f.
203. Jovanovic, J.; Zhou, W. Y.; Rebrov, E. V.; Nijhuis, T. A.; Hessel, V.; Schouten, J. C., Liquid-liquid slug flow: Hydrodynamics and pressure drop. *Chem Eng Sci* **2011**, 66 (1), 42-54. doi:10.1016/j.ces.2010.09.040.
204. Plutschack, M. B.; Pieber, B.; Gilmore, K.; Seeberger, P. H., The Hitchhiker's Guide to Flow Chemistry(II). *Chem Rev* **2017**, 117 (18), 11796-11893. doi:10.1021/acs.chemrev.7b00183.
205. Rieth, A. J.; Dinca, M., Controlled Gas Uptake in Metal-Organic Frameworks with Record Ammonia Sorption. *J Am Chem Soc* **2018**, 140 (9), 3461-3466. doi:10.1021/jacs.8b00313.
206. Dinca, M.; Rieth, A. J.; Tulchinsky, Y. Compositions comprising metal organic frameworks for the uptake of compounds and related methods 2017. <https://patents.google.com/patent/US10653993B2/en>.
207. Czaja, A. U.; Trukhan, N.; Muller, U., Industrial applications of metal-organic frameworks. *Chem Soc Rev* **2009**, 38 (5), 1284-1293. doi:10.1039/b804680h.
208. Barthe, P.; Guerneur, C.; Lobet, O.; Moreno, M.; Woehl, P.; Roberge, D. M.; Bieler, N.; Zimmermann, B., Continuous multi-injection reactor for multipurpose production - Part I. *Chem Eng Technol* **2008**, 31 (8), 1146-1154. doi:10.1002/ceat.200800132.
209. Eesa, M.; Barigou, M., CFD Simulation of Transverse Vibration Effects on Radial Temperature Profile and Thermal Entrance Length in Laminar Flow. *Aiche J* **2011**, 57 (1), 51-56. doi:10.1002/aic.12243.
210. Toh, K. H.; Ghajar, A. J., Heat-Transfer in the Thermal Entrance Region for Viscoelastic Fluids in Turbulent Pipe Flows. *Int J Heat Mass Tran* **1988**, 31 (6), 1261-1267. doi:10.1016/0017-9310(88)90068-3.

211. Hu, C., Reactor design and selection for effective continuous manufacturing of pharmaceuticals. *Journal of Flow Chemistry* **2021**. doi:10.1007/s41981-021-00164-3.
212. Rieth, A.; Dinca, M., Record-setting sorbents for water and ammonia: Engineering capacity, kinetics, and stability. *Abstr Pap Am Chem S* **2018**, 255. doi:10.1021/jacs.9b06246.
213. Rieth, A. J.; Wright, A. M.; Rao, S.; Kim, H.; LaPotin, A. D.; Wang, E. N.; Dinca, M., Tunable Metal-Organic Frameworks Enable High-Efficiency Cascaded Adsorption Heat Pumps. *J Am Chem Soc* **2018**, 140 (50), 17591-17596. doi:10.1021/jacs.8b09655.
214. Tulchinsky, Y.; Hendon, C. H.; Lomachenko, K. A.; Borfecchia, E.; Melot, B. C.; Hudson, M. R.; Tarver, J. D.; Korzynski, M. D.; Stubbs, A. W.; Kagan, J. J.; Lamberti, C.; Brown, C. M.; Dinca, M., Reversible Capture and Release of Cl₂ and Br₂ with a Redox-Active Metal-Organic Framework. *J Am Chem Soc* **2017**, 139 (16), 5992-5997. doi:10.1021/jacs.7b02161.
215. Roberge, D. M.; Gottsponer, M.; Eyholzer, M.; Kockmann, N., Industrial design, scale-up, and use of microreactors. *Chim Oggi* **2009**, 27 (4), 8-11.
216. LaPotin, A.; Kim, H.; Rao, S. R.; Wang, E. N., Adsorption-Based Atmospheric Water Harvesting: Impact of Material and Component Properties on System-Level Performance. *Accounts of Chemical Research* **2019**, 52 (6), 1588-1597. doi:10.1021/acs.accounts.9b00062.
217. Wang, S.; Peng, Y., Natural zeolites as effective adsorbents in water and wastewater treatment. *Chem Eng J* **2010**, 156 (1), 11-24. doi:10.1016/j.cej.2009.10.029.
218. Elimelech, M.; Phillip, W. A., The Future of Seawater Desalination: Energy, Technology, and the Environment. *Science* **2011**, 333 (6043), 712-717. doi:10.1126/science.1200488.
219. Kim, H.; Yang, S.; Rao, S. R.; Narayanan, S.; Kapustin, E. A.; Furukawa, H.; Umans, A. S.; Yaghi, O. M.; Wang, E. N., Water harvesting from air with metal-organic frameworks powered by natural sunlight. *Science* **2017**, 356 (6336), 430-434. doi:10.1126/science.aam8743.
220. Lee, A.; Moon, M.-W.; Lim, H.; Kim, W.-D.; Kim, H.-Y., Water harvest via dewing. *Langmuir* **2012**, 28 (27), 10183-10191. doi:10.1021/la3013987.
221. Kim, H.; Rao, S. R.; Kapustin, E. A.; Zhao, L.; Yang, S.; Yaghi, O. M.; Wang, E. N., Adsorption-based atmospheric water harvesting device for arid climates. *Nat Commun* **2018**, 9 (1). doi:10.1038/s41467-018-03162-7.
222. Logan, M. W.; Langevin, S.; Xia, Z., Reversible Atmospheric Water Harvesting Using Metal-Organic Frameworks. *Scientific Reports* **2020**, 10 (1). doi:10.1038/s41598-020-58405-9.
223. Huang, J.; Xia, X.; Hu, X.; Li, S.; Liu, K., A general method for measuring the thermal conductivity of MOF crystals. *International Journal of Heat and Mass Transfer* **2019**, 138, 11-16. doi:10.1016/j.ijheatmasstransfer.2019.04.018.
224. Williamson, J. W. CHARACTERIZING CIGARETTE LIGHTER FLAMES TO REDUCE UNWANTED IGNITION. University of Maryland, College Park, M.S. Thesis, 2003.
225. Gang, P.; Guiqiang, L.; Xi, Z.; Jie, J.; Yuehong, S., Experimental study and exergetic analysis of a CPC-type solar water heater system using higher-temperature circulation in winter. *Solar Energy* **2012**, 86 (5), 1280-1286. doi:10.1016/j.solener.2012.01.019.

226. Cui, S.; Qin, M.; Marandi, A.; Steggles, V.; Wang, S.; Feng, X.; Nouar, F.; Serre, C., Metal-Organic Frameworks as advanced moisture sorbents for energy-efficient high temperature cooling. *Scientific Reports* **2018**, *8* (1). doi:10.1038/s41598-018-33704-4.
227. Coley, C. W.; Thomas, D. A.; Lummiss, J. A. M.; Jaworski, J. N.; Breen, C. P.; Schultz, V.; Hart, T.; Fishman, J. S.; Rogers, L.; Gao, H.; Hicklin, R. W.; Plehiers, P. P.; Byington, J.; Piotti, J. S.; Green, W. H.; Hart, A. J.; Jamison, T. F.; Jensen, K. F., A robotic platform for flow synthesis of organic compounds informed by AI planning. *Science* **2019**, *365* (6453). doi:10.1126/science.aax1566.